

THERMOELECTRIC STUDIES OF THE ZINC-ANTIMONY PHASES

THERMOELECTRIC STUDIES OF THE ZINC–ANTIMONY PHASES

By

CHUN-WAN TIMOTHY LO, B.Sc.

A Thesis Submitted to the School of Graduate Studies in Partial Fulfillment of the
Requirements for the Degree Doctor of Philosophy

McMaster University

© Copyright by Chun-wan Timothy Lo, August 2022

DOCTOR OF PHILOSOPHY (2022)

McMaster University
Hamilton, Ontario (Chemistry)

TITLE: Thermoelectric Studies of the Zinc–Antimony Phases

AUTHOR: Chun-wan Timothy Lo, B. Sc. (McMaster University)

SUPERVISOR: Dr. Yuriy Mozharivskyj

NUMBER OF PAGES: xxxi, 262.

Lay Abstract

Thermoelectric materials are incorporated into thermoelectric devices to generate electricity from heat sources. As there are environmental concerns and increasing demand of energy supplies in the society, thermoelectricity may relieve some of the pressure by waste heat recovery, from internal combustion engines for example.

This work is dedicated to studying the zinc–antimony (Zn–Sb) materials and a focus on the $Zn_{13}Sb_{10}$ material for thermoelectric applications. This work aims to improve the thermoelectric efficiency of the $Zn_{13}Sb_{10}$ material, at the same time understand the changes on the physical properties brought by the structural and the compositional differences of the material. The relative Zn–Sb phases, such as ZnSb and Zn_3Sb_2 , were also characterized to compare their structures with their physical properties.

Abstract

This dissertation is dedicated to investigating the thermoelectric properties of the Zn – Sb phases and particularly the $Zn_{13}Sb_{10}$ material, which was shown to achieve a high ZT (1.3 at 670K) in 1997. The $Zn_{13}Sb_{10}$ material (known as “ Zn_4Sb_3 ”) was then extensively studied as a potential thermoelectric material. The $Zn_{13}Sb_{10}$ materials, however, were not widely adapted in thermoelectric applications.

A new synthetic procedure was developed to synthesize phase-pure $Zn_{13}Sb_{10}$ materials in this thesis, thus allowing a robust characterization of the $Zn_{13}Sb_{10}$ -based materials. This work aims to improve the thermoelectric performance of the $Zn_{13}Sb_{10}$ -based materials by substituting foreign elements into the structure of the $Zn_{13}Sb_{10}$ phase, at the same time characterize and navigate the synthesis-property-composition relationship of the doped $Zn_{13}Sb_{10}$ materials.

On the other hand, some relative Zn–Sb phases such as the α - and β - Zn_3Sb_2 were also studied in attempt to complete the characterizations of all Zn–Sb phases stable at room temperatures. The ZnSb phase, another well-studied Zn–Sb material, was investigated in coherence with the $Zn_{13}Sb_{10}$ materials to understand the effects to transport properties brought by the same atom replacement in the two systems. This was realized in the form of a comparison between the (Zn,Cd)Sb and (Zn,Cd) $_{13}Sb_{10}$ solid solution series.

Materials studied in this work were mostly made using the melt and solidification method. Powder and single-crystal X-ray diffractions were employed to characterize

samples' purity and structure determination. Energy-dispersive X-ray Spectroscopy (EDS) was used to determine sample compositions, especially to confirm the presence(s) of dopants in materials in small quantities. Physical properties of materials were measured to evaluate the thermoelectric performances of materials. Computational methods, such as the linear muffin-tin orbital (LMTO) method was used to help understand the transport properties of materials and the electron localization function (ELF) method to analyze the bonding natures between atoms.

Acknowledgements

The work achieved in this thesis would not have been possible without the tremendous support and inspirations from my supervisor, Dr. Yuriy Mozharivskyj, who has generously shared his knowledge and perspectives throughout the years. It has been an honour to complete my studies under his supervision since my undergraduate studies. I would also like to thank my other supervisory committee members, Dr. John Greedan and Dr. Gillian Goward, for their guidance and insights throughout my studies. They often offer different point of views, which has made this work more thorough. I am grateful to have worked with the present and former members in the BIMR, especially Dr. James Britten, Victoria Jarvis, Dr. Hanna Dabkowska and Dr. Anton Dabkowski, for their help and training in different facilities. I would also like to express my thanks to our collaborators, Dr. Taras Kolodiaznyi, Dr. Yu-Chih Tseng, Dr. Volodymyr Svitlyk and Dr. Eric Toberer, for the inputs and efforts put into part of this work.

I am thankful to have worked with my former group members, especially Dr. Scott Forbes, Dr. Fang Yuan, Dr. Allan He and Dr. Yafen Shang for their trainings and companion in the earlier stages of my studies and beyond. I would also like to thank my current group members for their support and encouragements during the hardships and frustrations in my research work. I would like to offer special thanks to my music-making friends, especially Paul Grimwood and my Strata friends. Singing and making music together are perfect refreshments after spending the whole day in research. Of course, also to friends around and in Hong Kong that we spent time off work and studies!

Last but not least, I would like to thank my family and relatives: my parents, my sister, 陳太, “auntie” Virginia and “uncle” Leon, for their immense support. My pursuit of scientific research would not have been possible without them.

Table of contents

Chapter 1. Introduction	1
1.1. Thermoelectric phenomena	1
1.1.1. Seebeck effect	1
1.1.2. Peltier effect	3
1.1.3. Thomson effect	4
1.2. Applications of Thermoelectrics	5
1.3. Thermoelectric Efficiency	6
1.4. Theories and Models in Thermoelectric Materials	9
1.4.1. Electronic Band Structures of Solids	9
1.4.1.1. Bloch Theorem and the NFE model	10
1.4.1.2. Visualization of Band Structures from a Chemist's View	12
1.4.1.3. The Tight-Binding Model	13
1.4.2. Transport Properties	13
1.4.2.1. Charge Transport Properties	13
1.4.2.2. Thermal Transport Properties	16
1.4.2.3. Scattering Mechanisms of Charge Carriers and Phonons	18
1.4.2.4. Charge Transport Regarding Electronic Band Structures	20
1.4.2.5. Thermal Transport in Calculations	22
1.4.2.6. Optimizing PF and Improving zT of a Thermoelectric Material	24
1.5. State-of-the-art Thermoelectric Materials	25
1.5.1. Chalcogen-based Materials	26
1.5.1.1. IV-Te Systems	26
1.5.1.2. <i>Pn-Ch</i> Systems	28
1.5.1.3. SnSe and Cu_{2-x}Se Selenides	29
1.5.2. Skutterudites	32
1.5.3. Clathrates	33

1.5.4. Other Zintl phase Materials	35
1.6. <i>Materials in Focus</i>	36
1.6.1. β -Zn ₁₃ Sb ₁₀	36
1.6.2. ZnSb	38
1.6.3. Other Zn-Sb Relative Phases	38
Chapter 2. Methodology and Experimentation	39
2.1. <i>Synthetic Approach</i>	39
2.2. <i>X-ray Diffractions</i>	40
2.2.1. Generation of X Ray	41
2.2.2. Miller Indices and Braggs' Law	43
2.2.3. Reciprocal Lattice and Ewald's Sphere	44
2.2.4. The Structure Factor and the Phase Problem	46
2.2.5. Single-Crystal X-ray Diffractions (SC XRD)	50
2.2.6. Laue Diffraction	51
2.2.7. Powder X-ray Diffractions (PXRD)	51
2.3. <i>Energy Dispersive X-ray Spectroscopy (EDS)</i>	53
2.3.1. Principle of Technique	53
2.3.2. Instrumentation	54
2.4. <i>Transport Property Measurements</i>	54
2.4.1. αT and Heat Capacity Measurements	54
2.4.2. Carrier Concentration Measurements	56
2.4.3. Magnetization Measurements	57
2.5. <i>Electronic Band Structure Calculations</i>	57
Chapter 3. The Updated Zn – Sb Phase Diagram. How to Make Pure Zn₁₃Sb₁₀ (“Zn₄Sb₃”)	59
3.1. <i>Introduction</i>	60
3.2. <i>Experimental</i>	64

3.2.1. Synthesis	64
3.2.2. Room Temperature Diffraction Studies and Elemental Analysis	66
3.2.3. High-temperature Synchrotron Diffraction Studies	66
3.3. Results and Discussion	67
3.3.1. Composition of $Zn_{13-\delta}Sb_{10}$ and ZnSb	67
3.3.2. Thermal Stability and Transformation of $Zn_{13}Sb_{10}$	71
3.3.3. Thermal Stability of ZnSb	74
3.3.4. Stability and Transformations in Zn_9Sb_7 and Zn_3Sb_2	76
3.3.5. Zn – Sb Phase Diagram	79
3.4. Conclusions	83
Chapter 4. Incorporation of Indium into the $Zn_{13}Sb_{10}$ Thermoelectric Material	84
4.1. Introduction	85
4.2. Experimental	86
4.2.1. Synthesis	86
4.2.2. Powder and Single Crystal X-ray Diffraction	87
4.2.3. Elemental Analysis	90
4.2.4. Physical Property Measurements	90
4.3. Results and Discussion	91
4.3.1. Composition, Purity and Structural Features of the In-doped Samples	91
4.3.2. Physical Properties	95
4.4. Conclusions	101
Chapter 5. Experimental Survey of Dopants in $Zn_{13}Sb_{10}$ Thermoelectric Material	103
5.1. Introduction	104
5.2. Materials and Methods	105

5.2.1. Synthesis	105
5.2.2. Powder and Single Crystal X-ray Diffraction	107
5.2.3. Elemental Analysis	110
5.2.4. Physical Property Measurements	111
5.2.5. Electronic Structure Calculations	111
5.3. Results and Discussion	112
5.3.1. Composition, Purity and Structure of the Pristine β -Zn ₁₃ Sb ₁₀	114
5.3.2. Composition and Purity of Substituted Samples	115
5.3.2.1. Divalently Substituted Zn ₁₃ Sb ₁₀ (Manganese and Cadmium)	115
5.3.2.2. Trivalently Substituted Zn ₁₃ Sb ₁₀ (Gallium and Indium)	115
5.3.2.3. Unsuccessful Incorporations	116
5.3.3. Structural Features of the Mn-, Ga-, Cd- and In-doped Zn ₁₃ Sb ₁₀ Crystals Grown from Sn Flux	118
5.3.4. Physical Properties	119
5.3.5. Electronic Band Structure and Bonding Characters	127
5.3.6. Estimation of Carrier Effective Mass of the Zn ₁₃ Sb ₁₀ Materials	130
5.4. Conclusions	132
5.5. Supplementary Materials	133
Chapter 6 – Comparative Study of the Zn_{1-x}Cd_xSb and (Zn_{1-z}Cd_z)₁₃Sb₁₀ Solid Solution Series	136
6.1. Introduction	137
6.2. Materials and Methods	138
6.2.1. Synthesis	138
6.2.2. Powder and Single Crystal X-ray Diffraction	140
6.2.3. Elemental Analysis	140
6.2.4. Physical Property Measurements	140
6.2.5. Electronic Structure Calculations	141

6.2.6. Electron Localization Function (ELF)	141
6.3. Results and Discussion	142
6.3.1. Characterization	142
6.3.2. Crystal Structure and Bonding	146
6.3.3. Electronic Band Structures	149
6.3.4. Phase Transition	151
6.3.5. Thermoelectric Properties	154
6.3.5.1. Charge Transport Properties of $Zn_{1-x}Cd_xSb$	154
6.3.5.2. Charge Transport Properties of $(Zn_{1-z}Cd_z)_{13}Sb_{10}$	159
6.3.5.3. Thermal Properties	163
6.4. Conclusion	167
6.5. Supplementary Materials	168
Chapter 7 – Synthesis, Structure and Thermoelectric Properties of α-Zn_3Sb_2 and Comparison to β-$Zn_{13}Sb_{10}$	178
7.1. Introduction	180
7.2. Experimental Section	183
7.2.1. Synthesis	183
7.2.2. Structure Analysis	184
7.2.3. Synchrotron Powder Diffraction Studies	187
7.2.4. Electron Microprobe Analysis (EMPA)	187
7.2.5. Physical Property Measurements	188
7.3. Results and Discussion	188
7.3.1. Crystal Structure and Composition	188
7.3.2. Temperature Stability and Transformations	192
7.3.3. Physical Properties	195
7.3.4. Thermal Properties and Debye–Callaway Modelling	200
7.4. Conclusion	207
7.5. Supplementary Materials	208

Chapter 8 – Conclusions and Future Work	214
8.1. α-Zn₃Sb₂	215
8.2. Zn₁₃Sb₁₀-based Materials	215
8.2.1. Synthesis, Structure and Properties	215
8.2.2. Thermoelectric Performance	217
8.2.3. Stability Under Different Conditions	217
8.3. ZnSb-based Materials	218
8.4. Future Work in the Zn–Sb Phases	219
Appendix 1 – Synthesis and Characterizations of the Metastable, High Temperature β-Zn₃Sb₂ phase	223
A1.1. Introduction	224
A1.2. Experimental	225
A1.2.1.Synthesis	225
A1.2.2.Powder and Single Crystal X-ray Diffractions	228
A1.3. Results and Discussion	229
A1.3.1.Structure Solution	229
A1.3.2.Synthetical Attempts of the β -Zn ₃ Sb ₂ phase	232
A1.4. Conclusion	233
Appendix 2 – Compaction Methods of the Thermoelectric Zn₁₃Sb₁₀-based Materials	234
A2.1. Introduction	235
A2.2. Experimental	236
A2.2.1.Synthesis	236
A2.2.2.Powder X-ray Diffractions	237
A2.2.3.Spark Plasma Sintering (SPS)	237
A2.2.4.Hot Pressing (HP)	237

A2.3. Results and Discussion	238
A2.3.1. Composition and Purity of the Pressed Pellets	238
A2.3.2. Hot Pressing of Zn ₁₃ Sb ₁₀	240
A2.3.3. Hot Extrusion of Zn ₁₃ Sb ₁₀	240
A2.4. Conclusion	241
Bibliography	242

List of Figures

Figure	Description	Page
1.1	A schematic diagram of Seebeck's experiment.	2
1.2	A schematic diagram of a thermoelectric couple using a <i>p</i> -type and an <i>n</i> -type material, in electricity generation mode (left) and refrigeration mode (right).	6
1.3	A schematic diagram of Peierls distortion in electronic band structures (before: left, after: right). The chain of hydrogen atoms was turned into hydrogen molecule chains, with the dashed line separating the hydrogen molecules.	11
1.4	The molecular orbital diagram of a long ring of equidistant hydrogen atoms, and its similarity to a six-membered ring delocalized π -system.	12
1.5	The temperature dependence of electrical resistivity in a metal-like conductor (left) and in an intrinsic semiconductor (right).	14
1.6	The Umklapp process of a phonon-phonon scattering event, shown in a 2D Brillouin zone.	19
1.7	The Fermi-Dirac distribution function and the Fermi window function. $k_B T$ is set to be 0.5 eV in the above drawing. (~ 0.025 eV at 293 K)	21
1.8	Movements of atoms in the acoustic (left) and optical mode (right) at frequency ω in a 1D chain. 2 atom case.	23
1.9	The rock salt (left) and the distorted rock salt (right) structure in the IV–Te system. In the distorted structure, only the short IV – Te distances are drawn.	27
1.10	Structure of Bi_2Te_3 . Note that the Bi atoms in the octahedra are distorted towards the gap between the quintuple layers.	28
1.11	Structures of SnSe, in <i>Pnma</i> (left, room temperature polymorph) and in <i>Cmcm</i> (right, high temperature polymorph) space groups. In the <i>Cmcm</i> structure, the intraplanar Sn – Se distances are ~ 2.7 and 3.0 Å, while the interplanar Sn – Se distance is ~ 3.7 Å.	30

1.12	Structures of Cu_{2-x}Se in the β -phase ($R\bar{3}m$, left) and the α -phase ($Fm\bar{3}m$, right) space groups. The Cu3 site in the $R\bar{3}m$ structure split into 3 sites and reach an occupancy of 1 by itself. The $Fm\bar{3}m$ structure is shown twice with and without the under occupied Cu interstitial sites (bottom and top, respectively). The Cu3 site in the $Fm\bar{3}m$ structure split into 4 sites and reach an occupancy ~ 1 together with Cu1 instead.	31
1.13	Structure of a skutterudite CoSb_3 (left) and a filled skutterudite $\text{NaFe}_4\text{Sb}_{12}$ (right).	33
1.14	Structures of a type-I clathrate $\text{Ba}_8\text{Ga}_{16}\text{Ge}_{30}$ (left), and a type-II clathrate $(\text{K}, \text{Ba})_{24}(\text{Ga}, \text{Sn})_{136}$ (right). Type-I: different shade of the two Ba indicate the two different polyhedral voids in which they are located. Type-II: different of the polyhedra represent the two different polyhedral shapes. The K/Ga site in the purple hexakaidecahedra is evenly split into 4 sites.	34
1.15	Structure of $\text{Yb}_{14}\text{MnSb}_{11}$. The right half shows the Yb atoms located in (distorted) octahedral voids, which share faces, while the left half features the MnSb_4^{9-} subunit.	36
2.1	The set up used for the flux growth. Alumina crucibles with the frit in-between are placed into quartz ampoules. Silica wool is placed on both sides of the alumina crucibles to provide a cushion during centrifugation. Silica shards are put to fill the space and improve the sealing; they are often darkened due to sealing.	40
2.2	Schematic diagram of the X-ray tube (left) and a typical X-ray emission spectrum (right), which includes the continuous, white radiation, highlighted in red and characteristic X-rays ($\text{K}\alpha_1$, $\text{K}\alpha_2$ and $\text{K}\beta$).	41
2.3	Schematic diagram of a synchrotron facility.	42
2.4	Schematic diagram of the demonstration of the Braggs' law with a set of hkl planes.	43
2.5	Schematics of the diffraction condition in reciprocal space using the Ewald's sphere.	45
2.6	\mathbf{F}_{hkl} shown as a vector in the real/imaginary coordinate system, in a non-centrosymmetric (left) and a centrosymmetric (right) structure, in the absence of anomalous scatterings. \mathbf{R}_{hkl} represents the real part and \mathbf{Im}_{hkl} represents the imaginary part in \mathbf{F}_{hkl} .	48

2.7	Schematics of the ULVAC-RIKO ZEM-3 system.	55
3.1	Rietveld refinement results for the Zn_4Sb_3 and $Zn_{13}Sb_{10}$ samples quenched from 750 °C. The elemental Zn is not detectable in the $Zn_{13}Sb_{10}$ sample, likely, due to its small particle size.	63
3.2	Powder diffraction patterns of the $Zn_{12.7-13.3}Sb_{10}$ samples cooled at 50 °C/h from 750 °C to room temperature. The Zn and ZnSb impurities are indicated on the graphs.	70
3.3	Powder diffraction data for the Zn_4Sb_3 sample during heating from 300 °C till 580 °C.	71
3.4	Occupancy of the main Zn site in $Zn_{13}Sb_{10}$ with temperature.	73
3.5	Unit cell volume of $Zn_{13}Sb_{10}$ with temperature.	73
3.6	Powder diffraction data for the ZnSb sample during heating from room temperature till 600 °C.	75
3.7	Powder diffraction data for the Zn_9Sb_7 sample during heating from room temperature till 620 °C.	77
3.8	Powder diffraction data for the Zn_3Sb_2 sample (quenched from 430 °C) during heating from room temperature till 600 °C.	78
3.9	Central part of the Zn – Sb phase diagram.	82
4.1	(left) X-ray diffraction patterns of $Zn_{13}Sb_{10}$ and $Zn_{12.5}In_{0.5}Sb_{10}$. (right) Crystal structure of $Zn_{13}Sb_{10}$ without interstitial Zn. The Zn atoms (grey) occupy the tetrahedral voids formed by Sb.	91
4.2	Heat capacities of (a) $Zn_{13}Sb_{10}$ and (b) $Zn_{11.5}In_1Sb_{10}$.	95
4.3	Electrical resistivity of $Zn_{13}Sb_{10}$ and $Zn_{11.5}In_1Sb_{10}$.	97
4.4	Seebeck coefficients of $Zn_{13}Sb_{10}$ and $Zn_{11.5}In_1Sb_{10}$.	98
4.5	(a) Total and (b) lattice thermal conductivities of $Zn_{13}Sb_{10}$ and $Zn_{11.5}In_1Sb_{10}$.	99
4.6	(a) Power factor and (b) figure-of-merit, zT for $Zn_{13}Sb_{10}$ and $Zn_{11.5}In_1Sb_{10}$.	101
5.1	Crystal structure of β - $Zn_{13}Sb_{10}$.	105
5.2	Electrical resistivity of the polycrystalline, pristine $Zn_{13}Sb_{10}$ and selected doped $Zn_{13}Sb_{10}$ samples.	120

5.3	Heat capacities of the polycrystalline, pristine $\text{Zn}_{13}\text{Sb}_{10}$ and selected doped $\text{Zn}_{13}\text{Sb}_{10}$ samples.	121
5.4	Seebeck coefficients of the selected samples.	122
5.5	Low temperature total thermal conductivities (a) and calculated lattice thermal conductivities (b) of $\text{Zn}_{13}\text{Sb}_{10}$, $\text{Zn}_{11.5}\text{In}_1\text{Sb}_{10}$ and $\text{Zn}_{12.75}\text{Mn}_{0.25}\text{Sb}_{10}$ sample.	125
5.6	Power factors (a) and Thermoelectric figure-of-merit ZT (b) of $\text{Zn}_{13}\text{Sb}_{10}$, $\text{Zn}_{11.5}\text{In}_1\text{Sb}_{10}$ and $\text{Zn}_{12.75}\text{Mn}_{0.25}\text{Sb}_{10}$ sample.	127
5.7	(a) Total and partial DOS of the $\text{Zn}_{13}\text{Sb}_{10}$ material, calculated for the ordered $\text{Zn}_{12}\text{Sb}_{10}$ structural motif of the $\text{Zn}_{13}\text{Sb}_{10}$ phase. (b) Total COHP plot. (c) Partial COHP plots of $\text{Zn}_{12}\text{Sb}_{10}$, depicting interactions between the three sites. The Fermi level of $\text{Zn}_{12}\text{Sb}_{10}$ is set at 0. The energy difference between the Fermi levels of $\text{Zn}_{12}\text{Sb}_{10}$ and $\text{Zn}_{13}\text{Sb}_{10}$ is ~ 0.44 eV.	127
5.8	Electronic band structure of the $\text{Zn}_{13}\text{Sb}_{10}$ material calculated from the $\text{Zn}_{12}\text{Sb}_{10}$ structural motif.	129
5.9	Pisarenko plots for the $\text{Zn}_{13}\text{Sb}_{10}$, $\text{Zn}_{12.75}\text{Mn}_{0.25}\text{Sb}_{10}$ and $\text{Zn}_{11.5}\text{In}_1\text{Sb}_{10}$ sample at 300 K.	131
5.S1	High-temperature total thermal conductivities of the $\text{Zn}_{12.75}\text{Mn}_{0.25}\text{Sb}_{10}$, $\text{Zn}_{12.55}\text{Ga}_{0.3}\text{Sb}_{10}$, $\text{Zn}_{11.96}\text{Cd}_{1.04}\text{Sb}_{10}$ and $\text{Zn}_{11.5}\text{In}_1\text{Sb}_{10}$ samples.	134
5.S2	Calculated high-temperature lattice thermal conductivities of the $\text{Zn}_{12.75}\text{Mn}_{0.25}\text{Sb}_{10}$, $\text{Zn}_{12.55}\text{Ga}_{0.3}\text{Sb}_{10}$, $\text{Zn}_{11.96}\text{Cd}_{1.04}\text{Sb}_{10}$ and $\text{Zn}_{11.5}\text{In}_1\text{Sb}_{10}$ samples.	134
5.S3	Magnetic susceptibility χ vs. temperature T of (a) the pristine $\text{Zn}_{13}\text{Sb}_{10}$ and (b) the $\text{Zn}_{12.8}\text{Mn}_{0.2}\text{Sb}_{10}$ sample.	135
6.1	Refined unit cell parameters of a) $\text{Zn}_{1-x}\text{Cd}_x\text{Sb}$ and b) $(\text{Zn}_{1-z}\text{Cd}_z)_{13}\text{Sb}_{10}$. The compositions (x -axis) were obtained from the EDS analyses.	145
6.2	Crystal structures of (a) $\text{Zn}_{13}\text{Sb}_{10}$, ZnSb (b) with Sb tetrahedra and Zn_2Sb_2 rhomboid rings.	146
6.3	The 2D ELF showing a) the Sb – Sb interaction and b) the Zn_2Sb_2 rhomboid ring in the ZnSb material.	147
6.4	(a) Density of States (DOS) plot and (b) the electronic band structures of the $\text{Zn}_{1-x}\text{Cd}_x\text{Sb}$ series. The high symmetry points are labelled in separate band structures in the Supplementary Information.	150

6.5	(a) Density of States (DOS) plot and (b) the electronic band structures of the $(\text{Zn}_{1-z}\text{Cd}_z)_{13}\text{Sb}_{10}$ series. The high symmetry points are labelled in separate band structures in the Supplementary Information.	150
6.6	Heat capacities of $(\text{Zn}_{1-z}\text{Cd}_z)_{13}\text{Sb}_{10}$ ($z = 0, 0.5, 1$).	152
6.7	Structures of the α - and β - $\text{Cd}_{13}\text{Sb}_{10}$, aligned along the Sb_2^{4-} dimers. The $\text{Cd}_3\text{Sb-SbCd}_3$ motif is shown on the right of the figure.	153
6.8	Low temperature (LT) (a) electrical resistivities and (b) Seebeck coefficients of SPS $\text{Zn}_{1-x}\text{Cd}_x\text{Sb}$ ($x = 0, 0.5, 1$).	154
6.9	Schematic band diagram with the impurity band in ZnSb . Population of the impurity band occurs in the 9 – 64 K region and leads to a decrease in the resistivity.	156
6.10	LT (a) electrical resistivities and (b) Seebeck coefficients of $\text{Zn}_{1-x}\text{Cd}_x\text{Sb}$ ($x = 0, 0.05$).	159
6.11	LT (a) electrical resistivities, (b) the Seebeck coefficients and (c) the room temperature Hall carrier concentrations of the $(\text{Zn}_{1-z}\text{Cd}_z)_{13}\text{Sb}_{10}$ series. Separate resistivities of samples are presented in Supplementary Information. The elemental ratios derived from EDS are used for the values of z in (c). The standard deviations of Hall carrier concentrations and mobilities are typically smaller than the squares (< 3.5% error), while the error of z could be larger due to the semiquantitative nature of SEM–EDS, in addition to possible sample inhomogeneity.	160
6.12	Low temperature (a) total and (b) lattice thermal conductivities of $\text{Zn}_{1-x}\text{Cd}_x\text{Sb}$.	164
6.13	Low temperature (a) total and (b) lattice thermal conductivities of $(\text{Zn}_{1-z}\text{Cd}_z)_{13}\text{Sb}_{10}$.	164
6.14	C_p/T^3 vs. T curves of the $(\text{Zn}_{1-z}\text{Cd}_z)_{13}\text{Sb}_{10}$ series.	167
6.S1	X-ray diffraction pattern of $\text{Zn}_{0.6}\text{Cd}_{0.4}\text{Sb}$ sample: as-synthesized, after SPS, and after reannealing following cold-press.	168
6.S2	PXRD pattern of $\text{Cd}_{13}\text{Sb}_{10}$, taken experimentally (black) and simulated pattern without symmetry reduction (structure of β - $\text{Cd}_{13}\text{Sb}_{10}$, red).	169
6.S3	Rietveld refinement of the $\text{Cd}_{13}\text{Sb}_{10}$ sample with (a) the current structural model, and (b) the $C2/c$ cell, derived from the low temperature α - $\text{Zn}_{13}\text{Sb}_{10}$ phase.	169

6.S4	Electronic band structures of $x =$ (a) 0, (b) 0.5 and (c) 1 in the $\text{Zn}_{1-x}\text{Cd}_x\text{Sb}$ series.	173
6.S5	Electronic band structures of $z =$ (a) 0, (b) 0.5 and (c) 1 in the $(\text{Zn}_{1-z}\text{Cd}_z)_{13}\text{Sb}_{10}$ series.	174
6.S6	Low-temperature (LT) electrical resistivities of the $(\text{Zn}_{1-z}\text{Cd}_z)_{13}\text{Sb}_{10}$ series, $z =$ (a) 0, (b) 0.5 and (c) 1.	176
6.S7	Electrical resistivities of melt ZnSb and SPS ZnSb .	177
7.1	Structures of the Zn-Sb phases that were obtained in bulk form. Orange atoms are Sb, gray atoms are Zn. Bonds in orange are Sb-Sb dimers. In each structure, Sb^{2-} anions make the Sb-Sb dimers, Sb^{3-} anions are isolated anions surrounded by only Zn^{2+} cations. In Zn_8Sb_7 , two split Zn sites are not shown; in $\text{Zn}_{13}\text{Sb}_{10}$, only the major Zn site is shown.	180
7.2	Rietveld refinement of the powder diffraction data for Zn_3Sb_2 . Only the $2\theta = 20\text{--}50^\circ$ range is shown. Black crosses and the red line represent observed and calculated intensities; the green line is the difference between the intensities. The vertical bars show positions of Bragg peaks.	186
7.3	Projection of the $\alpha\text{-Zn}_3\text{Sb}_2$ unit cell along the $[110]$ direction. Antimony atoms are shown in orange (left) and zinc in gray (center). The fraction of the gray for a given Zn atom represents the occupancy of the corresponding Zn site. The Sb polyhedra (right) show environments for selected deficient Zn atoms that are close to each other.	190
7.4	High-temperature diffraction patterns in projection during heating and cooling. The phases are in blue and the transformation temperatures ($^\circ\text{C}$) are in red. Red and blue arrows indicate heating and cooling. The region between the lines is a molten liquid.	194
7.5	Heat capacity (a,c) and electrical resistivity measurements (b) reveal multiple phase transitions in $\text{Zn}_{13}\text{Sb}_{10}$ and Zn_3Sb_2 . The $\alpha \rightarrow \alpha'$ phase transition in $\text{Zn}_{13}\text{Sb}_{10}$ is consistent with a first-order transition, while the $\alpha' \rightarrow \beta$ transition is of a λ -type shape characteristic of a second-order transition. The transition in Zn_3Sb_2 from $\zeta \rightarrow \alpha$ is not well characterized and is the subject of future investigations.	197

7.6	Seebeck coefficient measurements on Zn_3Sb_2 and $\text{Zn}_{13}\text{Sb}_{10}$ indicate p -type transport and temperature dependence consistent with heavily doped semiconductors. Phase transitions in Zn_3Sb_2 and $\text{Zn}_{13}\text{Sb}_{10}$ appear to have no appreciable effect on the Seebeck coefficient.	199
7.7	Total thermal conductivity (a) and calculated lattice thermal conductivity (b) for Zn_3Sb_2 and $\text{Zn}_{13}\text{Sb}_{10}$ are blue and black, respectively. We note that the thermal conductivity for Zn_3Sb_2 does not display the characteristic transition from boundary scattering to Umklapp scattering at low temperatures (e.g., peak in thermal conductivity for $\text{Zn}_{13}\text{Sb}_{10}$ at ~ 25 K). Instead the low-temperature thermal transport in Zn_3Sb_2 is more similar to that of an amorphous material.	202
7.8	Results of Debye–Callaway modeling of lattice thermal conductivity for $\text{Zn}_{13}\text{Sb}_{10}$ and Zn_3Sb_2 . Phase transitions are modeled explicitly using piecewise construction of the acoustic contribution to the model after the phase transitions. The overestimation of thermal conductivity in $\text{Zn}_{13}\text{Sb}_{10}$ for temperatures > 254 K is associated with an overestimation of the acoustic contribution. Considering the complex unit cells and multiple phase transitions, the Debye–Callaway does an adequate job of modeling the lattice thermal conductivity in $\text{Zn}_{13}\text{Sb}_{10}$ and Zn_3Sb_2 .	204
7.9	Breakdown of net relaxation time into constituent scattering sources as a function of phonon frequency for $\text{Zn}_{13}\text{Sb}_{10}$ and Zn_3Sb_2 at both 50 K and 300 K. As expected, boundary scattering is the primary scattering source of very low frequency phonons. Scattering in Zn_3Sb_2 appears to be dominated by point-defect scattering over all temperatures and most frequencies, whereas $\text{Zn}_{13}\text{Sb}_{10}$ has a much larger contribution from Umklapp scattering.	206
7.S1	Temperature dependent heat capacities for both $\text{Zn}_{13}\text{Sb}_{10}$ and Zn_3Sb_2 exhibit near identical temperature dependence. Phase transitions for $\text{Zn}_{13}\text{Sb}_{10}$ are well documented in the literature and agree well with our experimental data. The phase transition observed in Zn_3Sb_2 has not been previously observed; its nature is subject of a future investigation.	213
8.1	(a) Electrical resistivity and (b) Seebeck coefficients of the $\text{Zn}_{13}\text{Sb}_{10}$, $\text{Zn}_{12.55}\text{Ga}_{0.3}\text{Sb}_{10}$ and $\text{Zn}_{12.55}\text{In}_{0.3}\text{Sb}_{10}$ samples above room temperatures.	220

8.2	Heat capacities of a polycrystalline, pristine $\text{Zn}_{13}\text{Sb}_{10}$ sample (black), a polycrystalline $\text{Zn}_{13}\text{Sb}_{9.6}\text{Bi}_{0.4}$ sample, and a single-crystalline $\text{Zn}_{13}\text{Sb}_{10}$ from a $\text{Zn}_{1.1}\text{SbBi}_8$ flux.	221
A1.1	Rietveld refinement of the Zn_3Sb_2 sample which contained the $\text{Zn}_{13}\text{Sb}_{10}$ phase as the main phase and $\beta\text{-Zn}_3\text{Sb}_2$ as a minority phase, described above, and its peaks are not described by refinement.	226
A1.2	Synchrotron powder X-ray diffraction data for the $\alpha\text{-Zn}_3\text{Sb}_2$ sample (a) during heating from room temperature up to 600 °C, and (b) during cooling from 600 °C to room temperature.	227
A1.3	Cross section of the reciprocal space, the $h0l$ layer for the $\beta\text{-Zn}_3\text{Sb}_2$ grain, generated from STOE IPDS II diffractometer and the X-area software.	230

List of Tables

Figure	Description	Page
3.1	Samples compositions, heat treatment, phases present and elemental analysis results.	65
3.2	Lattice constants for the $Zn_{13-\delta}Sb_{10}$ phase as obtained from the full profile Rietveld refinement of the $Zn_{13-\delta}Sb_{10}$ and Zn_4Sb_3 samples. The phase compositions are also indicated.	69
3.3	Lattice parameters of the $Zn_{13}Sb_{10}$ phase in the $Zn_{12.7-13.3}Sb_{10}$ samples cooled from 750 °C to room temperature at 50 °C/h.	69
3.4	Phase analysis, transformation and invariant temperatures for four samples obtained from HT synchrotron diffraction studies during heating. The last column gives transformation temperatures taken from V. Izard <i>et al.</i>	80
4.1	Single Crystal X-ray Diffraction and refinements of crystal grown from flux $Zn_{4.4}Sb_3Sn_3$ and $Zn_{4.2}In_{0.2}Sb_3Sn_3$ at 293 K, $MoK_{\alpha 1}$, STOE IPDS II diffractometer.	88
4.2a	Atomic and isotropic displacement (U_{eq}) parameters for the crystal grown from the $Zn_{4.4}Sb_3Sn_3$ flux.	89
4.2b	Atomic and isotropic displacement (U_{eq}) parameters for the crystal grown from the $Zn_{4.2}In_{0.2}Sb_3Sn_3$ flux.	89
4.3	Lattice constants of $Zn_{13}Sb_{10}$ obtained from Rietveld refinements.	91
4.4	Elemental analysis of the pristine $Zn_{13}Sb_{10}$ and the In-doped $Zn_{13}Sb_{10}$.	93
4.5	Unit cell parameters of the flux-grown $Zn_{13}Sb_{10}$ single crystals derived from the powder diffraction data using the Rietveld refinement.	94
5.1	Crystallographic parameters and refinement results for the crystals grown from the $Zn_{4.4}Sb_3Sn_3$, $Zn_{4.2}Mn_{0.2}Sb_3Sn_3$, $Zn_{4.2}Ga_{0.2}Sb_3Sn_3$, $Zn_{4.2}Cd_{0.2}Sb_3Sn_3$ and $Zn_{4.2}In_{0.2}Sb_3Sn_3$ fluxes (293 K, $MoK_{\alpha 1}$, STOE IPDS II diffractometer).	107
5.2	Atomic and isotropic displacement (U_{eq}) parameters for the flux-grown crystals.	109

5.3	Summary of successful single element incorporations in $Zn_{13}Sb_{10}$.	112
5.4	Summary of unsuccessful single element incorporations into $Zn_{13}Sb_{10}$.	113
5.5	Semi-quantitative EDS elemental analyses, and unit cell parameters of the flux-grown $Zn_{13}Sb_{10}$ single crystals from the Rietveld refinement. The crystals were ground and the data were collected in the $20 - 140^\circ 2\theta$ range with collection time of 12 hours.	114
5.6	Pauling's radii of single-bonded elements.	114
5.7	Room temperature Hall carrier concentrations n_H (in cm^{-3}) and carrier mobilities μ_H (in $cm^2/(V\cdot s)$) of pristine and doped $Zn_{13}Sb_{10}$ samples.	123
6.1	SPS temperatures of the $Zn_{1-x}Cd_xSb$ samples.	139
6.2	Single crystal X-ray diffraction and refinements of the grain from the $Cd_{13}Sb_{10}$ melted ingot sample. Data were collected on a Bruker SMART APEX II diffractometer with a 3 kW sealed-tube Mo generator and APEX II CCD detector at room temperature.	143
6.3	Elemental compositions (in at. %) and chemical formulae of the $Zn_{1-x}Cd_xSb$ (left) and $(Zn_{1-z}Cd_z)_{13}Sb_{10}$ (right) solid solution series.	144
6.S1	Atomic and isotropic displacement (U_{eq}) parameters of the grain from the $Cd_{13}Sb_{10}$ melt ingot sample.	170
7.1	Crystallographic and Refinement Data for the α - Zn_3Sb_2 Crystal	184
7.2	Powder Refinement Data for the Zn_3Sb_2 Samples at 293 K, $CuK_{\alpha 1}$ Radiation, $2\theta = 20^\circ - 100^\circ$, Step 0.0042°	186
7.3	Physical Parameters of α - Zn_3Sb_2 and β - $Zn_{13}Sb_{10}$ at 300 K.	196
7.S1	Atomic coordinates, occupancies and equivalent isotropic displacement parameters from single crystal refinement.	208
7.S2	Anisotropic displacement parameters (\AA^2) from single crystal refinement.	210
7.S3	Atomic coordinates and occupancies from the Rietveld refinement of the X-ray powder diffraction data. Only the overall displacement parameter, B, for all atoms was refined; $B = 0.344(9) \text{\AA}^2$.	211

A1.1	Samples loading compositions, annealing temperatures, and annealing times to synthesize bulk β -Zn ₃ Sb ₂ .	228
A1.2	Comparison of R-factors of those obtained in this work and by Boström et al..	231
A1.3	Details of refinement of the β -Zn ₃ Sb ₂ crystal using the JANA2006 program.	231
A2.1	SPS conditions and results of the pressed samples.	238
A2.2	X-ray diffraction analyses of SPS-ed pellets after reannealing.	240

List of all Abbreviations and Symbols

Symbol	Description
(hkl)	Miller indices
A	Cross-section area of thermoelements
$\mathbf{a}^*, \mathbf{b}^*, \mathbf{c}^*$	Lattice vectors of the reciprocal space
a, b, c	Lattice parameters, length
$\mathbf{a}, \mathbf{b}, \mathbf{c}$	Lattice vectors
at. %	Atomic percent
B	Magnetic field
c_{hex}	Lattice parameter c in the hexagonal structure of Zn_3Sb_2
c_p	Heat capacity (specific heat) at constant pressure
c_v	Heat capacity (specific heat) per unit volume
$C_{v,g}$	Mass heat capacity at constant volume
$C_{v,mol}$	Molar heat capacity at constant volume
Ch	Chalcogen
D	Thermal diffusivity
DOS	Density of states
d_{hkl}	Interplanar distance (d-spacing)
\mathbf{d}_{hkl}^*	Reciprocal interplanar vectors
$D(E)$	Density of states as a function of energy
E	Energy
E	Normalized structure magnitude
e (or q)	Elementary charge (1.602×10^{-19} C)
E_F	Fermi energy
E_g	Band gap
$E(k)$	Energy function
F_c	Calculated structure amplitudes
\mathbf{F}_{hkl}	Structure amplitude for the (h,k,l) plane
$ \mathbf{F}_{hkl} ^2$	Structure factor
f_j	Atomic scattering factor
F_o	observed structure amplitudes
\mathbf{F}_{hkl}^{obs}	Absolute value of the observed structure amplitude
$ \mathbf{F}_{hkl}^{obs} ^2$	Absolute value of the structure factor
$f(E)$	Fermi-Dirac distribution function
G	Translational vector

g_j	Occupancy factor
h	Planck's constant
\hbar	Reduced Planck's constant
I	Electrical Current
I_{hkl}	Intensity of the reflection (hkl)
j	Current density
K	Total thermal conductance of the thermoelements
k	Wavevector of an electron
k	Wavevector of a phonon
\mathbf{k}_0	Incident beam
\mathbf{k}_1	diffracted beam
k_B	Boltzmann constant
K_T	Isothermal bulk modulus
l	Length of the thermoelements
L	Lorenz number
l	Mean free path of phonon
LA	Longitudinal acoustic mode of phonons
LO	Longitudinal optical mode of phonons
m	Mass
m^*	Effective mass of electron/hole
N	Total number of y_{io}
n_H	Hall carrier concentration
$N_{par.}$	Number of parameters
$N_{ref.}$	Number of independent reflections
n, p	Electron and hole concentrations
P	Number of adjusted parameters
P_{uvw}	Patterson function
Pn	Pnictogen
Q	Amount of heat evolved
\dot{Q}	Heat flow
Q_c	Heat transferred by conduction to the cold junction
Q_p	Heat due to Peltier effect
r	Total resistance of two thermoelements
R	Electrical resistance
R	gas constant (8.31 J/mol-K)
R_H	Hall coefficient
R_p	profile of the Rietveld refinement

R_{wp}	Weighted profile of the Rietveld refinement
T	Temperature
t	Thickness of sample
T_C	Temperature of the cold junction
T_C	Curie temperature
T_H	Temperature of the hot junction
t_j	Atomic displacement parameter
T_{max}	Temperature with maximum Seebeck coefficient
TA	Transverse acoustic mode of phonons
TO	Transverse optical mode of phonons
U_{eq}	Isotropic displacement parameters
$u_k(r)$	A periodic function
V	Volume
V_H	Hall voltage
V_m	Molar volume
v_s	Speed of sound
V_{Zn}	Atomic vacancy at Zn sites
$V(r)$	Atomic potential
W	Converted electrical energy
w	Weighting factor
w_i	weighting scheme
wt. %	Weight percent
y_{ic}	calculated intensities of the model
y_{io}	observed intensities in powder X-ray diffraction
z	Temperature-dependent thermoelectric figure-of-merit
Zn_{Sb}	Zn atoms at Sb sites
zT	Thermoelectric figure-of-merit
α	Seebeck coefficient (thermopower)
α	volume thermal expansion coefficient
α_{max}	Maximum Seebeck coefficient
α_{hkl}	phase angle of the reflection (hkl)
α, β, γ	Lattice parameters, angles
γ	Grüneisen parameter
γ	Sommerfeld constant
ΔV	Potential difference
η	Thermoelectric efficiency
η_{max}	Maximum thermoelectric efficiency
θ	Bragg angle

θ_D	Debye temperature
θ_E	Einstein temperature
κ	Thermal conductivity
κ_e	Electronic thermal conductivity
κ_l	Lattice thermal conductivity
κ_{total}	Total thermal conductivity
λ	Wavelength of radiation
μ	Charge carrier mobility
μ_h	hole mobility
μ_H	Hall mobility
μ_e	electron mobility
ν_E	Phonon frequency
ν_s	speed of sound
π	Peltier coefficient
ρ	Electrical resistivity
ρ	Mass density
ρ_i	Residual resistivity
$\rho_{ph}(T)$	Temperature-dependent electrical resistivity
ρ_{xyz}	Electron density at the (x,y,z) point
σ	Electrical conductivity
τ	Relaxation time of a charge carrier
τ	Relaxation time of phonon
τ_B	phonon relaxation time due to grain boundary scattering
τ_N	phonon relaxation time due to normal scattering
τ_T	Thomson coefficient
τ_U	phonon relaxation time due to Umklapp scattering
τ_{im}	phonon relaxation time due to impurity scattering
τ_{ph}	phonon relaxation time due to electron-phonon scattering
χ	Magnetic susceptibility
χ^2	Goodness of fit of the Rietveld refinement
$\psi(r)$	State function
ψ_k	Bloch function
ω	Phonon frequency
2D	Two-dimensional
ASA	Atomic sphere approximation
BTE	Boltzmann transport equation

BZ	Brillouin Zone
C.N.	Coordination number
CB	Conduction band
CFSE	Crystal-field stabilization energy
COHP	Crystal orbital Hamiltonian Population
DC	Direct current
DOS	Density of states
EDS	Energy Dispersive X-ray Spectroscopy
ELF	Electron localization function
EMPA	Electron microprobe analysis
EPFS	Electron-poor framework semiconductors
GGA	Generalized gradient approximation
HS	High spin
HSE	Heyd-Scuseria-Ernzerhof
HT	High temperature
ID	Inner diameter
LFA	Laser flash method
LMTO	Linear muffin tin orbital
LT	Low temperature
MPMS	Magnetic property measurement system
NFE	Nearly-free electron model
PBE	Perdew-Burke-Ernzerhof
PF	Power factor
PPMS	Physical Property Measurement System
PXRD	Powder X-ray diffraction
RSO	Reciprocating sample option
SC XRD	Single crystal X-ray diffraction
SD(s)	Standard deviation(s)
SEM	Scanning electron microscope
SPB	Single parabolic band
SPS	Spark plasma sintering
SQUID	Superconducting quantum interference device
TB	Tight-binding model
TDF	Transport distribution function
TEM	Transmission electron microscopy
TTO	Thermal transport option
VB	Valence band
WDS	Wavelength-dispersive X-ray Spectroscopy

Declaration of Academic Achievement

Published Manuscript

1. **Lo, C.-w. T.**; Pöhls, J.-H.; Johnson, M.; Kolodiazhnyi, T.; Britten, J. F.; Tseng, Y.-C.; Mozharivskyj, Y.. Comparative Study of the $Zn_{1-x}Cd_xSb$ and $(Zn_{1-z}Cd_z)_{13}Sb_{10}$ Solid Solution Series. *Journal of Solid State Chemistry*. **2022**, 315, 123448.
2. **Lo, C.-w. T.**; Kolodiazhnyi, T.; Song, S.; Tseng, Y.-C.; Mozharivskyj, Y.. Experimental Survey of Dopants in $Zn_{13}Sb_{10}$ Thermoelectric Material. *Intermetallics*. **2020**, 123, 106831.
3. **Lo, C.-w. T.**; Kolodiazhnyi, T.; Mozharivskyj, Y.. Incorporation of Indium into the $Zn_{13}Sb_{10}$ Thermoelectric Material. *J. Alloys Compd.* **2019**, 780, 334 – 340.
4. **Lo, C.-w. T.**; Svitlyk, V.; Chernyshov, D.; Mozharivskyj, Y.. The Updated Zn-Sb Phase Diagram. How to Make Pure $Zn_{13}Sb_{10}$ (“ Zn_4Sb_3 ”). *Dalton Trans.* **2018**, 47, 11512.
5. **Lo, C.-w. T.**; Ortiz, B. R.; Toberer, E. S.; He, A.; Svitlyk, V.; Chernyshov, D.; Kolodiazhnyi, T.; Lidin, S.; Mozharivskyj, Y.. Synthesis, Structure and Thermoelectric Properties of α - Zn_3Sb_2 and Comparison to β - $Zn_{13}Sb_{10}$. *Chem. Mater.* **2017**, 29, 5249 – 5258.
6. Song, S.; **Lo, C.-w. T.**; Aminzare, M.; Tseng, Y.-C.; Valiyaveetil, S. M.; Mozharivskyj, Y.. Enhancing Thermoelectric Performance of $Sn_{0.5}Ge_{0.5}Te$ via Doping with Sb/Bi and Alloying with Cu_2Te . Optimization of Transport Properties and Thermal Conductivity. *Dalton Trans.* **2020**, 18, 6135.
7. Keshavarz, M. K.; **Lo, C.-w. T.**; Turenne, S.; Mozharivskyj, Y.; Quitoriano, N. J.. Hot Extrusion of ZnSb-Based Thermoelectric Materials; A Novel Approach for Scale-Up Production. *J. Manuf. Mater. Process.* **2019**, 3, 58.
8. Shadap, L.; Tyagi, J. L.; Poluri, K. M.; Novikov, S.; **Lo, C.-w. T.**; Mozharivskyj, Y.; Kollipara, M. R.. Synthesis and Biological Evaluation of Some New Class of Benzothiazole-pyrazole Ligands Containing Arene Ruthenium, Rhodium and Iridium Complexes. *Trans. Met. Chem.* **2021**, 46, 231 – 240.
9. Shadap, L.; Tyagi, J. L.; Poluri, K. M.; Novikov, S.; **Lo, C.-w. T.**; Mozharivskyj, Y.; Kollipara, M. R.. Insights to the Strained Thiocarbamate Derivative Complexes of Platinum Group Metals Induced by Azide as a Co-ligand: Characterization and Biological Studies. *J. Organomet. Chem.* **2020**, 920, 121345.

Chapter 1. Introduction

1.1. Thermoelectric phenomena

There are three thermoelectric effects, namely the Seebeck effect, the Peltier effect and the Thomson effect. The discoveries of these phenomena are the cornerstones of the thermoelectric research.

1.1.1. Seebeck effect

In 1821, a German physicist Thomas Johann Seebeck reported an observation that a nearby compass magnet was deflected by a closed circuit made of two dissimilar metals, when the two junctions of the circuit are not isothermal. He concluded that the observed phenomenon was due to changes in magnetic field induced by temperature differences and named it thermomagnetism¹⁻³, defying the electrical nature of the phenomenon. Interestingly, more than twenty years earlier, an Italian physicist Alessandro Giuseppe Antonio Anastasio Volta observed violent muscle contractions of a dead frog, with its legs immersed in a glass of water, and its back spine in another one of different temperature, both glasses were short circuited by some conducting arc^{2,4}. After a series of experiments, he eventually concluded that the electromotive force originated from the temperature difference between two dissimilar conductors, unveiling the thermoelectric effect.

Nonetheless, in 1823, Hans Christian Ørsted and Jean Baptiste Joseph Fourier established the physical origin of the phenomenon: the current is induced in the closed

circuit due to a temperature difference between the metallic junctions, and the deflection of the magnet results from the electromagnetic interaction between itself and the induced current^{2,4,5}. The Seebeck effect is described today as the generation of electromotive force in the presence of a temperature gradient. An electrical current is produced in a loop of two dissimilar materials when the two junctions are at different temperatures. The Seebeck coefficient α (also called thermopower) is expressed as:

$$\alpha = -\frac{\Delta V}{\Delta T}, \quad (1 - 1)$$

where ΔV is potential difference (voltage), and ΔT is a temperature difference. Note that α is commonly expressed in $\mu V/K$ in the thermoelectric research. Depending on the material, the Seebeck coefficient can be either positive (*p*-type) or negative (*n*-type).

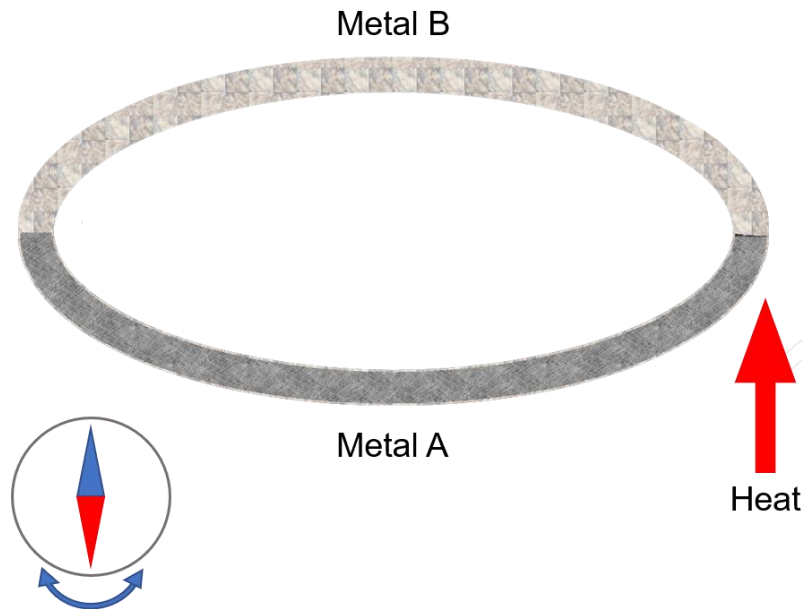


Figure 1.1. A schematic diagram of Seebeck's experiment.

1.1.2. Peltier effect

In 1834, a French watchmaker and scientist Jean Charles Athanase Peltier, discovered and measured the absorption/dissipation of heat at the junction of two dissimilar metals when electrical current is passed through^{2,4,6}. Peltier tried to relate the phenomenon to the Joule effect, the theory of heat dissipation, but was not able to draw a sound explanation. Later in 1838, a Russian physicist Heinrich Friedrich Emil Lenz, observed that water could be frozen at an electrical junction by the passage of an electric current^{2,4}. He proved that the effect discovered by Peltier is itself a physical phenomenon, and not directly related to the Joule effect. The Peltier effect is the release and absorption of heat by junctions between dissimilar conductors when an electrical current is passed through. The Peltier coefficient π is expressed as:

$$\pi = \frac{\dot{Q}}{I}, \quad (1 - 2)$$

where \dot{Q} is the heat flow and I is the electrical current.

Later in 1851, a British physicist and engineer William Thomson (also known as Lord Kelvin) has brought together the two effects with the laws of thermodynamics. The Seebeck and Peltier coefficients are related by one of the Thomson (Kelvin) relations:

$$\pi = \alpha T, \quad (1 - 3)$$

1.1.3. Thomson effect

W. Thomson published a paper about the observation of the Thomson effect. He observed heat flow when an electrical current I passes through a single conductor, under a temperature gradient^{7,8}. The amount of heat Q evolved per unit time and volume in a conductor is:

$$Q = \nabla \cdot (\kappa \nabla T) + j^2 \rho - T j \cdot \nabla \alpha \quad (1 - 4)$$

where j is the current density, ρ the electrical resistivity, and κ the thermal conductivity. The first term arises from the thermal conduction, while the second term is the Joule heat^{9,10}. The third term is the heat from the thermoelectric effects.

The change in α is only due to the temperature gradient if the conductor is homogeneous, then:

$$\nabla \alpha = \left(\frac{d\alpha}{dT} \right) \nabla T \quad (1 - 5)$$

Rewriting the third term in Eqn. 1 – 4, the amount of heat evolved due to the Thomson effect is:

$$\tau_T j \cdot \nabla T, \quad \tau_T = -T \left(\frac{d\alpha}{dT} \right) \quad (1 - 6)$$

where τ_T is the Thomson coefficient.

Eqn. 1 – 6 represents the other Thomson relation: $\tau_T = 0$ if the Seebeck coefficient is independent of temperature⁴.

1.2. Applications of Thermoelectrics

Thermoelectric devices rely on the Seebeck effect for generation of electricity, and on the Peltier effect for active cooling. The Seebeck effect is employed commonly in thermocouples for temperature measurements and in thermoelectric generators for the conversion of heat into electricity when coupled to a heat source. The Peltier effect on the other hand is employed commonly to cool charge-coupled device (CCD) cameras in X-ray diffraction instruments, for example.

Thermoelectric generators are mainly used in remote locations to produce electricity since they require little to no maintenance as they have no moving parts. For example, a multi-mission radioisotope thermoelectric generator is used in the Curiosity Mars Rover and Mars 2020 rover^{11,12}. For some terrestrial applications, thermoelectric materials are used to provide cathode protection for cross-country pipelines¹³.

Due to limiting natural energy resources, environmental concerns, and increasing demands for more energy in the society, thermoelectricity may play a role in relieving some of that pressure, together with other renewable energy sources, such as hydroelectricity, solar and wind power^{14–18}. Thermoelectric generators may reduce energy loss by recovering some of the waste heat. For instance, in internal combustion engines, about one-third of the energy from the fuel is lost via exhaust^{19,20}, thermoelectric generators can improve the overall efficiency of fuel consumption.

1.3. Thermoelectric Efficiency

A typical thermoelectric device requires both a p -type and an n -type material in order to produce an electrical current or perform active cooling. A set up of a simple thermoelectric couple is shown in **Figure 1.2**. In the electricity generation mode, the charge carriers travel from the hot end to the cold end, generating an electric current. On the other hand, in the Peltier cooling mode, when an electrical current is applied, the carriers travel and generate a temperature gradient.

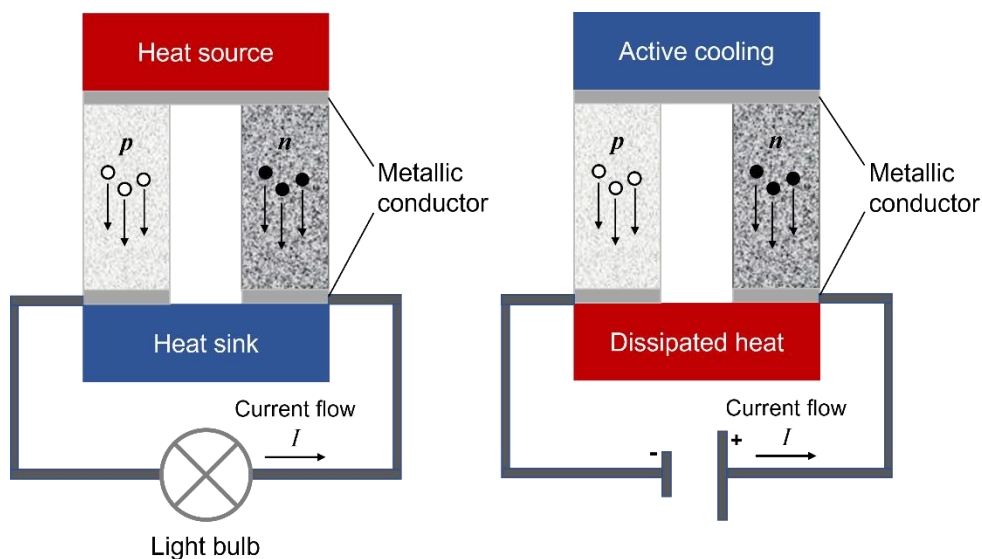


Figure 1.2. A schematic diagram of a thermoelectric couple using a p -type and an n -type material, in electricity generation mode (left) and refrigeration mode (right).

At the start of the 20th century, the German physicist Edmund Altenkirch first derived the maximum efficiency of a thermoelectric generator, η , in his work “Elektrothermische Kälteerzeugung und reversible elektrische Heizung”^{2,4,21}. He found that good

thermoelectric materials should have large Seebeck coefficients, low electrical resistance and low thermal conductance.

The figure-of-merit widely used today is adapted from the extensive investigations on semiconductors as thermoelectric materials by the Russian scientist, Abram Fedorovich Ioffe, whose book was published in 1957²². The efficiency η is defined as the ratio of useful electrical energy $W = I^2R$ delivered to the load (with resistance R) in **Figure 1.2**, to the energy consumed from the heat source Q :

$$Q = Q_P + Q_c - \frac{1}{2}I^2r \quad (1 - 7)$$

where Q_P is the Peltier heat, Q_c is the heat transferred by conduction to the cold junction, and the last term is the electrical energy returned to the heat source generated from the Joule effect.

r is the total resistance of the two thermoelements:

$$r = r_1 + r_2 = \left(\frac{\rho_1}{A_1} + \frac{\rho_2}{A_2} \right) l \quad (1 - 8)$$

where ρ is the electrical resistivity, A and l are the cross-section area and length of the thermoelements, respectively.

Following a series of derivations, it is found that the efficiency η :

$$\eta = \frac{W}{Q} = \frac{T_H - T_C}{T_H} \times \frac{\frac{m}{m+1}}{1 + \frac{Kr}{\alpha^2} \times \frac{m+1}{T_H} - \frac{1}{2}(T_H - T_C) \frac{1}{m+1}} \quad (1-9)$$

where T_H is the temperature at the hot junction, T_C is the temperature at the cold junction, $K (= K_1 + K_2)$ is the total thermal conductance of the thermoelements and $m = \frac{R}{r}$.

The efficiency η from Equation 1 – 9 is determined by the ratio m , and the properties of the materials in the thermoelements, z :

$$z = \frac{\alpha^2}{Kr} \quad (1-10)$$

where $\alpha = |\alpha_1| + |\alpha_2|$, α_1 and α_2 are Seebeck coefficients of the thermoelements.

The maximum efficiency η_{max} is obtained by maximizing z through minimizing Kr and optimizing m , through $\frac{d\eta}{dm} = 0$:

$$z_{max} = \frac{(|\alpha_1| + |\alpha_2|)^2}{(\sqrt{\kappa_1\rho_1} + \sqrt{\kappa_2\rho_2})^2} \quad (1-11)$$

$$\eta_{max} = \frac{T_H - T_C}{T_H} \times \frac{\sqrt{1 + z\bar{T}} - 1}{\sqrt{1 + z\bar{T}} + \frac{T_C}{T_H}} \quad (1-12)$$

where $\bar{T} = \frac{T_H - T_C}{2}$, the average temperature of the junctions.

The first term in Equation 1 – 12 is the Carnot efficiency. η_{max} of a thermoelectric device approaches the Carnot efficiency when $z\bar{T}$ is infinitely large. Note that z_{max} has the units of K^{-1} , and the dimensionless figure-of-merit zT of a single material from Eqn. 1 – 11 is:

$$zT = \frac{\alpha^2}{\rho\kappa} \quad (1 - 13)$$

The concept of power factor (PF) is often introduced in literatures:

$$PF = \frac{\alpha^2}{\rho} (= \alpha^2\sigma) \quad (1 - 14)$$

where σ is the electrical conductivity.

1.4. Theories and Models in Thermoelectric Materials

To understand and predict the charge transport properties of a material, electronic band structures are often calculated and presented in literatures. The below section summarizes several models that are more commonly applied to the field of thermoelectric research.

1.4.1. Electronic Band Structures of Solids

The Drude theory and the free electron theory were the earlier models to describe electron transport. They can be used to explain some transport properties, but both are inadequate to explain some transport phenomena (e.g. the presences of electrons and holes). The nearly-free electron (NFE) model, a successor of the free electron model, is a

significant improvement to describe the motions of electrons in a crystalline solid. The NFE model considers weak atomic potentials $V(r)$ in a crystal lattice, and the effects of the potentials are treated by a 2nd order perturbation method, as a correction to the original energy term derived from the free electron model.

1.4.1.1. Bloch Theorem and the NFE Model

The behaviour of an electron in a crystalline solid is explained starting with the Schrödinger equation^{23,24}:

$$\left[-\frac{\hbar}{2m} \nabla^2 + V(r) \right] \psi(r) = E\psi(r) \quad (1 - 15)$$

where $\psi(r)$ and E are the state function and energy of this electron, respectively. The Bloch theorem states that the solution of Eqn. 1 – 15 has the form:

$$\psi_k(r) = e^{ik \cdot r} u_k(r) \quad (1 - 16)$$

where k is the wavevector, or the crystal momentum of the electron. Both $V(r)$ and $u_k(r)$ are periodic and shares the same translational symmetry as the crystal lattice, and so ψ_k oscillates periodically from one cell to the next. The Bloch function ψ_k is a crystal orbital, and it is delocalized throughout the solid.

As mentioned, the NFE model is built on the free electron model. The correction of the energy function $E(k)$ is due to considering the atomic potentials in the crystal lattice, as a second-order perturbation. Comparing to the free electron model, the NFE model gives rise to energy gaps (i.e. band gaps) in band structures^{23,24}.

The NFE also describes the concept of holes in a material. For an electron that sits near the top of the valence band which is concave downwards (i.e. $E(k) \sim -k^2$), and:

$$\frac{1}{m^*} = \frac{1}{\hbar^2} \frac{d^2 E(k)}{dk^2}, \quad (1 - 17)$$

The effective mass m^* of that electron is now negative²⁴. Instead of using a negative mass, such electron is referred to as a particle with positive charge and positive mass, and is called a hole.

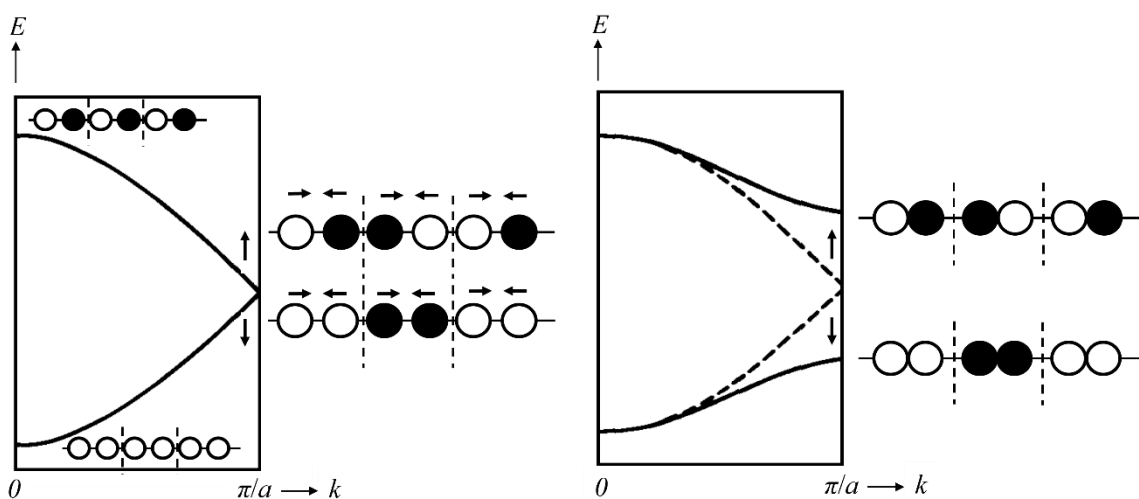


Figure 1.3. A schematic diagram of Peierls distortion in electronic band structures (before: left, after: right). The chain of hydrogen atoms was turned into hydrogen molecule chains, with the dashed line separating the hydrogen molecules²⁵.

Similar features in the band structure can be achieved using crystal orbitals built from the atomic orbitals. Such approach is more favoured by chemists as they are used to operate with atomic orbitals. As an example, formation of shorter and longer bonds within

the linear chain of H atoms due to the Peierls distortion leads to the opening of a band gap²⁵ (**Figure 1.3**). The final outcome of the Peierls distortion in this case is the formation of hydrogen molecules.

1.4.1.2. Visualization of Band Structures From a Chemist's View

Consider bonding in a large ring of equidistant hydrogen atoms. The wavefunctions of the hydrogens are added together to form molecular orbitals. Similar to cyclic, delocalized π -systems, the molecular orbital diagram of this ring of hydrogen atoms could be drawn in a similar fashion (Frost circle), except the difference between the energy levels between pairs of orbitals are infinitely small, though still finite²⁵ (**Figure 1.4**). This is a convenient picture from a chemist's point of view to immediately visualize the energy bands in an extended solid.

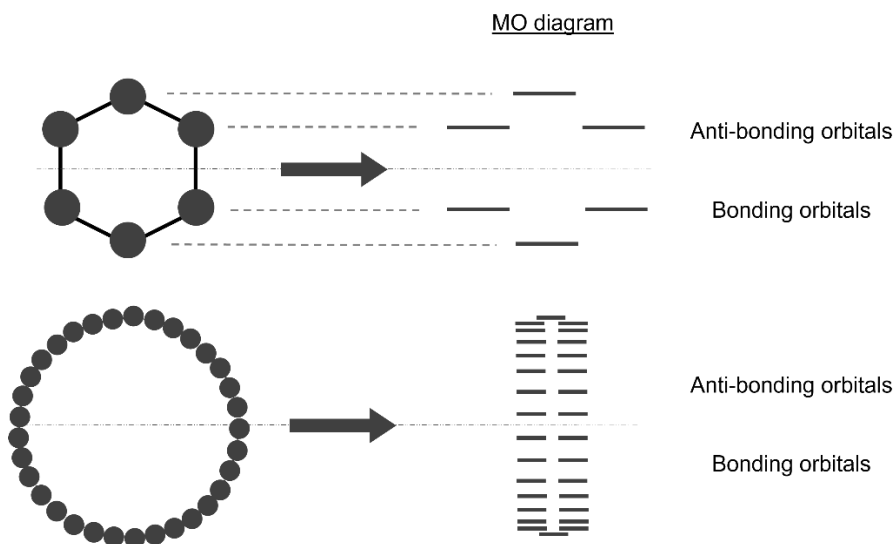


Figure 1.4. The molecular orbital diagram of a long ring of equidistant hydrogen atoms, and its similarity to a six-membered ring delocalized π -system²⁵.

1.4.1.3. The Tight-Binding Model

The tight-binding (TB) model is one of the approaches to approximate the atomic potentials in the crystal lattice for electronic band structure calculations. This model was used in this work to calculate band structures of the studied materials. If the atomic potentials are strong, the electrons remain close to the nuclei when they are moving through the lattice, which would lead to insulating and ionic materials.

1.4.2. Transport Properties

The Seebeck coefficient (α), electrical resistivity (ρ) and the total thermal conductivity (κ) in a material are included directly in the thermoelectric figure-of-merit zT .

In order to have a high energy output, the material is required to have:

- i) high α to have a large potential difference for a given temperature gradient;
- ii) low ρ to have a high current output for the generated potential difference; and,
- iii) low κ to maintain the temperature gradient in the thermoelements.

The thermoelectric performance of a material can be improved, by optimizing the above transport properties. The below section discusses these properties in more details.

1.4.2.1. Charge Transport Properties

The electrical resistivity ρ of a material is given by:

$$\rho = \frac{1}{\sigma}, \quad \sigma = ne\mu_e + pe\mu_h \quad (1 - 18)$$

$$\mu = \frac{e\tau}{m^*} \quad (1 - 19)$$

where n and p are the electron and hole concentrations in the material, respectively. μ is the charge carrier mobility in the material, subscript e and h represents electrons and holes, respectively. τ is the relaxation time of the charge carriers, and m^* is the effective mass of the charge carriers.

For a metal-like conductor, the electrical resistivity increases with increasing temperatures. This is due to the increased electron scatterings by vibrating atoms in a material. The carrier mobility then decreases, in turn increasing electrical resistivity. For an intrinsic semiconductor, the electrical resistivity decreases with increasing temperatures. More electrons from the valence band are thermally excited to the conduction band, which in turn increases concentrations of holes and electrons in the material.

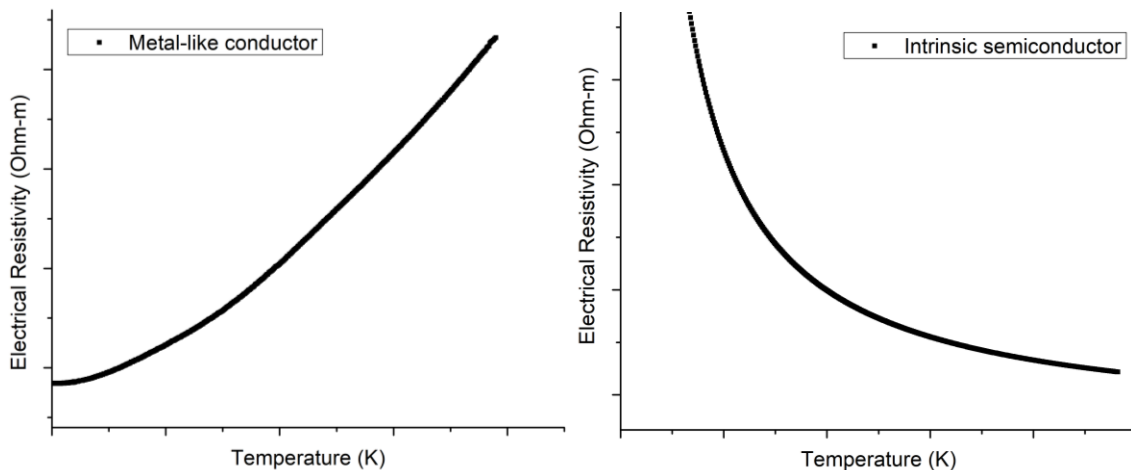


Figure 1.5. The temperature dependence of electrical resistivity in a metal-like conductor (left) and in an intrinsic semiconductor (right).

The Seebeck coefficient (also called thermopower) of a metal or a degenerate semiconductor from the NFE model is^{26,27}:

$$\alpha = \frac{8\pi^2 k_B^2}{3eh^2} m^* T \left(\frac{\pi}{3n} \right)^{\frac{2}{3}} \quad (1 - 20)$$

where h is the Planck's constant, and k_B is the Boltzmann constant. It shows that there is a linear dependence of α on T .

For a material where both electrons and holes are present, contributions from both carriers are considered in the overall Seebeck coefficient²⁸:

$$\alpha_{overall} = \frac{\alpha_e \sigma_e + \alpha_h \sigma_h}{\sigma_e + \sigma_h} \quad (1 - 21)$$

The absolute value of Seebeck coefficient of a non-degenerate semiconductor or an insulator is expected to decrease with temperature, since increasing temperature generates more minor carriers, and increasing the total electrical conductivity. The nominator in Eqn. 1 – 21 becomes smaller and the denominator becomes larger, as temperature increases.

The bipolar effect is another important factor in the thermoelectric research. It is the phenomenon when there is significant amount of the minor charge carriers, affecting the charge transport. The bipolar effect is easily observed during thermopower measurements, as $|\alpha|$ reaches a maximum at certain temperature T . It can be also detected in electrical resistivity, as the resistivity drops due to the bipolar effect. As the bipolar effect

is related to the excitation of electrons from the valence band to the conduction band, the width of thermal band gap (E_g) in a material can be estimated^{28,29}:

$$E_g = 2\alpha_{max}T_{max} \text{ (in eV)} \quad (1 - 22)$$

The band gap derived in this way is called the Goldsmid-Sharp band gap.

1.4.2.2. Thermal Transport Properties

The total thermal conductivity (κ) of a material is composed of the lattice thermal conductivity (κ_l) and electronic thermal conductivity (κ_e):

$$\kappa = \kappa_l + \kappa_e \quad (1 - 23)$$

κ_e is related to the σ of the material, according to the Wiedemann-Franz Law:

$$\kappa_e = L\sigma T \quad (1 - 24)$$

where L is the Lorenz number. L was known as a constant $\frac{\pi^2}{3} \left(\frac{k}{e}\right)^2$ for metals but can deviate depending on the electron band structures of materials. Currently, the following approximation of L is commonly used in the thermoelectric research³⁰:

$$L = 1.5 + \exp\left[-\frac{|\alpha|}{116}\right] \text{ (in } 10^{-8} W\Omega K^{-2}) \quad (1 - 25)$$

where α is in $\mu V/K$.

On the other hand, the lattice thermal conductivity from the kinetic theory is given by:

$$\kappa_l = \frac{1}{3} c_v v_s l = \frac{1}{3} c_v v_s^2 \tau \quad (1 - 26)$$

where c_v is the specific heat per unit volume, v_s is the speed of sound, l is the mean free path of the phonons and τ is the phonon relaxation time in the material.

The heat capacity (or the specific heat) C is defined as the amount of energy needed to increase the temperature of a material by 1 degree. There are c_v and c_p , which are heat capacities of a material at constant volume, and at constant pressure, respectively. c_p is usually measured in experiments.

Considering the total energy of harmonic atomic vibrations in a crystal lattice, the temperature dependence of specific heat c_v is described by the Debye model^{23,24}:

$$c_v = 9R \left(\frac{T}{\theta_D} \right)^3 \int_0^{\theta_D/T} \frac{x^4 e^x}{(e^x - 1)^2} dx \quad (1 - 27)$$

where θ_D is the Debye temperature, and $x = \frac{\theta_D}{T}$.

The specific heat is known to follow the T^3 dependence at low temperatures, and $c_v = 3R$ at $T \gg \theta_D$, which is also referred to as the Dulong-Petit law.

Experimentally, the heat capacity below θ_D can be written as:

$$C = \gamma T + AT^3 \quad (1 - 28)$$

and be plotted C/T against T^2 :

$$C/T = \gamma + AT^2$$

where γ is the Sommerfeld constant. The first term is the electronic contribution while the second is the phonon contribution to heat capacity.

1.4.2.3. Scattering Mechanisms of Charge Carriers and Phonons

The electrical resistivity of a material contains multiple contributions, such as impurity scattering and electron-phonon scattering (subscripts *im* and *ph*, respectively). The net relaxation time of carriers in a material is:

$$\frac{1}{\tau} = \frac{1}{\tau_{im}} + \frac{1}{\tau_{ph}} \quad (1 - 29)$$

Thus, the net resistivity:

$$\rho = \rho_{im} + \rho_{ph}(T) \quad (1 - 30)$$

Note that ρ_{im} is independent of temperature, while ρ_{ph} is dependent of temperature. When T approaches 0, ρ_{ph} approaches 0, and $\rho = \rho_{im}$, which is the residual resistivity. In general, ρ_i increases with impurity concentrations. The statement that ρ and $\frac{1}{\tau}$ can be split into few contributions is referred to as the Matthiessen rule.

The lattice thermal conductivity of a material depends heavily on temperature. Phonon scatterings are typically dominated by certain scattering mechanisms at different temperature ranges. At low temperatures, boundary scattering dominates the phonon

scattering in the material. Then, at higher temperatures and depending on the material, different scattering mechanisms, such as the Umklapp and point defect scatterings, may dominate. The Umklapp process, a phonon-phonon scattering mechanism, occurs at higher temperatures when there are phonons with high enough energies (i.e. $> \sim 0.5k_B\theta_D$). When two phonons with wavevectors K_1 and K_2 meet and collide, using the conservation of momentum:

$$K_1 + K_2 = K_3 \quad (1 - 31)$$

However, if K_3 exceeds the Brillouin Zone (BZ), Eqn. 1 – 30 should be rewritten as:

$$K_1 + K_2 = K_3 + G \quad (1 - 32)$$

where G is the reciprocal lattice vector. The only meaningful K 's lie in the first BZ, so a translational vector G is used to bring the resulting K back to the first BZ, hence the “flipping over” (Umklapp) process occurs.

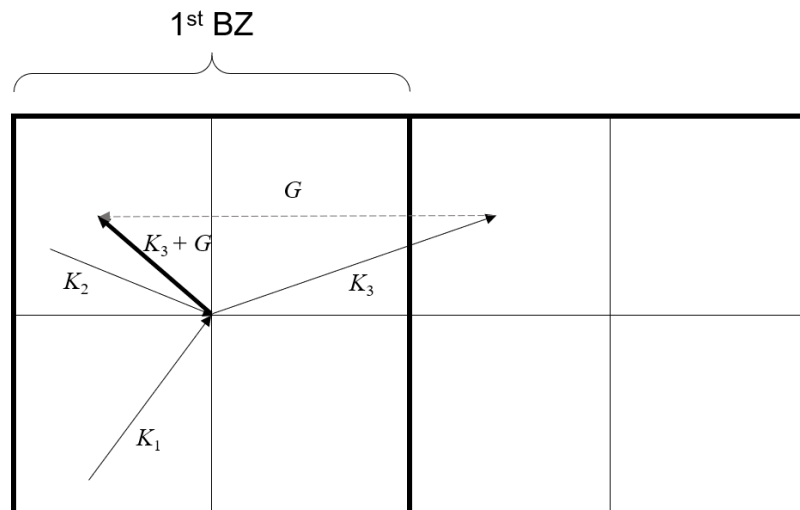


Figure 1.6. The Umklapp process of a phonon-phonon scattering event, shown in a 2D Brillouin zone.

The point defect scattering refers to the impurities in the crystal structure that disrupts the periodicity of the material. Similar to electron impurity scattering, point defects add a component to the relaxation time of a material, as stated in the Matthiessen rule. These defects, described in the Klemens model, are mainly mass differences, force constant differences and the structural distortions brought by the impurities³¹.

1.4.2.4. Charge Transport Regarding Electronic Band Structures

The Boltzmann transport equation (BTE) and the Landauer approach are the two theories to model charge transport properties with respect to the electronic band structure in a material. The expressions for σ , α and κ_e from the BTE include the term transport distribution function (TDF). Within the Landauer approach the TDF is interpreted to be proportional to the number of channels available for conduction and to the mean-free-path of backscattering³².

The expressions of electrical resistivity and Seebeck coefficient include the term $(-\frac{\partial f(E)}{\partial E})$, where $f(E)$ is the Fermi-Dirac distribution function. It describes electron statistics in a material near the Fermi energy E_F . The probability to find an electron at energy E near E_F at absolute temperature T is:

$$f(E) = \frac{1}{e^{(E-E_F)/k_B T} + 1} \quad (1 - 33)$$

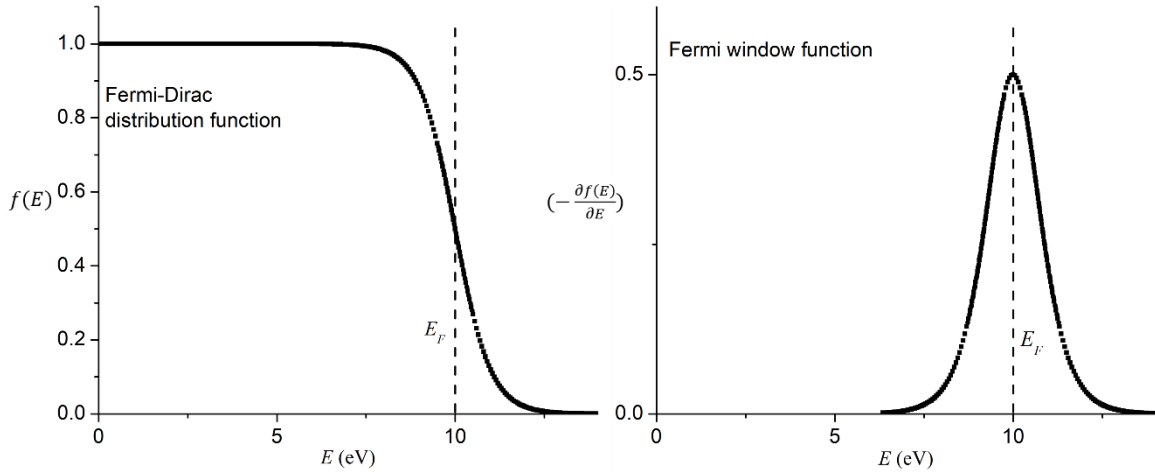


Figure 1.7. The Fermi-Dirac distribution function and the Fermi window function. $k_B T$ is set to be 0.5 eV in the above drawing. (~ 0.025 eV at 293 K)

$-\frac{\partial f(E)}{\partial E}$ on the other hand is the “Fermi window” function, the derivative function of Eqn. 1 – 33^{32–34}. This explains mathematically why only charge carriers near the Fermi energy is responsible for the charge transport properties of the material. For charge carriers to participate in charge transport, the carriers must be able to move in the band structure. Carriers far away from the Fermi energy have no nearby available states to move to, thus in general do not have a net contribution to charge transport of a material.

The Seebeck coefficient in a metal is usually small, while large in insulators. The phenomena can be examined using the Mott equation^{35–37}:

$$\alpha = \frac{\pi^2}{3} \left(\frac{k_B^2 T}{e} \right) \left(\frac{d \ln \sigma(E)}{dE} \right) \Big|_{E=E_F}$$

$$= \frac{\pi^2}{3} \left(\frac{k_B^2 T}{e} \right) \left(\frac{d(\ln(n(E)))}{dE} + \frac{d(\ln(\mu(E)))}{dE} \right) \Big|_{E=E_F} \quad (1 - 34)$$

From Eqn. 1 – 34, it can be seen that the Seebeck coefficient is roughly proportional to³⁸:

$$\alpha \propto \frac{\partial D(E)}{\partial E} \Big|_{E=E_F} \quad (1 - 35)$$

where $D(E)$ is density of states of the material. For a metal, the Fermi energy typically locates in the middle of a band, whereas for an insulator the Fermi energy locates at the edge of a band, and $D(E) \rightarrow 0$. In comparison, the slope of the density of states $\frac{\partial D(E)}{\partial E}$ at E_F is large in insulators and small in metals, hence the difference of Seebeck coefficients in metals and insulators. An electron in the band structure must move to another empty state to be responsible for charge transport, thus for an insulator, electrons must be excited across the band gap into another state, while for a metal, electrons have vacant states in the proximity. In insulators, the potential difference for electrons is large between the states than in metals. As a result, the Seebeck coefficient in insulators is larger.

1.4.2.5. Thermal Transport in Calculations

It is possible to predict lattice thermal conductivity by calculating the phonon dispersion curves of a material. Since phonons are quantized lattice vibrations, these curves are further broken down into different branches: transverse and longitudinal acoustic (TA and LA) modes, and transverse and longitudinal optical (TO and LO) modes. In a one-dimensional case, acoustic modes refer to in-phase vibrations, while optical modes refer to

out-of-phase vibrations. In general, if there are r atoms in a unit cell, there are total of $3r$ dispersion curves. 3 branches would be acoustic, while the remaining $(3r - 3)$ are optical. It is also possible to estimate the phonon velocity with the dispersion curves, and is given by the slope of the curves, at a particular phonon frequency ω .

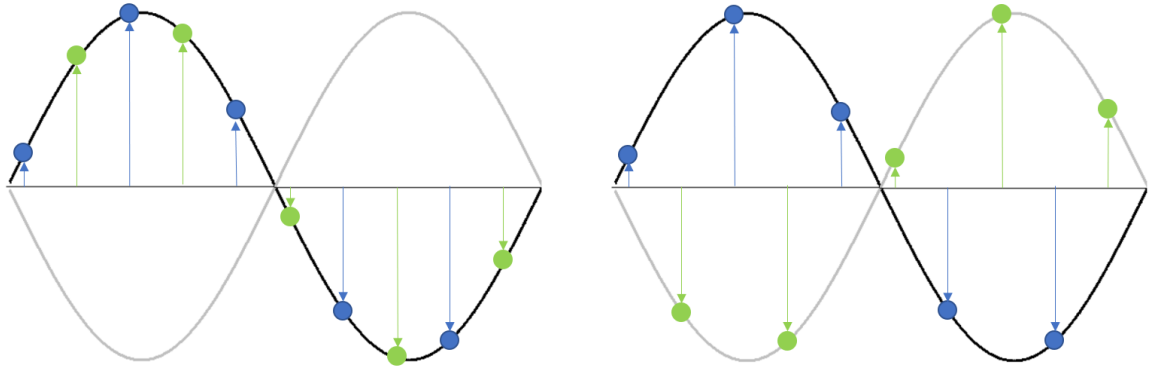


Figure 1.8. Movements of atoms in the acoustic (left) and optical (right) mode at frequency ω in a 1D chain 2 atom case.

There is also the Grüneisen parameter γ , which is a measure of anharmonicity of a material and can be computed, although is not studied in this dissertation:

$$\gamma = -\left(\frac{\Delta\omega}{\omega}\right)/\left(\frac{\Delta V}{V}\right), \quad (1 - 36)$$

where V is the unit cell volume of the structure. Thermal expansion in a material is due to the anharmonic vibration of the lattice, and γ relates the volume change and the vibrational frequencies in the material³⁹. Macroscopically:

$$\gamma = \frac{\alpha V_m K_T}{C_{v,mol}} = \frac{\alpha K_T}{C_{v,g}\rho}, \quad (1 - 37)$$

where α is the volume thermal expansion coefficient, V_m is the molar volume, K_T the isothermal bulk modulus, $C_{v,mol}$ and $C_{v,g}$ is the molar and mass heat capacity at constant volume, respectively, and ρ here is the mass density of the material⁴⁰. The anharmonic effect to lattice thermal conductivity is prominent at high temperatures, and:

$$\kappa_l \sim \frac{\rho v_s^3}{\gamma^2 T} a, \quad (1 - 38)$$

where a is the lattice parameter⁴¹.

1.4.2.6. Optimizing PF and Improving zT of a Thermoelectric Material

Equations in the previous sections state that several transport properties are correlated to each other. The thermopower and electrical resistivity are positively related to each other, and the electrical component of thermal conductivity depends on ρ . As a result, the power factor α^2/ρ in the figure-of-merit for a material should be as large as possible. The lattice component of the thermal conductivity does not directly correlate with any other property in zT , and thus it should be minimized. A good thermoelectric material should behave like a “phonon-glass, electron-crystal” material, a concept coined by G. A. Slack⁴². It suggests a low thermal conductivity, a high electrical conductivity and in the material, respectively.

A typical strategy to improve zT of a material would be by incorporating foreign elements in the crystal structure of the material. Under a rigid band regime, incorporating foreign elements in the crystal structure changes the Fermi energy of the material, thus the

material charge transport properties are affected. However, when the amount of incorporating elements is significant, the rigid band approximation no longer applies, and there are significant changes of the band structure in the material. This in turn drastically modifies the charge transport properties by affecting carrier concentrations and carrier effective masses of the material. Additional aspect of such incorporations is that foreign atoms act as impurities in the crystal structure and increase the material electrical resistivity by reducing the carrier relaxation times. On the other hand, impurities are effective means to reduce the lattice thermal conductivity by additional impurity scattering.

Some other strategies include synthesizing thermoelectric materials with nanoscale domains and using composite materials. Comparing to conventional bulk materials, nanostructuring provides an alternate route to manipulate charge and thermal transport in materials. Electrical resistivity will go up due to the increase in the number of boundaries, but the associated quantum confinement can lead to an increase of thermopower^{43,44}. Additionally, lattice mismatch and potential barriers at the interface between the nanoparticles and the host material can lead to high electrical resistance⁴⁵, while it can reduce the thermal conductivity. In general, inclusions should be carefully selected as they can affect the material transport properties significantly, and have either positive or negative effect on the figure-of-merit.

1.5. State-of-the-art Thermoelectric Materials

The following section introduces some known material systems as potential thermoelectric materials. It is essential to highlight the outstanding properties and at the

same time disadvantages of these systems, and to provide insights in the thermoelectric research.

1.5.1. Chalcogen-based Materials

This group of materials is further broken down into several large groups. They are group IV-tellurides (IV-Te), *Pn*-chalcogenides (*Pn* = pnictogens, *Pn-Ch*), and some notable selenides.

1.5.1.1. IV-Te Systems

Some IV-Te systems include GeTe-, SnTe- and PbTe-based materials. These materials crystallize in relatively simple structures. Pristine SnTe and PbTe crystallize in the rock salt structure (space group $Fm\bar{3}m$), while GeTe crystallizes in a distorted rock salt structure (space group $R\bar{3}m$) at room temperature, and GeTe undergoes a phase transition to $Fm\bar{3}m$ at 705 K⁴⁶⁻⁴⁸.

PbTe, being one of the earlier thermoelectric materials, has the outstanding feature of a low lattice thermal conductivity of 2 W/m-K at 300 K in single crystalline samples^{49,50}, due to a strong anharmonic coupling between the LA and TO modes in the phonon dispersion curve of PbTe⁵¹. The *p*-type Na-doped PbTe/SrTe has a reported peak zT of ~2.5 at 923 K⁵², while the *n*-type Bi-doped PbTe/Ag₂Te has a reported peak zT of ~2 at 800 K⁵³.

SnTe-based materials are investigated as a Pb-free, less toxic alternative to PbTe. The pristine SnTe however suffers from a high intrinsic carrier concentration due to the inherent Sn vacancies, smaller thermopower and a high thermal conductivity, thus it has a

lower zT than PbTe ^{37,54}. Nonetheless, Hwang J. *et al.* reported a peak zT of 1.9 at 923 K in a p -type In-doped SnTe grains with CdTe-based coated layers⁵⁵.

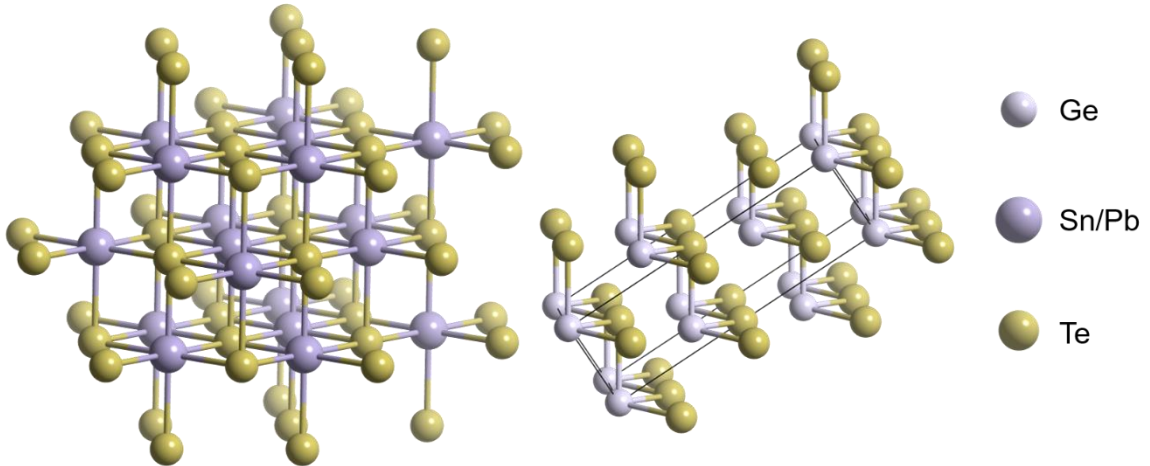


Figure 1.9. The rock salt (left) and the distorted rock salt (right) structure in the IV–Te system. In the distorted structure, only the short IV – Te distances are drawn.

GeTe is known and investigated in different fields of applications, such as ferroelectric, thermoelectric, spintronics and phase-change materials⁵⁶. GeTe has an intrinsically high carrier concentration due to Ge vacancies, it possesses a peak zT of ~ 1 at 700 K⁵⁷. M. Hong *et al.* reported a peak zT of 2.2 at ~ 650 K for a p -type Cd/Bi-codoped GeTe, with Cd for band engineering purposes and Bi for optimizing carrier concentration⁵⁸. In 2019, M. Samanta *et al.* realized an n -type GeTe material when it is alloyed with a certain amount of AgBiSe_2 . The material has a peak zT of ~ 0.6 at 500 K (n -type) and ~ 1.3 at 467 K (p -type)⁵⁹.

1.5.1.2. *Pn-Ch* Systems

A well-known member of the *Pn-Ch* group is Bi_2Te_3 , which is used for room temperature Peltier cooling purposes. Together with Sb_2Te_3 and Bi_2Se_3 , this group of materials crystallizes in the tetradymite structure (space group $R\bar{3}m$)⁶⁰. The structure is built up of alternating Bi and Te layers stacking along the *c* direction, with Bi sitting in the voids of the BiTe_6 octahedra and off centre. The motif repeats every Te–Bi–Te–Bi–Te layer, and these “quintuple” layers are held together by van der Waals forces.

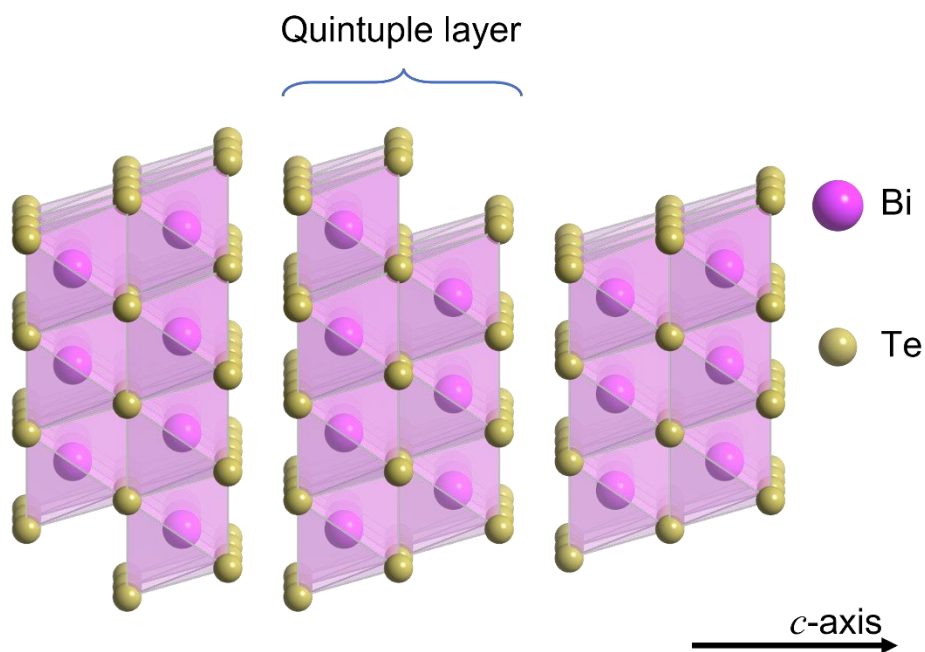


Figure 1.10. Structure of Bi_2Te_3 . Note that the Bi atoms in the octahedra are distorted towards the gap between the quintuple layers.

Due to its crystal structure, both the charge and thermal transport properties of this material are strongly anisotropic, namely along the *c* direction and the *ab* plane. In fact, Bi_2Te_3 is often alloyed with Sb (*p*-type) and Se (*n*-type) due to the isostructural nature of

the above-mentioned materials. S. I. Kim *et al.* reported a peak zT of as high as 1.86 at 320 K for a p -type melt-spun $\text{Bi}_{0.5}\text{Sb}_{1.5}\text{Te}_3$, fabricated using a liquid phase sintering with molten Te as sintering aid^{61,62}. However, such high zT values could not be reproduced by other groups using this technique. Using the same approach, Deng *et al.* only reached a peak zT of 1.2 at 350 K, and that authors concluded that the anisotropy of transport properties play a role in the thermoelectric measurements, and thus the obtained zT values⁶³.

1.5.1.3. SnSe and Cu_{2-x}Se Selenides

SnSe and Cu_{2-x}Se materials possess relatively high zT values and distinct crystal structures.

SnSe crystallizes in a three-dimensionally distorted NaCl structure, with $Pnma$ space group, at room temperature. It undergoes a shear phase transition at ~ 800 K, to a higher symmetry $Cmcm$ space group⁶⁴.

Similar to Bi_2Te_3 and due to its crystal structure, the transport properties of SnSe are anisotropic in nature. The material has higher power factor along the bc plane and low thermal conductivity along the a axis (in the $Pnma$ setting). It has an intrinsically low carrier concentration ($\sim 10^{17} \text{ cm}^{-3}$) at room temperature, however it is increased to $\sim 10^{19} \text{ cm}^{-3}$ when doped with Na. SnSe also features an ultralow thermal conductivity of 0.3 W/m-K along the a axis and ~ 0.5 along b and c axes. The p -type, Na-doped SnSe single crystal has a maximum peak zT of 2.4 at ~ 750 K along the b axis, with an average peak zT of 2.0 among 10 samples^{64–66}.

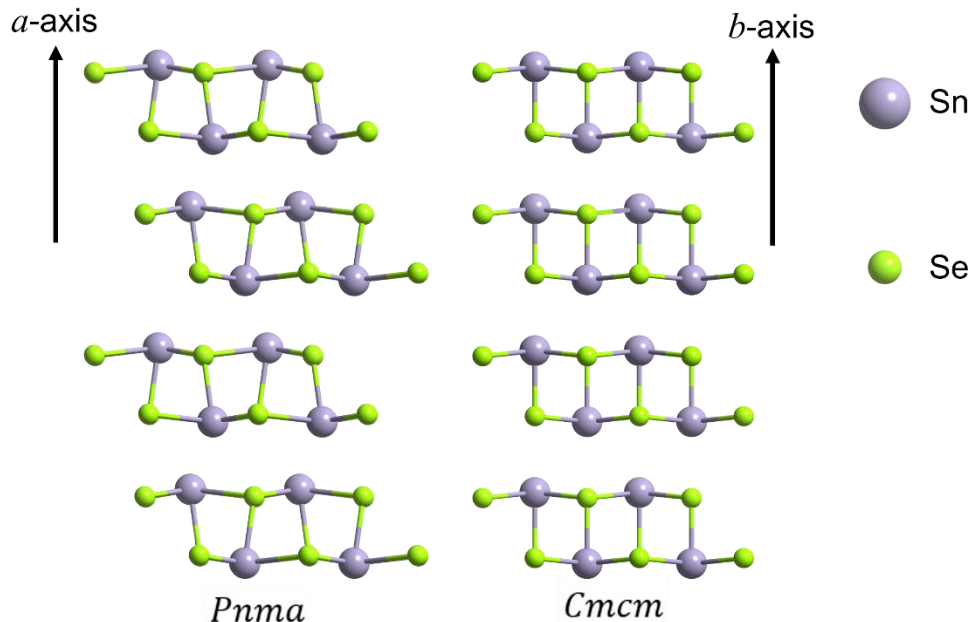


Figure 1.11. Structures of SnSe, in *Pnma* (left, room temperature polymorph) and in *Cmcm* (right, high temperature polymorph) space groups. In the *Cmcm* structure, the intraplanar Sn – Se distances are ~ 2.7 and 3.0 \AA , while the interplanar Sn – Se distance is $\sim 3.7 \text{ \AA}$.

Cu_{2-x}Se undergoes a phase transition in the temperature range $350 - 410 \text{ K}$, from the low temperature β -phase (space group of the average structure: $R\bar{3}m$) to the high temperature α -phase (space group: $Fm\bar{3}m$)⁶⁷. Gulay *et al.* reported a $C2/c$ superstructure for the β -phase, however, the R factor was high ($R_1 \approx 0.14$)⁶⁸.

The $\alpha\text{-Cu}_{2-x}\text{Se}$ with the main Cu atoms crystallizes in primarily the anti-fluorite structure. The true structure of $\beta\text{-Cu}_{2-x}\text{Se}$ is more complex, and **Figure 1.12** only represents its average structure. E. Eikeland *et al.* further proposed a superstructural cell with the $C2/c$ space group and described the $\alpha - \beta$ phase transition as a two-step visualization: a

symmetric reduction followed by a displacive phase transition. However neither their model fitted well with their experimental data, in particular with the superstructure reflections⁶⁷. The Cu3 atoms in the α -phase are located close to the main Cu site, while the Cu3 atoms in the β -phase are contributed almost evenly between the tetrahedral voids. These split Cu2 and Cu3 atomic positions imply high Cu mobility in the material⁶⁹, and the instability of Cu₂Se under operating conditions is a major issue for employing Cu₂Se in thermoelectric devices.

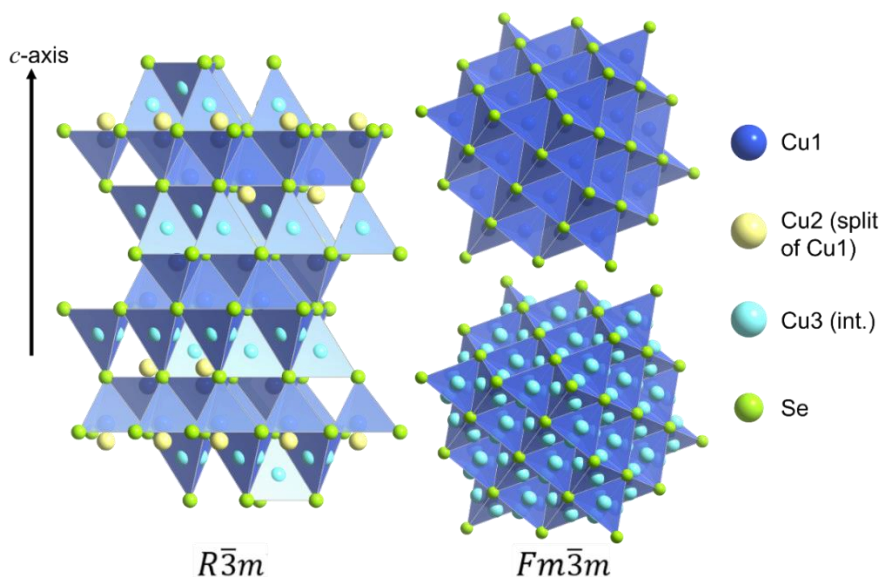


Figure 1.12. Structures of Cu_{2-x}Se in the β -phase ($R\bar{3}m$, left) and the α -phase ($Fm\bar{3}m$, right) space groups. The Cu3 site in the $R\bar{3}m$ structure split into 3 sites ($\sim 33\%$ site occupancy each) and reach ~ 1 Cu in the formula by itself. Cu1 and Cu2 combines to reach another ~ 1 Cu in the formula. The $Fm\bar{3}m$ structure is shown twice with and without the under occupied Cu in the formula. The $Fm\bar{3}m$ structure is shown twice with and without the under occupied Cu interstitial sites (bottom and top, respectively). The Cu3 site in the $Fm\bar{3}m$ structure split

into 4 sites (~9 % site occupancy each) and reach ~2 Cu in the formula together with Cu1 instead.

Despite the stability issue in the pristine Cu₂Se materials, a study by A. A. Olvera *et al.* reported a boost in the peak zT from 0.7 to 2.6 at ~850 K in a p -type In-doped Cu₂Se/CuInSe₂ composite material. The stability of the composite was tested by applying a current density of 100 A cm⁻² for 24 h, and no visible signs of copper extrusion were observed⁷⁰.

1.5.2. Skutterudites

The thermoelectric properties of CoSb₃, one of the earlier materials studied in this family, were reported by T. Caillat *et al.*⁷¹. Although the pristine CoSb₃ is a p -type material, it can be converted to n -type with dopants. Skutterudites crystallize in the cubic $Im\bar{3}$ structure and can be described as Zintl phases. The Sb atoms form square polyanionic Sb₄⁴⁻ rings, whose charge is balanced by that of Co³⁺ in the octahedral voids made of Sb. Each Sb vertex of the octahedron belong to a different Sb₄⁴⁻. There are also large icosahedral voids (C.N.=12) present in the structure, and they can be filled with a foreign element, allowing to tune the physical properties of skutterudites. In addition to thermoelectrics, skutterudites are investigated for their magnetic properties due to the structure's ability to host rare-earth elements⁷².

The pure CoSb₃ has a relatively high power factor, while suffers from high thermal conductivity, and the reported peak zT values are ~ 0.1 – 0.2 at ~ 700 K^{73–75}. Efforts were

made to reduce the thermal conductivity by introducing foreign atoms into the structure. S. Su *et al.* reported a peak zT of 1.1 at 800 K in an n -type Ge/Te-codoped CoSb_3 ⁷⁶.

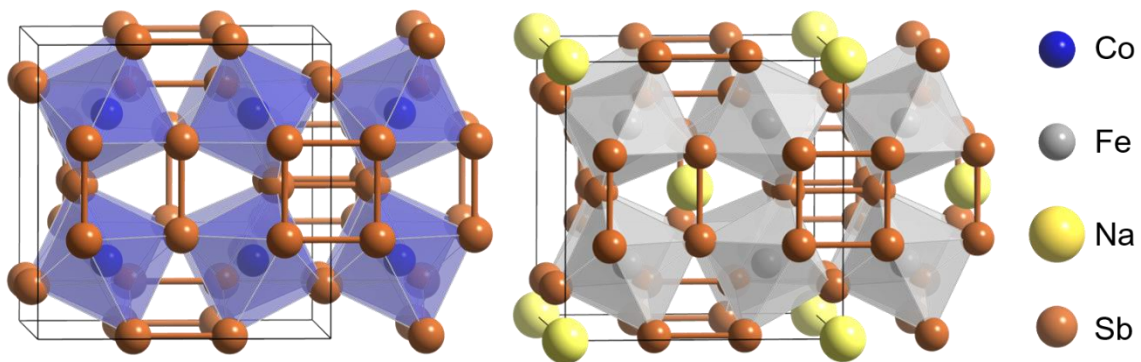


Figure 1.13. Structure of a skutterudite CoSb_3 (left) and a filled skutterudite $\text{NaFe}_4\text{Sb}_{12}$ (right).

On the other hand, the filled skutterudite material has the general composition AB_4X_{12} ⁷². The A atoms filling the icosahedral voids, can act as independent oscillators (rattlers) and suppress the thermal conductivity of the material⁷⁷, although the suppression mechanism is still debated⁷³. Nonetheless, X. Shi *et al.* reported a peak zT of 1.7 at 850 K in an n -type Ba/La/Yb-cofilled CoSb_3 ⁷⁸.

1.5.3. Clathrates

Clathrates are a large group of materials built up of polyhedral cages of tetrahedrally coordinated atoms while encapsulating guest atoms, ions or molecules in them. Some of these cage-like structured materials can also be classified as Zintl compounds, since the cages build polyanionic/polycationic frameworks, whose negative/positive charges are balanced by the guest ions⁷⁹. Clathrates are further broken into different types, according

to their structures. Type-I and type-II inorganic clathrates gained attention as potential thermoelectric materials; thus these two types of clathrates are introduced in this section. In general, clathrates are known to exhibit low thermal conductivity due to the disorder of the guest atoms⁸⁰. The electrical transport properties of clathrates are highly tunable, depending on the composition.

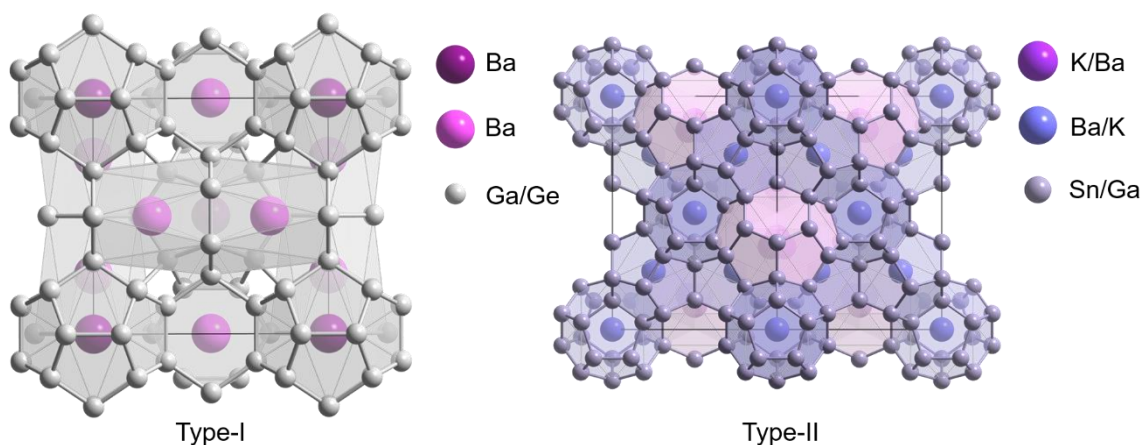


Figure 1.14. Structures of a type-I clathrate $\text{Ba}_8\text{Ga}_{16}\text{Ge}_{30}$ (left), and a type-II clathrate $(\text{K}, \text{Ba})_{24}(\text{Ga}, \text{Sn})_{136}$ (right). Type-I: different colours of the two Ba indicate the two different polyhedral voids in which they are located. Type-II: different shades of the polyhedra represent the two different polyhedral shapes. The K/Ga site in the purple hexakaidecahedra is evenly split into 4 sites⁸¹.

Type-I clathrates crystallize in the cubic space group $Pm\bar{3}n$ with the general composition $G_8A_{46-x}B_x$, where the $(A_{46-x}B_x)$ unit forms the face-sharing 6 tetrakaidecahedral ($3^{12}6^2$) and 2 dodecahedral (5^{12}) cages, hosting guest atoms/ions G . An n -type Czochralski grown $\text{Ba}_8\text{Ga}_{16-x}\text{Ge}_{30+x}$ single crystal achieved a zT of 1.35 at 900 K without passing

through a maximum. The material features tunable Seebeck coefficients, by varying Ga/Ge ratios⁸². On the other hand, L.-H. Wang *et al.* reported a zT of 1.10 at 823 K in a polycrystalline p -type $\text{Ba}_8\text{Ga}_{16+x}\text{Ge}_{30-y}$ material⁸³.

Type-II clathrates have general composition $A_8B_{16}X_{136}$, where X makes 8 hexakaidecahedral ($5^{12}6^4$) and 16 pentagonal dodecahedral (5^{12}) cages, with A and B atoms occupying the cages, respectively⁸⁴. This structure is highly tolerable in terms of compositional variances, such as in $\text{Na}_{24-x}\text{Si}_{136}$ ⁸⁵. K. Kishimoto *et al.* reported a peak zT of 1.19 at 630 K in a sintered, n -type $(\text{K}, \text{Ba})_{24}(\text{Ga}, \text{Sn})_{136}$ material⁸¹.

1.5.4. Other Zintl Phase Materials

There are a significant number of other structures that can be classified as Zintl phases. These Zintl phases seem to satisfy the “phonon-glass, electron-crystal” concept, as they involve both ionic and covalent bonding in their structures⁸⁶, contributing to the electron-crystal and phonon-glass part, respectively. The $\text{Yb}_{14}\text{MnSb}_{11}$ phase gained attention as potential thermoelectric materials back in 2006 due to its high peak zT of ~ 1 at 1223 K at that time. It crystallizes in the $I4_1/acd$ space group, and its structure is made up of 14 Yb^{2+} , 1 MnSb_4^{9-} , 1 Sb_3^{7-} and 4 Sb^{3-} per formula unit⁸⁷. S. R. Brown *et al.* reported a peak zT of ~ 1.0 at 1223 K in the p -type $\text{Yb}_{14}\text{MnSb}_{11}$ material in 2006⁸⁸, while another p -type Al-doped $\text{Yb}_{14}\text{MnSb}_{11}$ has a reported peak zT of 1.3 at 1223 K⁸⁹.

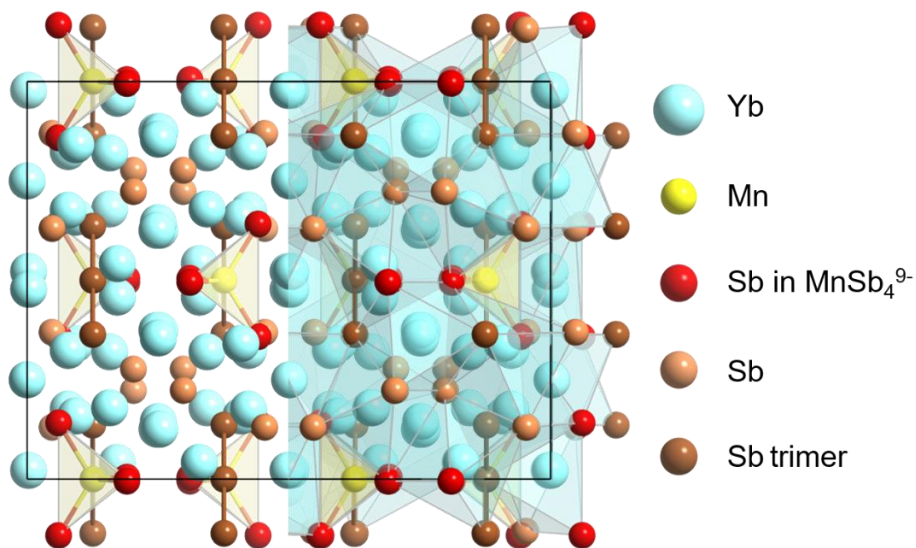


Figure 1.15. Structure of $\text{Yb}_{14}\text{MnSb}_{11}$. The right half shows the Yb atoms located in (distorted) octahedral voids, which share faces, while the left half features the MnSb_4^{9-} subunit.

1.6. Materials in Focus

This study aims to optimize and improve the thermoelectric performance of the $\text{Zn}_{13}\text{Sb}_{10}$ phase, by means of doping, and navigate its “structure–property–composition” relationship. It also explores the feasibility of employing the $\beta\text{-Zn}_{13}\text{Sb}_{10}$ phase in thermoelectric applications, by studying its syntheses, the Zn–Sb phase diagram, thermoelectric properties, and stability under different densification conditions.

1.6.1. $\beta\text{-Zn}_{13}\text{Sb}_{10}$

The “ $\beta\text{-Zn}_4\text{Sb}_3$ ” phase has gained attention as potential thermoelectric material near the end of 20th century since it was measured to have zT of ~ 1.3 at 670 K^{90} , although there

was an earlier report on the synthesis of the material by H. W. Mayer et al.⁹¹. The phase was made by quenching the sample with the Zn_4Sb_3 loading composition, which gave the purest sample. The Zn_4Sb_3 phase has transport properties that fits those of a “phonon-glass, electron-crystal”, since it possesses an extraordinarily low thermal conductivity, and electrical conductivity similar to a heavily doped semiconductor. The high zT achieved at that time has triggered waves of thermoelectric research on the Zn_4Sb_3 -based material.

The $Zn_{13}Sb_{10}$ material adopts the α' , α and β modifications below 235 K, between 235 and 254 K, and above 254 K, respectively⁹²⁻⁹⁴, with β - $Zn_{13}Sb_{10}$ being the phase of interest as thermoelectric materials. The structure of β - $Zn_{13}Sb_{10}$ has been extensively studied⁹⁴⁻⁹⁶. It crystallizes in the $R\bar{3}c$ space group, with Sb atoms building up the sublattice, and Zn atoms occupying the tetrahedral Sb voids. $Zn_{13}Sb_{10}$ is considered a Zintl phase due to the formation of Sb_2^{4-} dimers, and $Zn:Sb = 13:10$ is the charge-balanced composition of the material; The Sb sublattice contains two types of Sb, 6 Sb^{3-} isolated anions and 2 Sb_2^{4-} dimers, and 13 Zn^{2+} cations (13:10 composition) provides the charge balance.

The main Zn site occupies the Sb tetrahedra formed by 3 Sb^{3-} anions and one of Sb in an Sb_2^{4-} dimer. Accounting only the main Zn site, the composition of the material is $Zn_{12}Sb_{10}$. Moreover, the main Zn site is ~90% occupied, which makes the composition even more Zn poor in comparison to $Zn_{13}Sb_{10}$. The Zn amount of the material approaches the $Zn_{13}Sb_{10}$ composition due to the 3 deficient interstitial Zn sites, each with around 6% occupancy⁹⁶. Note that recently a (3+1)-D structural model of β - Zn_4Sb_3 was proposed⁹⁷.

A large portion of this work is devoted to optimizing the thermoelectric performance of the β -Zn₁₃Sb₁₀ phase by dopant incorporations and studying the corresponding changes in transport properties. Feasibility towards real life applications of the Zn₁₃Sb₁₀ material is also explored and evaluated.

1.6.2. ZnSb

ZnSb crystallizes in the *Pbca* space group. Compared to the β -Zn₁₃Sb₁₀ phase, ZnSb is an ordered phase, which also satisfies the Zintl-Klemm formalism. The Sb sublattice of ZnSb only contains Sb₂⁴⁻ dimers, and Zn²⁺ provides the charge balance. The Zn atoms occupy the Sb tetrahedra formed by four Sb from different Sb₂⁴⁻ dimers. Due to the structural similarity between the β -Zn₁₃Sb₁₀ and ZnSb, ZnSb was employed to understand the changes in transport properties of β -Zn₁₃Sb₁₀ brought by dopants.

1.6.3. Other Zn-Sb Relative Phases

In the Zn – Sb phase diagram, there are still some other phases with compositions close to the β -Zn₁₃Sb₁₀ phase, such as Zn₃Sb₂, Zn₉Sb₇ and Zn₈Sb₇ phases. This study also attempts to investigate these phases, in hope to aid the understanding of the “structure–property–composition” relationship in the (Zn,Sb) binary materials. A report on the Zn₈Sb₇ phase was published by J. Wang *et al.*⁹⁸, while the high-temperature, metastable Zn₉Sb₇ phase was previously studied in our group⁹⁹. Thus, the current study will focus on the findings for the Zn₃Sb₂ phase(s), on top of β -Zn₁₃Sb₁₀ and ZnSb.

Chapter 2. Methodology and Experimentation

2.1. Synthetic Approach

In this dissertation, elemental Zn, Sb and dopants were used to prepare different Zn – Sb phases. Zn and Sb have relatively low melting points, although possess high vapour pressures, especially Zn. Also, inert atmospheres are required for the reactions since they are easily oxidized at elevated temperatures. As a result, a closed, inert environment is required to synthesize materials in the Zn – Sb systems.

In general, traditional melting and solidification were used to synthesize the polycrystalline materials. Elements were put into quartz tubes, evacuated and sealed. Due to the high vapour pressures of Zn and Sb, quartz ampoules were minimized in size to reduce material losses in the sample ingots. Additionally, sample quenching was generally avoided for the same reason.

In attempt to study the anisotropic transport properties of the Zn – Sb materials and structural changes potentially brought by dopant incorporations, single-crystalline $Zn_{13}Sb_{10}$ materials were grown using the metal flux method. Starting materials were placed in alumina crucibles which were then sealed in quartz ampoules for the flux growth. The synthesized crystals were then separated from the flux by centrifugation.

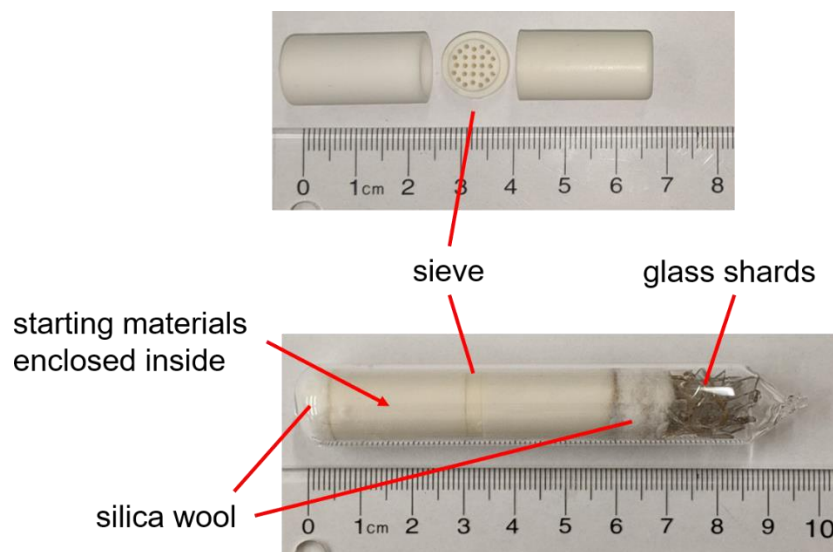


Figure 2.1. The set up used for the flux growth. Alumina crucibles with the frit in-between are placed into quartz ampoules. Silica wool is placed on both sides of the alumina crucibles to provide a cushion during centrifugation. Silica shards are put to fill the space and improve the sealing; they are often darkened due to sealing.

In addition, some compaction techniques, such as hot pressing and spark plasma sintering, were explored to examine the compatibilities of the Zn – Sb materials with these methods, since these techniques are employed to make thermoelectric devices in the industrialization processes. Some studies on the stabilities of the Zn – Sb materials were also examined in the later part of this work.

2.2. X-ray Diffraction

Powder X-ray diffraction is a routine characterization technique for the synthesized materials. Also, single-crystal X-ray diffraction is used to establish or verify the atomic

structures of materials. Understanding crystal structures of a material is the key to understand the structure-property relationship in the materials.

2.2.1. Generation of X Rays

Two common X-ray sources for X-ray diffractions are X-ray tubes for routine laboratory use, and synchrotron radiation where accelerated electrons are moving in a circular orbit. While X rays include electromagnetic waves with wavelengths from 0.1 to 100 Å, only wavelengths ~ 0.5 to 2.5 Å are used in crystallography since they are of similar magnitude as interatomic distances in materials.

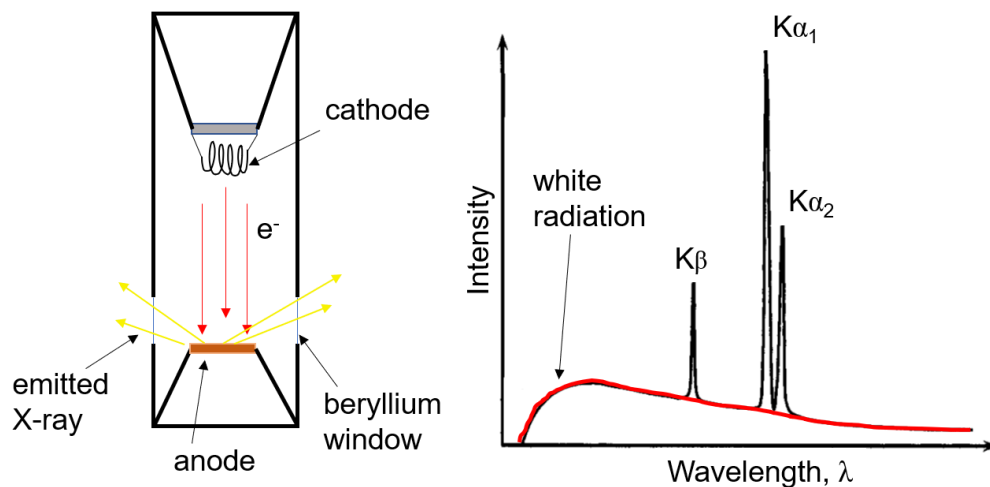


Figure 2.2. Schematic diagram of the X-ray tube (left) and a typical X-ray emission spectrum (right), which includes the continuous, white radiation, highlighted in red and characteristic X-rays ($K\alpha_1$, $K\alpha_2$ and $K\beta$)¹⁰⁰.

In an X-ray tube, electrons are emitted by the cathode, typically heated tungsten filament, and electrons are accelerated in high voltage and hit the anode of some metal. The

white radiation is generated from the decelerating electrons in different manners, thus X rays with a continuous range of wavelengths are emitted. On top of the white radiation, the more intense, characteristic X rays are emitted. These emissions result from transitions of electrons from the upper to vacant lower energy levels of an atom; electrons in the lower energy levels were ejected by the impact of electrons from the cathode. Thus, the wavelengths of the characteristic X rays are specific to the element in the anode target. For this study, Cu $K\alpha_1$ radiation is used for powder X-ray diffractions, while Mo $K\alpha$ radiation is used for single-crystal X-ray diffraction.

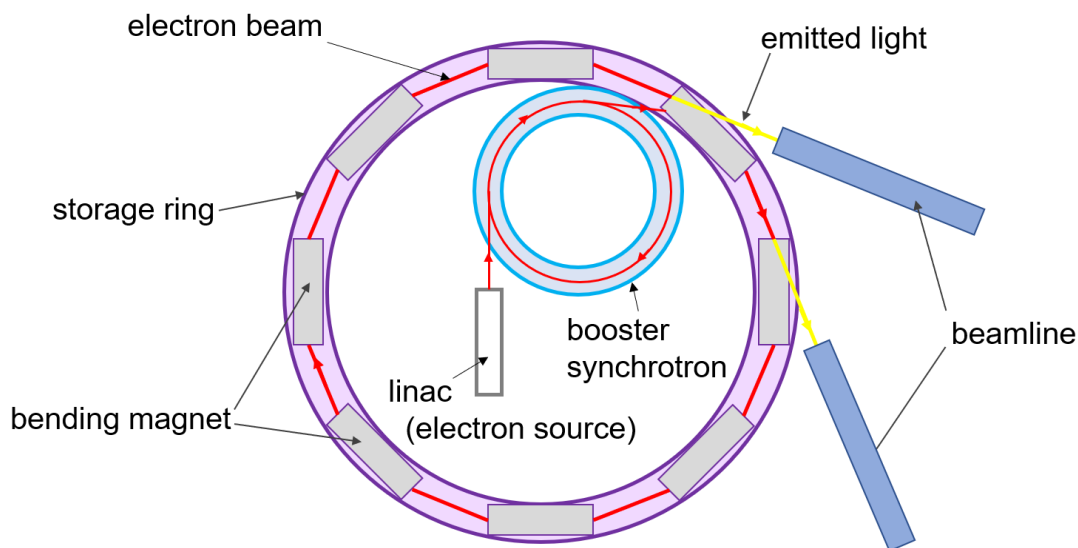


Figure 2.3. Schematic diagram of a synchrotron facility.

In a synchrotron, X-ray radiation is generated by changing the trajectory of moving electrons in the storage ring; this is done by employing magnets known as undulators and wigglers. The X-ray beam is emitted tangential to the electron orbit. X-rays from synchrotron radiation sources have intensity many orders of magnitude higher than that

generated from X-ray tubes, and a continuous range of wavelengths of X-rays can be selected. X-ray diffraction using a synchrotron source was employed to study the phase diagram and transitions in the Zn – Sb system.

2.2.2. Miller Indices and Braggs' Law

X-ray diffraction peaks of a material can be indexed using the Miller indices (hkl) of its unit cells. Since diffraction occurs from the plane, the Miller indices (hkl) represent a set of parallel, crystallographic planes that divide the lattice vectors \mathbf{a} , \mathbf{b} , \mathbf{c} into the h , k , and l parts, respectively. Another important parameter of the (hkl) planes is the interplanar distances (also referred to d -spacing), d_{hkl} .

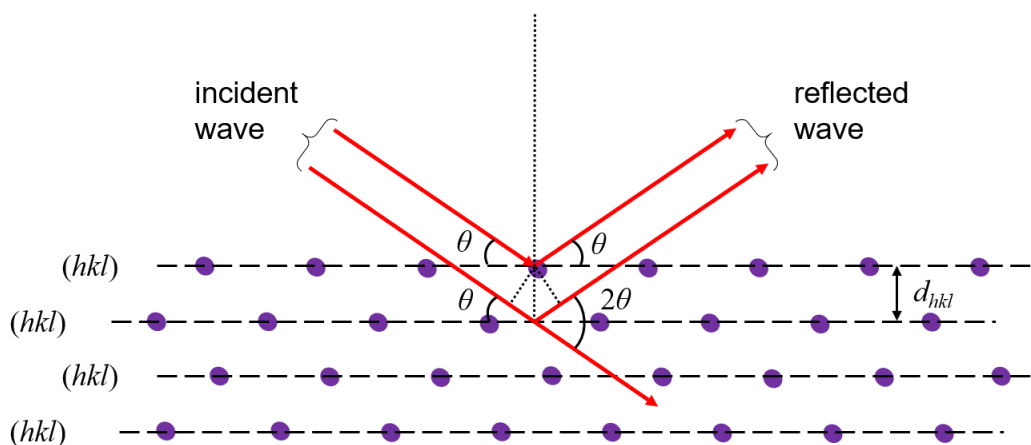


Figure 2.4. Schematic diagram of the demonstration of the Braggs' law with a set of hkl planes.

Observable X-ray diffraction events can be examined by the Braggs' law:

$$n\lambda = 2d_{hkl}\sin\theta \quad (2 - 1)$$

where n is an integer, λ is the wavelength of the radiation used, and θ is the Bragg angle. The Braggs' law is the result of constructive interference of the reflected radiations by a set of hkl planes. Other reflections which do not satisfy the Braggs' law are not observed due to destructive interferences.

2.2.3. Reciprocal Lattice and Ewald's Sphere

The concept of reciprocal lattice was first coined by J. W. Gibbs near the end of the 19th century¹⁰¹, and he insisted on the importance of reciprocal systems of three vectors. P. P. Ewald, on the other hand, was the first who introduced the relation between direct and reciprocal lattice through the Fourier transform.

For a 3-dimensional lattice (direct lattice) with lattice vectors \mathbf{a} , \mathbf{b} and \mathbf{c} , the lattice vectors of the reciprocal space are \mathbf{a}^* , \mathbf{b}^* and \mathbf{c}^* :

$$\mathbf{a}^* = \frac{\mathbf{b} \times \mathbf{c}}{V}, \mathbf{b}^* = \frac{\mathbf{a} \times \mathbf{c}}{V}, \mathbf{c}^* = \frac{\mathbf{a} \times \mathbf{b}}{V}, \quad (2 - 2)$$

where V is the unit cell volume of the direct lattice. The reciprocal interplanar vectors, \mathbf{d}_{hkl}^* , is perpendicular to the corresponding crystallographic plane and:

$$\mathbf{d}_{hkl}^* = h\mathbf{a}^* + k\mathbf{b}^* + l\mathbf{c}^* \quad (2 - 3)$$

And \mathbf{d}_{hkl}^* has the length of $1/d_{hkl}$. Consequently, the reciprocal lattice is formed and the individual lattice points can be indexed using the Miller indices.

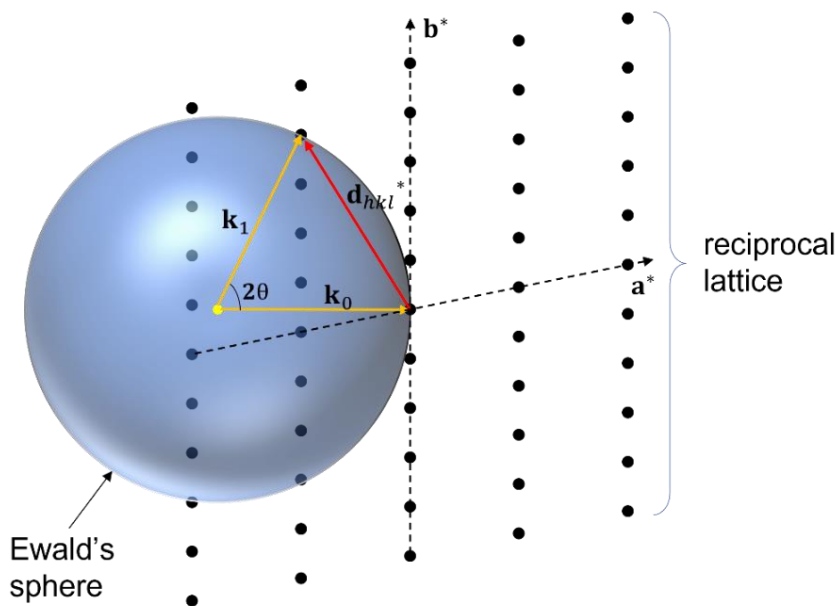


Figure 2.5. Schematics of the diffraction condition in reciprocal space using the Ewald's sphere.

The diffraction condition defined by the Bragg's law can be visualized using the Ewald's sphere in the reciprocal space. Consider the incident and diffracted beams with the wavevectors \mathbf{k}_0 and \mathbf{k}_1 , respectively, and $|\mathbf{k}_0| = |\mathbf{k}_1| = 1/\lambda$, which corresponds to an elastic scattering event. Also, from **Figure 2.5**:

$$\mathbf{k}_1 = \mathbf{k}_0 + \mathbf{d}_{hkl}^*, \quad (2 - 4)$$

and 2θ being the angle between \mathbf{k}_0 and \mathbf{k}_1 . Note that the Bragg's condition can be obtained using the above relation and the Ewald's sphere. The Ewald's sphere with radius $1/\lambda$ and centre at the common point of \mathbf{k}_0 and \mathbf{k}_1 visualizes possible diffraction events with relation to the reciprocal lattice. Essentially, the Bragg's condition is satisfied if the reciprocal lattice points touch the surface of the Ewald's sphere, and a diffraction event will be

observed. In single-crystal X-ray diffractions, the single-crystalline samples and the corresponding reciprocal lattices are rotated in different directions. The reciprocal lattice points then pass through the surface of the Ewald's sphere, and diffraction occurs.

X-ray diffractions for powders or polycrystalline samples is a slightly different case but can be explained in a similar fashion, using the Ewald's sphere. One can assume a random orientation of the grains/crystallites. As in the single-crystalline case, for any \mathbf{d}_{hkl}^* that satisfies the Bragg's Law, the diffraction occurs. Since the grains/crystallites are completely random, diffraction events for the same $|\mathbf{d}_{hkl}^*|$ would occur in one ring, which is perpendicular to \mathbf{k}_0 , with the same 2θ between \mathbf{k}_0 and \mathbf{k}_1 . A collection of rings, known as Debye rings, can be collected on an image plate detector if it is placed normal to \mathbf{k}_0 .

2.2.4. The Structure Factor and the Phase Problem

The intensity I_{hkl} of a diffraction peak depends on several factors, among which the structure factor, $|\mathbf{F}_{hkl}|^2$, is the most important as it carries the information about the atomic structure. For a unit cell of a crystalline solid containing n atoms, the structure amplitude, \mathbf{F}_{hkl} , for the (h,k,l) plane is the summation over all atoms with the unit cell (the expansion is based on the Euler's formula):

$$\mathbf{F}_{hkl} = \sum_{j=1}^n g_j t_j f_j \exp[2\pi i(hx^j + ky^j + lz^j)] \quad (2 - 5)$$

$$= \sum_{j=1}^n g_j t_j f_j \cos[2\pi(hx^j + ky^j + lz^j)] + \mathbf{i} \sum_{j=1}^n g_j t_j f_j \sin[2\pi(hx^j + ky^j + lz^j)]$$

In Eqn. 2 – 5, g_j is the occupancy factor, t_j is the atomic displacement parameter, f_j is the atomic scattering factor, and \mathbf{i} is the imaginary number. \mathbf{F}_{hkl} here is the sum of the real and imaginary parts. Mathematically, \mathbf{F}_{hkl} can be represented as a vector in two dimensions with a real and an imaginary axis which are mutually perpendicular to each other. The phase angle α describes the relationship between the real and imaginary vectors. A Fourier transformation can be applied to relate \mathbf{F}_{hkl} and electron density ρ_{xyz} at the (x, y, z) point in the unit cell:

$$\rho_{xyz} = \frac{1}{V} \sum_{h=-\infty}^{h=+\infty} \sum_{k=-\infty}^{k=+\infty} \sum_{l=-\infty}^{l=+\infty} |\mathbf{F}_{hkl}^{obs}| \cos[2\pi(hx + ky + lz) - \alpha_{hkl}] \quad (2 - 6)$$

where $|\mathbf{F}_{hkl}^{obs}|$ is the absolute value of the observed structure amplitude, and α_{hkl} is the phase angle of the reflection (hkl) .

During the diffraction, only I_{hkl} and $|\mathbf{F}_{hkl}|^2$ are measured, but the phase angle cannot be obtained. This is referred to as the phase problem in X-ray diffraction. On the other hand, when a crystal structure is centrosymmetric and there is no anomalous scattering, the resulting \mathbf{F}_{hkl} becomes a real number, since the sine terms are cancelled out. The phase angle α_{hkl} is either 0 or π , which yield either positive or negative sign for \mathbf{F}_{hkl} . In case of a centrosymmetric crystal structure and the finite number of diffraction data, equation 2 – 6 becomes:

$$\rho_{xyz} = \frac{1}{V} \sum_{h_{min}}^{h_{max}} \sum_{k_{min}}^{k_{max}} \sum_{l_{min}}^{l_{max}} s_{hkl} |\mathbf{F}_{hkl}^{obs}| \cos[2\pi(hx + ky + lz)] \quad (2-7)$$

where $s_{hkl} = 1$ or -1 , depending on α_{hkl} .

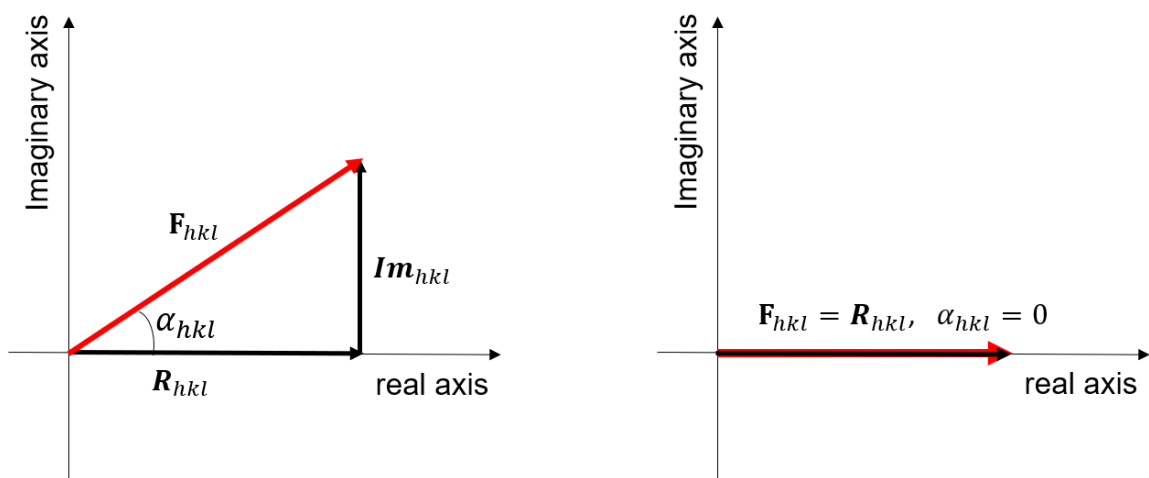


Figure 2.6. \mathbf{F}_{hkl} shown as a vector in the real/imaginary coordinate system, in a non-centrosymmetric (left) and a centrosymmetric (right) structure, in the absence of anomalous scatterings. \mathbf{R}_{hkl} represents the real part and \mathbf{Im}_{hkl} represents the imaginary part in \mathbf{F}_{hkl} .

Two known methods to tackle the phase problem in X-ray diffractions are the Patterson method and the direct method. The Patterson method applies the Fourier transformation on the absolute value of the structure factor $|\mathbf{F}_{hkl}^{obs}|^2$, and the phase angle information is not required to calculate the Patterson function P_{uvw} . The Patterson function does not reveal the electron density of atoms directly, but the interatomic vectors relative to the origin of the unit cell. Solving structures using the Patterson method however is challenging when the crystal structure involves many atoms, since the total number of

Patterson peaks obtained with n atoms in a structure is $n(n - 1)$, and overlapping of different interatomic vectors may occur. The Patterson method on the other hand is useful to locate strongly scattering atoms and construct a partial structural model with heavy atoms, thus the approach is often called the heavy atom method.

The direct method makes use of the phase relationships within a triplet of diffraction peaks whose indices are arithmetically related. The phase relationships however are not strict, and the probability is proportional to the magnitude of $|\mathbf{F}_{hkl}^{obs}|$ of the triplets. In centrosymmetric structures, the phase relationships are described by the Sayre equation:

$$s_{hkl} \approx s_{h'k'l'} s_{(h-h')(k-k')(l-l')} \quad (2 - 8)$$

where s is the sign (\pm) of the \mathbf{F}_{hkl} . For non-centrosymmetric structures, they are also given by the Sayre equation:

$$\alpha_{hkl} \approx \alpha_{h'k'l'} + \alpha_{(h-h')(k-k')(l-l')} \quad (2 - 9)$$

The direct method generates more than one set of phases for a data set. To aid in choosing the correct solution, the “E-statistics”, $\langle |E^2 - 1| \rangle$, is often used to help determine whether the data suggest a centrosymmetric space group, where E is the normalized structure magnitude. In general, $\langle |E^2 - 1| \rangle = 0.968$ for centrosymmetric structures and 0.736 for non-centrosymmetric structures¹⁰².

2.2.5. Single Crystal X-ray Diffractions (SC XRD)

In this dissertation, some single crystal X-ray diffraction measurements were done on a STOE IPDS II diffractometer, equipped with an image plate detector and MoK α radiation. Single crystals picked from samples were mounted on glass capillaries using epoxy glue. Diffraction frames were collected, and the peaks were used to construct a reciprocal lattice. A possible Bravais lattice and the unit cell parameters could be derived using the data collection software X-area¹⁰³. The diffraction peaks were integrated to obtain intensities; the numerical absorption correction was based on the crystal shape derived from optical face indexing and then optimized against the equivalent reflections via the STOE X-Shape software¹⁰⁴. Some data collections were done on a Bruker SMART APEX II diffractometer with a 3 kW sealed-tube Mo generator and APEX II CCD detector at the McMaster Analytical X-Ray (MAX) Diffraction Facility. A semi-empirical absorption correction was applied using redundant and equivalent reflections.

Preliminary data were processed using XPREP¹⁰⁵ and solved using the direct (SHELXS-97)^{106,107} or intrinsic (SHELXT)¹⁰⁸ method. Structure solutions and refinements were performed using the OLEX2 program¹⁰⁹. The obtained structures were refined using the least squares method, and several parameters were used to determine the level of agreement of the model to the obtained data:

$$R_1 = \frac{\sum ||F_o| - |F_c||}{\sum |F_o|} \quad (2 - 10)$$

$$wR_2 = \sqrt{\frac{\sum w(F_o^2 - F_c^2)^2}{\sum w(F_o^2)^2}} \quad (2 - 11)$$

$$Goof = S = \sqrt{\frac{\sum w(F_o^2 - F_c^2)^2}{N_{ref.} - N_{par.}}} \quad (2 - 12)$$

where F_o and F_c are the observed and calculated structure amplitudes, respectively. $N_{ref.}$ is the number of independent reflections, $N_{par.}$ is the number of parameters, and w is the weighting factor, which is based on the intensities and standard deviations of the observed reflections.

2.2.6. Laue Diffraction

Laue diffraction analysis was performed on the flux-grown samples to assess the surface quality and determine the orientation of the grown crystals. Laue diffraction employs the use of X-rays directly from an X-ray tube, without any filter or monochromator. The Laue diffractions were performed using a tungsten tube source at a voltage of 10 kV and current of 20 mA. The diffracted X-rays were detected with a Multiwire Laboratories detector, and the data were collected with the NORTH STAR software. The orientation of the crystals was determined by fitting the diffracted patterns using the ORIENT EXPRESS.

2.2.7. Powder X-ray Diffractions (PXRD)

Routine powder X-ray diffractions experiments were performed using a PANalytical X'Pert Pro diffractometer with Cu $K\alpha_1$ radiation using a Ge crystal monochromator and an X'Celerator linear detector. Samples were ground and deposited

evenly on a zero-background silicon sample holder. Diffraction patterns of samples were obtained and plotted as intensities against 2θ .

Temperature dependent powder X-ray diffraction data were collected at the Swiss-Norwegian Beam Lines, BM01A station at the ESRF (Grenoble, France) with a Dectris Pilatus2M detector in a ramp mode. The temperature was controlled with an in-house developed heat blower. Experimental powder diffraction data were integrated and processed with the DIOPTAS software¹¹⁰.

The obtained data were analyzed and evaluated by full-profile Rietveld refinements, using the Rietica program¹¹¹. In general, the background profile, lattice parameters, peak shape, occupancies and atomic coordinates were refined. Displacement parameters were also refined at the end of each refinement. Similar to the single-crystal experiments, the quality of the refinement was determined by the following agreement parameters:

$$R_p = \frac{\sum |y_{io} - y_{ic}|}{\sum y_{io}} \quad (2 - 13)$$

$$R_{wp} = \sqrt{\frac{\sum w_i (y_{io} - y_{ic})^2}{\sum w_i y_{io}^2}} \quad (2 - 14)$$

$$\chi^2 = \frac{\sum w_i (y_{io} - y_{ic})^2}{N - P} \quad (2 - 15)$$

where R_p , R_{wp} and χ^2 are the profile, weighted profile, and the goodness of fit of the refinement, respectively. These parameters represent the agreement between the observed

y_{io} and calculated y_{ic} intensities of the model. Also, N is the total number of data points, y_{io} , P is the number of adjusted parameters, after the background is refined, and w_i is the weighting scheme. w_i is assigned to each individual step and it depends on y_{io} of the step.

2.3. Energy Dispersive X-ray Spectroscopy (EDS)

Energy dispersive X-ray spectroscopy was used to verify or establish the composition of prepared phases. While X-ray diffraction techniques can be used for elemental analysis, it can be difficult to establish the presence of dopants or deficiencies and quantify their amount, especially from the powder diffraction data.

2.3.1. Principle of Technique

Similar to X-ray analysis, the elemental EDS analyses relies on the generation of X-ray radiations. In the SEM instrument, an electron beam hits the sample, generating continuous and characteristic X rays (see **Figure 2.2**). The elemental analyses employ characteristic X rays since the energies of photons emitted are specific to each element. The energy and intensity of the emitted X rays are analyzed, and this information provides the elemental composition/ratio of the analyzed area.

Since the electron beam is finely focused, the analyzed area can be relatively small. Due to this feature and ability to discriminate between different elements, SEM analysis is often used for the elemental mapping of grains in the sample. While the SEM analysis can provide important compositional information, the data obtained are considered only as semi-quantitative due to the nature of the technique and in some cases sample morphology.

2.3.2. Instrumentation

The EDS experiments were performed using an X-Max (80 mm²) X-ray EDS spectrometer (Oxford Instruments) on a TESCAN VEGA II LSU scanning electron microscope (20 kV accelerating voltage). Some EDS experiments were also performed using an INCA-Energy-350 X-ray EDS spectrometer (Oxford Instruments) on a Jeol JSM-6480LV scanning electron microscope (20 kV accelerating voltage, 0.7 nA beam current and 50 μm beam diameter). Depending on the compatibility of instruments and samples, samples were either mounted in a conductive epoxy resin and polished, or polished samples were attached to a sample holder using double-sided carbon tape.

2.4. Transport Property Measurements

Electrical resistivity, Seebeck coefficient and thermal conductivity measurements, which determine the figure-of-merit zT , were measured. To gain deeper understanding of the changes in the physical properties, carrier concentration and heat capacity were also measured. If a magnetically active element is present, the magnetization, M , vs. temperature, T , was explored to fully comprehend the material's properties.

2.4.1. zT and Heat Capacity Measurements

Samples were typically cut into rectangular bars (3 × 3 × 9 mm) using a low-speed saw equipped with either alumina, silicon carbide or diamond blade, and kerosene as a lubricant to avoid sample oxidation. High temperature electrical resistivity and Seebeck coefficient measurements (room temperature to 400 °C) were collected on the sample bars

under a He atmosphere using the ULVAC-RIKO ZEM-3 instrument system, located at CanmetMATERIALS, Natural Resources of Canada, Hamilton, ON. Seebeck coefficients were measured under a 10 – 15 °C temperature difference within the bar sample. High-temperature thermal diffusivities, D , were measured on plate samples (10 × 10 × 1 mm) using the laser flash method (LFA) on the Netzsch LFA-457 instrument, also in CanmetMATERIALS, with the help of Dr. Yu-Chih Tseng. The high-temperature thermal conductivities κ were calculated using $\kappa = DC_p\rho$, where ρ is the density of the material. The densities ρ of the samples were measured using a home-built Archimedes setup at room temperature.

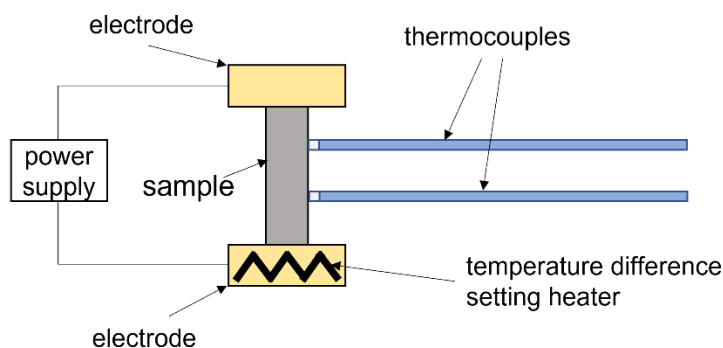


Figure 2.7. Schematics of the ULVAC-RIKO ZEM-3 system¹¹².

Low-temperature electrical resistivity, Seebeck coefficient, thermal conductivity and heat capacity data (5 – 400 K) were collected on bar (2 × 2 × 8 mm) or block samples (4 × 4 × 4 mm) using a Quantum Design Physical Property Measurement System (PPMS) at the National Institute for Materials Science, Tsukuba, Ibaraki, Japan, by Dr. Taras Kolodiaznyhnyi, and in Dalhousie University, Halifax, Nova Scotia, by Michel Johnson.

Seebeck coefficient and thermal conductivity measurements were done using the thermal transport option (TTO).

2.4.2. Carrier Concentration Measurements

The Hall carrier concentration and mobility at room temperature, n_H and μ_H , were derived from the Hall coefficient R_H measured on a home-built instrument using the Van der Pauw method with a GMW 5403 electromagnet at CanmetMATERIALS. The Hall coefficient R_H and concentration n_H of a sample were obtained using:

$$R_H = \frac{tV_H}{IB} \quad (2 - 16)$$

$$n_H = \frac{1}{eR_H} \quad (2 - 17)$$

where e is the charge of an electron, t is the thickness of the sample, I the fixed DC current (40/50 mA), B the magnetic field sweeping from around -10,000 to 10,000 G (-1 to 1 T), and V_H the Hall voltage at room temperature. Note that Equation (2 – 17) is valid when only one type of carriers is present in the material. For materials which both n and p carriers are present, the Hall coefficient R_H is:

$$R_H = \frac{p_H\mu_h^2 - n_H\mu_e^2}{e(p_H\mu_h + n_H\mu_e)^2}, \quad (2 - 18)$$

Where p_H and n_H are the Hall carrier concentrations of holes and electrons, respectively. A V_H vs. B graph was plotted using the obtained data and a linear regression was used to

obtain the $\frac{V_H}{B}$ slope to minimize experimental errors. μ_H is also derived from R_H and the electrical resistivity ρ of the plate sample, which was measured using the Van der Pauw method:

$$\mu_H = \frac{R_H}{\rho} \quad (2 - 19)$$

2.4.3. Magnetization Measurements

Temperature dependent magnetization measurements were performed using the superconducting quantum interference device (SQUID) on the magnetic property measurement system (MPMS) with the reciprocating sample option (RSO), at the Brockhouse Institute of Materials Research (BIMR), McMaster University, by Dr. Yafen Shang. A small solid sample was mounted on a glass rod with Apiezon grease and wrapped with Teflon tape.

2.5. Electronic Band Structure Calculations

To understand the structure-property relationship of the materials, electronic band structures were calculated and used to explain the property changes. The density of states (DOS), Crystal Orbital Hamiltonian Population (COHP) and band structure of materials were calculated using the tight-binding, linear muffin tin orbital method with the atomic sphere approximation (TB-LMTO-ASA). Empty spheres were included into the unit cell to fulfill the overlap criteria of atomic spheres in the TB-LMTO-ASA. This method

provides fast estimations of the electronic band structures and thus permits comparison between pristine and doped materials.

Chapter 3. The Updated Zn – Sb Phase Diagram. How to Make Pure $\text{Zn}_{13}\text{Sb}_{10}$ (“ Zn_4Sb_3 ”)

This chapter contains the material covered in the manuscript “The Updated Zn – Sb Phase Diagram. How to Make Pure $\text{Zn}_{13}\text{Sb}_{10}$ (“ Zn_4Sb_3 ””, which was published in *Dalton Transactions* (*Dalton Trans.*, **2018**, 47, 11512). The experimental procedures were performed by the candidate. The high-temperature synchrotron data were collected by Drs. Volodymyr Svitlyk and Dmitry Chernyshov at the European Synchrotron Radiation Facility (ESRF), Grenoble, France. Microprobe analysis of materials was performed by Dr. Alex V. Morozkin. Data interpretation and manuscript preparation were done together with my supervisor.

Reproduced with permission from Volodymyr Svitlyk, Dmitry Chernyshov and Yuriy Mozharivskyj, *Dalton Trans.*, **2018**, 47, 11512. Copyright 2018 Royal Society of Chemistry.

The Zn–Sb system contains two well-known thermoelectric materials, $\text{Zn}_{1-\delta}\text{Sb}$ and $\text{Zn}_{13-\delta}\text{Sb}_{10}$ (“ Zn_4Sb_3 ”), and two other phases, $\text{Zn}_{9-\delta}\text{Sb}_7$ and $\text{Zn}_{3-\delta}\text{Sb}_2$, stable only at high temperatures. The current work presents the updated phase diagram constructed using the high-temperature diffraction studies and elemental analysis. All phases are slightly Zn deficient with respect to their stoichiometric compositions, which is consistent with their *p*-type charge transport properties. Either at room or elevated temperatures, $\text{Zn}_{1-\delta}\text{Sb}$ and $\text{Zn}_{13-\delta}\text{Sb}_{10}$ display deficiencies of the main Zn sites and partial Zn occupancy of the other interstitial sites. A phase pure $\text{Zn}_{13-\delta}\text{Sb}_{10}$ sample can be obtained from the $\text{Zn}_{13}\text{Sb}_{10}$ loading composition, and there is no need to use a Zn-rich composition such as Zn_4Sb_3 . While the $\text{Zn}_{13-\delta}\text{Sb}_{10}$ phase is stable till its decomposition temperature of 515 °C, it may incorporate some additional Zn around 412 °C, if elemental Zn is present.

3.1. Introduction

The $\text{Zn}_{13-\delta}\text{Sb}_{10}$ phase, known in the literature as “ Zn_4Sb_3 ”, has been identified as one of the promising *p*-type thermoelectric materials 20 years ago⁹⁰. Extensive research that followed elucidated the nature of the low-temperature phase transitions^{93,94}, revealed details of its atomic structure^{92,96,113}, and established its composition^{93,94,113–116}. Both diffraction and elemental (such as EMPA) analyses indicate that the real composition of “ Zn_4Sb_3 ” is best represented as $\text{Zn}_{13-\delta}\text{Sb}_{10}$, but the value of δ is not well defined. Diffraction experiments on the room-temperature β -modification of $\text{Zn}_{13-\delta}\text{Sb}_{10}$ gave $\delta = 0.18 - 0.23$ ^{96,113}, while those on the low-temperature α - and α' -modifications yielded $\delta \approx 0.3$ ⁹³.

The electron microprobe analysis (EMPA) suggested a similar but wider variation in composition from $\delta = 0.45$ ¹¹⁴ to $\delta \approx 0$ ^{94,114} depending on the sample preparation method. It has to be mentioned that $\delta \approx 0$ was observed only for single crystals grown from flux, and some foreign atoms were present in the structure. In some cases, EPMA gave even a Zn-rich composition $\text{Zn}_{13+\delta}\text{Sb}_{10}$ with δ up to 0.16¹¹⁶ or even 0.37–0.42¹¹⁵, however such an increase in the Zn amount results from presence of elemental Zn in the form of nano- or micro-inclusions inside or between the domains^{117,118}. Additionally, excess of Zn in the structure would contradict the available structural data and physical properties.

Since the intrinsic composition of $\text{Zn}_{13}\text{Sb}_{10}$ dictates its thermoelectric properties as well as the nature of its low-temperature phase transitions, there were many attempts to elucidate these relationships. Toberer *et al.*¹¹⁶ looked at the correlation between the Zn loading amount and transport properties, and the works by Nylén *et al.*¹¹⁴ and Pan *et al.*¹¹⁹ showed that dopants influence both the electrical resistivity and low-temperature structural transformations. Other studies^{120–122} also reported on the modification of transport properties due to the doping on either the Zn or Sb sites. Unfortunately, a solid relationship between the composition, atomic structure and physical properties could not be established. To complicate the matter even further, the Zn_4Sb_3 samples with the same loading composition but prepared by different methods display rather incoherent properties; e.g. the samples prepared by gradient freeze and spark plasma sintering possess vastly different charge transport properties^{123,124}.

The primary reason for our inability to properly navigate the “synthesis–composition–property” relationship in $\text{Zn}_{13}\text{Sb}_{10}$ is lack of solid understanding of how to prepare phase-pure samples with reproducible properties and of the reasons to use the Zn-rich samples. Typically, the polycrystalline samples of $\text{Zn}_{13}\text{Sb}_{10}$ are synthesized from a Zn-richer Zn_4Sb_3 composition, which inevitably yield Zn impurities. The first synthetic step in making a polycrystalline Zn_4Sb_3 sample is melting of elemental Zn and Sb in the 4 : 3 ratio in an evacuated silica tube above the melting temperature of Sb (631 °C), which is the highest temperature on the Zn–Sb diagram¹²⁵. Many researchers use 750 °C or higher temperatures to speed up the reaction and then quickly cool/quench the sample to room temperature^{90,95,116,126}. According to the experimental phase diagram¹²⁵, $\text{Zn}_{13}\text{Sb}_{10}$ decomposes peritectoidally at 490 °C into a Zn-poorer high-temperature $\gamma\text{-Zn}_{13-\delta}\text{Sb}_{10}$ modification, and Zn_3Sb_2 , and thus quenching allows to bypass the solid-state reaction between $\gamma\text{-Zn}_{13-\delta}\text{Sb}_{10}$ and Zn_3Sb_2 and to obtain the $\text{Zn}_{13}\text{Sb}_{10}$ phase directly (known as $\beta\text{-Zn}_{13}\text{Sb}_{10}$). Recently, He *et al.* have shown that $\gamma\text{-Zn}_{13-\delta}\text{Sb}_{10}$ is in reality $\text{Zn}_{9-\delta}\text{Sb}_7$ with a different structure⁹⁹.

While the peritectoid decomposition of $\text{Zn}_{13}\text{Sb}_{10}$ provided a rationale for quenching samples, the choice of the 4 : 3 composition was not clear. High vapour pressure of Zn at 750 °C can deplete the sample of some Zn, however Zn losses are rather small and typically not sufficient to yield pure $\text{Zn}_{13}\text{Sb}_{10}$ from the Zn_4Sb_3 loading composition at least within the experimental setup used in this work. We believe that the origin of the Zn_4Sb_3 loading composition and subsequently its historic formula can be partially attributed to Mayer *et al.*, who observed that the Zn_4Sb_3 loading composition gives the most pure sample⁹¹.

Subsequently Mayer *et al.* assumed and refined a Zn/Sb mixture on one of the Sb sites to retain the Zn_4Sb_3 composition. Likewise, other researchers, including present authors, have also established but not explicitly reported on the fact that the 4 : 3 and not 13 : 10 ratio yielded the highest purity sample after quenching. To validate this hypothesis, we prepared the $\text{Zn}_{13}\text{Sb}_{10}$ and Zn_4Sb_3 samples by melting at 750 °C in the same furnace, followed by quenching them in cold water. The Rietveld refinement (**Figure 3.1**) unequivocally proves that the Zn_4Sb_3 sample contains more $\text{Zn}_{13}\text{Sb}_{10}$. Quenched Zn_4Sb_3 samples are typically ground and consolidated either through hot press sintering^{90,116} or spark plasma sintering.¹²⁷ Even when the preparation method is different, the Zn_4Sb_3 formula is still used for the $\text{Zn}_{13}\text{Sb}_{10}$ phase.^{128,129}

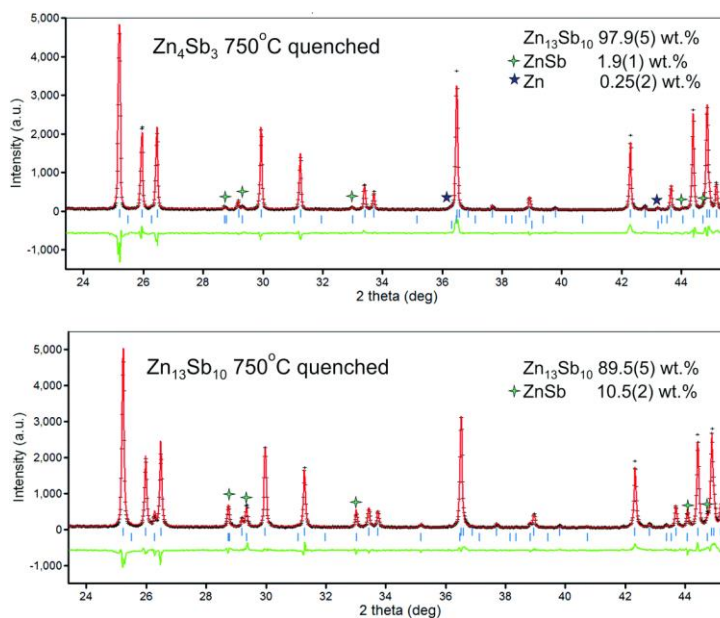


Figure 3.1. Rietveld refinement results for the Zn_4Sb_3 and $\text{Zn}_{13}\text{Sb}_{10}$ samples quenched from 750 °C. The elemental Zn is not detectable in the $\text{Zn}_{13}\text{Sb}_{10}$ sample, likely, due to its small particle size.

The discrepancy between the historic “Zn₄Sb₃” and real Zn₁₃Sb₁₀ compositions prompted us to investigate ways of preparing the Zn₁₃Sb₁₀ phase from the Zn₁₃Sb₁₀ loading composition. Additionally, our goal was to understand stability of the Zn₁₃Sb₁₀ phase at high temperatures and to construct the detailed Zn – Sb phase diagram. It has to be mentioned that the thermal stability of Zn₁₃Sb₁₀ was studied before. However, high-temperature diffraction experiments were performed under either dynamic vacuum⁹⁴ or inert atmosphere¹³⁰ in large diffraction chambers, which creates non-equilibrium conditions leading to the sample decomposition *via* Zn losses. The current work eliminates such conditions.

3.2. Experimental

3.2.1. Synthesis

The starting materials were Zn (99.99 wt%, Alfa Aesar) and Sb (99.999 wt% Alfa Aesar) pieces. Samples with the ZnSb, Zn₉Sb₇, Zn_{13±x}Sb₁₀ ($x = 0, 0.1, 0.2, 0.3$), Zn₄Sb₃ and Zn₃Sb₂ compositions and with the total mass of 2 grams were prepared. Few identical batches of the Zn₁₃Sb₁₀ and Zn₄Sb₃ samples were prepared (see **Table 3.1**). The Zn and Sb metals were loaded into silica tubes, evacuated till 10⁻³ torr and sealed. All samples were heated to 750 °C at 100 °C/h, kept for 4 hours while shaken twice in-between. Next, the samples were cooled at 50 °C/h to 350 °C or 450 °C, kept at the target temperatures for 48 hours, and then quenched in cold water. One of the Zn₁₃Sb₁₀ samples was cooled directly at 50 °C/h from 750 °C to room temperature. It has to be mentioned that a semitransparent

layer of Zn metal close to the sample was observed on the walls of silica tubes in all samples.

This suggests that tiny amounts of Zn metal are always lost.

Table 3.1. Samples compositions, heat treatment, phases present and elemental analysis results.

Sample	Heat treatment ^a	Phases at R.T.	Compositional analysis
ZnSb	750 °C → 450 °C → quench	ZnSb	Zn _{49.8(2)} Sb _{50.2(2)}
	750 °C → 350 °C → quench	ZnSb	Zn _{49.7(2)} Sb _{50.3(2)}
Zn ₉ Sb ₇	750 °C → quench	Zn ₁₃ Sb ₁₀ + ZnSb	
Zn _{12.7} Sb ₁₀	750 °C → R.T.	Zn ₁₃ Sb ₁₀ + ZnSb	
Zn _{12.8} Sb ₁₀	750 °C → R.T.	Zn ₁₃ Sb ₁₀ + ZnSb	
Zn _{12.9} Sb ₁₀	750 °C → R.T.	Zn ₁₃ Sb ₁₀	
Zn ₁₃ Sb ₁₀	750 °C → 450 °C → quench	Zn ₁₃ Sb ₁₀	Zn _{55.9(2)} Sb _{44.1(2)}
	750 °C → 350 °C → quench	Zn ₁₃ Sb ₁₀	Zn _{56.0(2)} Sb _{44.0(2)}
	750 °C → R.T.	Zn ₁₃ Sb ₁₀	Zn _{55.8(2)} Sb _{44.2(2)}
	750 °C → quench	Zn ₁₃ Sb ₁₀ + ZnSb + Zn ^b	
Zn _{13.1} Sb ₁₀	750 °C → R.T.	Zn ₁₃ Sb ₁₀ + Zn	
Zn _{13.2} Sb ₁₀	750 °C → R.T.	Zn ₁₃ Sb ₁₀ + Zn	
Zn _{13.3} Sb ₁₀	750 °C → R.T.	Zn ₁₃ Sb ₁₀ + Zn	
Zn ₄ Sb ₃	750 °C → 450 °C → quench	Zn ₁₃ Sb ₁₀ + Zn	Zn _{56.1(2)} Sb _{43.9(2)}
	750 °C → 350 °C → quench	Zn ₁₃ Sb ₁₀ + Zn	Zn _{56.0(2)} Sb _{44.0(2)}
	750 °C → quench	Zn ₁₃ Sb ₁₀ + Zn + ZnSb	
Zn _{3.26} Sb ₂	750 °C → 500 °C → 430 °C → quench	α-Zn ₃ Sb ₂ + Zn ^c	Zn _{2.96(2)} Sb ₂

^a 750 °C → 450 °C → quench and 750 °C → 350 °C → quench: cooling at 50 °C/h from 750 to 450 and 350 °C, followed by rapid quenching in ice-cold water. 750 °C → 500 °C → 430 °C → quench: cooling at 50 °C/h from 750 to 500 °C, then at 5 °C/h from 500 to 430 °C, followed by rapid quenching in ice-cold water. 750 °C → quench: direct quenching from 750 °C in ice-cold water. 750 °C → RT: cooling at 50 °C/h from 750 °C to room temperature.

^b Some Zn was deposited on the walls of silica tube. Zn is required to balance the loading composition.

^c Some Zn was deposited on the walls of silica tube and also found inside the Zn_{3.26}Sb₂ sample as elemental inclusions. Zn was not detected on the X-ray powder diffraction.

3.2.2. Room Temperature Diffraction Studies and Elemental Analysis

The samples were subjected to X-ray powder diffraction analysis on a PANalytical X'Pert Pro diffractometer with an X'Celerator detector and $\text{CuK}_{\alpha 1}$ radiation. The samples were ground and deposited on a zero-background Si samples holder. Diffraction data were collected in the $20 - 70^\circ 2\theta$ range. A full-profile Rietveld refinement (Rietica program) was employed to refine the lattice parameters and to assess the purity of bulk products. For the refinement, crystallographic data of ZnSb and $\text{Zn}_{13}\text{Sb}_{10}$ were adopted from previous work⁹⁵.

Quantitative elemental analysis was performed using an INCA-Energy-350 X-ray EDS spectrometer (Oxford Instruments) on a Jeol JSM-6480LV scanning electron microscope (SEM) (20 kV accelerating voltage, 0.7 nA beam current and 50 μm beam diameter). Small pieces of the samples were mounted in a conductive epoxy resin and polished with $\sim 10 \mu\text{m}$ diamond dust during the final polishing stage. Zn metal and Sb_2S_3 were used as standards. Signals averaged over three points per phase gave estimated standard deviations of 0.2 at% for Zn (measured by K-series lines) and Sb (measured by L-series lines).

3.2.3. High-temperature Synchrotron Diffraction Studies

The temperature-dependent powder diffraction data for the ZnSb, Zn_9Sb_7 , $\text{Zn}_{13}\text{Sb}_{10}$, Zn_4Sb_3 and Zn_3Sb_2 samples were collected at the Swiss-Norwegian Beam Lines, BM01A station at the ESRF (Grenoble, France) with a Dectris Pilatus2M detector in a ramp mode in the $20-650^\circ\text{C}$ temperature range with a typical step width of 2°C . The wavelength was

set to 0.6889, 0.6890, 0.7225, 0.7787 and 0.9682 Å, respectively. The temperature was controlled with an in-house developed heat blower. Experimental powder diffraction data were integrated and processed with the DIOPTAS software.¹¹⁰

3.3. Results and Discussion

The composition and stability of $\text{Zn}_{13-\delta}\text{Sb}_{10}$ and ZnSb will be addressed first. These results will be combined with the published data on $\text{Zn}_{9-\delta}\text{Sb}_7$ and Zn_3Sb_2 to construct the middle part of the Zn–Sb diagram. We will use the $\text{Zn}_{13-\delta}\text{Sb}_{10}$ formula to indicate Zn deficiency in this phase. It is worth mentioning that all Zn–Sb phases are Zn deficient, but this deficiency is more pronounced in $\text{Zn}_{13-\delta}\text{Sb}_{10}$ than in ZnSb or Zn_3Sb_2 .

3.3.1. Composition of $\text{Zn}_{13-\delta}\text{Sb}_{10}$ and ZnSb

To test homogeneity ranges of $\text{Zn}_{13-\delta}\text{Sb}_{10}$ and ZnSb as a function of temperature, the samples were annealed at 350 and 450 °C and quenched in cold water. The composition of $\text{Zn}_{13-\delta}\text{Sb}_{10}$ at room temperature is based on the $\text{Zn}_{13}\text{Sb}_{10}$ sample that was cooled from 750 °C to room temperature at 50 °C per hour. The elemental analysis results are summarized in **Table 3.1**. Both at 350 °C and 450 °C, the ZnSb samples yielded slightly Zn-deficient compositions that are within 2 standard deviations (SDs) from the stoichiometric one. Considering that ZnSb is a *p*-type conductor, such small Zn deficiency is expected.

The compositions obtained for $\text{Zn}_{13-\delta}\text{Sb}_{10}$ from the $\text{Zn}_{13}\text{Sb}_{10}$ and Zn_4Sb_3 samples are identical or within 1 SD from each other for the same annealing temperature. For the

same samples, the elemental results are also within 1 SD across different temperatures (**Table 3.1**). However, the EDS compositions for the two Zn_4Sb_3 samples have to be treated with caution as the X-ray powder diffraction revealed presence of elemental Zn in both samples. As shown in other studies^{117,118}, elemental Zn can be present as nano-inclusions inside or between the domains, and while these inclusions are visible under TEM, they cannot be detected with SEM. Thus, we cannot exclude presence of Zn nano-inclusions in our Zn_4Sb_3 samples. Potentially, we can use the unit cell volumes to evaluate compositions, but since no solid relationship has been established between the Zn composition and lattice parameters, such analysis can be qualitative at best. **Table 3.2** presents lattice parameters in comparison to the EDS compositions. The unit cell volumes for the $\text{Zn}_{13}\text{Sb}_{10}$ samples are similar to each other (within 2 combined SDs for the two compositions compared), which supports similarity in the samples' compositions in agreement with the EDS results. For the Zn_4Sb_3 samples annealed at 450 and 350 °C degrees, the unit cell volumes are significantly different and they deviate from the $\text{Zn}_{13}\text{Sb}_{10}$ ones. We suggest that the larger unit cell for Zn_4Sb_3 annealed at 450 °C corresponds to a larger Zn amount in the structure, and some support for this argument comes from the experiments described below.

A series of samples with loading compositions $\text{Zn}_{12.7-13.3}\text{Sb}_{10}$ with 0.1 intervals was prepared. The samples were cooled at 50 °C h^{-1} from 750 °C to room temperature. X-ray powder diffraction (**Figure 3.2**) showed that the $\text{Zn}_{13.1-13.3}\text{Sb}_{10}$ samples contained elemental Zn as impurity, while $\text{Zn}_{12.7-12.8}\text{Sb}_{10}$ contained ZnSb. The lattice parameters derived for the $\text{Zn}_{13}\text{Sb}_{10}$ phase from the Rietveld refinement are summarized in **Table 3.3**. As the Zn loading amount decreases from $\text{Zn}_{13.3}\text{Sb}_{10}$ to $\text{Zn}_{12.9}\text{Sb}_{10}$, the unit cell becomes

smaller, which suggests that (1) Zn amount is variable in the $\text{Zn}_{13}\text{Sb}_{10}$ structure and (2) a larger Zn concentration yields a larger unit cell. The $\text{Zn}_{12.8}\text{Sb}_{10}$ and $\text{Zn}_{12.7}\text{Sb}_{10}$ samples have the unit cell volume similar to that of $\text{Zn}_{12.9}\text{Sb}_{10}$.

Table 3.2. Lattice parameters for the $\text{Zn}_{13-\delta}\text{Sb}_{10}$ phase as obtained from the full profile Rietveld refinement of the $\text{Zn}_{13-\delta}\text{Sb}_{10}$ and Zn_4Sb_3 samples. The phase compositions are also indicated.

Sample	$\text{Zn}_{13}\text{Sb}_{10}$	Zn_4Sb_3
Phase	$\text{Zn}_{13}\text{Sb}_{10}$ ($\text{Zn}_{56.5}\text{Sb}_{43.5}$)	$\text{Zn}_{13}\text{Sb}_{10}$ ($\text{Zn}_{56.5}\text{Sb}_{43.5}$)
450°C	$\text{Zn}_{55.9(2)}\text{Sb}_{44.1(2)}$ $a=12.2334(2)$ Å $c=12.4287(3)$ Å $V=1610.83(5)$ Å ³	$\text{Zn}_{56.1(2)}\text{Sb}_{43.9(2)}$ $a=12.2334(2)$ Å $c=12.4301(2)$ Å $V=1611.02(4)$ Å ³
350°C	$\text{Zn}_{56.0(2)}\text{Sb}_{44.0(2)}$ $a=12.2328(2)$ Å $c=12.4285(2)$ Å $V=1610.63(4)$ Å ³	$\text{Zn}_{56.0(2)}\text{Sb}_{44.0(2)}$ $a=12.2336(2)$ Å $c=12.4292(2)$ Å $V=1609.94(4)$ Å ³
RT ^a	$\text{Zn}_{55.8(2)}\text{Sb}_{44.2(2)}$ $a=12.2334(2)$ Å $c=12.4282(2)$ Å $V=1610.76(4)$ Å ³	

350 and 450 °C corresponds to final annealing temperatures after which the samples were quenched.

^a RT for $\text{Zn}_{13}\text{Sb}_{10}$ indicates that this sample was cooled from 750 °C to room temperature at 50 °C/h.

Table 3.3. Lattice parameters of the $\text{Zn}_{13}\text{Sb}_{10}$ phase in the $\text{Zn}_{12.7-13.3}\text{Sb}_{10}$ samples cooled from 750 °C to room temperature at 50 °C/h.

Sample	$\text{Zn}_{13.3}\text{Sb}_{10}$	$\text{Zn}_{13.2}\text{Sb}_{10}$	$\text{Zn}_{13.1}\text{Sb}_{10}$	$\text{Zn}_{13}\text{Sb}_{10}$
a (Å)	12.2354(3)	12.2337(3)	12.2341(3)	12.2320(2)
c (Å)	12.4313(3)	12.4301(3)	12.4309(3)	12.4274(2)
V (Å ³)	1611.70(6)	1611.09(6)	1611.30(6)	1610.29(4)
Sample	$\text{Zn}_{12.9}\text{Sb}_{10}$	$\text{Zn}_{12.8}\text{Sb}_{10}$	$\text{Zn}_{12.7}\text{Sb}_{10}$	
a (Å)	12.2314(2)	12.2338(2)	12.2328(2)	
c (Å)	12.4270(2)	12.4298(2)	12.4288(2)	
V (Å ³)	1610.09(5)	1611.08(4)	1610.68(5)	

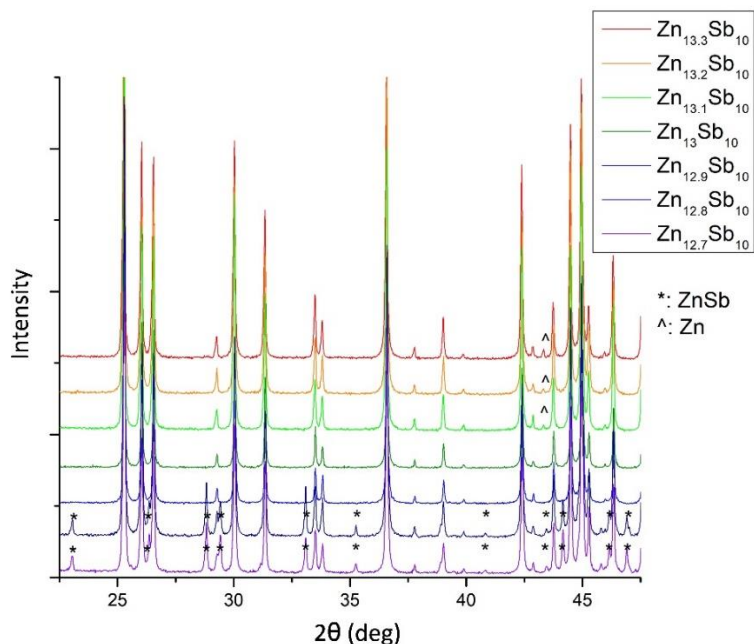


Figure 3.2. Powder diffraction patterns of the $\text{Zn}_{12.7-13.3}\text{Sb}_{10}$ samples cooled at $50\text{ }^\circ\text{C/h}$ from $750\text{ }^\circ\text{C}$ to room temperature. The Zn and ZnSb impurities are indicated on the graphs.

It is difficult to pinpoint the exact homogeneity range for the $\text{Zn}_{13}\text{Sb}_{10}$ phase and to establish its temperature dependence. If we consider only the EDS results from the $\text{Zn}_{13}\text{Sb}_{10}$ samples and assume no Sb deficiencies in the structure, then the composition of $\text{Zn}_{13-\delta}\text{Sb}_{10}$ can be written as $\text{Zn}_{12.62(5)}\text{Sb}_{10}$ – $\text{Zn}_{12.72(5)}\text{Sb}_{10}$ or with $\delta = 0.28$ – $0.38(5)$. This proposed homogeneity agrees well with the values found in literature; *e.g.* Nylén *et al.* reported the EPMA composition of $\text{Zn}_{12.6(1)}\text{Sb}_{10}$ for the Zn_4Sb_3 sample quenched from $450\text{ }^\circ\text{C}$.¹¹⁴ The unit cell volumes for our non-stoichiometric samples suggest that a larger compositional range is still possible; however precise elemental analysis for such samples may be challenging because of Zn nano-inclusions.

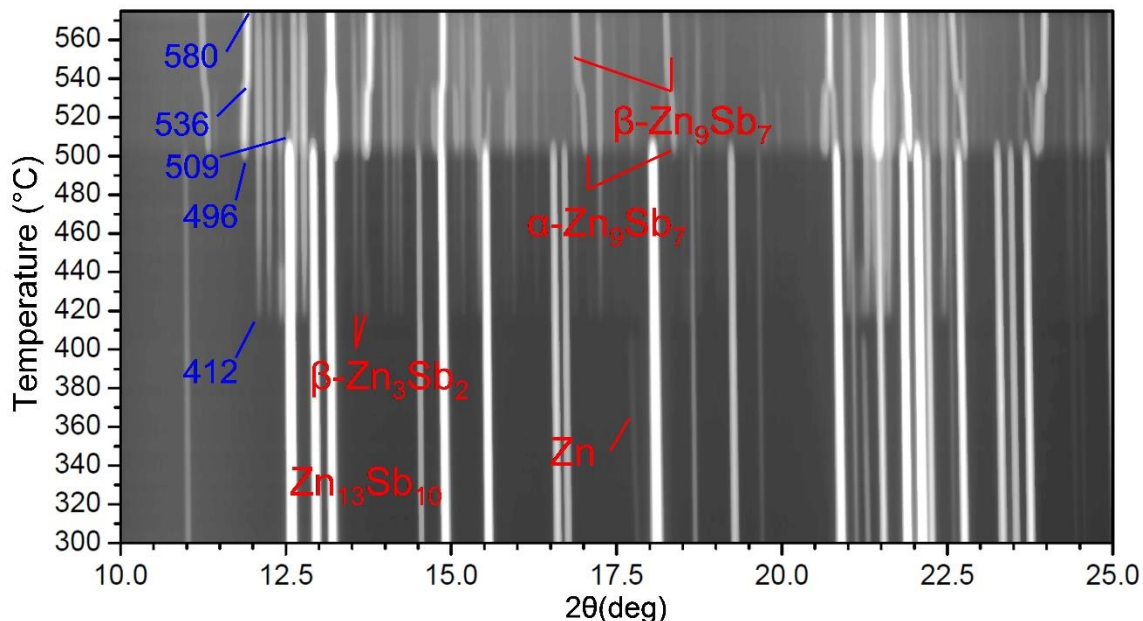
3.3.2. Thermal Stability and Transformation of $Zn_{13}Sb_{10}$ 

Figure 3.3 Powder diffraction data for the Zn_4Sb_3 sample during heating from 300 °C till 580 °C.

The thermal stability of $Zn_{13}Sb_{10}$ was evaluated by heating the Zn_4Sb_3 sample sealed inside a silica capillary with argon gas from room temperature to 650 °C. The temperature scans are compiled in **Figure 3.3**. The Zn_4Sb_3 sample contained $Zn_{13}Sb_{10}$ and Zn (0.80(5) wt. %). The thermal expansion coefficients of $Zn_{13}Sb_{10}$ and Zn are different, which is easily detectable from the different temperature slope of the Zn reflections. The following transformation temperatures are observed:

(1) 412 °C: Zn metal disappears and the Zn_3Sb_2 phase appears. It is worth mentioning that the melting point of pure Zn metal is 419.5 °C, and disappearance of Zn and appearance of

Zn_3Sb_2 in the sample can be explained by melting of Zn metal and its reaction with $\text{Zn}_{13}\text{Sb}_{10}$ according to: $\text{Zn}_{13}\text{Sb}_{10} + 2 \text{Zn} \rightarrow 5 \text{Zn}_3\text{Sb}_2$.

At 412 °C, the slope of the unit cell volume vs. temperature changes and the occupancy of the main Zn site in the structure increases abruptly (see **Figures 3.4** and **3.5**). While the unit cell volume continues to increase with temperature at higher temperatures, the thermal expansion is slower. These changes can be explained by incorporation of additional Zn into the structure after it melts at 412 °C. The HT diffraction data for the $\text{Zn}_{13}\text{Sb}_{10}$ sample without Zn impurity (not discussed here) do not exhibit such behaviour; there is a linear increase in the volume and linear decrease in the occupancy of the main Zn site till the decomposition temperature.

(2) 496 °C: $\text{Zn}_{13}\text{Sb}_{10}$ phase starts to decompose peritectoidally into $\alpha\text{-Zn}_9\text{Sb}_7$ and $\beta\text{-Zn}_3\text{Sb}_2$, Zn-poorer and Zn-richer phases, and then completely disappears at 509 °C. Peritectoid decomposition of $\text{Zn}_{13}\text{Sb}_{10}$ over the 13 °C range suggests some non-equilibrium conditions inside the capillary, likely resulting from fast heating. Such non-equilibrium behaviour is also observed for other transformations.

(3) 536 °C: $\alpha\text{-Zn}_9\text{Sb}_7$ transforms into the $\beta\text{-Zn}_9\text{Sb}_7$.

(4) 575 °C is the eutectic temperature, at which $\beta\text{-Zn}_3\text{Sb}_2$ decomposes into liquid and $\beta\text{-Zn}_9\text{Sb}_7$.

(5) 580 °C: $\beta\text{-Zn}_9\text{Sb}_7$ disappears. This is the temperature of liquidus for the Zn_4Sb_3 composition.

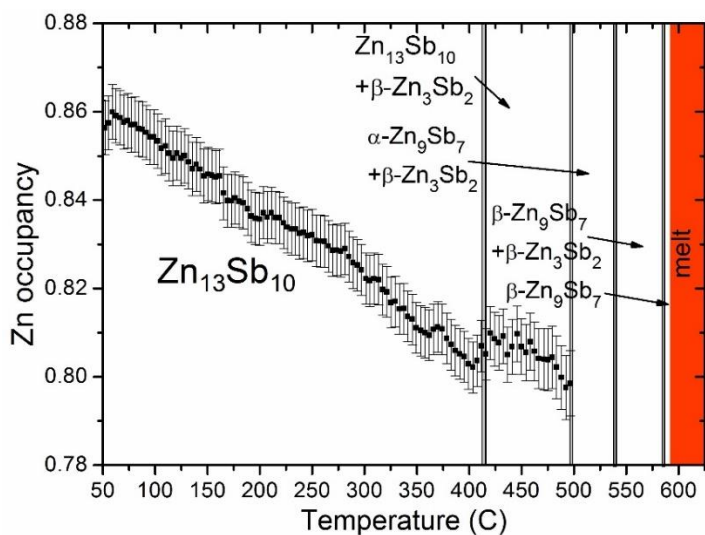


Figure 3.4. Occupancy of the main Zn site in $Zn_{13}Sb_{10}$ with temperature.

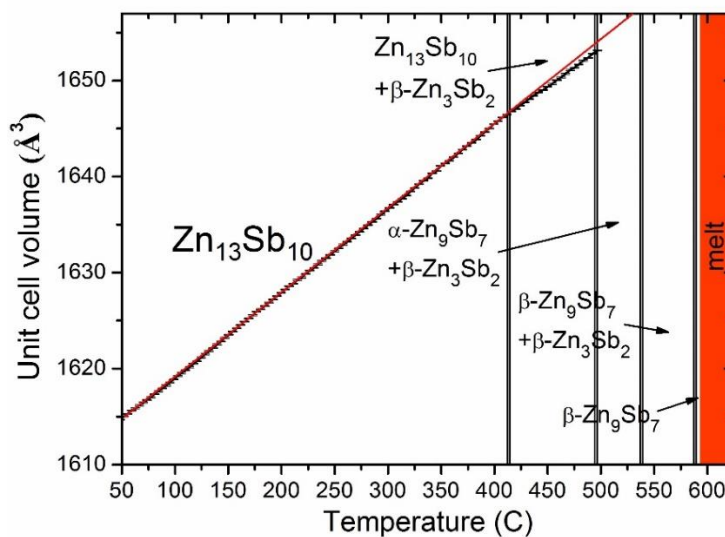


Figure 3.5. Unit cell volume of $Zn_{13}Sb_{10}$ with temperature. The red line indicates a linear fit to the refined unit cell volumes in black before 412 °C.

Figure 3.4 provides insights into the occupancy of the main Zn site and gives some indications about the presence of additional and deficient Zn sites. The composition of the $Zn_{13}Sb_{10}$ and Zn_4Sb_3 samples quenched from 350 and 450 °C is very similar to each other

and to that of the $\text{Zn}_{13}\text{Sb}_{10}$ sample slowly cooled to room temperature (**Table 3.1**). Thus, the total Zn content inside the $\text{Zn}_{13}\text{Sb}_{10}$ structure must be similar at various temperatures; and since the occupancy of the main Zn site decreases with temperature (**Figure 3.4**), the occupancy of the Zn interstitial sites must increase. Such Zn redistribution between different sites suggests high Zn mobility in $\text{Zn}_{13}\text{Sb}_{10}$ at elevated temperatures. Similar behaviour was observed in Zn_9Sb_7 .⁹⁹

Finally, we would like to address possibility of the retrograde solubility of Zn in $\text{Zn}_{13}\text{Sb}_{10}$ at low temperatures identified through first-principle thermodynamic calculations. The theoretical analysis by Pomrehn *et al.*¹³¹ suggests that when $\text{Zn}_{13}\text{Sb}_{10}$ and Zn are in equilibrium, Zn amount in $\text{Zn}_{13}\text{Sb}_{10}$ is higher at low and high temperatures, but lower in the intermediate temperatures (around 400 °C). The Zn occupancy data in **Figure 3.4** support this statement; additionally the HT diffraction data directly tie an increase in the Zn amount at 412 °C to the melting of elemental Zn.

3.3.3. Thermal Stability of ZnSb

In contrast to other Zn–Sb binary phases, the ZnSb phase displays no structural transformation from liquid helium temperatures¹³² till its decomposition. The HT diffraction data show appearance of Sb metal in the 207–531 °C range and its amount slowly increases with temperature (**Figure 3.6**). Above 514 °C, Sb metal gradually disappears over a range of 17 °C. The temperature of 514 °C corresponds neither to the melting temperature of Sb (630.8 °C) nor the transformation temperatures of other Zn–Sb phases. Additionally, appearance and disappearance of Sb is not matched by appearance or

disappearance of any other phase (one would expect to see Zn metal when Sb metal is present). Most likely, non-uniform temperature conditions are present inside the capillary, which leads to Zn being transported to the colder zone of capillary and out of the diffraction zone.

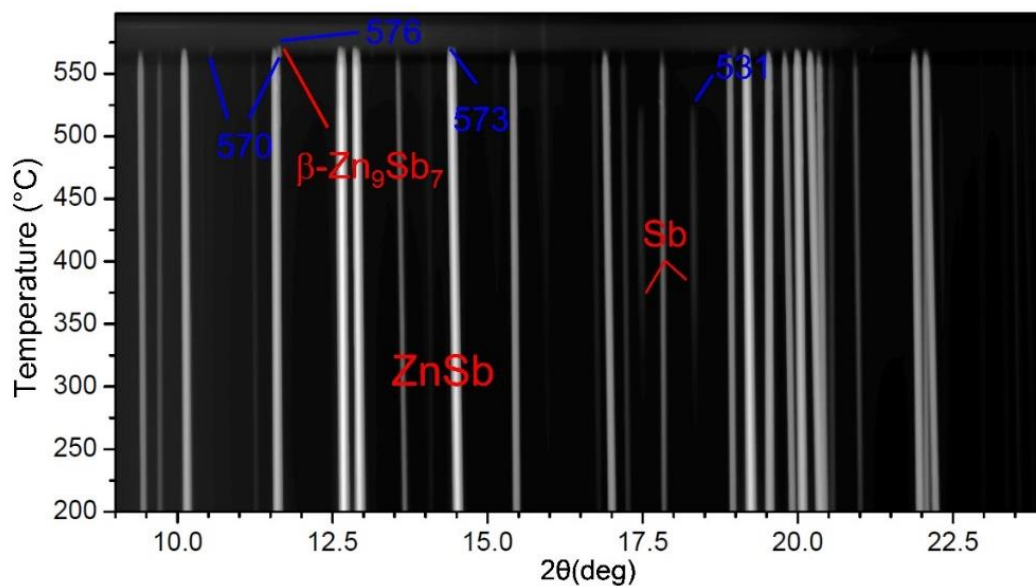


Figure 3.6. Powder diffraction data for the ZnSb sample during heating from room temperature till 600 °C.

The following phase transformations are detected:

- (1) 570 °C: ZnSb starts to decompose peritectically into β -Zn₉Sb₇ and Sb-rich liquid and disappears completely at 573 °C. The peritectic temperature of 570 – 573 °C is slightly higher than 565 °C detected for ZnSb in the Zn₉Sb₇ sample (see below).
- (2) 576 °C: β -Zn₉Sb₇ disappears. This is the temperature of liquidus for the ZnSb composition.

We have also refined the occupancy of the Zn site in ZnSb at selected temperatures from room temperature till 550 °C. The Zn site becomes deficient above 150 °C and has the occupancy of 0.91(1) at 350 °C, 0.90(1) at 450 °C and 0.87(1) at 550 °C. Since the EDS compositions of the ZnSb samples quenched from 350 and 450 °C are close to $Zn_{0.99}Sb$ (**Table 3.1**), we propose that at high temperatures majority of “missing” Zn atoms migrate from the main Zn site into the neighbouring tetrahedral voids made of Sb atoms. Such behaviour would be similar to the Zn distribution in $Zn_{13}Sb_{10}$, except that in $Zn_{13}Sb_{10}$ some Zn disorder is already present at room temperature, while in ZnSb it occurs at higher temperatures.

3.3.4. Stability and Transformations in Zn_9Sb_7 and Zn_3Sb_2

Structure and stability of Zn_9Sb_7 and Zn_3Sb_2 were discussed in details in our two previous works.^{99,133} Here, we provide only a summary of the structural transformations. Zn_9Sb_7 has two polymorphs that exist only at the high temperatures and at rather narrow temperature ranges. **Figure 3.7** shows the diffraction patterns for the Zn_9Sb_7 sample in the 400–620 °C range. Since Zn_9Sb_7 is stable only above 514 °C, the Zn_9Sb_7 sample contains ZnSb and $Zn_{13}Sb_{10}$ at lower temperatures.

Upon heating, the following transformations are detected:

(1) 510 °C: $Zn_{13}Sb_{10}$ phase starts to decompose peritectoidally into α - Zn_9Sb_7 and β - Zn_3Sb_2 and is gone completely at 520 °C. The decomposition temperature of 510 – 520 °C for $Zn_{13}Sb_{10}$ is different from 496 – 509 °C, observed in the Zn_4Sb_3 sample. Such difference

is above an estimated instrumental uncertainty of ~ 5 °C, and may result from either a compositional variation in the $\text{Zn}_{13}\text{Sb}_{10}$ phase or from overheating $\text{Zn}_{13}\text{Sb}_{10}$, or both. Presence of three phases, ZnSb , $\alpha\text{-Zn}_9\text{Sb}_7$ and $\beta\text{-Zn}_3\text{Sb}_2$ above 520 °C, suggests non-equilibrium conditions inside the capillary. Amount of $\beta\text{-Zn}_3\text{Sb}_2$ diminishes with temperature and its diffraction peaks disappear around 548 °C, most likely due to its reaction with ZnSb to yield Zn_9Sb_7 .

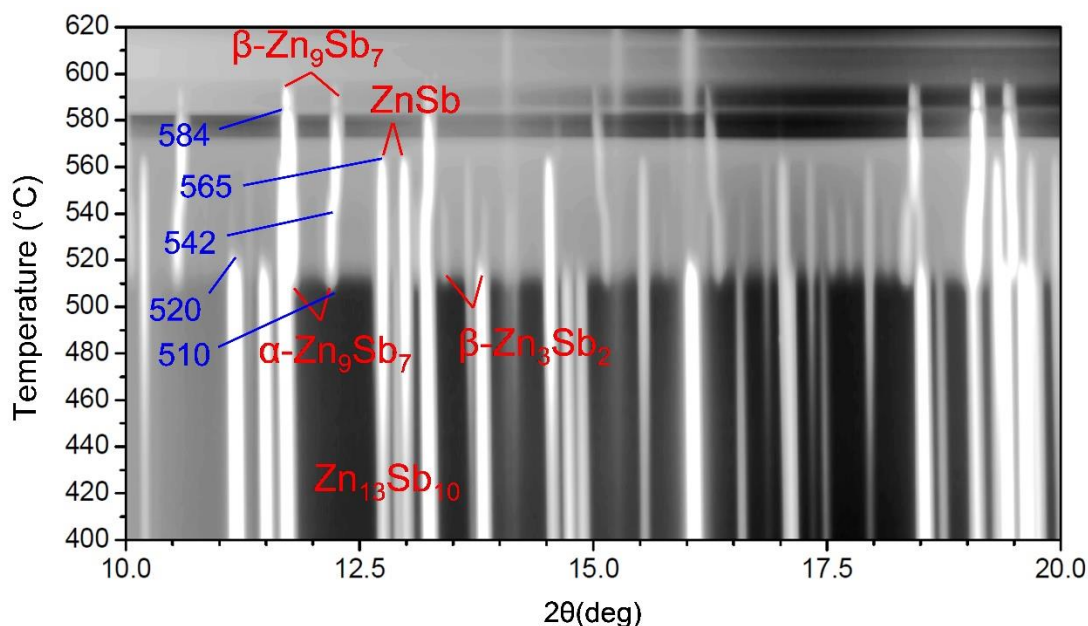


Figure 3.7. Powder diffraction data for the Zn_9Sb_7 sample during heating from room temperature till 620 °C.

- (2) 542 °C: $\alpha\text{-Zn}_9\text{Sb}_7$ transforms into $\beta\text{-Zn}_9\text{Sb}_7$. The α -to- $\beta\text{-Zn}_9\text{Sb}_7$ transformation temperature of is similar to 536 °C observed in the Zn_4Sb_3 sample.
- (3) 565 °C: ZnSb decomposes.
- (4) 584 °C: $\beta\text{-Zn}_9\text{Sb}_7$ melts.

Similar to Zn_9Sb_7 , the Zn_3Sb_2 phase has two modifications and is thermodynamically stable at higher temperatures (**Figure 3.8**). While none of the polymorphs of Zn_9Sb_7 could be quenched to room temperature, the low-temperature α - Zn_3Sb_2 can be kinetically stabilized at room temperature by rapid quenching from 430 °C.¹³³ The Zn_3Sb_2 sample shows different behaviour during heating and cooling at the rate of 2 °C min⁻¹.¹³³ While both α - and β - Zn_3Sb_2 are observed during heating, only β - Zn_3Sb_2 is detected during cooling. Formation of α - Zn_3Sb_2 during cooling is achieved only by some prolonged annealing around 430 °C.¹³³ Here we discuss transformations for the quenched Zn_3Sb_2 sample during heating:

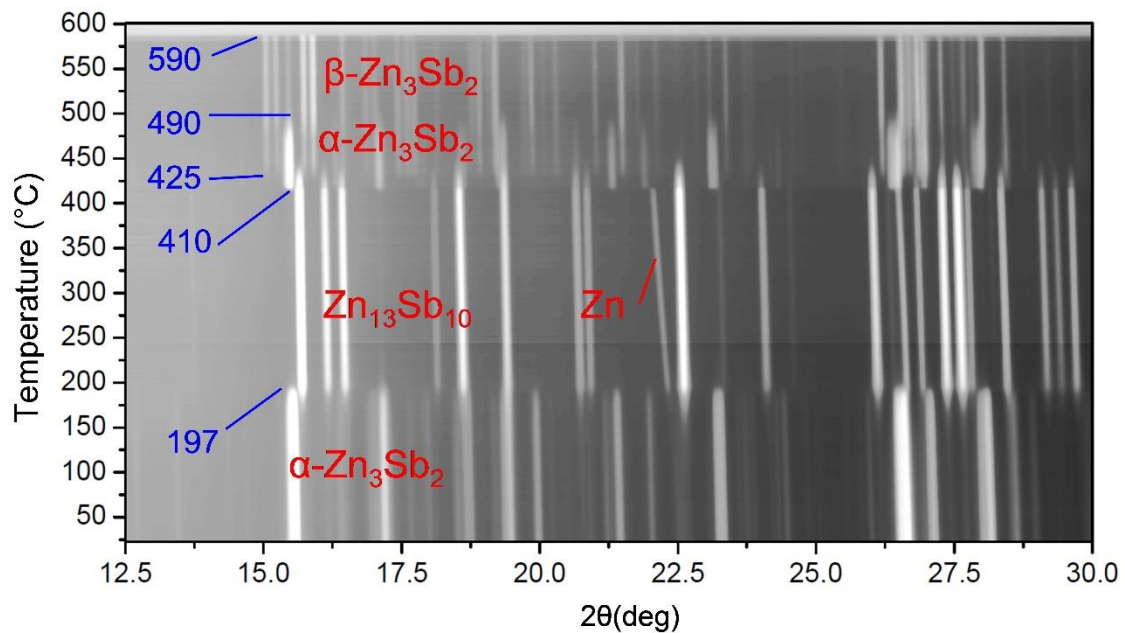


Figure 3.8. Powder diffraction data for the Zn_3Sb_2 sample (quenched from 430 °C) during heating from room temperature till 600 °C.

- (1) 197 °C: the quenched metastable α -Zn₃Sb₂ phase decomposes into Zn₁₃Sb₁₀ and Zn.
- (2) 410 °C: Zn₁₃Sb₁₀ and Zn react back to give α -Zn₃Sb₂.
- (3) 425 °C: remnant β -Zn₁₃Sb₁₀ and Zn, not fully consumed at 410 °C, combine to give the β -Zn₃Sb₂ phase. α - and β -Zn₃Sb₂ coexist together till 490 °C.
- (4) 490 °C: α -Zn₃Sb₂ transforms into β -Zn₃Sb₂.
- (5) 590 °C: β -Zn₃Sb₂ melts.

3.3.5. Zn – Sb Phase Diagram

The HT diffraction experiments, discussed above, allowed us to establish the transformation and/or melting temperatures for Zn_{1- δ} Sb, Zn_{9- δ} Sb₇, Zn_{13- δ} Sb₁₀, and Zn_{3- δ} Sb₂ (the δ is used to represent Zn deficiency). **Table 3.4** summarizes the phase transformations and invariant temperatures, and also lists corresponding temperatures taken from Izard *et al.*¹²⁵ In general, there is a good agreement between the phase diagram proposed by us and the one given by Izard *et al.*¹²⁵ The largest difference is the presence of Zn_{9- δ} Sb₇, which is identified as γ -Zn₄Sb₃ in ref. ¹²⁵. Some of the transformation temperatures are close to the literature data, but some are higher than the reported one. This discrepancy in the temperatures likely stems from at least two sources: a difference between the temperatures inside the capillary and at the heater, and use of the different characterization methods (diffraction vs. thermal analysis) with different heating rates.

Table 3.4. Phase analysis, transformation and invariant temperatures for four samples obtained from HT synchrotron diffraction studies during heating. The last column gives transformation temperatures taken from V. Izard *et al.*¹²⁵.

Sample	Phases at R.T.	Transformations	<i>T</i> (°C)	Ref. 125 ^b
ZnSb	ZnSb	ZnSb → β-Zn ₉ Sb ₇ + L	570 – 573	549
		β-Zn ₉ Sb ₇ + L → L	576	557
			(liquidus)	
Zn ₉ Sb ₇	Zn ₁₃ Sb ₁₀ + ZnSb	Zn ₁₃ Sb ₁₀ → α-Zn ₉ Sb ₇ + β-Zn ₃ Sb ₂	510 – 520	494
		α-Zn ₉ Sb ₇ → β-Zn ₉ Sb ₇	542	532
		ZnSb → β-Zn ₉ Sb ₇ + L	565	n/a
		β-Zn ₉ Sb ₇ → L	584	568
Zn ₄ Sb ₃	Zn ₁₃ Sb ₁₀ + Zn	Zn ₁₃ Sb ₁₀ + Zn → β-Zn ₃ Sb ₂	412	412
		Zn ₁₃ Sb ₁₀ → α-Zn ₉ Sb ₇ + β-Zn ₃ Sb ₂	498 – 503	495
		α-Zn ₉ Sb ₇ → β-Zn ₉ Sb ₇	536	532
		β-Zn ₃ Sb ₂ → β-Zn ₉ Sb ₇ + L	575	n/a
		β-Zn ₉ Sb ₇ + L → L	580	568
			(liquidus)	
Zn _{3.26} Sb ₂	α-Zn ₃ Sb ₂ + Zn ^a	α-Zn ₃ Sb ₂ → Zn ₁₃ Sb ₁₀ + Zn (non-equilibrium)	197	n/a
		Zn ₁₃ Sb ₁₀ + Zn → α-Zn ₃ Sb ₂	410	407
		Zn ₁₃ Sb ₁₀ + Zn → β-Zn ₃ Sb ₂	425	413
		α-Zn ₃ Sb ₂ → β-Zn ₃ Sb ₂	490	458
		β-Zn ₃ Sb ₂ → L	590	568

^a Some Zn was deposited on the walls of silica tube and also found inside the Zn_{3.26}Sb₂ sample as elemental inclusions. Zn was not detected on the X-ray powder diffraction.

^b The following compositions from V. Izard *et al.* were used for comparison: ZnSb, ~Zn₉Sb₇ (56.30 at. % for Zn), Zn₄Sb₃ and Zn₃Sb₂.

The data from **Table 3.4** combined with the elemental analyses are used to construct the central part of the Zn–Sb phase diagram (**Figure 3.9**). It has to be stated that the composition of the eutectic between Zn_{13–δ}Sb₁₀ and Zn_{3–δ}Sb₂ is unknown. The DSC data by Izard *et al.*¹²⁵ were also inconclusive for the eutectic, and thus could not be used as a guide. In addition, the dashed liquidus lines are approximations. The proposed

temperatures and compositions are the best ones that could be derived from our experiments. The eutectic temperatures of 415 and 509 °C are adopted from the work of Izard *et al.*¹²⁵ A short summary on all the phases is provided below. The temperature accuracy is close to 5 °C.

(1) **Zn_{1-δ}Sb**. It is given as a line compound with the composition of Zn_{0.99}Sb (Zn_{49.8}Sb_{50.2}). Its decomposition temperature of 569 °C is the average of 573 and 565 °C obtained from the ZnSb and Zn₉Sb₇ samples.

(2) **Zn_{9-δ}Sb₇**. The α- and β-Zn_{9-δ}Sb₇ polymorphs are Zn-poorer compared to Zn_{13-δ}Sb₁₀; also α-Zn_{9-δ}Sb₇ is located to the right of β-Zn_{9-δ}Sb₇. The exact composition of the polymorphs is unknown as only their approximate compositions could be extracted from the high-temperature diffraction experiments.⁹⁹ The α – β transition temperature is the average one based on the Zn₄Sb₃ and Zn₉Sb₇ samples.

(3) **Zn_{13-δ}Sb₁₀**. The β-Zn_{13-δ}Sb₁₀ modification, or simply Zn_{13-δ}Sb₁₀, is stable above –19 °C (ref. ¹³³) till 496 – 509 °C in the Zn₄Sb₃ sample or till 510 – 520 °C in the Zn₉Sb₇ one. As discussed above, such difference may result from a varying Zn amount: a Zn-richer Zn_{13-δ}Sb₁₀ phase in the Zn₄Sb₃ sample has a lower decomposition temperature than the Zn-poorer one in the Zn₉Sb₇ sample. Such conclusions would be in agreement with the phase diagram proposed by Izard *et al.*¹²⁵. 515 °C (average of 510 and 520 °C) is taken as the peritectoid temperature for the Zn-poorer composition, while 503 °C for the Zn-richer composition. The proposed homogeneity range is Zn_{12.62}Sb₁₀-Zn_{12.72}Sb₁₀ (Zn = 55.8 –

56.0 %). Likely, the composition of $\text{Zn}_{13-\delta}\text{Sb}_{10}$ is temperature dependent but we could not establish this.

(4) $\text{Zn}_{3-\delta}\text{Sb}_2$. The α - and β - $\text{Zn}_{3-\delta}\text{Sb}_2$ polymorphs are given as line compounds. The electron microprobe analysis on α - $\text{Zn}_{3-\delta}\text{Sb}_2$ yielded $\text{Zn}_{2.96(2)}\text{Sb}_2$ and the Zn deficiency was supported by a positive Seebeck coefficient.¹³³ β - $\text{Zn}_{3-\delta}\text{Sb}_2$ is Zn-poorer compared to α - $\text{Zn}_{3-\delta}\text{Sb}_2$. There can be some homogeneity ranges for both polymorphs, but there is no data to postulate them.

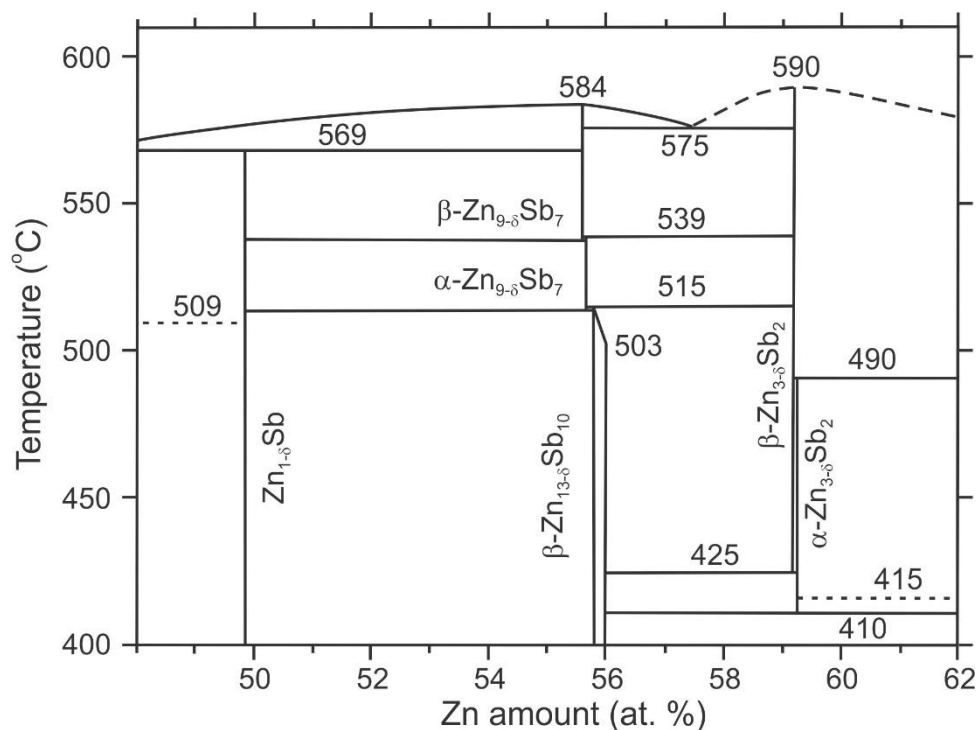


Figure 3.9. Central part of the Zn – Sb phase diagram.

3.4. Conclusions

The updated Zn–Sb phase diagram provides new details about the composition, transformation and stability temperatures for the four binary phases. While the $\text{Zn}_{13-\delta}\text{Sb}_{10}$ phase is well known, its formula was written as $\text{Zn}_{4-\delta}\text{Sb}_3$, which is incorrect based on its structure and composition. The updated diagram uses the proper formula for this phase. Additionally, we have demonstrated that a phase pure $\text{Zn}_{13}\text{Sb}_{10}$ sample can be easily prepared from the $\text{Zn}_{13}\text{Sb}_{10}$ composition and there is no need for extra Zn as in the Zn_4Sb_3 samples. Ability to prepare phase pure $\text{Zn}_{13}\text{Sb}_{10}$ samples can be used as a springboard for doping studies, optimizing thermoelectric properties and improving temperature stability of $\text{Zn}_{13}\text{Sb}_{10}$.

The high-temperature diffraction studies on ZnSb, $\text{Zn}_{13}\text{Sb}_{10}$ and Zn_9Sb_7 suggest that Zn atoms are very mobile at elevated temperatures and easily migrate from the main Zn site into the interstitial ones. While such Zn migration can be beneficial for the thermal conductivity, it can be detrimental for the thermal stability since Zn atoms can easily escape from the structure. Arresting Zn migration can be a key in improving high-temperature thermoelectric performance of ZnSb and $\text{Zn}_{13}\text{Sb}_{10}$.

Chapter 4. Incorporation of Indium into the $Zn_{13}Sb_{10}$ Thermoelectric Material

This chapter contains the material covered in the manuscript “Incorporation of Indium into the $Zn_{13}Sb_{10}$ Thermoelectric Material”, which was published in *Journal of Alloys and Compounds (J. Alloys Compd., 2019, 780, 334 – 340)*. The physical property measurements were collected by Dr. Taras Kolodiazhnyi at the National Institute for Materials Science (NIMS), Tsukuba, Ibaraki, Japan. The experimental procedures, structure determination, data interpretation and manuscript preparation were completed by the candidate.

Reproduced with permission from Taras Kolodiazhnyi and Yuriy Mozharivskyj, *J. Alloys Compd., 2019, 780, 334 – 340*. Copyright 2018 Elsevier B. V..

The composition of the In-substituted $\text{Zn}_{13}\text{Sb}_{10}$ phases follows the $\text{Zn}_{13-1.5x}\text{In}_x\text{Sb}_{10}$ charge-balanced formula and the reduction in the Zn content is due to the In^{3+} oxidation state, compared to the Zn^{2+} oxidation state. Zn deficiency in the In-doped samples is supported by the X-ray powder diffraction and EDS elemental analyses. Single-crystal X-ray diffraction refinement backs the Zn deficiency by revealing absence of Zn atoms in the interstitial sites and decreased occupancy of the main Zn site.

The heat capacity measurements indicate that incorporation of In suppresses the $\alpha' \rightarrow \alpha$ (235 K) and $\alpha \rightarrow \beta$ (254 K) phase transitions, which could be due to the disappearance of some interstitial Zn atoms and/or difficulty in ordering the remaining ones. Both electrical resistivity and Seebeck coefficient data suggest a decrease in charge carrier concentration, stemming from an increased occupancy of the valence band. The thermal conductivity reveals changes in the phonon scattering pathways upon In doping; dominance of point defect scattering in $\text{Zn}_{13-1.5x}\text{In}_x\text{Sb}_{10}$ vs. Umklapp scattering in the pristine $\text{Zn}_{13}\text{Sb}_{10}$.

4.1. Introduction

A good thermoelectric material can be described as a “phonon-glass, electron-crystal”⁴²; it possesses a low thermal conductivity of a phonon-glass and a low electrical resistivity of an electron-crystal. The $\text{Zn}_{13}\text{Sb}_{10}$ phase, known as Zn_4Sb_3 , is one of such materials; it possesses very low thermal conductivity, rivalling that of amorphous solids, and maintains good electrical conductivity⁹⁰. Research performed on $\text{Zn}_{13}\text{Sb}_{10}$ targeted different aspects of this material, including its synthesis^{123,134}, atomic structure^{92,94–96}, and thermal

stability^{95,130,135}. There are also doping studies, such as Cd^{136–138} and Bi¹³⁹ incorporation, in attempt to improve its thermoelectric properties. Indium substitution in Zn₁₃Sb₁₀ has also been explored; e.g. Tang *et al.* investigated incorporation of In on the Sb sites¹⁴⁰, Wei *et al.* prepared In-doped “Zn₄Sb₃” by Bridgman method¹⁴¹, and Liu *et al.* compared thermoelectric properties of Al, Ga and In-doped “Zn₄Sb₃” at low temperatures¹⁴². In this work we attempted to understand the compositional changes in the In-doped Zn₁₃Sb₁₀ phases and to develop connections between the composition, transport properties and structural changes.

4.2. Experimental

4.2.1. Synthesis

Pieces of pure elements Zn (99.99 wt. % CERAC), Sb (99.999 wt. % 5N. Plus), and In (99.99 wt. % Alfa Aesar) were used as starting materials. Originally, samples with the general loading compositions Zn_{13-x}In_xSb₁₀ ($x = 0.1, 0.2, 0.3, 0.4$ and 0.5) and Zn_{12.5- δ} In_{0.5}Sb₁₀ ($\delta = 0 - 0.5$) were prepared. However based on the diffraction and EDS results, it was established that the composition of the In-doped samples follows the Zn_{13-1.5x}In_xSb₁₀ formula. As the results, the series of the Zn_{13-1.5x}In_xSb₁₀ samples with $x = 0.2 - 2$ and 0.2 intervals were made. All the samples were sealed in the evacuated silica tubes and placed in the same box furnace to eliminate temperature variances. The heating trend was adopted from our previous work¹⁴³. The samples were heated at 750 °C for 16 h and were shaken in between to ensure mixing of the molten elements. The samples were cooled from 750 °C to 350 °C at a rate of 50 °C/h and annealed for 2 days to achieve the phase homogeneity.

The samples were finally cooled down to room temperature at a rate of 50 °C/h. Larger samples were sequentially made with the same procedure and cut into bars for physical property measurements.

Single crystals of pure and In-doped $\text{Zn}_{13}\text{Sb}_{10}$ were grown from the Sn flux, using the ternary phase diagram of Ondřej Zobač *et al.*¹⁴⁴ and following the experimental work by H.-X. Liu *et al.*¹⁴⁵. Samples with the loading compositions of $\text{Zn}_{4.4}\text{Sb}_3\text{Sn}_3$ and $\text{Zn}_{4.2}\text{In}_{0.2}\text{Sb}_3\text{Sn}_3$ were placed into alumina crucibles inside silica tubes. The silica tubes were sealed under vacuum, and put in the furnace. The same furnace was used to reduce variances of the heating trends. The samples were heated at 750 °C for 16 h and were shaken in between to ensure mixing of the molten elements. They were then cooled from 750 °C to 320 °C at varying rates and centrifuged after 12 h at 320 °C. Chunks of single crystals were obtained after centrifugation; polycrystalline-like ingots formed on the top of the melt, and larger crystals were found under the ingots. This suggests that crystals grow on top of the liquid mixture, and larger crystals prefer to grow under the ingot portion of the sample, at the solid-liquid interface.

4.2.2. Powder and Single Crystal X-ray Diffraction

Polycrystalline samples were analyzed on a PANalytical X'Pert Cu $K\alpha_1$ powder X-ray diffractometer (PXRD) at room temperature. The samples were ground and deposited on a silicon zero background holder. The data were collected with the 2θ range of 20 – 80 degrees and the total collection time of 1 hour. Rietveld refinement¹¹¹ was performed to evaluate samples' purity and to derive lattice parameters.

The flux-grown single crystals were analyzed on a STOE IPDS II single crystal diffractometer with the Mo K α radiation and in the whole reciprocal sphere. A numerical absorption correction was based on the crystal shape that was originally derived from the optical face indexing but was later optimized against equivalent reflections using STOE X-Shape software¹⁴⁶. The data were collected for both pristine and In-doped Zn₁₃Sb₁₀ crystals. Structural determinations and refinements were performed using the SHELXL program¹⁴⁷. During the single-crystal refinement, 3 interstitial Zn sites could be detected in the structure of the pristine Zn₁₃Sb₁₀, which agrees with our previous findings⁹⁴ and those of Snyder *et al.*⁹⁶. However, in the In-doped Zn₁₃Sb₁₀, only 1 interstitial Zn (Zn2) site could be located. For the In-containing crystal, electron density on the Zn/In sites were assumed to stem from Zn only. The crystallographic parameters and refinement results are summarized in **Tables 4.1, 4.2a and 4.2b**.

Table 4.1. Single Crystal X-ray Diffraction and refinements of crystal grown from flux Zn_{4.4}Sb₃Sn₃ and Zn_{4.2}In_{0.2}Sb₃Sn₃ at 293 K, MoK α 1, STOE IPDS II diffractometer

Sample	Zn _{4.4} Sb ₃ Sn ₃	Zn _{4.2} In _{0.2} Sb ₃ Sn ₃
Refined composition	Zn _{12.33} Sb ₁₀	Zn _{11.53} Sb ₁₀
Space group	$R\bar{3}c$	$R\bar{3}c$
Lattice Parameters (Å)	$a = 12.215(2)$ $c = 12.388(2)$	$a = 12.221(2)$ $c = 12.419(3)$
Volume (Å ³)	1600.8(6)	1606.2(6)
Z	3	3
Density (calculated), g/cm ³	6.298	6.115
2 θ range for data collection (°)	6.67 to 69.27	6.66 to 69.16
Index Ranges	-19 ≤ h ≤ 19, -18 ≤ k ≤ 15,	-18 ≤ h ≤ 19, -15 ≤ k ≤

	-16 ≤ l ≤ 19	16, -7 ≤ l ≤ 19
Independent reflections	5460 [R(int) = 0.0632]	3269 [R(int) = 0.0385]
Completeness to max 2θ	100.0 %	100.0 %
Data/restraints/parameters	765 / 0 / 33	744 / 0 / 24
Goodness-of-fit of F ²	1.058	1.037
Final R indices [I > 2σ(I)]	R ₁ = 0.0324, wR ₂ = 0.0730	R ₁ = 0.0371, wR ₂ = 0.0748
R indices (all data)	R ₁ = 0.0395, wR ₂ = 0.0757	R ₁ = 0.0575, wR ₂ = 0.0803
Extinction coefficient	0.0043(2)	0.0016(1)
Largest diff. peak/hole, e ⁻ /Å ³	1.908/-1.468	1.804/-1.536

Table 4.2a. Atomic and isotropic displacement (U_{eq}) parameters for the crystal grown from the Zn_{4.4}Sb₃Sn₃ flux.

Atom	Site	Occupancy	x/a	y/b	z/c	$U_{eq}(\text{Å}^2)^*$
Zn1	36f	0.919(5)	0.24416(8)	0.07946(8)	0.09697(7)	0.0255(3)
Zn2	36f	0.044(6)	0.199(3)	0.099(3)	0.016(3)	0.0255(3)
Zn3	36f	0.042(5)	0.175(3)	0.925(3)	0.111(3)	0.0255(3)
Zn4	36f	0.022(5)	0.103(6)	0.869(6)	0.263(5)	0.0255(3)
Sb1	18e	1	0	0.35622(4)	0.25	0.0169(2)
Sb2	12c	1	0	0	0.136745	0.0162(2)

*: the displacement parameters for Zn2, Zn3 and Zn4 were refined isotropically and were set to be the same as for Zn1.

Table 4.2b. Atomic and isotropic displacement (U_{eq}) parameters for the crystal grown from the Zn_{4.2}In_{0.2}Sb₃Sn₃ flux.

Atom	Site	Occupancy	x/a	y/b	z/c	$U_{eq}(\text{Å}^2)^*$
Zn1	36f	0.930(6)	0.24397(8)	0.07955(9)	0.09722(9)	0.0241(3)
Zn2	36f	0.030(6)	0.206(3)	0.104(3)	0.016(2)	0.0241(3)
Sb1	18e	1	0	0.35646(5)	0.25	0.0168(2)
Sb2	12c	1	0	0	0.13679(6)	0.0160(2)

*: the displacement parameter for Zn2 was refined isotropically and was set to be the same as for Zn1.

The single crystal grown from the $\text{Zn}_{4.2}\text{In}_{0.2}\text{Sb}_3\text{Sn}_3$ flux was also analyzed at 100 K on the STOE IPDS II single crystal diffractometer. Peak splitting was detected at high angles, suggesting a symmetry lowering. The symmetry reduction, however, appears to be subtle and refinement with the $C2/c$ space group, observed for $\text{Zn}_{13}\text{Sb}_{10}$ ⁹⁴ at lower temperatures, did not improve refinement results compared to the $R\bar{3}c$ space group.

4.2.3. Elemental Analysis

Quantitative elemental analysis was performed using an INCA-Energy-350 X-ray EDS spectrometer (Oxford Instruments) on a Jeol JSM-6480LV scanning electron microscope (SEM) (20 kV accelerating voltage, 0.7 nA beam current and 50 μm beam diameter). Small pieces of the samples were mounted in a conductive epoxy resin and polished with ~ 10 μm diamond dust during the final polishing stage. Zn metal, Sb metal and InAs were used as standards. Signals averaged over three points per phase gave estimated standard deviations of 0.2 at.% for Zn (measured by K -series lines) and Sb (measured by L -series lines), and 0.07 at.% for In (measured by L -series lines).

4.2.4. Physical Property Measurements

The $\text{Zn}_{11.5}\text{In}_1\text{Sb}_{10}$ sample was cut into an approximately $3 \times 3 \times 8$ mm bar using an alumina saw and kerosene as lubricant to avoid sample oxidation. The density of the sample was 99% of the crystallographic densities. Electrical resistivity, Seebeck coefficient, thermal conductivity, and heat capacity were measured on a Quantum Design Physical Property Measurement System (PPMS). Copper leads were attached using Epo-Tek H20E

silver epoxy. The contacts for all samples were cured under a stream of ultrahigh purity Ar inside a tube furnace.

4.3. Results and Discussion

4.3.1. Composition, Purity and Structural Features of the In-doped Samples

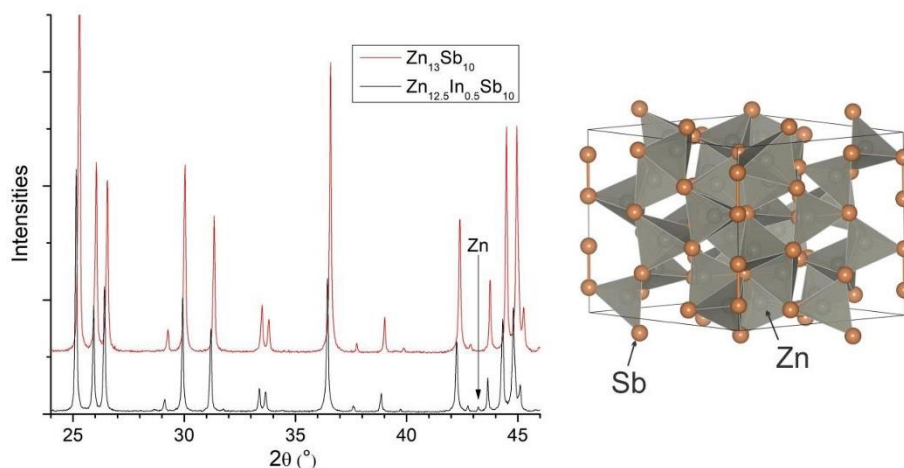


Figure 4.1. (left) X-ray diffraction patterns of $\text{Zn}_{13}\text{Sb}_{10}$ and $\text{Zn}_{12.5}\text{In}_{0.5}\text{Sb}_{10}$. (right) Crystal structure of $\text{Zn}_{13}\text{Sb}_{10}$ without interstitial Zn. The Zn atoms (grey) occupy the tetrahedral voids formed by Sb.

Table 4.3. Lattice parameters of $\text{Zn}_{13}\text{Sb}_{10}$ obtained from Rietveld refinements.

Loading Composition	Lattice parameters
$\text{Zn}_{13}\text{Sb}_{10}$	$a = 12.2337(2) \text{ \AA}$ $c = 12.4295(2) \text{ \AA}$ $V = 1611.01(5) \text{ \AA}^3$
$\text{Zn}_{12.5}\text{In}_{0.5}\text{Sb}_{10}$	$a = 12.2570(2) \text{ \AA}$ $c = 12.4337(2) \text{ \AA}$ $V = 1617.71(5) \text{ \AA}^3$

Rietveld refinement performed for $\text{Zn}_{12.5}\text{In}_{0.5}\text{Sb}_{10}$, one of the originally prepared In-doped samples, indicated a change in the unit cell parameters compared to the pure $\text{Zn}_{13}\text{Sb}_{10}$ (**Table 4.3** and **Figure 4.1**). The $\text{Zn}_{12.5}\text{In}_{0.5}\text{Sb}_{10}$ sample, however, contained elemental Zn as an impurity. Another series of samples with the loading composition $\text{Zn}_{12.5-\delta}\text{In}_{0.5}\text{Sb}_{10}$ ($\delta = 0, 0.1, 0.2, 0.3, 0.4, 0.5$) was made. The sample with $\delta = 0$ contained Zn in agreement with the previous findings, while the samples with $\delta = 0.4$ and 0.5 contained ZnSb, suggesting Zn deficiency. The samples with $\delta = 0.1, 0.2$ and 0.3 had no detectable impurities. These results could be rationalized in terms of the common oxidation states, $3+$ for In and $2+$ for Zn, and the tendency of $\text{Zn}_{13}\text{Sb}_{10}$ to be charge balanced with some Zn deficiency (a *p*-type material). Thus, for the In-substituted phases to remain charge balanced, the amount of Zn taken out of the structure should be 50% more than the amount of In put in. When In is at 0.5, the expected composition is $\text{Zn}_{12.25}\text{In}_{0.5}\text{Sb}_{10}$. Absence of impurities in the powder diffraction patterns of the $\text{Zn}_{12.2-12.4}\text{In}_{0.5}\text{Sb}_{10}$ samples can be explained by their low concentration, below the detection limit.

Compositions of the $\text{Zn}_{12.5-\delta}\text{In}_{0.5}\text{Sb}_{10}$ with $\delta = 0.1, 0.2$ and 0.3 as well as the pure $\text{Zn}_{13}\text{Sb}_{10}$ sample were also investigated using the quantitative elemental analysis (**Table 4.4**). The pristine $\text{Zn}_{13}\text{Sb}_{10}$ sample is Zn-deficient in agreement with the literature data^{94,96,113,143}. In comparison to $\text{Zn}_{13}\text{Sb}_{10}$, the $\text{Zn}_{12.5-z}\text{In}_{0.5}\text{Sb}_{10}$ phases are even more metal deficient, which stems from the trivalent nature of indium. It is also obvious that as the In concentration increases, the overall metal content decreases.

Table 4.4. Elemental analysis of the pristine $\text{Zn}_{13}\text{Sb}_{10}$ and the In-doped $\text{Zn}_{13}\text{Sb}_{10}$.

Loading composition	Zn (at. %)	In (at. %)	Sb (at. %)	Formula
$\text{Zn}_{13}\text{Sb}_{10}$	55.9(2)	n/a	44.1(2)	$\text{Zn}_{12.66(4)}\text{Sb}_{10.00(3)}$ $\text{Zn}_{12.66(4)}\text{Sb}_{10.00(3)}$
$\text{Zn}_{12.4}\text{In}_{0.5}\text{Sb}_{10}$	54.0(2)	1.72(7)	44.3(2)	$\text{Zn}_{12.17(4)}\text{In}_{0.39(2)}\text{Sb}_{10.00(3)}$ $(\text{Zn},\text{In})_{12.56(5)}\text{Sb}_{10.00(3)}$
$\text{Zn}_{12.3}\text{In}_{0.5}\text{Sb}_{10}$	53.5(2)	1.99(7)	44.5(2)	$\text{Zn}_{12.03(4)}\text{In}_{0.45(2)}\text{Sb}_{10.00(3)}$ $(\text{Zn},\text{In})_{12.48(5)}\text{Sb}_{10.00(3)}$
$\text{Zn}_{12.2}\text{In}_{0.5}\text{Sb}_{10}$	53.0(2)	2.46(7)	44.5(2)	$\text{Zn}_{11.90(4)}\text{In}_{0.55(2)}\text{Sb}_{10.00(3)}$ $(\text{Zn},\text{In})_{12.45(5)}\text{Sb}_{10.00(3)}$

Based on the results from the $\text{Zn}_{12.5-\delta}\text{In}_{0.5}\text{Sb}_{10}$ samples and to establish the highest In level, a series of the $\text{Zn}_{13-1.5x}\text{In}_x\text{Sb}_{10}$ samples ($x = 0.2 - 2$, with 0.2 interval) was prepared. Rietveld refinement suggested $x = 1$ to be the highest substitution level, as samples with $x > 1$ contained the InSb impurity. Next, samples with the $\text{Zn}_{11.5+\delta}\text{In}_1\text{Sb}_{10}$ ($\delta = 0, 0.2, 0.4$) loading composition were made and analyzed. The samples with $\delta = 0$ and 0.2 were pure by X-ray analyses, while the sample with $\delta = 0.4$ contained the $\text{Zn}_5\text{Sb}_4\text{In}_{2-\delta}$ ternary phase¹⁴⁸. While there may be some tolerance for a slightly larger Zn amount, it is unlikely that extra Zn, beyond the charge-balanced amount, enters the structure as all samples are *p*-type conductors and elemental Zn is found deposited on the walls of silica tubes. Additionally, there is a possibility of Zn nanoparticles being embedded between the grains of the polycrystalline samples, which cannot be detected by X-ray diffractions¹¹⁷.

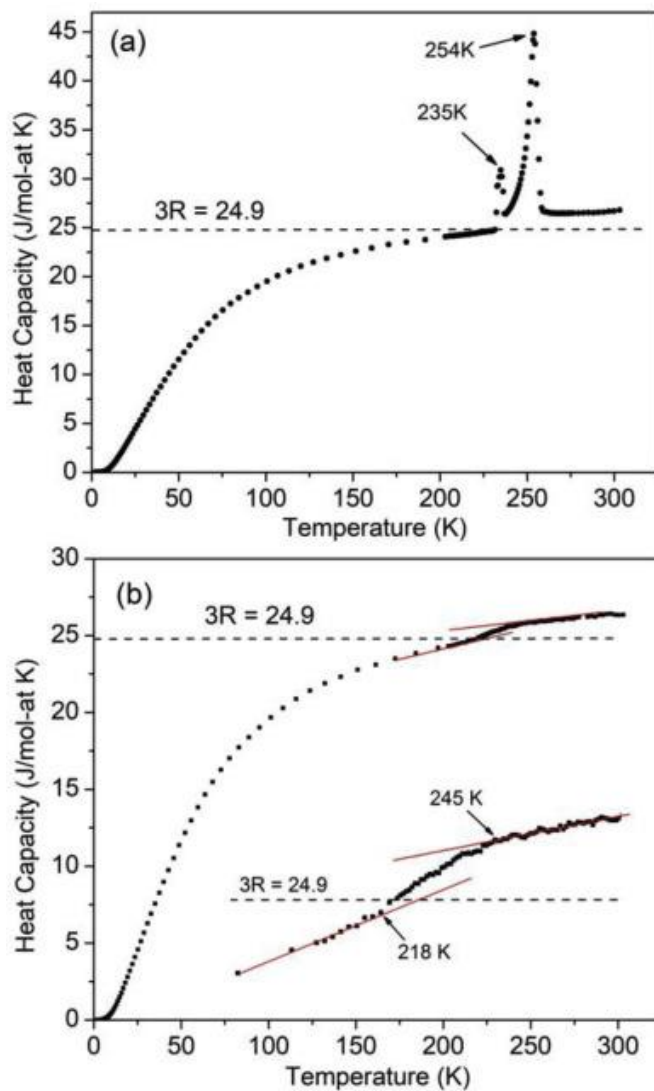
Structural and composition analysis of the flux-grown crystals also supports indium incorporation into $\text{Zn}_{13}\text{Sb}_{10}$. First, crystals from the $\text{Zn}_{4.4}\text{Sb}_3\text{Sn}_3$ and $\text{Zn}_{4.2}\text{In}_{0.2}\text{Sb}_3\text{Sn}_3$ fluxes were analyzed by PXRD and EDS. The unit cell parameters derived from the powder

diffraction differ between the two crystals, with the In-doped $\text{Zn}_{13}\text{Sb}_{10}$ crystal having larger lattice parameters (**Table 4.5**). This serves as an evidence of In incorporation in the structure, since the Pauling's single-bond radius of In (1.497 Å) is larger than that of Zn (1.249 Å)¹⁴⁹. Elemental analysis of the unpolished In-doped crystal also shows the presence of In in $\text{Zn}_{13}\text{Sb}_{10}$ (0.79 at. %) along with Zn (54.44 at. %) and Sb (44.77 at. %) only. During the structural refinement of the single crystal from the $\text{Zn}_{4.2}\text{In}_{0.2}\text{Sb}_3\text{Sn}_3$ flux, the In/Zn ratio could not be refined (due to the metal site deficiencies) and all sites were assumed to be occupied by Zn atoms only. In this crystal, the occupancy of the main Zn site was found to be larger, which could be due to either an increase in the Zn amount or presence of In with a larger scattering factor on this site. Out of the three interstitial Zn sites observed in the pristine $\text{Zn}_{13}\text{Sb}_{10}$, only one site could be reliably identified and refined in the In-containing $\text{Zn}_{13}\text{Sb}_{10}$. In overall, the In-doped structure is metal deficient compared to the pure $\text{Zn}_{13}\text{Sb}_{10}$ even if only Zn atoms are assumed on the metal sites during the refinement. Such outcome agrees well with the Zn-deficient loading composition required to obtain pure bulk samples.

Table 4.5. Unit cell parameters of the flux-grown $\text{Zn}_{13}\text{Sb}_{10}$ single crystals derived from the powder diffraction data using the Rietveld refinement.

Flux composition	Lattice parameters
$\text{Zn}_{4.4}\text{Sb}_3\text{Sn}_3$	$a = 12.2290(2) \text{ \AA}$ $c = 12.4221(2) \text{ \AA}$ $V = 1608.82(5) \text{ \AA}^3$
$\text{Zn}_{4.2}\text{In}_{0.2}\text{Sb}_3\text{Sn}_3$	$a = 12.2430(2) \text{ \AA}$ $c = 12.4263(2) \text{ \AA}$ $V = 1613.05(4) \text{ \AA}^3$

4.3.2. Physical Properties

Figure 4.2. Heat capacities of (a) $\text{Zn}_{13}\text{Sb}_{10}$ and (b) $\text{Zn}_{11.5}\text{In}_1\text{Sb}_{10}$.

Heat capacity and electrical resistivity of $\text{Zn}_{13}\text{Sb}_{10}$ and $\text{Zn}_{11.5}\text{In}_1\text{Sb}_{10}$ are plotted in **Figure 4.2**. The heat capacity measurements clearly show that $\text{Zn}_{13}\text{Sb}_{10}$ exhibits two phase transitions during heating, a first-order at 235 K ($\alpha' \rightarrow \alpha$) and a second-order one at 254 K ($\alpha \rightarrow \beta$). The two transitions have been previously reported in the literature, and they

are associated with the ordering of the Zn atoms and associated symmetry changes. The transition temperatures found in the heat capacity measurements agree well with those obtained from current (**Figure 4.3**) and published electrical resistivity measurements and low-temperature single-crystal X-ray diffractions^{93,95,133}.

In contrast to $\text{Zn}_{13}\text{Sb}_{10}$, the heat capacity for $\text{Zn}_{11.5}\text{In}_1\text{Sb}_{10}$ indicates a gradual phase transformation between 218 and 245 K; however this anomaly resembles neither the first-order phase transition at 235 K ($\alpha' \rightarrow \alpha$) nor the second-order one at 254 K ($\alpha \rightarrow \beta$) of $\text{Zn}_{13}\text{Sb}_{10}$ ⁹⁴. The transition in $\text{Zn}_{11.5}\text{In}_1\text{Sb}_{10}$ appears to be suppressed; it is not well defined and extends over 27 K. It is worth noting that the low-temperature diffraction on the In-doped crystal suggests that its symmetry breaking may be structurally similar to the $\beta \rightarrow \alpha$ transformation in $\text{Zn}_{13}\text{Sb}_{10}$. The heat capacities of both $\text{Zn}_{13}\text{Sb}_{10}$ and $\text{Zn}_{11.5}\text{In}_1\text{Sb}_{10}$ exceed the Dulong-Petit limit $3R = 24.9 \text{ J/mol at.}\cdot\text{K}$, which suggests an additional contribution to the heat capacity beyond harmonic atomic vibrations.

The electrical resistivity of the pure $\text{Zn}_{13}\text{Sb}_{10}$ has features that can be associated with the two phase transitions. On the other hand, the electrical resistivity in $\text{Zn}_{11.5}\text{In}_1\text{Sb}_{10}$ has no features reminiscent of a phase transition. The residual resistivity of $\text{Zn}_{11.5}\text{In}_1\text{Sb}_{10}$ (ρ_0) is higher than that of $\text{Zn}_{13}\text{Sb}_{10}$ and likely results from the presence of the In atoms in the structure. Typically, the residual resistivity stems from impurity atom and defect scatterings, both of which are independent of temperature¹⁵⁰. In our case, the In atoms would act as impurities, thus increasing the residual resistivity. Additionally, instead

of following the dependence of $\text{Zn}_{13}\text{Sb}_{10}$ ¹⁵¹, electrical resistivity of $\text{Zn}_{11.5}\text{In}_1\text{Sb}_{10}$ increases polynomially.

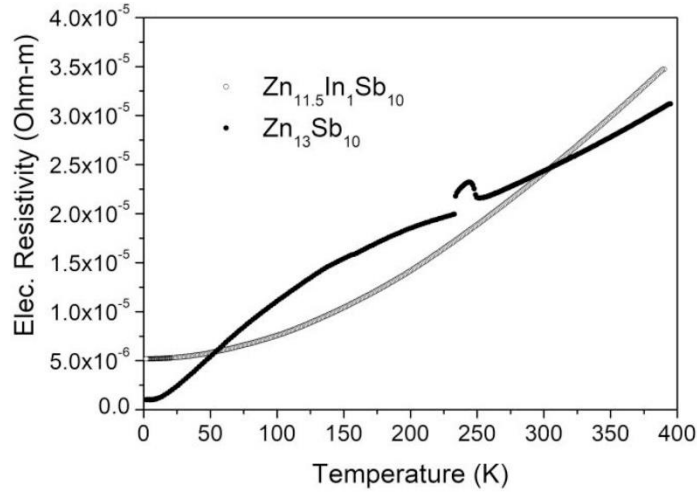


Figure 4.3. Electrical resistivity of $\text{Zn}_{13}\text{Sb}_{10}$ and $\text{Zn}_{11.5}\text{In}_1\text{Sb}_{10}$.

Seebeck coefficients of $\text{Zn}_{13}\text{Sb}_{10}$ and $\text{Zn}_{11.5}\text{In}_1\text{Sb}_{10}$ are plotted in **Figure 4.4**. Above 275 K, Seebeck coefficients for the two samples are parallel to each other, and increase linearly with temperature, as expected from the Mott equation:

$$\alpha = \frac{8\pi^2 k_B^2}{3eh^2} m^* T \left(\frac{\pi}{3n}\right)^{\frac{2}{3}},$$

where m^* is the effective mass of the charge carrier and n is the charge carrier concentration¹⁵². In the 100 – 250 K range for $\text{Zn}_{13}\text{Sb}_{10}$ and 150 – 250 K for $\text{Zn}_{11.5}\text{In}_1\text{Sb}_{10}$, the temperature behaviour of the Seebeck coefficient is also linear but the slopes are different, additionally the two graphs intersect at ~240 K, which is close to the phase transition temperatures. The described changes in the Seebeck coefficient likely suggest

variations in the carrier concentrations in the two samples. However, the exact origin of these changes and its relationship to the Zn/In ordering will need to be clarified.

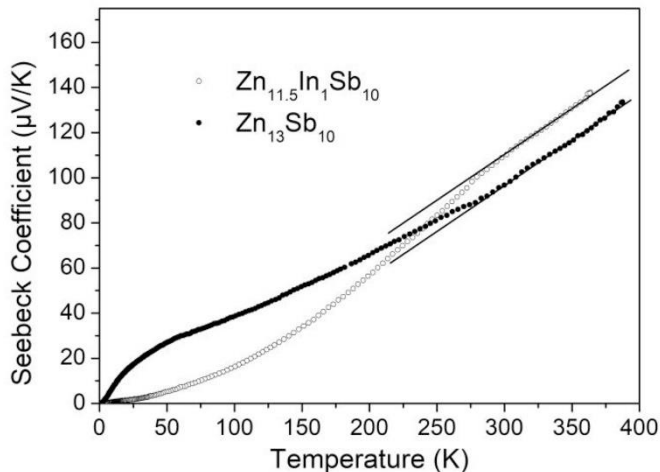


Figure 4.4. Seebeck coefficients of $\text{Zn}_{13}\text{Sb}_{10}$ and $\text{Zn}_{11.5}\text{In}_1\text{Sb}_{10}$.

From both the Seebeck coefficients and electrical resistivity at the higher temperatures, it can be inferred that the carrier concentration in $\text{Zn}_{11.5}\text{In}_1\text{Sb}_{10}$ is lower than that in $\text{Zn}_{13}\text{Sb}_{10}$. This conclusion is also supported by the elemental analysis. Referring to **Table 4.4**, there are $75.32 e^-$ for the $\text{Zn}_{12.66}\text{Sb}_{10}$ phase (sample 1), whereas $75.41 - 75.51 e^-$ for the In-substituted phases (samples 2 – 4). The charge balance, i.e. full occupancy of the valence band, is expected at $76 e^-$, which corresponds to the stoichiometric $\text{Zn}_{13}\text{Sb}_{10}$ composition. Larger electron concentration in the In-substituted materials means lower hole concentration, thus higher electrical resistivity and larger Seebeck coefficient.

Thermal conductivities of the $\text{Zn}_{13}\text{Sb}_{10}$ and $\text{Zn}_{11.5}\text{In}_1\text{Sb}_{10}$ are plotted in **Figure 4.5**. The lattice thermal conductivities κ_l are calculated using $\kappa_l = \kappa_{total} - \kappa_e$, where κ_{total} is

the total thermal conductivity and κ_e is the electronic contribution. The κ_e can be obtained using the Wiedemann–Franz law: $\kappa_e = L\sigma T = LT/\rho$, where L is the Lorenz number. The Lorenz number is estimated according to $L \approx 1.5 + \exp[-\alpha/116]$, where L is given in units of $10^{-8} W\Omega/K^2$ and α is in units of $\mu V/K$ ¹⁵³.

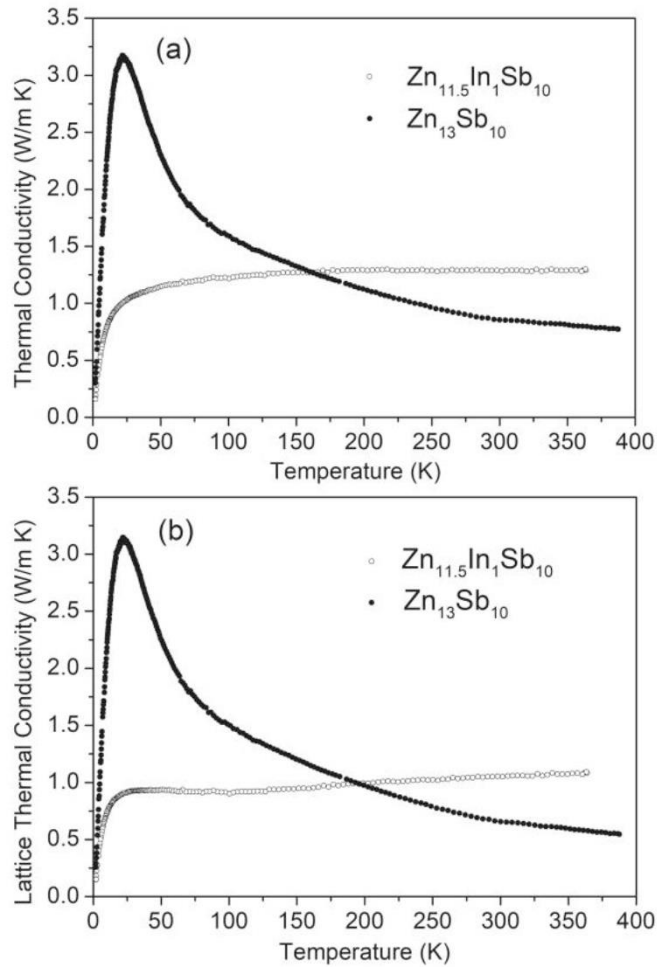


Figure 4.5. (a) Total and (b) lattice thermal conductivities of $Zn_{13}Sb_{10}$ and $Zn_{11.5}In_1Sb_{10}$.

The behaviour of the $Zn_{13}Sb_{10}$ thermal conductivity is typical of a crystalline solid; there is a peak at low temperatures representative of the boundary scattering and a decrease

at higher temperatures stemming from the Umklapp scattering. On the other hand, the $\text{Zn}_{11.5}\text{In}_1\text{Sb}_{10}$ does not exhibit the low-temperature transition from boundary scattering to Umklapp scattering. In fact, thermal conductivity of $\text{Zn}_{11.5}\text{In}_1\text{Sb}_{10}$ is quite similar to that of $\alpha\text{-Zn}_3\text{Sb}_2$ (Chapter 7)¹³³. Based on the results for $\alpha\text{-Zn}_3\text{Sb}_2$, it could be stated that the $\text{Zn}_{11.5}\text{In}_1\text{Sb}_{10}$ exhibits a strong point-defect scattering and weak Umklapp scattering. The dominance of point-defect scattering can be rationalized in terms of heavier In atoms, randomly distributed on the metal sites.

The power factor and zT values for $\text{Zn}_{13}\text{Sb}_{10}$ and $\text{Zn}_{11.5}\text{In}_1\text{Sb}_{10}$ are given in **Figure 4.6**. $\text{Zn}_{11.5}\text{In}_1\text{Sb}_{10}$ possesses a higher power factor above 200 K, which originates from its larger Seebeck coefficient. However, the increased thermal conductivity brought by weakened Umklapp scattering neglects gains in the power factor and yields a lower figure-of-merit for $\text{Zn}_{11.5}\text{In}_1\text{Sb}_{10}$.

The In-doped samples were also investigated by Liu *et al.*¹⁴². It has to be mentioned that their samples were synthesized using the Zn-rich Zn_4Sb_3 composition and thus impurities are expected. Additionally, the exact In doping amount was not verified. The electrical resistivity of their $(\text{Zn}_{0.98}\text{In}_{0.02})_4\text{Sb}_3$ sample is lower than that of “ Zn_4Sb_3 ” below the phase transition temperatures in “ Zn_4Sb_3 ”, but become similar after the phase transitions. The $(\text{Zn}_{0.98}\text{In}_{0.02})_4\text{Sb}_3$ sample possesses a lower Seebeck coefficient than that of “ Zn_4Sb_3 ” from 5 to 310 K. Also, the thermal conductivity of the $(\text{Zn}_{0.98}\text{In}_{0.02})_4\text{Sb}_3$ is lower than that of “ Zn_4Sb_3 ”, a peak at low temperatures representative of boundary scattering is retained in $(\text{Zn}_{0.98}\text{In}_{0.02})_4\text{Sb}_3$, similarly to Zn_4Sb_3 . The disagreement between Liu, F. *et al.*¹⁴² and our

data for In-doped $\text{Zn}_{13}\text{Sb}_{10}$ phase is likely due to different doping levels of In and presence of impurities.

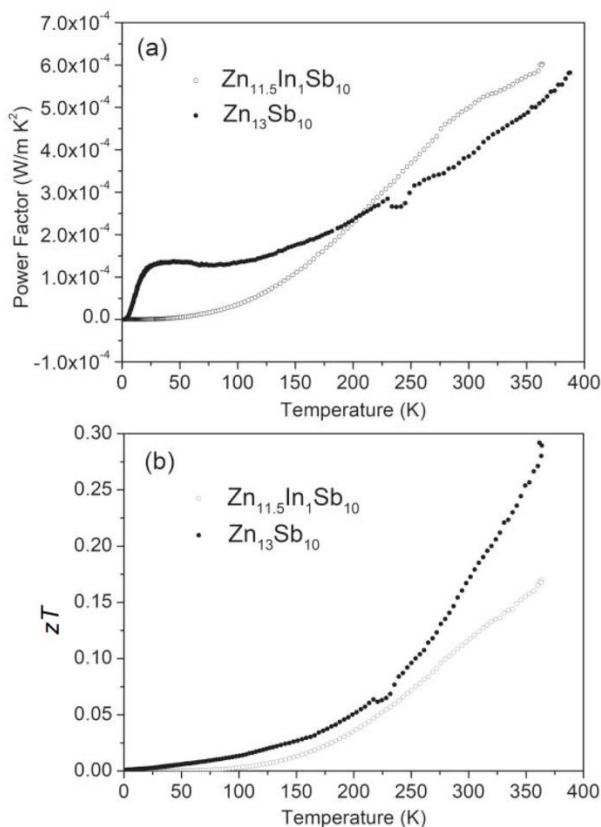


Figure 4.6. (a) Power factor and (b) figure-of-merit, zT for $\text{Zn}_{13}\text{Sb}_{10}$ and $\text{Zn}_{11.5}\text{In}_1\text{Sb}_{10}$.

4.4. Conclusions

Synthesis of phase-pure $\text{Zn}_{13-1.5x}\text{In}_x\text{Sb}_{10}$ phases proves that there is no need for extra Zn as in the Zn_4Sb_3 samples if the proper synthetic conditions are followed. This conclusion echoes the results outlined earlier by our group¹⁴³. Not surprisingly, the composition of $\text{Zn}_{13-1.5x}\text{In}_x\text{Sb}_{10}$ is driven by the trivalent nature of indium and the tendency of the phase to remain charge balanced and even slightly metal deficient.

The thermoelectric measurements on $\text{Zn}_{11.5}\text{In}_1\text{Sb}_{10}$ suggest that it is possible to optimize the power factor of the $\text{Zn}_{13}\text{Sb}_{10}$ -based materials. However, the data also point that impurity atoms may have negative effects on the thermal conductivity of $\text{Zn}_{13}\text{Sb}_{10}$ and yield significantly higher lattice thermal conductivity (in contrast to the accepted wisdom). An increase in the lattice thermal conductivity appears to come from the suppression of the Umklapp scattering. The origin of such behaviour needs to be understood if the properties of the $\text{Zn}_{13}\text{Sb}_{10}$ -based materials were to be optimized. Based on the current results, an ideal dopant for $\text{Zn}_{13}\text{Sb}_{10}$ would be an element which keeps the thermal conductivity suppressed while it increases the power factor of the material.

Chapter 5. Experimental Survey of Dopants in $Zn_{13}Sb_{10}$ Thermoelectric Material

This chapter contains the material covered in the manuscript “Experimental Survey of Dopants in $Zn_{13}Sb_{10}$ Thermoelectric Material”, which was published in *Intermetallics* (*Intermetallics*, **2020**, 123, 106831). The low temperature physical property measurements were collected by Dr. Taras Kolodiazhnyi at the National Institute for Materials Science (NIMS), Tsukuba, Ibaraki, Japan. The high temperature thermal diffusivities of materials were collected by Dr. Yu-Chih Tseng at CanmetMATERIALS, Natural Resources of Canada, Hamilton, Ontario, Canada. Partial Hall measurements were collected by Mr. Shaochang Song. The experimental procedures, structure determination, data interpretation and manuscript preparation were completed by the candidate.

Reproduced with permission from Taras Kolodiazhnyi, Shaochang Song, Yu-Chih Tseng and Yuriy Mozharivskyj, *Intermetallics*, **2020**, 123, 106831. Copyright 2020 Elsevier Ltd..

This work explores a variety of dopant incorporations into the $\text{Zn}_{13}\text{Sb}_{10}$ thermoelectric material synthesized from the stoichiometric composition by slow cooling. The experimental results revealed the preference for the dopant atoms that can adopt a tetrahedral coordination environment of the Zn site. The incorporations of dopants restrict the movement of Zn atoms, as evident from the suppressed $\alpha/\alpha' - \beta$ phase transitions. Incorporations affect both the electrical and thermal transport properties of the material, with outcomes being specific to the dopant. For instance, doping with Ga and In (both in group 13) affects the charge carrier concentration in a different way. Also, depending on the dopants, the dominant phonon scattering pathway can either be preserved (as Umklapp scattering) or switched to a less effective point defect scattering. The origin of the Zn deficiency in $\text{Zn}_{13}\text{Sb}_{10}$ is not electronic in nature, but thermodynamic instead.

5.1. Introduction

In the literature, the $\text{Zn}_{13}\text{Sb}_{10}$ phase is more often referred to as “ Zn_4Sb_3 ”, due to an early work on “ Zn_4Sb_3 ” by Mayer *et al.*^{91,143}, who observed that the quenched sample with Zn_4Sb_3 loading composition gives the most pure sample. However, both the experimental (elemental analysis, X-ray diffraction^{92,93,96,113,143}) and theoretical studies^{92,94,154} support the $\text{Zn}_{13}\text{Sb}_{10}$ formula for the phase. In terms of the electronic structure analysis, the valence band is filled at 76 electrons, which correspond to the $\text{Zn}_{13}\text{Sb}_{10}$ composition ($13 \times 2 e^-$ from Zn + $10 \times 5 e^-$ from Sb). Recently, a synthetic procedure, which allows a pure $\text{Zn}_{13}\text{Sb}_{10}$ material to be synthesized from the $\text{Zn}_{13}\text{Sb}_{10}$ loading composition, has been developed by

us¹⁴³. The proposed synthetic method permits a more rigorous analysis of dopants in the $Zn_{13}Sb_{10}$ phase since there is minimal presence of a Zn impurity, aside from possible presence of Zn nanoparticles in the material¹¹⁷.

In this work, we have employed the newly developed method to study incorporation of foreign elements into $Zn_{13}Sb_{10}$. Our goal is to enhance the power factor of $Zn_{13}Sb_{10}$ and, at the same time, to suppress its thermal conductivity through additional impurity-based scattering of phonons. It has to be mentioned that various substitutions have been explored for the Zn_4Sb_3 composition: Cd^{136–138}, Bi¹⁵⁵, In^{140–142} on the polycrystalline samples and the M ($M = Cd, Ga, In, Sn$) doping^{156–158} on the flux-grown single crystals. In this study, we also aimed to compile the survey of successful incorporations.

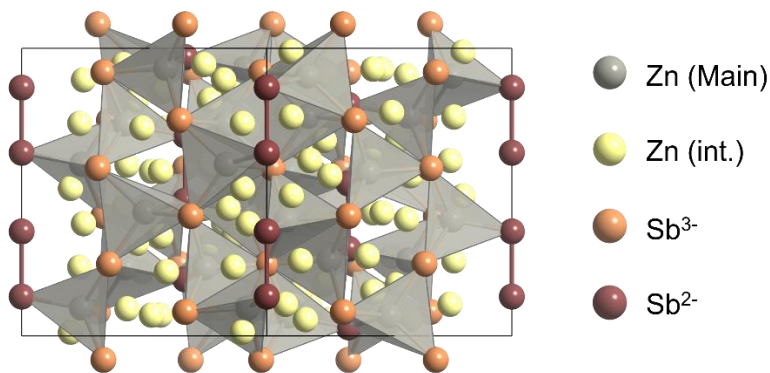


Figure 5.1. Crystal structure of β - $Zn_{13}Sb_{10}$.

5.2. Materials and Methods

5.2.1. Synthesis

Pieces of elemental Zn (99.99 wt. % CERAC) and Sb (99.999 wt. % 5N Plus) were used as starting materials. Incorporations of other elements followed the $Zn_{13-x}M_xSb_{10}$ and

$Zn_{13}Sb_{10-z}A_z$ loading formulas, where $M = Cr$ (99.98 wt. % Alfa Aesar), Mn (99.9 wt. % Alfa Aesar), Fe (99.98 wt. % Alfa Aesar), Co (99.9 wt. % Alfa Aesar), Cu (99.9999 wt. % Alfa Aesar), Ga (99.999 wt. % Alfa Aesar), Ge (99.999 wt. % Alfa Aesar), Y (99.9 wt. % Alfa Aesar), Ag (99.9 wt. % Alfa Aesar), Cd (99.99 wt. % 5N Plus), In (99.99 wt. % Alfa Aesar) and Sn (99.9 wt. % CERAC); and $A = Sn$, Te (99.999 wt. % Alfa Aesar) and Bi (99.999 wt. % Alfa Aesar). Depending on the oxidation state of the incorporated element, the loading composition was modified to achieve the charge balance. This approach was used by us in our previous work on the In-substituted $Zn_{13}Sb_{10}$ material; the sample's composition was adjusted to $Zn_{13-1.5x}In_xSb_{10}$ to account for the 3+ oxidation state of In^{159} . The weighted elements were sealed in the evacuated silica tubes and placed in the same box furnace to eliminate temperature variances. The samples were heated to 750°C at 150°C/h and annealed for 16 h, while being shaken in between to ensure mixing of the molten elements. The samples were cooled from 750 °C to 350 °C at a rate of 50°C/h and annealed at 350 °C for 2 days to achieve phase homogeneity. The samples were finally cooled down to room temperature at a rate of 50 °C/h. Larger samples were sequentially made with the same procedure and cut into bars and plates for physical property measurements^{143,159}.

Single crystals of pristine and doped $Zn_{13}Sb_{10}$ were grown from the Sn flux, using the ternary phase diagram of Ondřej Zobač *et al.*¹⁴⁴ and adapting the experimental work of H.-X. Liu *et al.*¹⁴⁵. Samples with the loading compositions of $Zn_{4.4}Sb_3Sn_3$ and $Zn_{4.2}M_{0.2}Sb_3Sn_3$ ($M = Mn, Ga, Cd$ and In) were placed into alumina crucibles inside silica tubes. The tubes were sealed under vacuum, and put in the same box furnace to reduce

variances of the heating trends. The samples were heated at 750 °C for 16 h and shaken in-between to facilitate mixing of the molten elements. They were then cooled from 750 to 500 °C at 50°C/h, then to 320 °C at 1°C/h, and kept at 320°C for 12h. Crystals were separated from the flux by centrifugation.

5.2.2. Powder and Single Crystal X-ray Diffraction

Powder X-ray diffraction data for the polycrystalline samples were collected on a PANalytical X'Pert Pro CuK α_1 diffractometer with an X'Celerator detector. Samples were ground and deposited evenly on a zero-background silicon sample holder. The data were collected in the 20 – 80° 2θ range with collection time of 1 hour. Phase purity and unit cell parameters were evaluated by full-profile Rietveld refinements, using the Rietica program¹¹¹.

Table 5.1. Crystallographic parameters and refinement results for the crystals grown from the Zn_{4.4}Sb₃Sn₃, Zn_{4.2}Mn_{0.2}Sb₃Sn₃, Zn_{4.2}Ga_{0.2}Sb₃Sn₃, Zn_{4.2}Cd_{0.2}Sb₃Sn₃ and Zn_{4.2}In_{0.2}Sb₃Sn₃ fluxes (293 K, MoK α_1 , STOE IPDS II diffractometer).

Flux	Zn _{4.4} Sb ₃ Sn ₃	Zn _{4.2} Mn _{0.2} Sb ₃ Sn ₃
Refined composition	Zn _{11.60} Sb ₁₀	Zn _{11.54} Sb ₁₀
Space group	$R\bar{3}c$	$R\bar{3}c$
Lattice Parameters (Å)	$a = 12.215(2)$ $c = 12.388(2)$	$a = 12.206(2)$ $c = 12.409(3)$
Volume (Å ³)	1600.8(6)	1601.0(6)
Z	3	3
Density (calculated), g/cm ³	6.185	6.139
2θ range for data collection (°)	6.67 to 69.27	6.67 to 69.61
Index Ranges	$-19 \leq h \leq 19, -18 \leq k \leq 15,$ $-16 \leq l \leq 19$	$-19 \leq h \leq 19, -16 \leq k \leq 19,$ $-19 \leq l \leq 19$

Independent reflections	5483 [R(int) = 0.0632]	7040 [R(int) = 0.0600]
Completeness to max 2 θ	99.6 %	99.9 %
Data/restraints/parameters	765 / 0 / 28	762 / 0 / 28
Goodness-of-fit of F ²	1.043	1.133
Final R indices [I > 2 σ (I)]	R ₁ = 0.0330, wR ₂ = 0.0751	R ₁ = 0.0295, wR ₂ = 0.0640
R indices (all data)	R ₁ = 0.0401, wR ₂ = 0.0779	R ₁ = 0.0312, wR ₂ = 0.0650
Extinction coefficient	0.0043(2)	0.0028(1)
Largest diff. peak/hole, e ⁻ /Å ³	1.907/-1.367	2.175/-1.328

Zn _{4.2} Ga _{0.2} Sb ₃ Sn ₃	Zn _{4.2} Cd _{0.2} Sb ₃ Sn ₃	Zn _{4.2} In _{0.2} Sb ₃ Sn ₃
Zn _{11.71} Sb ₁₀	Zn _{11.73} Sb ₁₀	Zn _{11.87} Sb ₁₀
<i>R</i> $\bar{3}c$	<i>R</i> $\bar{3}c$	<i>R</i> $\bar{3}c$
<i>a</i> = 12.188(2)	<i>a</i> = 12.229(2)	<i>a</i> = 12.222(2)
<i>c</i> = 12.445(2)	<i>c</i> = 12.416(3)	<i>c</i> = 12.412(3)
1601.0(6)	1608.0(6)	1605.6(6)
3	3	3
6.062	6.148	6.183
7.60 to 70.42	6.47 to 69.97	6.67 to 69.32
-19 ≤ <i>h</i> ≤ 19, -19 ≤ <i>k</i> ≤ 16, -19 ≤ <i>l</i> ≤ 19	-19 ≤ <i>h</i> ≤ 19, -16 ≤ <i>k</i> ≤ 18, -15 ≤ <i>l</i> ≤ 19	-19 ≤ <i>h</i> ≤ 19, -19 ≤ <i>k</i> ≤ 19, -19 ≤ <i>l</i> ≤ 14
8889 [R(int) = 0.0448]	5680 [R(int) = 0.0624]	8977 [R(int) = 0.0618]
99.9 %	99.2 %	99.9%
772 / 0 / 28	765 / 0 / 28	771 / 0 / 28
1.112	1.173	1.153
R ₁ = 0.0312, wR ₂ = 0.0540	R ₁ = 0.0344, wR ₂ = 0.0777	R ₁ = 0.0383, wR ₂ = 0.0713
R ₁ = 0.0418, wR ₂ = 0.0567	R ₁ = 0.0364, wR ₂ = 0.0788	R ₁ = 0.0498, wR ₂ = 0.0749
0.0032(2)	0.0019(1)	0.0022(1)
2.066/-1.224	2.287/-1.563	2.362/-1.150

Room temperature single-crystal data of the flux-grown crystals were collected on a STOE IPDS II Mo K α diffractometer. Numerical absorption correction was based on the crystal shapes that were first derived from optical face indexing, and then later optimized against equivalent reflections using the STOE X-Shape software¹⁴⁶. Structural determinations and refinements were performed using the OLEX2 program¹⁶⁰. The single-crystal refinements were performed based on the structural model developed earlier in our group⁹⁴, which has 1 main Zn site, 3 interstitial Zn sites and 2 Sb sites. The displacement parameters for the interstitial Zn sites were refined anisotropically and were set to be the same as for main Zn site (Zn1). For the dopant-containing crystals, the electron densities on the Zn/dopant sites were assumed to stem from Zn only. Also, interstitial Zn sites with occupancies below 2 % were neglected. Note that not all interstitial Zn sites could be located during the refinements. The crystallographic parameters and refinement results are summarized in **Tables 5.1** and **5.2**.

Table 5.2. Atomic and isotropic displacement (U_{eq}) parameters for the flux-grown crystals.

Atom	Site	Occupancy	x/a	y/b	z/c	$U_{eq}(\text{\AA}^2)$
Zn_{4.4}Sb₃Sn₃						
Zn ₁	36f	0.914(5)	0.24416(8)	0.07943(8)	0.09699(7)	0.0254(3)
Zn ₂	36f	0.027(3)	0.076(3)	0.252(3)	0.109(3)	0.025(2)
Zn ₃	36f	0.026(3)	0.198(3)	0.100(3)	0.014(3)	0.025(2)
Sb ₁	18e	1	0	0.35623(4)	0.25	0.0169(2)
Sb ₂	12c	1	0	0	0.13674(5)	0.0162(2)
Zn_{4.2}Mn_{0.2}Sb₃Sn₃						
Zn ₁	36f	0.916(4)	0.24423(7)	0.07950(7)	0.09681(6)	0.0253(2)
Zn ₂	36f	0.027(3)	0.072(3)	0.246(2)	0.100(2)	0.025(2)
Zn ₃	36f	0.025(2)	0.194(3)	0.095(3)	0.017(2)	0.025(2)
Sb ₁	18e	1	0	0.35609(4)	0.25	0.0167(2)

Sb ₂	12c	1	0	0	0.13661(4)	0.0164(2)
Zn_{4.2}Ga_{0.2}Sb₃Sn₃						
Zn ₁	36f	0.930(4)	0.244091(7)	0.07943(8)	0.09690(6)	0.0230(2)
Zn ₂	36f	0.023(2)	0.074(3)	0.247(3)	0.106(2)	0.023(2)
Zn ₃	36f	0.022(2)	0.201(3)	0.103(3)	0.014(2)	0.023(2)
Sb ₁	18e	1	0	0.35630(4)	0.25	0.0150(1)
Sb ₂	12c	1	0	0	0.13664(4)	0.0142(1)
Zn_{4.2}Cd_{0.2}Sb₃Sn₃						
Zn ₁	36f	0.923(4)	0.24406(8)	0.07932(8)	0.09706(7)	0.0254(2)
Zn ₂	36f	0.029(3)	0.076(3)	0.252(3)	0.107(2)	0.025(2)
Zn ₃	36f	0.026(3)	0.196(3)	0.101(3)	0.013(2)	0.025(2)
Sb ₁	18e	1	0	0.35627(4)	0.25	0.0170(2)
Sb ₂	12c	1	0	0	0.13677(4)	0.0163(2)
Zn_{4.2}In_{0.2}Sb₃Sn₃						
Zn ₁	36f	0.936(5)	0.24406(8)	0.07941(9)	0.09715(9)	0.0253(3)
Zn ₂	36f	0.024(3)	0.076(3)	0.251(3)	0.110(3)	0.025(2)
Zn ₃	36f	0.029(3)	0.203(3)	0.102(3)	0.018(2)	0.025(2)
Sb ₁	18e	1	0	0.35639(5)	0.25	0.0173(2)
Sb ₂	12c	1	0	0	0.13680(5)	0.0165(2)

*: Zn₂, Zn₃ and were refined anisotropically and their displacement parameters were restricted to be the same as for Zn₁.

5.2.3. Elemental Analysis

Semi-quantitative elemental analysis was performed using an X-Max (80mm²) X-ray EDS spectrometer (Oxford Instruments) on a TESCAN VEGA II LSU scanning electron microscope (SEM) (20 kV accelerating voltage). Small pieces of the samples were initially mounted in a conductive bakelite resin by applying 30 MPa pressure at 175 °C for 5 min. The samples prepared under these conditions were found to decompose based on the surface X-ray diffraction analysis, echoing the work by Keshavarz *et al.*¹⁶¹. Instead, polished bar-cut samples were used for elemental analyses.

5.2.4. Physical Property Measurements

The $\text{Zn}_{12.8}\text{Mn}_{0.2}\text{Sb}_{10}$, $\text{Zn}_{12.75}\text{Mn}_{0.25}\text{Sb}_{10}$, $\text{Zn}_{12.55}\text{Ga}_{0.3}\text{Sb}_{10}$, $\text{Zn}_{11.96}\text{Cd}_{1.04}\text{Sb}_{10}$ and the $\text{Zn}_{12.5}\text{Sn}_{0.5}\text{Sb}_{10}$ samples were cut into an approximately $2 \times 2 \times 8 \text{ mm}^3$ bar and $10 \times 10 \times 1 \text{ mm}^3$ plates using an alumina saw and kerosene as lubricant to avoid sample oxidation. The densities of the samples were 99% of the crystallographic densities. Low temperature electrical resistivity, Seebeck coefficient, thermal conductivity and heat capacity were measured on a Quantum Design Physical Property Measurement System (PPMS). The high temperature thermal diffusivities, D , were measured using the laser flash method (LFA) on the Netzsch LFA-457 instrument. The high temperature thermal conductivity κ was calculated using $\kappa = DC_p\rho$, where C_p is the heat capacity and ρ is the density of the material. The heat capacities of the samples were assumed to be a constant, and were taken from the room temperature values from the PPMS measurements. The densities ρ of the samples were measured using the Archimedes method at room temperature and were also treated as a constant. The carrier concentration at room temperature, n , was derived from the Hall coefficient measured on a home-built instrument with a GMW 5403 electromagnet. The room temperature resistivity was also measured on this instrument using the Van der Pauw method.

5.2.5. Electronic Structure Calculations

The total density of states (DOS), the Crystal Orbital Hamiltonian Population (COHP) plot and the electronic band structure of the $\text{Zn}_{13}\text{Sb}_{10}$ material were calculated using the TB-LMTO-ASA method.¹⁶² The $\text{Zn}_{12}\text{Sb}_{10}$ structural motif of the room

temperature β -Zn₁₃Sb₁₀ phase was used in the calculation. Empty spheres were included into the unit cell to fulfill the overlap criteria of atomic spheres in the TB-LMTO-ASA method. The DOS data agree well with the previous published ones⁹⁴, and the same structural parameters were subsequently used to calculate the COHP plot and the electronic band structure.

5.3. Results and Discussion

Table 5.3. Summary of successful single element incorporations in Zn₁₃Sb₁₀.

Dopants	Loading composition	Zn ₁₃ Sb ₁₀ unit cell volume (Å ³)	EDS composition (at. %)	Formula
Mn	Zn _{13-x} Mn _x Sb ₁₀ $x = 0.2$	1608.26(4)	Zn (53.7(5) %), Mn (0.7(2) %), Sb (45.6(3)%)	Zn _{11.80} Mn _{0.16} Sb ₁₀ (Zn,Mn) _{11.96} Sb ₁₀
Ga	Zn _{13-1.5x} Ga _x Sb ₁₀ $x = 0.3$	1604.15(5)	Zn (53.4(5) %), Ga (1.0(3) %), Sb (45.6(3)%)	Zn _{11.70} Ga _{0.23} Sb ₁₀ (Zn,Ga) _{11.93} Sb ₁₀
Cd	Zn _{13-x} Cd _x Sb ₁₀ $x = 1.04$	1632.52(4)	Zn (51.2(5) %), Cd (3.5(1) %), Sb (45.4(3)%)	Zn _{11.29} Cd _{0.76} Sb ₁₀ (Zn,Cd) _{12.05} Sb ₁₀
In	Zn _{13-1.5x} In _x Sb ₁₀ $x = 1$	1619.58(4)	Zn (50.4(5) %), In (4.0(2) %), Sb (45.6(3) %)	Zn _{11.05} In _{0.89} Sb ₁₀ (Zn,In) _{11.94} Sb ₁₀
---	Zn ₁₃ Sb ₁₀	1610.10(4)	Zn (54.6(4) %), Sb (45.4(2) %)	Zn _{11.97} Sb ₁₀

Table 5.3 below provides a summary of the successful incorporations, including the highest doping levels derived from the phase analysis, refined unit cell volumes and semi-quantitative elemental EDS analyses. The standard deviations for the compositions were obtained from the instrumental wt. % errors. On the other hand, **Table 5.4** summarizes

unsuccessful incorporations, including general loading compositions, refined unit cell volumes of $\text{Zn}_{13}\text{Sb}_{10}$ and impurities as obtained from the powder X-ray diffraction.

Table 5.4. Summary of unsuccessful single element incorporations into $\text{Zn}_{13}\text{Sb}_{10}$.

Dopants	Loading composition	$\text{Zn}_{13}\text{Sb}_{10}$ unit cell volume (\AA^3)	Impurities
Cr	$\text{Zn}_{13-x}\text{Cr}_x\text{Sb}_{10}$, $x = 0.1 - 0.5$	$\sim 1607 - 1608$	CrSb + unknown
	$\text{Zn}_{13-1.5x}\text{Cr}_x\text{Sb}_{10}$, $x = 0.2 - 1$		CrSb + unknown
Fe	$\text{Zn}_{13-x}\text{Fe}_x\text{Sb}_{10}$, $x = 0.1 - 0.3$	$\sim 1607 - 1609$	ZnSb, $\text{ZnFe}_{0.92}\text{Sb}$
Co	$\text{Zn}_{13-x}\text{Co}_x\text{Sb}_{10}$, $x = 0.1 - 0.5$	$\sim 1607 - 1608$	unknown
Cu	$\text{Zn}_{13-x}\text{Cu}_x\text{Sb}_{10}$, $x = 0.1 - 0.5$	$\sim 1609 - 1610$	ZnSb, brass
	$\text{Zn}_{13-x}\text{Cu}_{2x}\text{Sb}_{10}$, $x = 0.1 - 0.5$		ZnSb, brass
Ge	$\text{Zn}_{13-x}\text{Ge}_x\text{Sb}_{10}$, $x = 0.4 - 0.8$	$\sim 1609 - 1610$	ZnSb, Ge
*Y	$\text{Zn}_{13-x}\text{Y}_x\text{Sb}_{10}$, $x = 0.2, 0.8$	~ 1609	YSb
*Ag	$\text{Zn}_{12.8}\text{Ag}_{0.2}\text{Sb}_{10}$	~ 1609	AgZn, AgZn_3 , ZnSb
Sn	$\text{Zn}_{13-x}\text{Sn}_x\text{Sb}_{10}$, $x = 0.1 - 0.5$	~ 1610	Sn
	$\text{Zn}_{13}\text{Sb}_{10-x}\text{Sn}_x$, $x = 0.1 - 0.5$	~ 1610	Sn, Zn
Te	$\text{Zn}_{13}\text{Sb}_{10-x}\text{Te}_x$, $x = 0.1 - 0.5$	$\sim 1610 - 1611$	ZnTe
	$\text{Zn}_{13}\text{Sb}_{10-x}\text{Te}_{1.5x}$, $x = 0.1 - 0.5$		ZnTe
Bi	$\text{Zn}_{13}\text{Sb}_{10-x}\text{Bi}_x$, $x = 0.05 - 0.5$	$\sim 1610 - 1613$	Bi, Zn

*: Limited studies were done on these elements.

Several factors were considered as evidence for the successful incorporation:

- 1) Absence of impurities in the powder X-ray diffraction (PXRD) data;
- 2) Change in the unit cell parameters (PXRD);
- 3) Presence of dopants in the $\text{Zn}_{13}\text{Sb}_{10}$ phase during the EDS analysis.

Changes in the unit cell parameters were used as the primary evidence for the incorporation into the structure, due to the differences between the Pauling's single-bond radii^{149,163} of Zn, Sb and the substituting elements (Table 5.6).

Table 5.5. Semi-quantitative EDS elemental analyses, and unit cell parameters of the flux-grown $Zn_{13}Sb_{10}$ single crystals from the Rietveld refinement. The crystals were ground and the data were collected in the $20 - 140^\circ 2\theta$ range with collection time of 12 hours.

Flux composition	Zn (at. %)	M (at. %)*	Sb (at. %)	Lattice parameters
$Zn_{4.4}Sb_3Sn_3$	55.8(5)	--	44.2(2)	$a = 12.23119(9) \text{ \AA}$ $c = 12.42453(9) \text{ \AA}$ $V = 1609.71(2) \text{ \AA}^3$
$Zn_{4.2}Mn_{0.2}Sb_3Sn_3$	53.4(5)	2.6(6)	44.1(3)	$a = 12.22901(9) \text{ \AA}$ $c = 12.4207(1) \text{ \AA}$ $V = 1608.65(2) \text{ \AA}^3$
$Zn_{4.2}Ga_{0.2}Sb_3Sn_3$	52.4(5)	1.6(5)	46.0(3)	$a = 12.21712(6) \text{ \AA}$ $c = 12.40348(8) \text{ \AA}$ $V = 1603.29(1) \text{ \AA}^3$
$Zn_{4.2}Cd_{0.2}Sb_3Sn_3$	54.0(5)	0.95(4)	45.0(3)	$a = 12.2452(1) \text{ \AA}$ $c = 12.4346(1) \text{ \AA}$ $V = 1614.71(3) \text{ \AA}^3$
$Zn_{4.2}In_{0.2}Sb_3Sn_3$	54.4(5)	0.79(4)	44.8(3)	$a = 12.24230(7) \text{ \AA}$ $c = 12.42557(8) \text{ \AA}$ $V = 1612.77(2) \text{ \AA}^3$

Table 5.6. Pauling's radii of single-bonded elements.

Element	Zn	Mn	Ga	Cd	In	Cr	Fe	Co
Radius (\AA)	1.307	1.250	1.258	1.466	1.442	1.260	1.250	1.230
	Cu	Ge	Y	Ag	Sn	Sb	Te	Bi
	1.245	1.225	1.659	1.412	1.405	1.41	1.37	1.52

5.3.1. Composition, Purity and Structure of the Pristine β - $Zn_{13}Sb_{10}$

The pristine sample was used as a reference for the dopant-incorporated samples. The pristine β - $Zn_{13}Sb_{10}$ has a unit cell volume of $1610.10(4) \text{ \AA}^3$, and the EDS elemental analysis yields the $Zn_{11.97}Sb_{10}$ composition. There is a significant difference between the

expected $\text{Zn}_{13}\text{Sb}_{10}$ formula and the one obtained from the elemental analyses. On the other hand, the results of the elemental analyses are close to the compositions (**Table 5.1** and **5.3**, around $\text{Zn}_{12.8}\text{Sb}_{10}$) derived from single-crystal refinements of the crystals from the $\text{Zn}_{4.4}\text{Sb}_3\text{Sn}_3$ and $\text{Zn}_{4.2}\text{M}_{0.2}\text{Sb}_3\text{Sn}_3$ fluxes. This Zn deficiency agrees also well with the literatures^{95,96,113} and with its *p*-type charge transport behavior.

5.3.2. Composition and Purity of Substituted Samples

5.3.2.1. Divalently Substituted $\text{Zn}_{13}\text{Sb}_{10}$ (Manganese and Cadmium)

Pure Mn- and Cd-substituted $\text{Zn}_{13}\text{Sb}_{10}$ materials can be synthesized using the $\text{Zn}_{13-x}\text{M}_x\text{Sb}_{10}$ composition, $M = \text{Mn}$ or Cd . The unit cell parameters of their polycrystalline and single-crystalline samples obtained from powder diffraction differ from those of the pristine sample (**Table 5.3** and **5.5**). These changes can be rationalized using the Pauling's single-bonded radii and serve as evidence of the Mn and Cd incorporation into the structure. Mn has a smaller radius and Cd has a larger radius than Zn, and the unit cell volumes reflect this.

Cd-substituted $\text{Zn}_{13}\text{Sb}_{10}$ phases have been studied earlier, and Cd was found to fully replace Zn, yielding $\text{Cd}_{12.7(1)}\text{Sb}_{10}$ with the same space group $R\bar{3}c$ ¹⁶⁴. A $\text{Zn}_{13}\text{Sb}_{10}$ sample with 8 at. % Cd on the Zn site has been prepared to compare its physical properties to those of the In-containing $\text{Zn}_{13}\text{Sb}_{10}$ sample, which has the same substitution level.

5.3.2.2. Trivalently Substituted $\text{Zn}_{13}\text{Sb}_{10}$ (Gallium and Indium)

Single phase Ga- and In-substituted $Zn_{13}Sb_{10}$ samples can be synthesized using the off- stoichiometric loading compositions $Zn_{13-1.5x}M_xSb_{10}$, $M = Ga$ or In . As discussed in the previous work (Chapter 4)¹⁵⁹, the $Zn_{13-x}M_xSb_{10}$ samples contained a Zn impurity for $M = Ga$ and In , because of the 3+ oxidation states of Ga and In. In order to achieve the charge balanced structure and a pure $Zn_{13}Sb_{10}$ sample, 50 % more Zn is taken out for every Ga/In put in. Unit cell parameters of the Ga- and In-doped polycrystalline samples and single crystals obtained from powder diffraction differ from those of the pristine sample (**Tables 5.3 and 5.5**). These changes follow the relative sizes of Ga, In and Zn (**Table 5.6**); the Ga-substituted sample has a smaller unit cell and the In-substituted one has a larger unit cell than the pristine $Zn_{13}Sb_{10}$. Note that the unit cell volume of the Cd-substituted phase is larger than that of the In-doped one, although the Pauling's single-bonded radii of Cd and In (1.466 and 1.442 Å) are close and the Cd substitution level was found to be lower experimentally. Likely, this discrepancy is due to the higher oxidation state of In (hence the radius of In in the structure is below 1.442 Å), and/or the lower total amount of metal cations in the material, leading to a smaller than expected increase in the unit cell volume.

It is worth mentioning that the elements of the four successful incorporations have d^5 (Mn^{2+}) and d^{10} (Ga^{3+} , Cd^{2+} , In^{3+}) electron configurations, and they tend to adopt tetrahedral environments.

5.3.2.3. Unsuccessful incorporations

Most of these incorporations were considered unsuccessful due to presence of dopant-containing impurity phases and/or the dopant itself, subsequent formation of the

Zn-Sb impurities, and insignificant changes in the $\text{Zn}_{13}\text{Sb}_{10}$ unit cell volume. There were however some exceptions, namely the Cr-, Co-, Sn- and Bi-doped samples, which are discussed below.

I. Cr- and Co-doped samples

Rietveld refinements of these samples showed a change in the unit cell volume from $1610.10(4) \text{ \AA}^3$ for the pristine one to $1607 - 1608 \text{ \AA}^3$ in an irregular order with respect to the Cr and Co amounts put in. Also, unidentifiable impurity peaks were present in the diffraction patterns. EDS analysis of the Co-containing samples provided no evidence for the Co incorporation into the $\text{Zn}_{13}\text{Sb}_{10}$ material and revealed that some intergrain regions had the composition close to $\text{Zn}_3\text{Co}_2\text{Sb}_3$. Elemental analysis of the Cr-containing sample revealed some Cr-rich area that had compositions close to ZnCrSb . The origin of the smaller $\text{Zn}_{13}\text{Sb}_{10}$ unit cells volume should be further investigated.

Within the framework of the crystal field theory, the d elements with configurations other than d^0 , d^5 (high spin, HS) or d^{10} prefer an octahedral environment over a tetrahedral one, due to a larger crystal-field stabilization energy (CFSE). There is no CFSE for the d^0 , d^5 (HS) or d^{10} atoms in either tetrahedral or octahedral environments.

In the $\text{Zn}_{13}\text{Sb}_{10}$ structure, Zn atoms occupy the tetrahedral voids. Additionally, the ligand-field splitting parameter in $\text{Zn}_{13}\text{Sb}_{10}$ is expected to be small and thus the substituting 3d elements will be in the HS state. Metal atoms with configurations other than d^0 , d^5 (HS) or d^{10} will prefer to form phases that can provide large CFSE energy and therefore they will not be incorporated into $\text{Zn}_{13}\text{Sb}_{10}$. Common oxidation states for chromium are $2+(d^4)$ and

$3+(d^3)$, while that of cobalt is $2+ (d^7)$, and they will prefer octahedral environments instead.¹⁶⁵

II. Sn-containing samples

Samples with the Sn substitution either on the Zn or Sb site were not phase pure. In the $Zn_{13-x}Sn_xSb_{10}$ samples, a Sn phase was found, however ZnSb, expected due to the deficiency in the loading composition, was not observed. Additionally, there was no increase in the $Zn_{13}Sb_{10}$ unit cell volume, which would have been expected upon successful Sn incorporation (Sn is larger than that of Zn). The $Zn_{13}Sb_{10-x}Sn_x$ samples contained Sn and Zn as impurities, with Zn suggesting a Zn-rich composition. Similar to the other Sn-containing series, the unit cell volume of $Zn_{13}Sb_{10}$ did not increase for larger Sn amounts.

III. Bi-containing samples

This series of samples shows a small, steady increase in the refined unit cell volumes of the $Zn_{13}Sb_{10}$ phase for larger Bi amounts, at the same time, elemental Bi and Zn impurities were detected. Surprisingly, EDS elemental analysis performed on the $Zn_{13}Sb_{9.6}Bi_{0.4}$ sample did not confirm the Bi presence in the $Zn_{13}Sb_{10}$ phase. This is possibly due to the small amount of Bi incorporated, below the detection limit.

5.3.3. Structural Features of the Mn-, Ga-, Cd- and In-doped $Zn_{13}Sb_{10}$ Crystals Grown from Sn Flux

The crystals from the $Zn_{4.4}Sb_3Sn_3$, $Zn_{4.2}Mn_{0.2}Sb_3Sn_3$, $Zn_{4.2}Ga_{0.2}Sb_3Sn_3$, $Zn_{4.2}Cd_{0.2}Sb_3Sn_3$ and $Zn_{4.2}In_{0.2}Sb_3Sn_3$ samples were analyzed by the PXRD and EDS

(Table 5.6). The refined unit cell parameters obtained from the ground crystals via the powder diffraction agreed with those from the corresponding polycrystalline samples and follow changes in the Pauling's single-bonded radii of the elements. Elemental analyses of the unpolished, doped crystals confirmed the presence of the substituents. During the structural refinements of the single crystals from the $Zn_{4.2}M_{0.2}Sb_3Sn_3$ fluxes ($M = Mn, Ga, Cd$ and In), the M/Zn ratios were not refined and all sites were assumed to be occupied by Zn atoms only.

Also, not all 3 interstitial Zn sites could be identified in the crystals. Only 2 interstitial sites were located in the crystal from the $Zn_{4.4}Sb_3Sn_3$ flux, which differs from the structural model used. This is possibly due to the fact that some Sn is still incorporated into the structure, as reflected from the suppressed phase transitions in the heat capacity and electrical resistivity measurements (discussed below). The refinement results of the pristine and In-containing crystal are different from what was reported in our earlier work due to a different refinement approach¹⁵⁹. Here, the displacement parameters of the interstitial Zn (Zn2, Zn3) were refined anisotropically and were set to be the same as for the main Zn site (Zn1).

5.3.4. Physical Properties

Heat capacity and low temperature electrical resistivity of $Zn_{13}Sb_{10}$, $Zn_{12.75}Mn_{0.25}Sb_{10}$, $Zn_{12.55}Ga_{0.3}Sb_{10}$, $Zn_{11.5}In_1Sb_{10}$ and $Zn_{12.5}Sn_{0.5}Sb_{10}$ are plotted in **Figures 5.2** and **5.3**. Properties of $Zn_{12.75}Mn_{0.25}Sb_{10}$ were collected instead of $Zn_{12.8}Mn_{0.2}Sb_{10}$ since the $Zn_{12.75}Mn_{0.25}Sb_{10}$ sample has a smaller $Zn_{13}Sb_{10}$ unit cell volume than that of the

$\text{Zn}_{12.8}\text{Mn}_{0.2}\text{Sb}_{10}$ sample, despite the minute presence of the $\text{SbMn}_{0.89}\text{Zn}_{0.94}$ impurity. Physical properties were not measured for the $\text{Zn}_{11.96}\text{Cd}_{1.04}\text{Sb}_{10}$ sample. The heat capacity measurement of $\text{Zn}_{13}\text{Sb}_{10}$ shows its two phase transitions during heating, which were reported previously^{94,133,143,159}: a first-order at 235 K ($\alpha' - \alpha$), and a second-order at 254 K ($\alpha - \beta$) associated with the Zn disorder. All other samples appear to have suppressed, gradual transitions, instead of clear, sharp ones. Also, heat capacities of all samples exceed the Dulong-Petit limit of $3R = 24.9 \text{ J/mol at.-K}$, which suggests additional contribution to heat capacity beyond harmonic atomic vibrations.

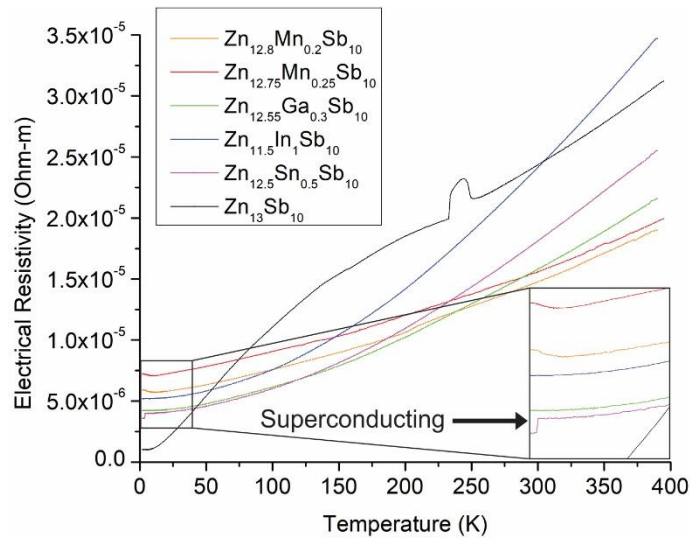


Figure 5.2. Electrical resistivity of the polycrystalline, pristine $\text{Zn}_{13}\text{Sb}_{10}$ and selected doped $\text{Zn}_{13}\text{Sb}_{10}$ samples.

The electrical resistivities of the doped samples also reflect the suppressed phase transitions, in contrast to clear anomalies in the pure $\text{Zn}_{13}\text{Sb}_{10}$ in the 230 – 250 K range. Additionally, resistivities of the doped samples increase with temperature in a polynomial-type fashion, in contrast to the logarithmic-type evolution in the pure $\text{Zn}_{13}\text{Sb}_{10}$ before the

phase transitions. The different behavior of the electrical resistivity in the samples is likely representative of how dopants and Zn disorder (and Zn mobility) affect the carrier relaxation times. The electrical resistivity of a material is expressed as: $\rho = 1/\sigma = 1/ne\mu = m^*/ne^2\tau$, where m^* is the carrier effective mass, n is the carrier concentration, and τ is the carrier relaxation time. Below 40 K, pure $\text{Zn}_{13}\text{Sb}_{10}$ has the lowest resistivity, which can be explained by its atomic structure with fully ordered Zn sites^{93–95}. Since the doped samples forgo this ordering, the remnant Zn disorder and dopant atoms scatter electrons more significantly, leading to a larger resistivity at low temperatures. At higher temperatures, the increasing Zn disorder in pure $\text{Zn}_{13}\text{Sb}_{10}$ appears to be dominant factor; however, in the doped samples, the Zn mobility is suppressed by dopants and thus their resistivity is below that of pure $\text{Zn}_{13}\text{Sb}_{10}$ (except for $\text{Zn}_{11.5}\text{In}_1\text{Sb}_{10}$).

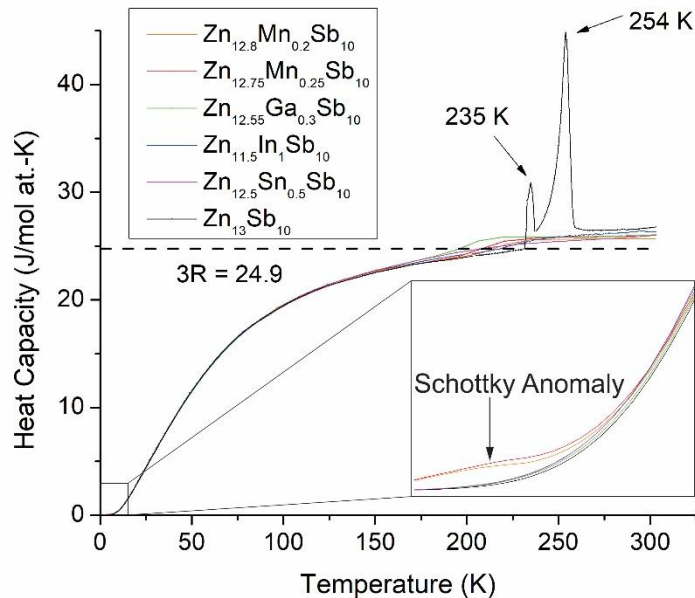


Figure 5.3. Heat capacities of the polycrystalline, pristine $\text{Zn}_{13}\text{Sb}_{10}$ and selected doped $\text{Zn}_{13}\text{Sb}_{10}$ samples.

The discussed suppression of both the α' – α and α – β transitions associated with the Zn ordering may serve as an indication of the incorporation of small quantities of dopants into the structure, even if the dopants are not detected through the XRD and EDS analyses. Thus, absence of peaks in the heat capacity and electrical resistivity of the $\text{Zn}_{12.5}\text{Sn}_{0.5}\text{Sb}_{10}$ sample suggests presence of Sn atoms in the structure. The electrical resistivity of $\text{Zn}_{12.5}\text{Sn}_{0.5}\text{Sb}_{10}$ also points at the presence of elemental Sn in the sample, as it displays a superconducting feature at < 5 K. The charge transport properties of the Mn-containing samples are similar, except that they exhibit a Schottky anomaly around 5 K. This anomaly is possibly due to the magnetic interactions introduced by Mn.

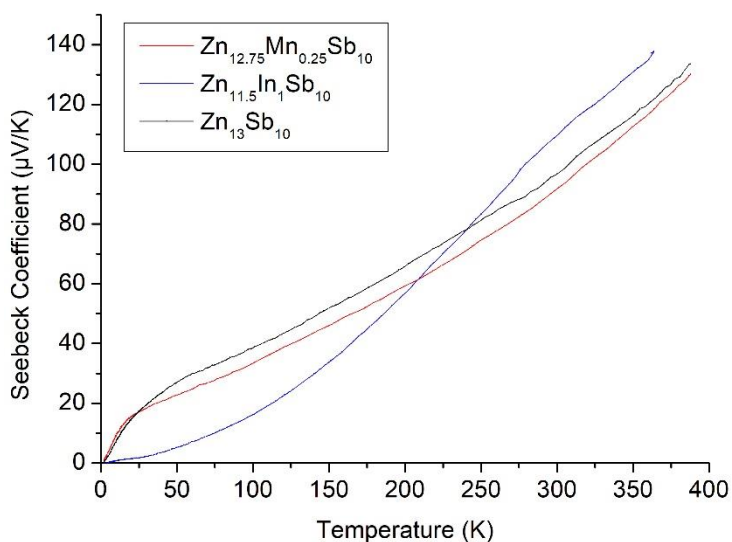


Figure 5.4. Seebeck coefficients of the selected samples.

The low-temperature Seebeck coefficients of $\text{Zn}_{13}\text{Sb}_{10}$, $\text{Zn}_{12.75}\text{Mn}_{0.25}\text{Sb}_{10}$ and $\text{Zn}_{11.5}\text{In}_1\text{Sb}_{10}$ are plotted in **Figure 5.4**. Seebeck coefficients of all the samples show a positive relationship with respect to temperature, in agreement with the Mott equation¹⁵²:

$$\alpha = \frac{8\pi^2 k_B^2}{3eh^2} m^* T \left(\frac{\pi}{3n}\right)^{\frac{2}{3}}$$

However, a linear relationship between the Seebeck coefficient and temperature, expected from the Mott formula, is truly obeyed only after 275 K.

The room-temperature carrier concentrations of $\text{Zn}_{13}\text{Sb}_{10}$, $\text{Zn}_{12.75}\text{Mn}_{0.25}\text{Sb}_{10}$, $\text{Zn}_{12.55}\text{Ga}_{0.3}\text{Sb}_{10}$, $\text{Zn}_{11.96}\text{Cd}_{1.04}\text{Sb}_{10}$ and $\text{Zn}_{11.5}\text{In}_1\text{Sb}_{10}$ were derived from the Hall measurements and are shown in **Table 5.7**. The carrier concentration of the $\text{Zn}_{12.75}\text{Mn}_{0.25}\text{Sb}_{10}$ sample is larger than that of the pristine $\text{Zn}_{13}\text{Sb}_{10}$ sample, but its carrier mobility is reduced, most likely due to the presence of the Mn atoms in the structure. The origin of the increased carrier concentration is not fully understood. If manganese is assumed to be Mn^{2+} in the structure, then the increased hole concentration (lower Fermi level) should stem from a larger Zn deficiency. EDS results indicate that the total metal amount in the $\text{Zn}_{12.75}\text{Mn}_{0.25}\text{Sb}_{10}$ sample is almost identical to that in the pristine $\text{Zn}_{13}\text{Sb}_{10}$ sample (**Table 5.1**). Another possibility is that Mn with its d^5 configuration acts as an electron acceptor when substituting for Zn (d^{10} configuration). This hypothesis will need to be verified through a detailed analysis of the band structure of the Mn-doped $\text{Zn}_{13}\text{Sb}_{10}$.

Table 5.7. Room temperature Hall carrier concentrations n_H (in cm^{-3}) and carrier mobilities μ_H (in $\text{cm}^2/(\text{V}\cdot\text{s})$) of pristine and doped $\text{Zn}_{13}\text{Sb}_{10}$ samples.

	$\text{Zn}_{13}\text{Sb}_{10}$	$\text{Zn}_{12.75}\text{Mn}_{0.25}\text{Sb}_{10}$	$\text{Zn}_{12.55}\text{Ga}_{0.3}\text{Sb}_{10}$	$\text{Zn}_{11.96}\text{Cd}_{1.04}\text{Sb}_{10}$	$\text{Zn}_{11.5}\text{In}_1\text{Sb}_{10}$
n_H	$8.3(2)\times 10^{19}$	$1.41(2)\times 10^{20}$	$1.76(3)\times 10^{20}$	$9.4(1)\times 10^{19}$	$8.36(7)\times 10^{19}$
μ_H	29.0(7)	18.3(2)	18.3(3)	16.9(2)	28.5(2)

The carrier concentration and mobility of the $\text{Zn}_{11.5}\text{In}_1\text{Sb}_{10}$ sample at room temperature are similar to those of the pristine $\text{Zn}_{13}\text{Sb}_{10}$ sample. This would be in line with the fact that the resistivity lines for the two samples cross at 304 K. However, the T dependences of resistivity and thermopower for the two samples are different from each other, which is likely due to the different values of the charge carrier effective mass and relaxation time. The effective mass for $\text{Zn}_{11.5}\text{In}_1\text{Sb}_{10}$ appears to be larger, as its thermopower slope is steeper. Based on the resistivity behavior, the relaxation time at the intermediate temperatures is larger for $\text{Zn}_{11.5}\text{In}_1\text{Sb}_{10}$, but then decreases rapidly at higher temperatures. Similar room-temperature values for the mobility, and consequently for the relaxation time, for $\text{Zn}_{11.5}\text{In}_1\text{Sb}_{10}$ and $\text{Zn}_{13}\text{Sb}_{10}$ are rather puzzling, as presence of larger In atoms is expected to enhance charge carrier scattering, as seen for other dopants.

The carrier mobility in the $\text{Zn}_{12.55}\text{Ga}_{0.3}\text{Sb}_{10}$ sample is lower than in the pristine $\text{Zn}_{13}\text{Sb}_{10}$ sample, which can be attributed to the Ga dopants acting as scatters for electron waves. However, its carrier concentration is larger and we cannot currently pinpoint the origin of such increase. Based on the EDS analysis (**Table 5.3**) and assuming Ga^{3+} , the $\text{Zn}_{12.55}\text{Ga}_{0.3}\text{Sb}_{10}$ sample should possess more electrons and thus less holes than the pristine $\text{Zn}_{13}\text{Sb}_{10}$ sample. This contradiction may question the accuracy of the elemental analysis or suggests that Ga acts as an electron acceptor in the $\text{Zn}_{13}\text{Sb}_{10}$ structure.

The $\text{Zn}_{11.96}\text{Cd}_{1.04}\text{Sb}_{10}$ sample has a slightly higher carrier concentration than that of the pristine sample. In fact, one should not expect any significant changes if the total metal

amount remains the same since Cd has the same oxidation state as Zn. The Cd-doping however effectively lowers the carrier mobility of the sample by impurity scattering.

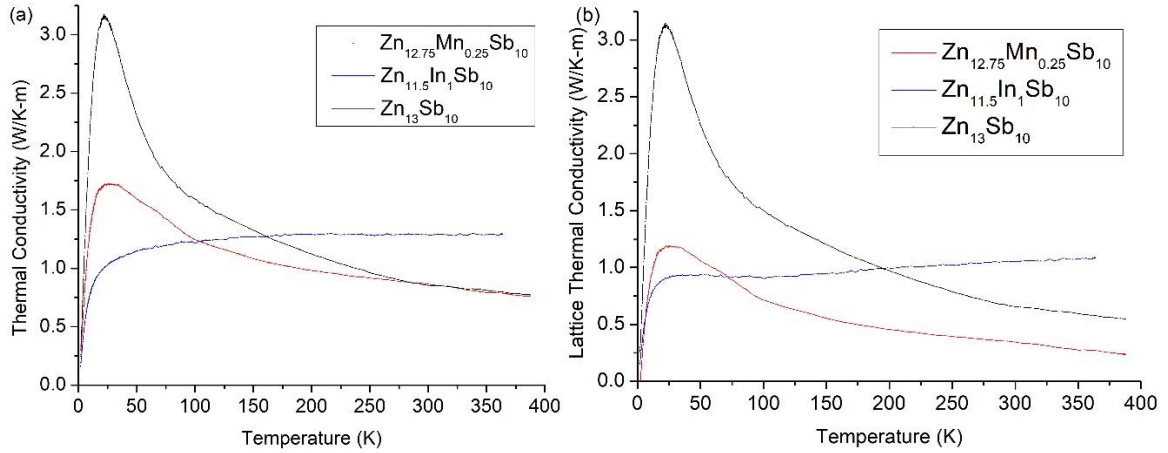


Figure 5.5. Low temperature total thermal conductivities (a) and calculated lattice thermal conductivities (b) of $\text{Zn}_{13}\text{Sb}_{10}$, $\text{Zn}_{11.5}\text{In}_1\text{Sb}_{10}$ and $\text{Zn}_{12.75}\text{Mn}_{0.25}\text{Sb}_{10}$ sample.

Thermal conductivities of $\text{Zn}_{13}\text{Sb}_{10}$, $\text{Zn}_{11.5}\text{In}_1\text{Sb}_{10}$ and $\text{Zn}_{12.75}\text{Mn}_{0.25}\text{Sb}_{10}$ at low temperatures are plotted in **Figure 5.5(a)**. The lattice thermal conductivities κ_l of the samples were calculated using $\kappa_l = \kappa_{total} - \kappa_e$, where κ_{total} is the total thermal conductivity and κ_e is the electronic contribution. κ_e is calculated using the Wiedemann-Franz law, $\kappa_e = LT/\rho$, where L is the Lorenz number. The Lorenz number was estimated according to $L \approx 1.5 + \exp[-|\alpha|/116]$, with α being the Seebeck coefficient (L is in the unit of $10^{-8} \text{ W}\Omega/\text{K}^2$ and α is in units of $\mu\text{V}/\text{K}$)¹⁵³. As discussed in our previous work (Chapter 4)¹⁵⁹, the In-substituted sample has a higher thermal conductivity at elevated temperatures due to the change in the phonon scattering pathway, from the temperature-dependent Umklapp scattering in the pristine $\text{Zn}_{13}\text{Sb}_{10}$ to the temperature-independent point defect scattering in

the $\text{Zn}_{11.5}\text{In}_1\text{Sb}_{10}$ sample. This is related to a significant upturn in defects (larger In atoms and more vacancies in the structure). In the case of the Mn-containing sample, the scattering pathways of the pristine $\text{Zn}_{13}\text{Sb}_{10}$ sample are mostly preserved. However, in comparison to $\text{Zn}_{13}\text{Sb}_{10}$, the $\text{Zn}_{12.75}\text{Mn}_{0.25}\text{Sb}_{10}$ sample exhibits a suppressed boundary scattering at lower temperatures and enhanced Umklapp scattering at elevated temperatures. Thus there is no change in the dominant scattering pathway in $\text{Zn}_{12.75}\text{Mn}_{0.25}\text{Sb}_{10}$, which is beneficial to its thermoelectric performance. Similarly, the dominant scattering pathway in the Cd-doped $\text{Zn}_{13}\text{Sb}_{10}$ is preserved, while that in the Ga-doped $\text{Zn}_{13}\text{Sb}_{10}$ is changed, deduced from the high-temperature thermal conductivities of the doped samples in **Figures 5.S1** and **5.S2** (supplied in supplementary information). The change in the dominant scattering pathway in $\text{Zn}_{11.5}\text{In}_1\text{Sb}_{10}$ and in $\text{Zn}_{12.55}\text{Ga}_{0.3}\text{Sb}_{10}$ is under investigation.

The power factors and zT values of $\text{Zn}_{13}\text{Sb}_{10}$, $\text{Zn}_{11.5}\text{In}_1\text{Sb}_{10}$ and $\text{Zn}_{12.75}\text{Mn}_{0.25}\text{Sb}_{10}$ are plotted in **Figure 5.6 (a)** and **(b)**. The doped samples have higher power factors than the pristine $\text{Zn}_{13}\text{Sb}_{10}$ at high temperatures. The boost in the power factor of $\text{Zn}_{12.75}\text{Mn}_{0.25}\text{Sb}_{10}$ originates from its lower electrical resistivity since the Seebeck coefficient is similar to that of the pristine sample. The thermal conductivity of $\text{Zn}_{12.75}\text{Mn}_{0.25}\text{Sb}_{10}$ is also similar, thus an increase in its zT value is due to the improved electrical conductivity. In case of $\text{Zn}_{11.5}\text{In}_1\text{Sb}_{10}$, the power factor is above that of the pristine sample, however its high thermal conductivity, brought by the weakened Umklapp scattering, leads to a lower thermoelectric figure-of-merit.

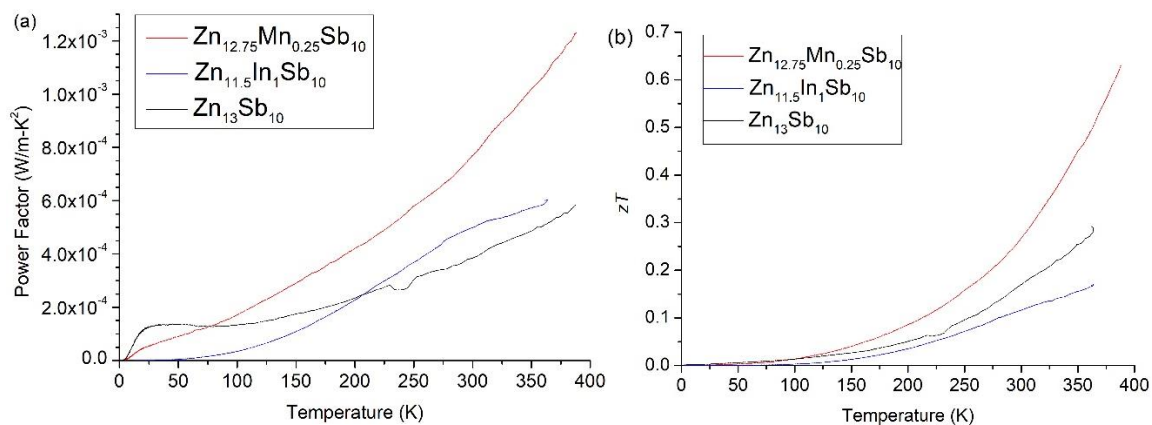
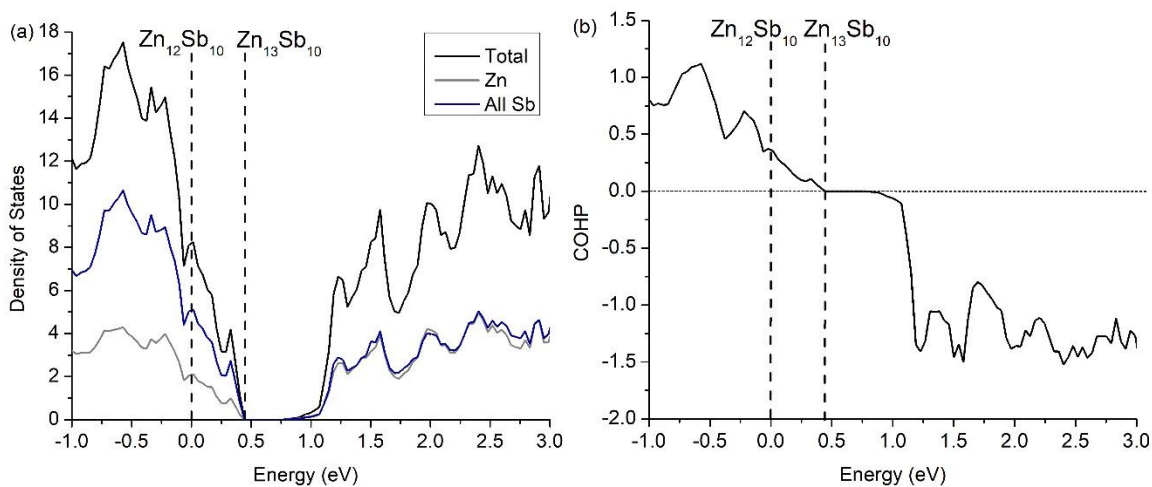


Figure 5.6. Power factors (a) and Thermoelectric figure-of-merit zT (b) of $\text{Zn}_{13}\text{Sb}_{10}$, $\text{Zn}_{11.5}\text{In}_1\text{Sb}_{10}$ and $\text{Zn}_{12.75}\text{Mn}_{0.25}\text{Sb}_{10}$ sample.

5.3.5. Electronic Band Structure and Bonding Characters



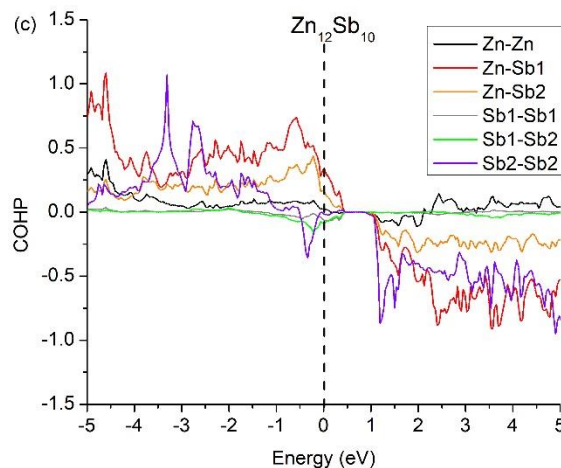


Figure 5.7. (a) Total and partial DOS of the $\text{Zn}_{13}\text{Sb}_{10}$ material, calculated for the ordered $\text{Zn}_{12}\text{Sb}_{10}$ structural motif of the $\text{Zn}_{13}\text{Sb}_{10}$ phase. (b) Total COHP plot. (c) Partial COHP plots of $\text{Zn}_{12}\text{Sb}_{10}$, depicting interactions between the three sites. The Fermi level of $\text{Zn}_{12}\text{Sb}_{10}$ is set at 0. The energy difference between the Fermi levels of $\text{Zn}_{12}\text{Sb}_{10}$ and $\text{Zn}_{13}\text{Sb}_{10}$ is ~ 0.44 eV.

The Density of States (DOS) plot of $\text{Zn}_{13}\text{Sb}_{10}$ was reported earlier⁹⁴ and is shown again in **Figure 5.7(a)**. The electronic structure was calculated for the $\text{Zn}_{12}\text{Sb}_{10}$ composition with fully ordered structure. The Fermi level (set at 0 eV) is located in the valence band for the $\text{Zn}_{12}\text{Sb}_{10}$ composition. The valence band is filled at exactly 2 more electrons, corresponding to the $\text{Zn}_{13}\text{Sb}_{10}$ composition. The Crystal Orbital Hamiltonian Population (COHP) analysis is presented in **Figures 5.7(b)** and **(c)**. The full COHP (**Figure 5.7(b)**) shows an overall bonding character and an antibonding one above the band gap. The antibonding character above the band gap suggests that it may be difficult (if not impossible) to obtain an *n*-type $\text{Zn}_{13}\text{Sb}_{10}$. On the other hand, the overall positive bonding character till the band gap suggests that the origin of the Zn deficiency in this material is

not electronic in nature. Among the interactions present in the $\text{Zn}_{13}\text{Sb}_{10}$ structure (**Figure 5.7(c)**), only Sb2-Sb2 dimers have significant antibonding contribution below the Fermi level. Those interactions are clearly outweighed by other bonding interactions and thus are unlikely to be consequential for the Zn deficiency. A computational study by G. S. Pomrehn *et al.* suggested that the $\text{Zn}_{13}\text{Sb}_{10}$ material is thermodynamically stabilized through the combination of the lower formation enthalpy of the crystallographically disordered $\text{Zn}_{13}\text{Sb}_{10}$ (compared to $\text{Zn}_{12}\text{Sb}_{10}$, $\text{Zn}_{14}\text{Sb}_{10}$, and $\text{Zn}_{15}\text{Sb}_{10}$) and the vibrational free energy of the lattice¹⁵⁴.

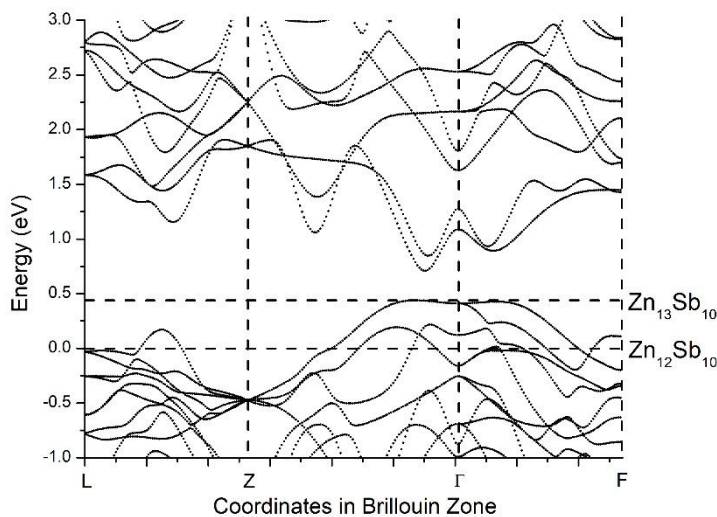


Figure 5.8. Electronic band structure of the $\text{Zn}_{13}\text{Sb}_{10}$ material calculated from the $\text{Zn}_{12}\text{Sb}_{10}$ structural motif.

The band structure of the material is shown in **Figure 5.8**. Assuming the Fermi level of $\text{Zn}_{13}\text{Sb}_{10}$ material lies between 0 eV and the top of the valence band, the material displays a multi-band feature around the gamma point (Γ), and has a slight indirect band

gap of ~ 0.27 eV next to Γ , similar to that reported by Qiu *et al.*¹⁶⁶. On the other hand Tapiero *et al.* reported an optical band gap of ~ 1.2 eV based on a reflectivity measurement¹⁶⁷. The flat bands at the top of valence band suggest heavy charge carriers if the Fermi level sits at that region, i.e. if Zn deficiency is low. On the other hand, if Zn-deficiency is larger, one may expect lighter charge carriers, provided the band features are preserved.

The experimental bandgap of the material (E_g) could be estimated¹⁶⁸ by observing the maximum in the Seebeck coefficient:

$$E_g = 2\alpha_{max}T_{max} \text{ (in eV)},$$

with α_{max} being the maximum Seebeck coefficient at temperature, T_{max} . Assuming the calculated 0.27 eV bandgap and extrapolating the Seebeck coefficient with a linear relationship ($\alpha = (4.065 \times 10^{-7})T - 2.528 \times 10^{-5}$) at higher temperatures, the maximum Seebeck coefficient of the undoped $Zn_{13}Sb_{10}$ sample is expected around 608 K. In the literature, however, Seebeck effect measurements on the polycrystalline “ Zn_4Sb_3 ” materials do not show a maximum at such temperature, therefore suggesting that the true bandgap of the material is larger than 0.27 eV found in our LMTO calculations^{169–172}. Also, $Zn_{13}Sb_{10}$ starts to decompose by losing Zn around 700 K, which restricts high-temperature thermopower measurements.

5.3.6. Estimation of Carrier Effective Mass of the $Zn_{13}Sb_{10}$ Materials

A single parabolic band (SPB) model was used to evaluate the carrier effective

masses of the $\text{Zn}_{13}\text{Sb}_{10}$, $\text{Zn}_{12.75}\text{Mn}_{0.25}\text{Sb}_{10}$ and $\text{Zn}_{11.5}\text{In}_1\text{Sb}_{10}$ samples at 300 K. This approach is an approximation as the calculated electronic band structure of the pristine $\text{Zn}_{13}\text{Sb}_{10}$ (**Figure 5.8**) indicates doubly degenerate, flat-like bands at the top of the valence band (valley degeneracy, $N_v \neq 1$). The experimental carrier concentrations and Seebeck coefficients of the samples were used to calculate the carrier effective mass through the Pisarenko plot by obtaining the density of state effective mass¹⁷³, as shown in **Figure 5.9**. The Mn- and In-doped $\text{Zn}_{13}\text{Sb}_{10}$ materials have higher carrier effective masses than the pristine $\text{Zn}_{13}\text{Sb}_{10}$ material. An increase in the effective mass for $\text{Zn}_{12.75}\text{Mn}_{0.25}\text{Sb}_{10}$ is likely associated with the presence of the flat d bands around the Fermi level. On the other hand, the origin of the increased effective mass in $\text{Zn}_{11.5}\text{In}_1\text{Sb}_{10}$ is not immediately clear, considering very similar carrier concentrations for $\text{Zn}_{13}\text{Sb}_{10}$ and $\text{Zn}_{11.5}\text{In}_1\text{Sb}_{10}$ and potentially similar band structures.

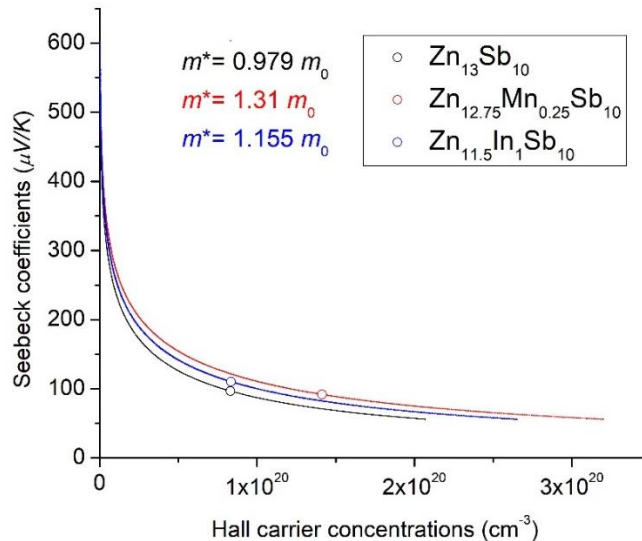


Figure 5.9. Pisarenko plots for the $\text{Zn}_{13}\text{Sb}_{10}$, $\text{Zn}_{12.75}\text{Mn}_{0.25}\text{Sb}_{10}$ and $\text{Zn}_{11.5}\text{In}_1\text{Sb}_{10}$ sample at 300 K.

5.4. Conclusions

A pure $\text{Zn}_{13}\text{Sb}_{10}$ material could be synthesized using a slow-cooling method, with the charge-precise $\text{Zn}_{13}\text{Sb}_{10}$ loading composition. This approach eliminates any detectable Zn impurities and thus provides a more reliable analysis of the $\text{Zn}_{13}\text{Sb}_{10}$ -based phases. The survey of dopants for the Zn site reveals the preferences for the atoms that can adopt a tetrahedral coordination environment of the Zn site. The incorporations of dopants effectively restrict the movement of Zn atoms, as evident from the suppressed phase transitions at 230 – 250 K. The dopants also affect the charge carrier properties (concentration, mobility, effective mass) and phonon propagation. Generally, the carrier mobility in the doped $\text{Zn}_{13}\text{Sb}_{10}$ materials is lowered due to the impurity scattering, which decreased the carrier relaxation times. The carrier effective mass in the studied samples is increased, but the origin of such an increase is specific to the dopant.

Dopant incorporation may affect the dominant phonon scattering pathway and even increase the lattice contribution to the thermal conductivity at higher temperatures. For example, the defect scattering dominant in the In-doped $\text{Zn}_{13}\text{Sb}_{10}$ does not disrupt phonon propagation as effectively as the Umklapp scattering in the pristine and Mn-doped $\text{Zn}_{13}\text{Sb}_{10}$. As a result, the In-doped $\text{Zn}_{13}\text{Sb}_{10}$ shows a lower thermoelectric figure-of-merit than pristine $\text{Zn}_{13}\text{Sb}_{10}$, despite having a higher power factor. Therefore, it is crucial to maintain the Umklapp scattering as the dominant phonon scattering pathway when optimizing the power factor of the $\text{Zn}_{13}\text{Sb}_{10}$ -based materials through doping.

The electronic band structure calculations of the $\text{Zn}_{13}\text{Sb}_{10}$ material indicate that the Zn deficiency in $\text{Zn}_{13}\text{Sb}_{10}$ cannot be explained by the bonding consideration. Instead, the Zn-deficient $\text{Zn}_{13}\text{Sb}_{10}$ phase is stabilized by a configurational disorder and vibrational free energy of the lattice.

5.5. Supplementary Materials

The high-temperature total and lattice thermal conductivities of the selected samples are plotted in **Figure 5.S1** and **5.S2**. The thermal conductivities of the Mn- and In- $\text{Zn}_{13}\text{Sb}_{10}$ sample at lower temperatures measured by the laser flash analysis (LFA) method agree with those from the Quantum Design Physical Property Measurement System (PPMS) at similar temperature ranges.

The retentions/changes in the dominant phonon scattering pathways in the doped materials can be deduced from the LFA thermal conductivities. Similar to the In- $\text{Zn}_{13}\text{Sb}_{10}$ sample, the Ga-doped sample shows a change in the dominant phonon scattering pathway, as reflected by the elevated thermal conductivity when compared to the undoped $\text{Zn}_{13}\text{Sb}_{10}$ sample. On the other hand, the dominant phonon scattering pathways in the Mn- and Cd-doped samples remain the same. Additionally, the thermal conductivities of the Ga- and In-doped $\text{Zn}_{13}\text{Sb}_{10}$ samples decrease at elevated temperatures, which is due to the increased Umklapp scattering in this temperature range.

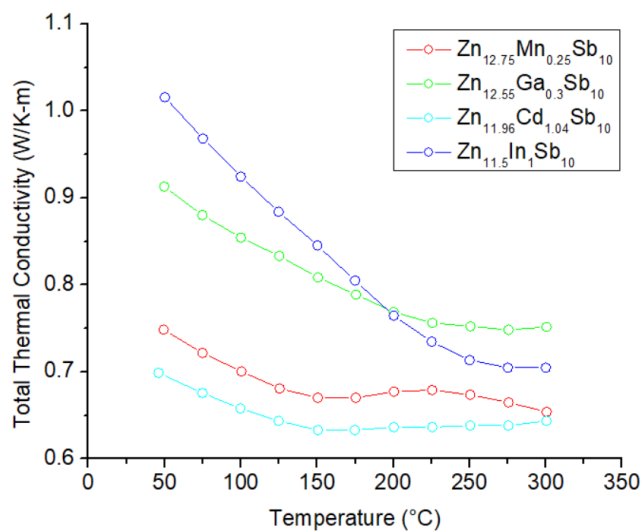


Figure 5.S1. High-temperature total thermal conductivities of the $\text{Zn}_{12.75}\text{Mn}_{0.25}\text{Sb}_{10}$, $\text{Zn}_{12.55}\text{Ga}_{0.3}\text{Sb}_{10}$, $\text{Zn}_{11.96}\text{Cd}_{1.04}\text{Sb}_{10}$ and $\text{Zn}_{11.5}\text{In}_1\text{Sb}_{10}$ samples.

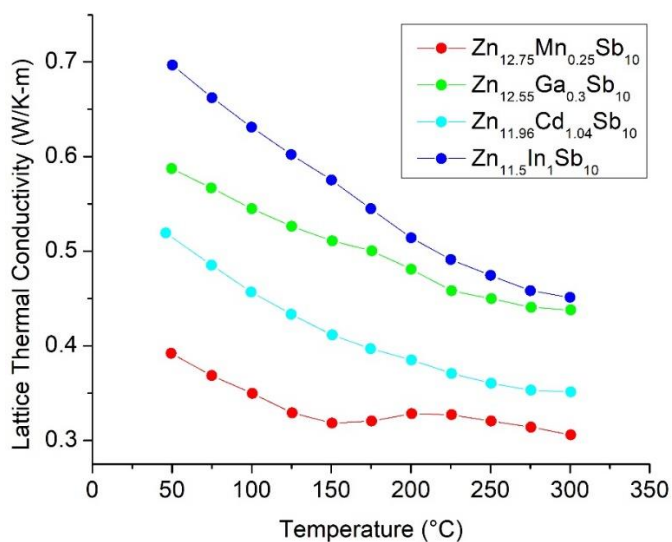


Figure 5.S2. Calculated high-temperature lattice thermal conductivities of the $\text{Zn}_{12.75}\text{Mn}_{0.25}\text{Sb}_{10}$, $\text{Zn}_{12.55}\text{Ga}_{0.3}\text{Sb}_{10}$, $\text{Zn}_{11.96}\text{Cd}_{1.04}\text{Sb}_{10}$ and $\text{Zn}_{11.5}\text{In}_1\text{Sb}_{10}$ samples.

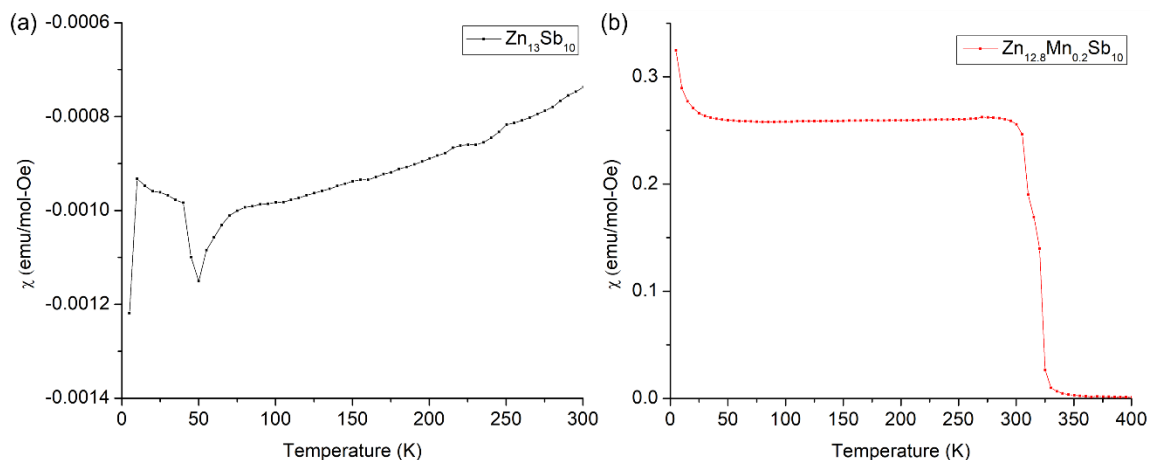


Figure 5.S3. Magnetic susceptibility χ vs. temperature T of (a) the pristine $\text{Zn}_{13}\text{Sb}_{10}$ and (b) the $\text{Zn}_{12.8}\text{Mn}_{0.2}\text{Sb}_{10}$ sample.

The magnetic susceptibility vs. temperature of the pristine $\text{Zn}_{13}\text{Sb}_{10}$ and the $\text{Zn}_{12.8}\text{Mn}_{0.2}\text{Sb}_{10}$ sample were measured using the superconducting quantum interference device (SQUID) on the magnetic property measurement system (MPMS), and are plotted in **Figure 5.S3**. A diamagnetic behaviour is expected in the pristine $\text{Zn}_{13}\text{Sb}_{10}$ sample, while a paramagnetic behaviour is expected if Mn is incorporated into the $\text{Zn}_{13}\text{Sb}_{10}$ structure. The χ in the pristine $\text{Zn}_{13}\text{Sb}_{10}$ sample confirms the diamagnetic behaviour in the pristine $\text{Zn}_{13}\text{Sb}_{10}$ sample. On the other hand, the χ in the $\text{Zn}_{12.8}\text{Mn}_{0.2}\text{Sb}_{10}$ sample has displayed a ferromagnetic behaviour with T_c around 320 K and a paramagnetic tail below 25 K. This suggests that some Mn is incorporated into the $\text{Zn}_{13}\text{Sb}_{10}$ structure, while the $\text{SbMn}_{0.89}\text{Zn}_{0.94}$ impurity phase is responsible for the ferromagnetic behaviour, where it is reported to have a similar T_c .¹⁷⁴ Although this confirms the Mn incorporation into the $\text{Zn}_{13}\text{Sb}_{10}$ structure, at the same time this suggests that the $\text{Zn}_{12.8}\text{Mn}_{0.2}\text{Sb}_{10}$ sample is not truly phase pure, and the amount of Mn incorporation is less than expected.

Chapter 6. Comparative Study of the $\text{Zn}_{1-x}\text{Cd}_x\text{Sb}$ and $(\text{Zn}_{1-z}\text{Cd}_z)_{13}\text{Sb}_{10}$ Solid Solution Series

This chapter contains the material covered in the manuscript “Comparative Study of the $\text{Zn}_{1-x}\text{Cd}_x\text{Sb}$ and $(\text{Zn}_{1-z}\text{Cd}_z)_{13}\text{Sb}_{10}$ Solid Solution Series”, which was published in *Journal of Solid State Chemistry (J. Solid State Chem., 2022, 315, 123448)*. The low temperature physical property measurements were collected by Dr. Taras Kolodiazhnyi at the National Institute for Materials Science (NIMS), Tsukuba, Ibaraki, Japan, Michel Johnson at Dalhousie University, Halifax, Nova Scotia, Canada and Subin Kim at the University of Toronto, Toronto, Ontario, Canada. The high temperature charge transport properties and partial room temperature carrier concentration of materials were collected by Dr. Yu-Chih Tseng at CanmetMATERIALS, Natural Resources of Canada, Hamilton, Ontario, Canada. Partial Single-crystal X-ray diffraction data were collected by Dr. James F. Britten. The ELF method was calculated by Dr. Jan-Hendrik Pöhls. The experimental procedures, structure determination, data interpretation and manuscript preparation were completed by the candidate.

Reproduced with permission from Michel Johnson, Jan-Hendrik Pöhls, Taras Kolodiazhnyi, James F. Britten, Yu-Chih Tseng, Yuriy Mozharivskyj, *Journal of Solid State Chemistry*.
Copyright 2022 Elsevier Inc..

Comparison of the $(\text{Zn}_{1-z}\text{Cd}_z)_{13}\text{Sb}_{10}$ and $\text{Zn}_{1-x}\text{Cd}_x\text{Sb}$ series allows better understanding of changes in the transport properties brought by the Cd substitution. Incorporation of a single dopant affects charge transport properties non-monotonously, and these changes are likely dependent on the intrinsic properties of the main phase. The dominant phonon scattering pathway in both solution series remains the Umklapp process even when the Zn:Cd ratio is 1:1, contrary to the expected point defect scattering. Lastly, the electron localization function (ELF) calculations suggested that the bonding character in ZnSb and $\text{Zn}_{13}\text{Sb}_{10}$ is well-described using the Zintl-Klemm concept, as a mix of covalent and ionic interactions.

6.1. Introduction

A considerable amount of work has been done to understand the thermoelectric properties of the ZnSb and “ Zn_4Sb_3 ” materials^{91–93,95,96,175–178}, thereby allowing us to use them as models and to explore the ways to improve thermoelectric performances of other materials. The $\text{Zn}_{13}\text{Sb}_{10}$ material has the α' , α and β polymorphs^{93,94}, and the room temperature β - $\text{Zn}_{13}\text{Sb}_{10}$ (above 254 K) is the thermoelectric phase of interest. β - $\text{Zn}_{13}\text{Sb}_{10}$ features an extraordinarily low thermal conductivity, with electrical resistivity similar to a heavily-doped semiconductor, resulting a zT of 1.3 at 670 K^{90,136}. On the other hand, ZnSb also features a low thermal conductivity, with electrical resistivity higher than that of β - $\text{Zn}_{13}\text{Sb}_{10}$, with a resulting zT of 0.6 at 460 K¹⁷⁹. There are some discrepancies in the literature about the bonding nature of these Zn-Sb phases, some describe them using the

Zintl-Klemm formalism^{92,179,180}, while some describe them as “electron-poor framework semiconductors” (EPFS)¹⁸¹.

In this work, Zn is replaced with Cd in the ZnSb and Zn₁₃Sb₁₀ structures. Cd is chosen for incorporation mainly due to the relative ease of syntheses and the existences of the Cd analogues for both phases: CdSb and Cd₁₃Sb₁₀^{164,182}, although a formation of superstructure was found in Cd₁₃Sb₁₀. Cd incorporation into ZnSb and Zn₁₃Sb₁₀ (“Zn₄Sb₃”) has been explored separately earlier^{137,183–185}, usually in small amounts, while CdSb has been studied recently as an emerging thermoelectric material^{186,187}. In this work, we aim to understand the effects to the transport properties brought by the same atom replacement (Cd is replacing for Zn) in two crystal systems. Regarding the bonding nature in the ZnSb material, the Electron Localization Function (ELF) method was used to elucidate bonding interactions between the atoms.

6.2. Materials and Methods

6.2.1. Synthesis

Pieces of elemental Zn (99.99 wt. % CERAC), Cd (99.99 wt. % 5N Plus) and Sb (99.999 wt. % 5N Plus) were used as starting materials, following the loading formulae Zn_{1-x}Cd_xSb and (Zn_{1-z}Cd_z)₁₃Sb₁₀ ($x, z = 0, 0.2, 0.4, 0.6, 0.8, 1$). The weighted elements were sealed in the evacuated silica tubes and placed in the same box furnace to eliminate temperature variances.

For the (Zn_{1-z}Cd_z)₁₃Sb₁₀ samples, the samples were heated to 750 °C at 150 °C/h and annealed for 16 h, while being shaken in between to ensure mixing of the molten

elements. The samples were cooled from 750 °C to 350 °C at a rate of 50 °C/h and annealed at 350 °C for 2 days to achieve phase homogeneity. The samples were finally cooled down to room temperature at a rate of 50 °C/h. Similarly, for the $Zn_{1-x}Cd_xSb$ samples, the samples were heated to 750 °C at 150 °C/h and annealed for 16 h, being shaken in between. The samples were cooled from 750 °C to 400 °C at a rate of 50 °C/h and annealed at 400 °C for 2 days before cooling down to room temperature at a rate of 50 °C/h.

The $Zn_{1-x}Cd_xSb$ samples were ground in an agate mortar, loaded in graphite dies (15 mm ID) and pressed into pellets using the Spark Plasma Sintering method (SPS) with a Dr. Sinter SPS 211 Lx instrument. A pressure of 45 MPa was applied to all samples; they were heated to the sintering temperatures at a rate of 50 K/min and sintered for 25 min. The samples were finally cooled down to room temperature without pressure and current. The sintering temperatures of samples are shown in **Table 6.1**.

Table 6.1. SPS temperatures of the $Zn_{1-x}Cd_xSb$ samples.

Sample composition	Sintering temperature (K)
ZnSb	450
$Zn_{0.8}Cd_{0.2}Sb$	420
$Zn_{0.6}Cd_{0.4}Sb$	420
$Zn_{0.4}Cd_{0.6}Sb$	400
$Zn_{0.2}Cd_{0.8}Sb$	380
CdSb	380

Large bulk $(Zn_{1-z}Cd_z)_{13}Sb_{10}$ samples and $Zn_{1-x}Cd_xSb$ SPS pellets were cut into bars and plates for physical property measurements.

6.2.2. Powder and single crystal X-ray diffraction

Powder X-ray diffraction (PXRD) data for the polycrystalline samples were collected on a PANalytical X'Pert Pro CuK α_1 diffractometer with an X'Celerator detector. Samples were ground and deposited evenly on a zero-background silicon sample holder. The data were collected in the $20 - 80^\circ 2\theta$ range with the collection time of 1 hour. Phase purity and unit cell parameters were evaluated by full-profile Rietveld refinements, using the Rietica program¹¹¹.

Room temperature single-crystal data for a crystal picked from the bulk Cd₁₃Sb₁₀ sample were collected on a Bruker SMART APEX II diffractometer with a 3 kW sealed-tube Mo generator and APEX II CCD detector at the McMaster Analytical X-Ray (MAX) Diffraction Facility. A semi-empirical absorption correction was applied using redundant and symmetry related data. Structural determinations and refinements were performed using the OLEX2 program¹⁶⁰.

6.2.3. Elemental analysis

Semi-quantitative elemental analysis was performed using an X-Max (80mm²) X-ray EDS spectrometer (Oxford Instruments) on a TESCAN VEGA II LSU scanning electron microscope (SEM) (20 kV accelerating voltage).

6.2.4. Physical property measurements

The melted (Zn_{1-z}Cd_z)₁₃Sb₁₀ ($z = 0, 0.2, 0.4, 0.6, 0.8, 1$) and SPS Zn_{1-x}Cd_xSb ($x = 0, 0.2, 0.4, 0.6, 0.8, 1$) samples were cut into approximately $2 \times 2 \times 9$ mm³ bar and $10 \times 10 \times$

1 mm³ plates using a diamond saw and kerosene as lubricant to avoid sample oxidation. The carrier concentration at room temperature, n , was derived from the Hall coefficient measured on a home-built instrument with a GMW 5403 electromagnet. The room temperature resistivity was also measured on this instrument using the Van der Pauw method. A separate set of the $(\text{Zn}_{1-z}\text{Cd}_z)_{13}\text{Sb}_{10}$ ($z = 0, 0.5, 1$) and the SPS $\text{Zn}_{1-x}\text{Cd}_x\text{Sb}$ ($x = 0, 0.5, 1$) samples were cut into $4 \times 4 \times 4$ mm³ cubes, and the electrical resistivities, Seebeck coefficients, thermal conductivities and heat capacities were measured using a Quantum Design Physical Property Measurement System (PPMS). Note that some measurements on $\text{Zn}_{13}\text{Sb}_{10}$ were published previously¹⁸⁸.

6.2.5. Electronic structure calculations

The total density of states (DOS) and electronic band structures of the $\text{Zn}_{13}\text{Sb}_{10}$, $(\text{Zn}_{0.5}\text{Cd}_{0.5})_{13}\text{Sb}_{10}$, $\text{Cd}_{13}\text{Sb}_{10}$, ZnSb , $(\text{Zn}_{0.5}\text{Cd}_{0.5})\text{Sb}$ and CdSb were calculated using the TB-LMTO-ASA method¹⁶². The $\text{Zn}_{12}\text{Sb}_{10}$ structural motif of the room temperature β - $\text{Zn}_{13}\text{Sb}_{10}$ phase was used in the calculation for the $(\text{Zn}_{1-z}\text{Cd}_z)_{13}\text{Sb}_{10}$ materials, despite the superstructure in the $\text{Cd}_{13}\text{Sb}_{10}$ sample. Empty spheres were included into the unit cell to fulfill the overlap criteria of atomic spheres in the TB-LMTO-ASA method. A $16 \times 16 \times 16$ k grid is used for both solid solution series, and the basis sets consisted of the Zn 4s/4p/3d, Cd 5s/5p/4d/4f and Sb 5s/5p/4d/4f orbitals, where the Cd 4f and Sb 4d/4f orbitals were downfolded.

6.2.6. Electron Localization Function (ELF)

The electron localization function (ELF) of ZnSb was computed using the post processing package in the Quantum ESPRESSO¹⁸⁹ with the Perdew-Burke-Ernzerhof (PBE) generalized gradient approximation (GGA)¹⁹⁰ and the projector augmented-wave (PAW) method. The cut-off energy of the wavefunction (charge density) was set to 50 (600) Ry and a cold smearing of 0.001 Ry was applied. Spin-orbit coupling was included into the calculations. Prior to the ELF calculations, the ZnSb structure was fully relaxed using a Γ -centered $5 \times 5 \times 5$ k -point mesh and force (energy) threshold of 10^{-5} Ry Bohr⁻¹ (10^{-9} Ry). ELF was calculated on a $128 \times 128 \times 128$ mesh with a b-spline interpolation, and heat maps of the ELF were drawn to dissect parallel to the Zn₂Sb₂ rhomboid ring to gain an advanced understanding of its bonding character.

6.3. Results and Discussion

6.3.1. Characterization

PXRD patterns of the as-synthesized Zn_{1-x}Cd_xSb (all except $x = 0$ and 1) samples suggest inhomogeneity (varying Zn/Cd ratios) in the materials, as witnessed from the presence of double peaks (**Figure 6.S1** in supplementary information). The inhomogeneity features disappear either after SPS, or after a reannealing the cold pressed sample. The experimental powder X-ray pattern of the Cd₁₃Sb₁₀ sample show significant peak-splitting behaviour (**Figure 6.S2**), suggesting a symmetry reduction in the crystal structure. Analysis of the single crystal diffraction data for Cd₁₃Sb₁₀ indicated the presence of a superstructure. An automatic indexing of the superstructure reflections yielded a large monoclinic cell with $a = 11.44$ Å, $b = 26.05$ Å, $c = 26.05$ Å and $\beta = 100.74^\circ$. A superstructure in the Pn space group with similar cell parameters was reported earlier by S. Ponou et al.¹⁹¹.

Table 6.2. Single crystal X-ray diffraction and refinements of the grain from the Cd₁₃Sb₁₀ melted ingot sample. Data were collected on a Bruker SMART APEX II diffractometer with a 3 kW sealed-tube Mo generator and APEX II CCD detector at room temperature.

Sample	Cd ₁₃ Sb ₁₀	
Refined composition	Cd ₁₃ Sb ₁₀	
Space group	<i>P2₁/n</i>	
Lattice Parameters (Å)	<i>a</i> = 11.4696(3) <i>b</i> = 26.1217(6) <i>c</i> = 26.1066 (6)	<i>β</i> = 100.738(1)°
Volume (Å ³)	7684.7(3)	
Z	12	
Density (calculated), g/cm ³	6.949	
2θ range for data collection (°)	2.22 to 74.46	
Index Ranges	-19 ≤ <i>h</i> ≤ 19, -44 ≤ <i>k</i> ≤ 44, -44 ≤ <i>l</i> ≤ 44	
Independent reflections	406878 [R(int) = 0.0954]	
Completeness to max 2θ	99.5 %	
Data/restraints/parameters	39535/0/663	
Goodness-of-fit of F ²	1.174	
Final R indices [I > 2σ(I)]	R ₁ = 0.0858, wR ₂ = 0.1291	
R indices (all data)	R ₁ = 0.1590, wR ₂ = 0.1497	
Extinction coefficient	0.0000052(8)	
Largest diff. peak/hole, e ⁻ /Å ³	5.305/ -7.354	

The obtained structural model for Cd₁₃Sb₁₀ has the *P2₁/n* space group, which is a supergroup of the *Pn* space group, with an additional inversion centre. Crystallographic parameters and refinement results for the Cd₁₃Sb₁₀ sample are summarized in **Table 6.2**. Atomic and isotropic displacement (*U*_{eq}) parameters are presented in **Table 6.S1**. Note the relatively high residual electron densities, which are located close to the already assigned

atoms. The obtained data can be also refined with the Pn space group with the twin law (-1 0 0 0 -1 0 0 0 -1), and $BASF = 0.5(1)$.

We have also checked the possibility of $Cd_{13}Sb_{10}$ adopting the structure of the low-temperature $Zn_{13}Sb_{10}$ phase⁹²⁻⁹⁴ ($C2/c$ space group), and that the current unit cell results from twinning of the $C2/c$ structure. Rietveld refinements of the $Cd_{13}Sb_{10}$ samples with two different structural models ($P2_1/n$ and $C2/c$) are presented in **Figure 6.S3**. The refinement with the $C2/c$ symmetry does not describe the small peaks (e.g. at $\sim 31^\circ$ and 33° , labelled with *), and these small peaks belong to neither Cd nor CdSb. The Rietveld refined unit cell parameters for the $C2/c$ space group are: $a = 11.4547(5)$ Å, $b = 13.0490(6)$ Å, $c = 8.6947(4)$ Å, $\beta = 100.728(3)^\circ$. The $P2_1/n$ superstructure cell has the unit cell parameters roughly equal to a , $2 \times b$, $3 \times c$ of the $C2/c$ cell. This comparison demonstrates that the $P2_1/n$ structure observed during the single crystal diffraction does not result from the twinning of the smaller $C2/c$ cell.

Table 6.3. Elemental compositions (in at. %) and chemical formulae of the $Zn_{1-x}Cd_xSb$ (left) and $(Zn_{1-z}Cd_z)_{13}Sb_{10}$ (right) solid solution series.

Sample	Elemental composition	Formula	Sample	Elemental composition	Formula
$x = 0$	Zn (49.4(6)) Sb (50.6(3))	$Zn_{0.98}Sb$	$z = 0$	Zn (54.5(6)) Sb (45.5(3))	$Zn_{11.98}Sb_{10}$
$x = 0.2$	Zn (39.3(6)) Cd (9.0(3)) Sb (51.7(3))	$Zn_{0.76}Cd_{0.17}Sb$	$z = 0.2$	Zn (45.4(6)) Cd (9.4(3)) Sb (45.2(3))	$(Zn_{0.83}Cd_{0.17})_{12.12}Sb_{10}$
$x = 0.4$	Zn (27.1(6)) Cd (21.8(3)) Sb (51.1(3))	$Zn_{0.53}Cd_{0.43}Sb$	$z = 0.4$	Zn (34.5(6)) Cd (20.0(3)) Sb (45.5(3))	$(Zn_{0.63}Cd_{0.37})_{11.98}Sb_{10}$
$x = 0.6$	Zn (20.6(6)) Cd (28.9(3)) Sb (50.5(3))	$Zn_{0.41}Cd_{0.57}Sb$	$z = 0.6$	Zn (23.7(6)) Cd (32.1(3)) Sb (44.2(3))	$(Zn_{0.42}Cd_{0.58})_{12.62}Sb_{10}$

$x = 0.8$	Zn (10.3(6)) Cd (39.9(3)) Sb (49.8(3))	$\text{Zn}_{0.21}\text{Cd}_{0.80}\text{Sb}$	$z = 0.8$	Zn (12.5(6)) Cd (43.8(3)) Sb (43.7(3))	$(\text{Zn}_{0.22}\text{Cd}_{0.78})_{12.88}\text{Sb}_{10}$
$x = 1$	Cd (50.5(3)) Sb (49.5(3))	$\text{Cd}_{1.02}\text{Sb}$	$z = 1$	Cd (56.2(3)) Sb (43.8(3))	$\text{Cd}_{12.83}\text{Sb}_{10}$

The **Table 6.3** summarizes the results from the EDS elemental analyses of the $\text{Zn}_{1-x}\text{Cd}_x\text{Sb}$ and $(\text{Zn}_{1-z}\text{Cd}_z)_{13}\text{Sb}_{10}$ series. Note that for the $(\text{Zn}_{1-z}\text{Cd}_z)_{13}\text{Sb}_{10}$ series, there is a cation deficiency compared to the charge-balanced $\text{Zn}_{13}\text{Sb}_{10}$ composition, which is consistent with the previously published data¹⁸⁸. The composition comes close to the 13:10 ratio only for the Cd-rich samples ($z = 0.6, 0.8$ and 1), which agrees with the compositions obtained from X-ray diffractions. The refined X-ray composition of the $\text{Cd}_{13}\text{Sb}_{10}$ material is $\text{Cd}_{13.0(1)}\text{Sb}_{10}$, while the refined X-ray composition of $\text{Zn}_{13}\text{Sb}_{10}$ is $\text{Zn}_{11.6(1)}\text{Sb}_{10}$ ¹⁸⁸.

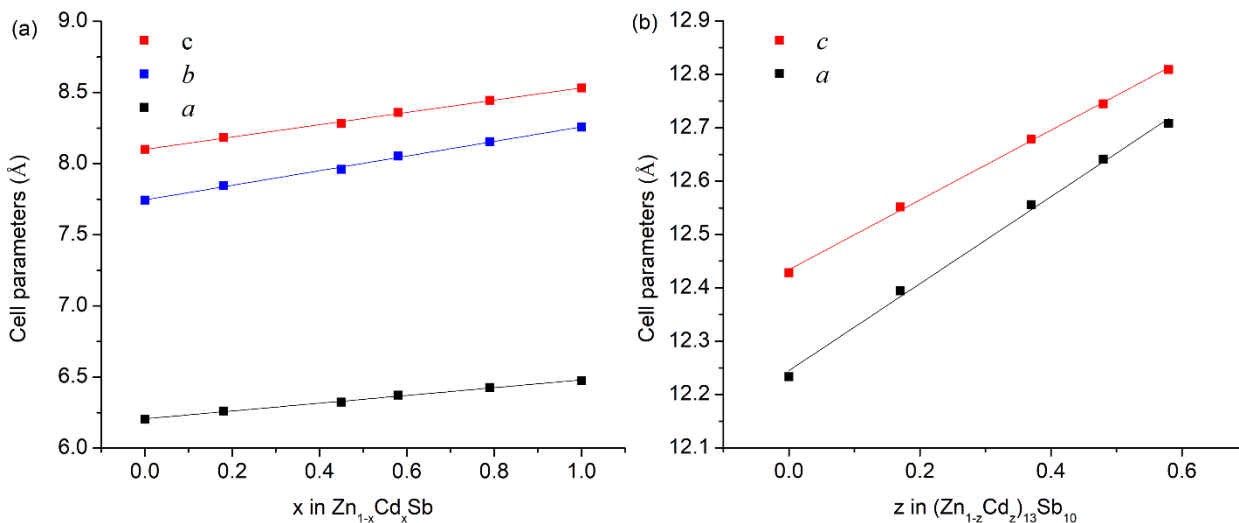


Figure 6.1. Refined unit cell parameters of a) $\text{Zn}_{1-x}\text{Cd}_x\text{Sb}$ and b) $(\text{Zn}_{1-z}\text{Cd}_z)_{13}\text{Sb}_{10}$. The compositions (x -axis) were obtained from the EDS analyses.

Figure 6.1 shows changes in the unit cell parameters of $\text{Zn}_{1-x}\text{Cd}_x\text{Sb}$ and $(\text{Zn}_{1-z}\text{Cd}_z)_{13}\text{Sb}_{10}$, which reveal a linear relationship with the Cd content, following the Vegard's

law. Note that for the $(\text{Zn}_{1-z}\text{Cd}_z)_{13}\text{Sb}_{10}$ series, only $z = 0 - 0.6$ is shown due to the observable peak splitting in the $z = 0.8$ and 1 samples.

6.3.2. Crystal Structure and Bonding

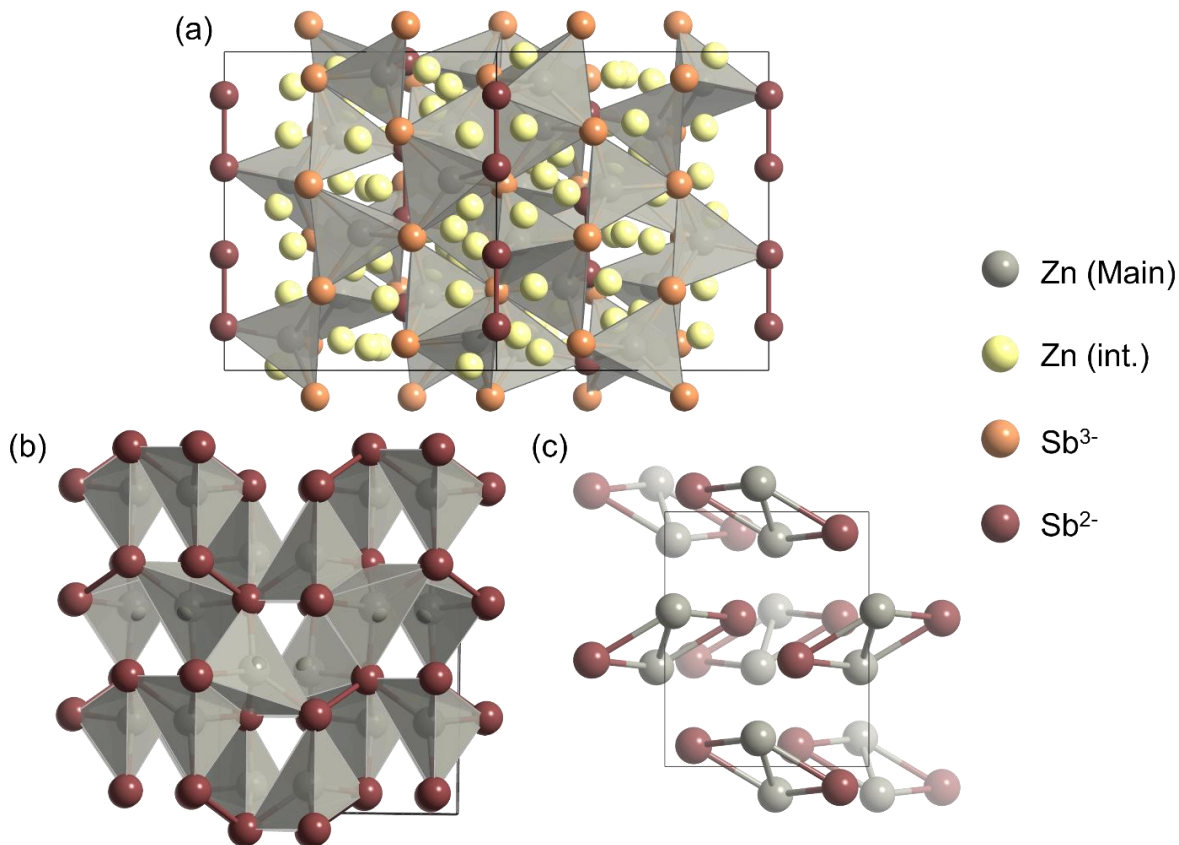


Figure 6.2. Crystal structures of (a) $\text{Zn}_{13}\text{Sb}_{10}$, ZnSb (b) with Sb tetrahedra and (c) Zn_2Sb_2 rhomboid rings.

The structures of both ZnSb and $\beta\text{-Zn}_{13}\text{Sb}_{10}$ can be described using the Zintl–Klemm formalism. The $\beta\text{-Zn}_{13}\text{Sb}_{10}$ is built up of Sb atoms, with Zn atoms occupying the tetrahedral voids in the Sb sublattice (**Figure 6.2(a)**). The Sb sublattice contains two types of Sb, Sb^{3-} anions and Sb_2^{4-} dimers, and the main-Zn-occupied Sb tetrahedra are formed by 3 Sb^{3-} and one Sb from an Sb_2^{4-} dimer (**Figure 6.2(a)**). The main Zn site is ~90% occupied,

and there are 3 deficient interstitial Zn site with ~6% occupancy each, reaching the $\text{Zn}_{13}\text{Sb}_{10}$ composition⁹⁶. On the other hand, the Sb sublattice of ZnSb contains only one type of Sb, all of them as Sb_2^{4-} dimers. The Zn-occupied Sb tetrahedra are formed by Sb from four different Sb_2^{4-} dimers (**Figure 6.2(b)**). Note that the crystal structure of ZnSb is also referred to as a bonded semiconductor in the literature, as linked Zn_2Sb_2 rhomboid rings in the structure^{192,193}.

The bonding interactions between atoms are essential to understand the thermal transport properties of thermoelectric materials. The exceptionally low thermal conductivities of both the ZnSb and $\text{Zn}_{13}\text{Sb}_{10}$ materials at room temperatures prompted us to investigate their bonding features.

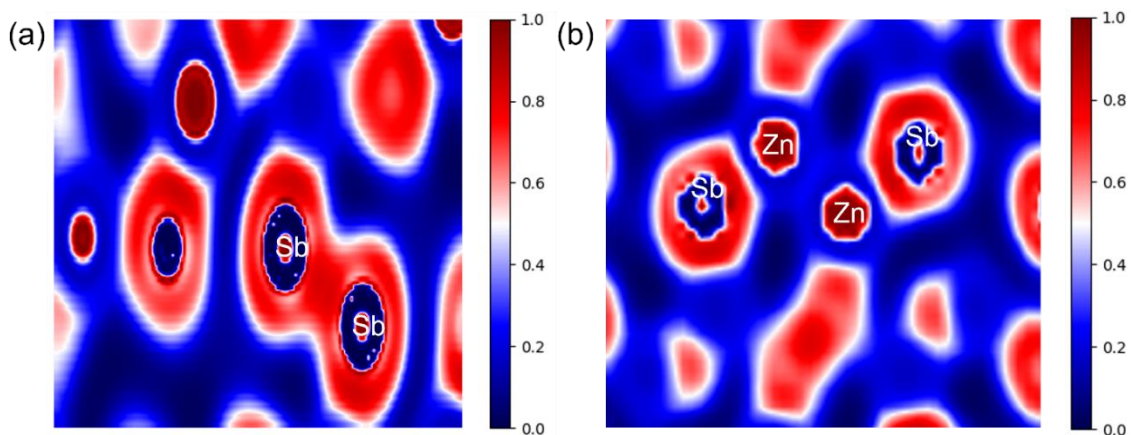


Figure 6.3. The 2D ELF showing (a) the Sb – Sb interaction and (b) the Zn_2Sb_2 rhomboid ring in the ZnSb material.

Figure **6.3(a)** and **(b)** shows the results of the 2D ELF for a Sb – Sb dimer and Zn_2Sb_2 rhomboid ring respectively. The ELF calculations are based on the following:

$$ELF = \frac{1}{1 + \chi(r)}, \quad (2)$$

where $\chi(r)$ is the ratio of the energy density, $D(r)$, with respect to the energy density for a uniform electron gas, $D_h(r)$ ¹⁹⁴:

$$\chi(r) = \frac{D(r)}{D_h(r)}. \quad (3)$$

The energy density $D(r)$ in the structure is defined as the difference between the kinetic energy and bosonic kinetic energy (the von Weizsäcker term). Electrons are seen as localized when ELF is high ($ELF > 0.7$), and are similar to electron gas/metallic bonds when ELF is lower ($0.2 < ELF < 0.7$)¹⁹⁴. Under these criteria, it is clear that the Sb – Sb interaction in **Figure 6.3(a)** resembles a covalent bond, since electrons are localized between the Sb atoms. Additionally, the Sb – Sb dumbbell is surrounded by additional electron density, which is indicative of gained electrons and anionic nature of the Sb – Sb dumbbell.

On the other hand, the Zn atom has only core-like localized electrons, which would be consistent with the closed d shell (**Figure 6.3(b)**). Also, the Zn – Sb interaction seems to be ionic in nature, as there is no apparent electron localization between the two atoms. Furthermore, the Zn – Zn interaction appears to be metallic in nature, due to the low ELF between the two atoms ($ELF \sim 0.25$).

The ELF method suggests that the atomic interactions in the ZnSb material is a mix of covalent Sb – Sb, ionic Zn – Sb, and metallic Zn – Zn interactions, and thus agrees with the Zintl-Klemm picture of ZnSb. The local environments of Zn and Sb in the Zn₁₃Sb₁₀

material are similar to that in the ZnSb material, except for the additional Sb^{3-} in the Sb sublattice. Although the ELF is not calculated for the $\text{Zn}_{13}\text{Sb}_{10}$ material due to its structural complexity, the Zn – Zn and Zn – Sb interactions are considered similar, thus the bonding picture based on the Zintl-Klemm formalism should be an accurate description of the $\text{Zn}_{13}\text{Sb}_{10}$ structure as well.

Vibrations of the Sb – Sb dumbbells were considered to play an important role in the low lattice thermal conductivity of $\text{Zn}_{13}\text{Sb}_{10}$ ¹⁹⁵. However, theoretical studies by Bjerg et al.¹⁷⁵ on ZnSb and $\text{Zn}_{13}\text{Sb}_{10}$ found that there are significant Zn vibrational contributions to the low-energy modes in $\text{Zn}_{13}\text{Sb}_{10}$ and soft Zn phonon modes in ZnSb, which are more consequential for the low thermal conductivity.

6.3.3. Electronic Band Structures

The density of states (DOS) and electronic band structures of the $\text{Zn}_{1-x}\text{Cd}_x\text{Sb}$ and the $(\text{Zn}_{1-z}\text{Cd}_z)_{13}\text{Sb}_{10}$ series are shown in **Figures 6.4** and **6.5**, respectively. The DOS and electronic band structures predict semimetallic character for the $\text{Zn}_{1-x}\text{Cd}_x\text{Sb}$ series, and this is due to the fact that the valence band (VB) maximum is slightly higher in energy than the conduction band (CB) minimum. (**Figure 6.4**). The absence of band gaps in this series would suggest the presence of bipolar effects at low temperatures. However, it is more likely that LMTO calculations underestimate band gaps. Electronic structure calculations of ZnSb using the Heyd-Scuseria-Ernzerhof (HSE) hybrid exchange-correlation functional yielded an indirect bandgap of 0.58 eV¹⁹⁶, which is close to the experimental bandgap of 0.53 eV from an absorption edge experiment¹⁹⁷. Additionally, band structure calculations of CdSb

using the FPLO[®] – 23 scheme revealed a lower band gap of 0.44 eV¹⁹⁸, which is close to the bandgap of 0.43 eV from absorption edge experiment^{199,200}.

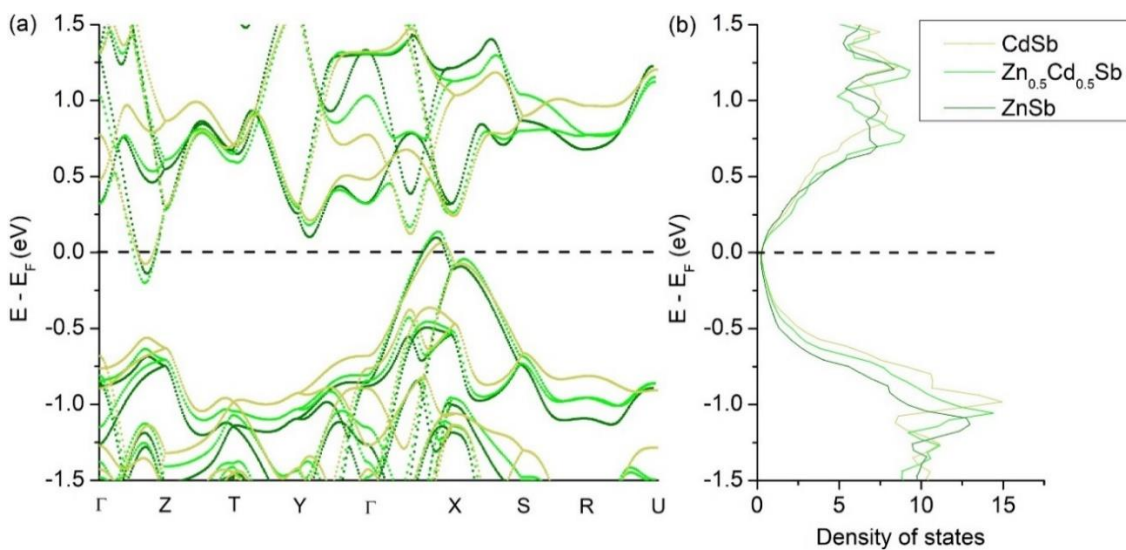


Figure 6.4. (a) Density of States (DOS) plot and (b) the electronic band structures of the $Zn_{1-x}Cd_xSb$ series. Note that the high symmetry points in the three structures are slightly different, and they are labelled in separate band structures in the Supplementary Information, Figure 6.S4.

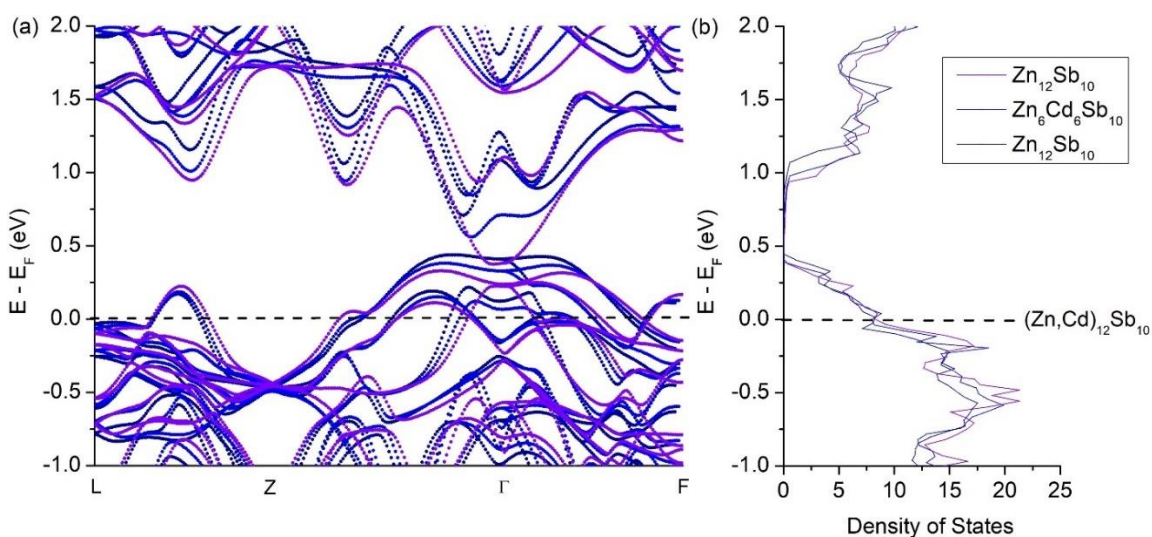


Figure 6.5. (a) Density of States (DOS) plot and (b) the electronic band structures of the $(\text{Zn}_{1-z}\text{Cd}_z)_{13}\text{Sb}_{10}$ series. Note that the high symmetry points in the three structures are slightly different, and they are labelled in separate band structures in the Supplementary Information, Figure 6.S5.

In the $(\text{Zn}_{1-z}\text{Cd}_z)_{13}\text{Sb}_{10}$ series, the Fermi level (set at 0 eV) is located in the valence band for the $\text{Zn}_{12}\text{Sb}_{10}$ composition and it is at the top of the valence band for the $\text{Zn}_{13}\text{Sb}_{10}$ composition. The DOS of $\text{Zn}_{13}\text{Sb}_{10}$ has a bandgap of ~ 0.27 eV, which is in close agreement with the calculations by Faghaninia et al. (0.257 eV)¹⁹⁶ and Qiu et al. (0.26 eV)²⁰¹. The band gap becomes smaller as Cd is introduced (**Figure 6.5(b)**). The Fermi level for the stoichiometric $\text{Cd}_{13}\text{Sb}_{10}$ phases crosses the bottom of the conduction band (Supplementary Information, **Figure 6.S5(c)**), which is antibonding and energetically unfavourable. The Fermi level of the $\text{Cd}_{13}\text{Sb}_{10}$ sample is likely lower due to the cation deficiency, suggested by the elemental analysis, and a dominant *p*-type behaviour is still expected with a smaller hole concentration.

6.3.4. Phase Transition

As previously reported, the anomalies in the $z = 0$ sample of $(\text{Zn}_{1-z}\text{Cd}_z)_{13}\text{Sb}_{10}$ refers to the $\alpha' - \alpha$ and $\alpha - \beta$ $\text{Zn}_{13}\text{Sb}_{10}$ phase transitions at 235 and 254 K, as shown in **Figure 6.6**^{133,188}. The $z = 0.5$ and 1 samples also show single anomaly at 247 K and ~ 370 K, respectively.

The anomaly in the heat capacity of the $z = 0.5$ sample appears to be a 1st order phase transition only, judging by the symmetrical nature of the peak. While such transition is different from the two transitions ($\alpha' - \alpha$, 1st order and $\alpha - \beta$, 2nd order) in the pristine

$\text{Zn}_{13}\text{Sb}_{10}$ and the other doped- $\text{Zn}_{13}\text{Sb}_{10}$ samples¹⁸⁸, it suggests that the Zn/Cd mobility is retained in the sample. Single crystal X-ray diffraction analysis at 100 K indicates that the $z = 0.5$ phase crystallizes in a structure resembling the $C2/c$ one of the pristine $\text{Zn}_{13}\text{Sb}_{10}$ at such temperature, and there are no observable superstructure peaks similar to the α' - $\text{Zn}_{13}\text{Sb}_{10}$ phase. The heat capacities of the $z = 0$ and 0.5 samples exceed the Dulong-Petit limit of $3R = 24.9$ J/mol at.-K, which suggests an additional contribution to heat capacity beyond harmonic atomic vibrations.

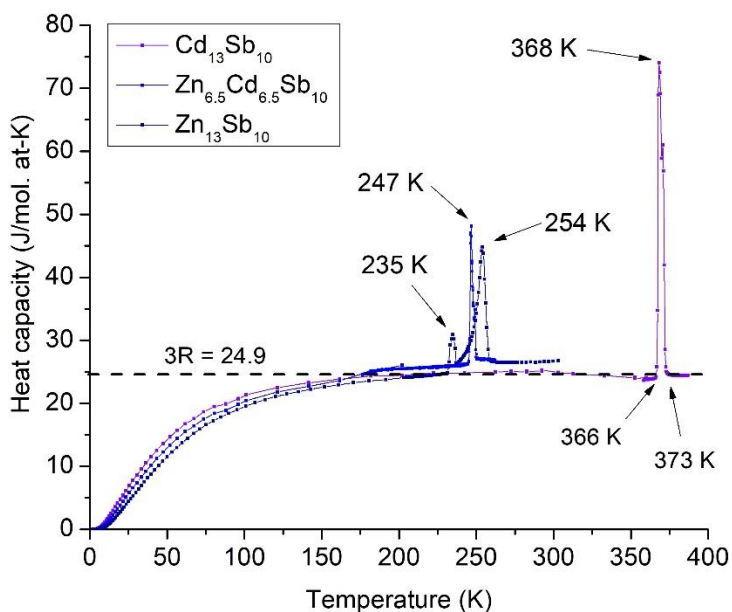


Figure 6.6. Heat capacities of $(\text{Zn}_{1-z}\text{Cd}_z)_{13}\text{Sb}_{10}$ ($z = 0, 0.5, 1$).

The $z = 1$ sample ($\text{Cd}_{13}\text{Sb}_{10}$) has a phase transition at 368 K (95 °C), which appears to be a 1st order transition. The crystal structure of $\text{Cd}_{13}\text{Sb}_{10}$ at room temperature has been characterized above and by Ponou et al¹⁹¹. Another crystal structure of $\text{Cd}_{13}\text{Sb}_{10}$ has also been reported by O. Zelinska et al.¹⁶⁴. Since the rhombohedral $R\bar{3}c$ structure, similar to the β - $\text{Zn}_{13}\text{Sb}_{10}$ one, was obtained by quenching the $\text{Cd}_{13}\text{Sb}_{10}$ sample from high temperatures

(430 °C), we suspect that the rhombohedral $R\bar{3}c$ structure is stable above the 1st order phase transition temperature of 95 °C. The heat capacity of $\text{Cd}_{13}\text{Sb}_{10}$ at elevated temperatures is close to the Dulong-Petit limit, suggesting contribution mostly from the harmonic atomic vibrations.

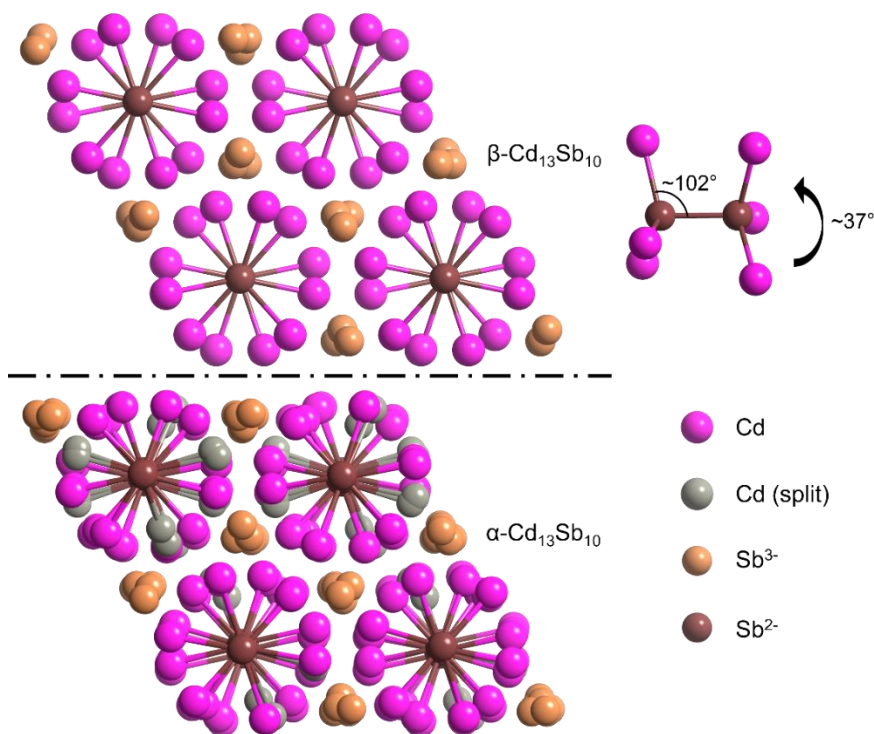


Figure 6.7. Structures of the α - and β - $\text{Cd}_{13}\text{Sb}_{10}$, aligned along the Sb_2^{4-} dimers. The $\text{Cd}_3\text{Sb-SbCd}_3$ motif is shown on the right of the figure.

The α - β transition in $\text{Cd}_{13}\text{Sb}_{10}$ is considered an order-disorder transition, similar to the α - β transition of $\text{Zn}_{13}\text{Sb}_{10}$ ^{92,93}. The $P2_1/n$ structural model (α - $\text{Cd}_{13}\text{Sb}_{10}$) has 33 fully occupied and 6 split Cd sites, whereas the β - $\text{Cd}_{13}\text{Sb}_{10}$ has 1 main site with $\sim 80\%$ occupancy and 5 interstitial Cd sites with no more than 7% occupancies¹⁶⁴. Some of the originally interstitial Cd atoms are now fully occupied, while some main Cd atoms are vacant, and

the atomic distribution is similar to the α' - $\text{Zn}_{13}\text{Sb}_{10}$ case. The most obvious difference is the absence of consistent $\text{Cd}_3\text{Sb-SbCd}_3$ motif in the α - $\text{Cd}_{13}\text{Sb}_{10}$ structure that is present in the β - $\text{Cd}_{13}\text{Sb}_{10}$ structure, shown in **Figure 6.7**. The $\text{Cd}_3\text{Sb-SbCd}_3$ motif is made up of a Sb_2^{4-} dimer and 6 main Cd atoms that resembles an ethane molecule with a dihedral angle of $\sim 37^\circ$, and a Cd–Sb–Sb bond angle of $\sim 102^\circ$. Some main Cd sites in the α - $\text{Cd}_{13}\text{Sb}_{10}$ structure are either vacant, shifted, or split.

6.3.5. Thermoelectric Properties

6.3.5.1. Charge Transport Properties of $\text{Zn}_{1-x}\text{Cd}_x\text{Sb}$

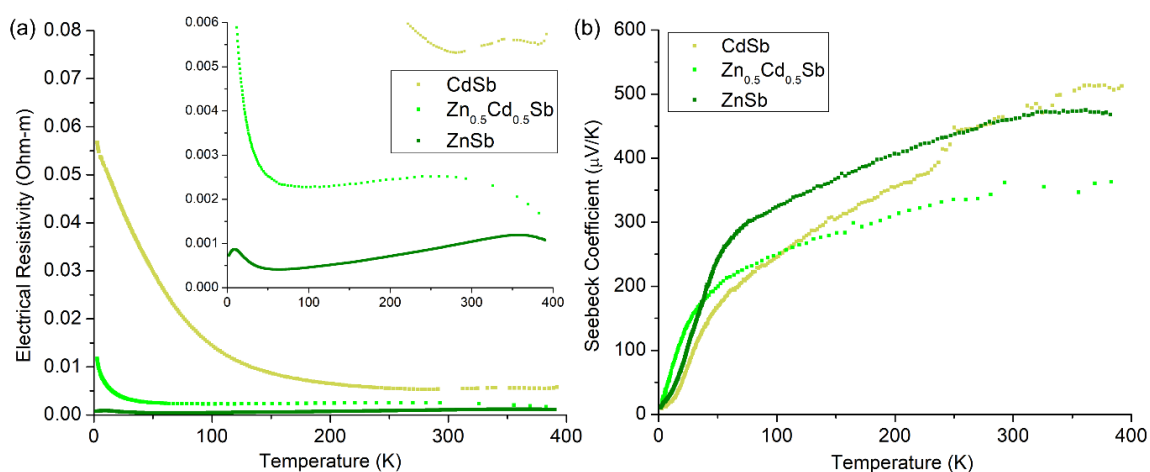


Figure 6.8. Low temperature (LT) (a) electrical resistivities and (b) Seebeck coefficients of SPS $\text{Zn}_{1-x}\text{Cd}_x\text{Sb}$ ($x = 0, 0.5, 1$).

The electrical resistivity and Seebeck coefficient measurements of the SPS $\text{Zn}_{1-x}\text{Cd}_x\text{Sb}$ series are shown in **Figure 6.8**. The electrical resistivity, ρ , points at intrinsic semiconducting behaviour and increases with the Cd content; most likely due to a decrease in the carrier concentration. The initial increase in ρ of ZnSb to 9 K has also been reported

previously by D. Eklöf et al., however the cold-pressed and single-crystalline ZnSb samples displaying no such maxima¹⁹². To verify such behaviour, we compared resistivity of the melted and SPS samples prepared during this study (**Figure 6.S6**). The melted sample does not have a peak at low temperatures. Presence of the peak for the SPS sample may stem from an incompletely filled valence band due to a small Zn deficiency, as suggested by the elemental analysis (**Table 6.3**). The SPS ZnSb samples in this study and in that of D. Eklöf et al. employed a sintering temperature close to or higher than the melting point of Zn (~420 °C). Such high temperature may promote some Zn losses during the SPS annealing under dynamic vacuum.

As the temperature increases, the resistivity of the melted and SPS ZnSb drops to a minimum at 64 K and then raise steadily (**Figure 6.8** and **6.S6**). Song et al.²⁰² attributed such behavior to a shallow localized impurity band with activation energy of 0.002 eV. Analysis of the resistivity data for the SPS ZnSb in the 9 – 64 K region yielded the activation energy of 0.0016 eV, which is similar to the value reported by Song et al. The exact origin of the impurity band remains unknown, although Song et al. proposed that it originates from intrinsic defects in ZnSb, which as we suggest are Zn deficiencies. A drop in resistivity is observed above 358 K, which is most likely due to bipolar effect.

A schematic band diagram with the impurity band for ZnSb is illustrated in **Figure 6.9**. When the valence band is fully occupied, which appears to be the case for $\text{Zn}_{0.5}\text{Cd}_{0.5}\text{Sb}$ and CdSb, the LT peak is absent, and the decrease in the resistivity reflects the excitation of charge carriers from the valence band into the impurity band. When the impurity band becomes full (exhaustion range), the resistivity starts to increase with temperature due to

the electron-phonon scattering. This proceeds until the temperature is high enough to promote the charge carriers into the conduction band; at this point the resistivity starts to decrease and this is known as the bipolar effect. This “decrease-increase-decrease” in resistivity is observed for all the $Zn_{1-x}Cd_xSb$ samples, and thus the impurity band is likely to be present in all of them. However, the activation energy, width of the impurity band, and initial occupancy (at $T = 0$ K) of the valence band depend on the preparation method and amount of Cd.

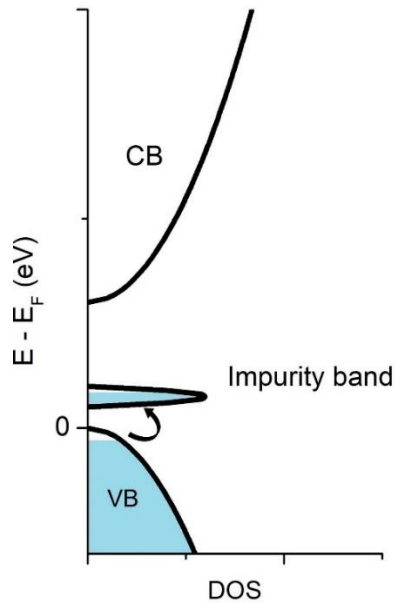


Figure 6.9. Schematic band diagram with the impurity band in ZnSb. Population of the impurity band occurs in the 9 – 64 K region and leads to a decrease in the resistivity.

As mentioned above, the valence band in the SPS $Zn_{0.5}Cd_{0.5}Sb$ sample appears to be fully occupied. Also, analysis of the LT resistivity data for $Zn_{0.5}Cd_{0.5}Sb$ suggests that the activation energy between the valence and impurity bands is below 0.001 eV. In comparison to ZnSb, the minimum (~35 K) and maximum (~260 K) in the resistivity of

$\text{Zn}_{0.5}\text{Cd}_{0.5}\text{Sb}$ are shifted to lower temperatures, which would suggest a narrower impurity band and smaller band gap.

The ρ of CdSb sample exhibits a consistent drop in resistivity until 250 K, which may be an indication of a broader impurity band. The resistivity increases steadily after 250 K and then drops after ~340 K, with the latter being attributed due to a bipolar effect. The onset (358, 260 and 340 K for $x = 0, 0.5, 1$ samples, respectively) of the bipolar effect suggests that the band gap decreases from ZnSb to CdSb, followed by $\text{Zn}_{0.5}\text{Cd}_{0.5}\text{Sb}$, and this is consistent with the reported experimental band gaps^{196,199,200}. It is worth mentioning that the resistivity data of CdSb above room temperature are one order of magnitude higher than the values reported by S. Wang et al.²⁰³ and B. Zhou et al.¹⁸⁷.

All $\text{Zn}_{1-x}\text{Cd}_x\text{Sb}$ materials exhibit positive Seebeck coefficients, α (**Figure 6.8(b)**), indicating holes as the dominant charge carrier. For the $x = 0$ sample, the Seebeck coefficient can be roughly separated into 3 pseudo-linear regions: (i) 2 – 10 K, (ii) 10 – 60 K, and (iii) 60 K to around room temperature, and changes between the regions can be correlated with the occupancy of the valence, impurity, and conduction bands. From region (i) to (ii), there is an increase in the α vs. T slope, while electrical resistivity starts to decrease (**Figure 6.8(a)**). This would be consistent with the occupancy of the localized impurity band; more charge carriers are generated, and resistivity is lowered. But since the impurity band is highly localized, the effective mass of extra charge carriers and Seebeck coefficient are higher. On the other hand, there is a decrease in steepness from region (ii) to (iii), which coincides with a slow increase in resistivity from 60 – 300 K. These changes can be attributed to the full occupancy of the impurity bands, which leads to the lower

number of charge carriers with higher effective mass. Thus, the behavior of ρ and α in ZnSb resembles that of an impure semiconductor with an acceptor band.

The temperature dependence of the α of the $\text{Zn}_{0.5}\text{Cd}_{0.5}\text{Sb}$ sample resembles that of the ZnSb one (**Figure 6.8(b)**), except there is no region (i). The transition between regions (ii) and (iii) shifted to around 35 K in $\text{Zn}_{0.5}\text{Cd}_{0.5}\text{Sb}$ and is close to the impurity band feature in its electrical resistivity. Note that the α of the $\text{Zn}_{0.5}\text{Cd}_{0.5}\text{Sb}$ sample is higher than that of ZnSb past 40 K. On the other hand, the α of the CdSb sample is below that of $\text{Zn}_{0.5}\text{Cd}_{0.5}\text{Sb}$ till around 250 K. The general shape of the Seebeck curve for CdSb resembles that of ZnSb; there is a similar change in between regions (i) and (ii); the transition between the regions (ii) and (iii) is also present but becomes more gradual. The first transition is rather surprising as there is no maximum in the electrical resistivity of CdSb at the corresponding temperature; this may indicate small underoccupancy of the valence band, which does not represent itself in the resistivity data. The thermopower of the CdSb sample increases abruptly at 230 – 250 K, which is before the minimum at 260 K in the electrical resistivity. Currently, we cannot rationalize this change.

Regarding the bipolar effect seen in the electrical resistivity, the thermopowers of the $\text{Zn}_{0.5}\text{Cd}_{0.5}\text{Sb}$ and CdSb samples do not clearly show the corresponding maxima, thus Seebeck measurements to higher temperatures are required to better establish the trends.

We have also explored the $\text{Zn}_{0.95}\text{Cd}_{0.05}\text{Sb}$ sample to gain extra information into the effects of Cd substitution. **Figure 6.10** shows the ρ and α of SPS $\text{Zn}_{0.95}\text{Cd}_{0.05}\text{Sb}$ in comparison to SPS ZnSb. The general behaviour is quite similar between the two phases,

but the lower ρ and α of $\text{Zn}_{0.95}\text{Cd}_{0.05}\text{Sb}$ suggest a higher carrier concentration. These data in combination with the ones for $x = 0, 0.5, 1$ (**Figure 6.8**) indicate non-monotonous changes in charge transport properties upon the Cd substitution in the $\text{Zn}_{1-x}\text{Cd}_x\text{Sb}$ system.

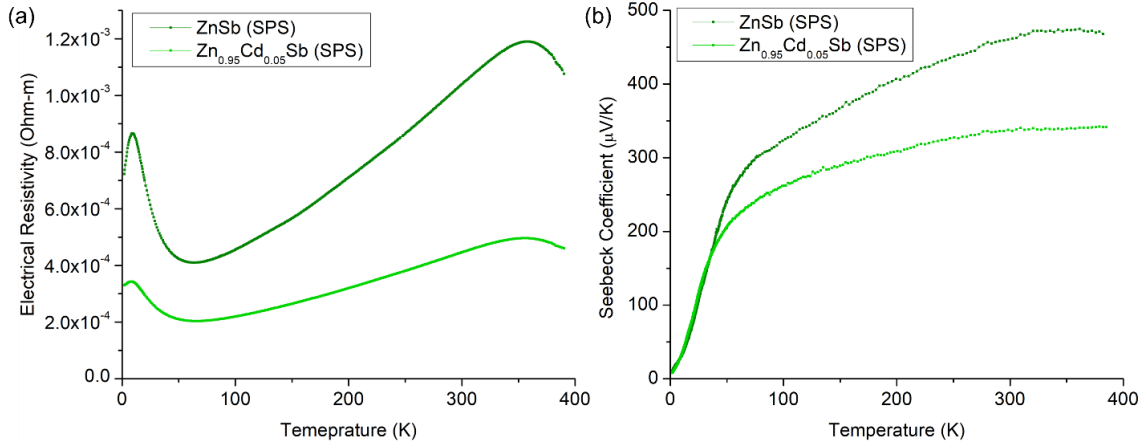


Figure 6.10. LT (a) electrical resistivities and (b) Seebeck coefficients of $\text{Zn}_{1-x}\text{Cd}_x\text{Sb}$ ($x = 0, 0.05$).

6.3.5.2. Charge Transport of $(\text{Zn}_{1-z}\text{Cd}_z)_{13}\text{Sb}_{10}$

Electrical resistivities of $(\text{Zn}_{1-z}\text{Cd}_z)_{13}\text{Sb}_{10}$ are plotted in **Figure 6.11(a)**. The ρ in the $(\text{Zn}_{1-z}\text{Cd}_z)_{13}\text{Sb}_{10}$ series increase with increasing Cd content, which suggests a lower charge carrier concentration and/or shorter relaxation time. The residual electrical resistivities of the 3 samples are significantly different. For the $z = 0.5$ sample, the higher ρ is likely due to the impurity scattering by the Zn/Cd disorder. The resistivity of the $z = 1$ sample is the highest within the series and is similar to those obtained by A. Tengå et al.¹⁸². On the other hand, the residual electrical resistivity of $\text{Cd}_{13}\text{Sb}_{10}$ reported by O. Zelinska et al.¹⁶⁴ is two magnitudes ($\sim 10^{-5}$ $\Omega\cdot\text{m}$) lower than that of the $z = 1$ sample. This disagreement is most

likely due to their $\text{Cd}_{13}\text{Sb}_{10}$ sample retaining the β -polymorph structure with a large cation deficiency (their refined composition was $\text{Cd}_{12.7}\text{Sb}_{10}$), while our $\text{Cd}_{13}\text{Sb}_{10}$ sample adopts the α -polymorph with a lower Cd deficiency (the refined composition was $\text{Cd}_{13}\text{Sb}_{10}$, or $\text{Cd}_{12.83}\text{Sb}_{10}$ from elemental analysis). Both the $z = 0.5$ and 1 samples have observable differences in their resistivities during heating and cooling, which stems most likely from the temperature hysteresis of the structural transitions.

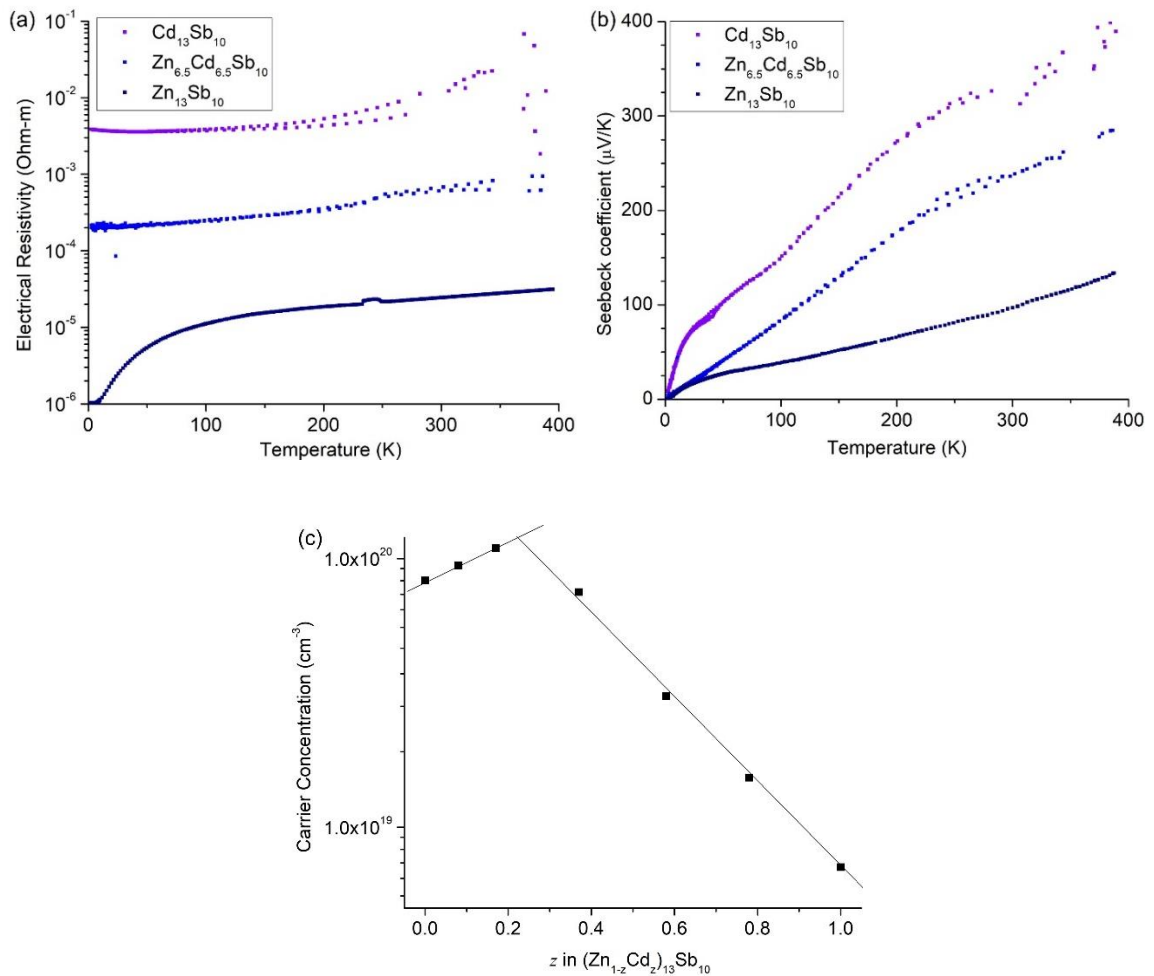


Figure 6.11. LT (a) electrical resistivities, (b) the Seebeck coefficients and (c) the room temperature Hall carrier concentrations of the $(\text{Zn}_{1-z}\text{Cd}_z)_{13}\text{Sb}_{10}$ series. Separate resistivities

of samples are presented in the Supplementary Information, **Figure 6.S7**. The elemental ratios derived from EDS are used for the values of z in (c). The standard deviations of Hall carrier concentrations are typically smaller than the squares ($< 3.5\%$ error), while the error of z could be larger due to the semiquantitative nature of SEM–EDS, in addition to possible sample inhomogeneity.

Similar to the $\text{Zn}_{1-x}\text{Cd}_x\text{Sb}$ series, thermopower of $(\text{Zn}_{1-z}\text{Cd}_z)_{13}\text{Sb}_{10}$ at low temperatures is dominated by hole carriers (**Figure 6.11(b)**). The Seebeck coefficients of this series increase with the Cd content, which suggests a lower carrier concentration (and/or larger effective mass), in agreement with the electrical resistivity measurements. The Seebeck coefficients however do not follow a simple linear T dependence. Changes in the temperature dependence between samples in this series are expected, since carrier concentration and effective mass are also expected to change upon substitution of Zn by Cd (due to the different occupancy of the Zn/Cd sites).

The thermopower for the $z = 0.5$ sample in this temperature range can be separated to two linear regions, 2 – 220 K and 220 – 400 K. This change of slope can be due to the suppressed phase transition as seen in the heat capacity measurements or changes in band structure. For the $\text{Cd}_{13}\text{Sb}_{10}$ sample, the measurement can be roughly separated into 3 pseudo-linear regions: (i) 2 – 25 K, (ii) 25 – 220 K and (iii) 220 – 400 K. The heat capacity of $\text{Cd}_{13}\text{Sb}_{10}$ does not indicate any other phase transitions except the 373 K one. Thus, these changes in the T dependence can be attributed to changes in the electronic band structure, which can be rather complex due the large unit cell and low symmetry of $\text{Cd}_{13}\text{Sb}_{10}$.

Figure 6.11(c) represents Hall data for the $(\text{Zn}_{1-z}\text{Cd}_z)_{13}\text{Sb}_{10}$ series with smaller z intervals. The data clearly show that the substitution of Zn by Cd does not change the charge

transport properties in a linear way. The Hall carrier concentrations of $(\text{Zn}_{1-z}\text{Cd}_z)_{13}\text{Sb}_{10}$ increases from $z = 0$ to $z = 0.2$ and then drops from $z = 0.4$ to $z = 1$. Such trend with respect to Cd content shows the non-monotonous change of charge transport properties upon the Cd substitution in the $(\text{Zn}_{1-z}\text{Cd}_z)_{13}\text{Sb}_{10}$ series, similar to the $\text{Zn}_{1-x}\text{Cd}_x\text{Sb}$ series. Since Zn and Cd are isoelectronic, and one could expect a similar carrier concentration but a lower carrier mobility upon the Zn/Cd substitution leading to larger electrical resistivities. Instead, there is an apparent change in the carrier concentration that cannot be rationalized by simple substitution arguments.

Similar phenomena were also observed in the $\text{Zn}_{1-x}\text{Cd}_x\text{Sb}$ series, Cd-doped $\text{Zn}_{0.995}\text{Na}_{0.005}\text{Sb}^{184}$, the Sn-doped GeTe^{204} , and Ag-doped $\text{Cu}_2\text{Se}^{205}$. All doped samples (on the cation side) have higher carrier concentrations than their respective pristine phases. W. Liu et al. attributed this to a bond softening effect when Cu is replaced by Ag in Cu_2Se since bond length Ag – Se is longer than Cu – Se²⁰⁵. In general, it is true that elements down the group are larger, thus the bonds are longer when smaller atoms are replaced by the larger ones.

The non-monotonous change in charge transport in the $(\text{Zn,Cd})\text{Sb}$, $(\text{Zn,Cd})_{13}\text{Sb}_{10}$ systems with increasing Cd content can be described as a combination of a bond softening effect, followed by an increase in the (Zn,Cd) concentration, which leads to a drastic decrease in carrier concentrations. The bond softening effect increases the carrier concentration when the Cd content is low, but this effect is overridden by the increase in the cation content, leading to a smaller (Zn,Cd) deficiency, and lower carrier concentration when the Cd content is high.

Note that high-temperature (HT) electrical properties measurements were performed but the Cd-rich samples ($x, z = 0.6, 0.8$ and 1) were partly/fully decomposed to (Zn,Cd)Sb, Cd and Sb, as confirmed by X-ray powder diffractions. Additionally, grey droplets formed on the samples were identified as Cd through EDS analyses. Compared to other successful elemental substitutions done previously¹⁸⁸, Cd does not increase the stability of the $Zn_{13}Sb_{10}$ -based materials, but rather makes it more unstable at higher temperatures.

6.3.5.3. Thermal Properties

Thermal conductivities of $(Zn_{1-z}Cd_z)_{13}Sb_{10}$ and $Zn_{1-x}Cd_xSb$ are plotted in **Figures 6.12** and **6.13**. The lattice thermal conductivities κ_l of the samples were calculated using $\kappa_l = \kappa_{total} - \kappa_e$, where κ_{total} is the total thermal conductivity and κ_e is the electronic contribution. κ_e is calculated using the Wiedemann-Franz law, $\kappa_e = LT/\rho$, where L is the effective Lorenz number. The effective Lorenz number was estimated according to $L \approx 1.5 + \exp[-|\alpha|/116]$, with α being the Seebeck coefficient (L is in the unit of $10^{-8} W\Omega/K^2$ and α is in units of $\mu V/K$)³⁰.

Thermal conductivities of all samples in both series retain the Umklapp scattering with increasing Cd content similar to the pristine $Zn_{13}Sb_{10}$ and ZnSb. Still, it is surprising that the samples with $x, z = 0.5$, which are the most atomically disordered, retain the Umklapp scattering, since the previous results showed that that point defect scattering may become the dominant contributor in the disordered systems. As an example, substitution of In for Zn in the $Zn_{13}Sb_{10}$ material makes point defects the dominant phonon scattering

contributor^{159,188}. In addition to the Zn/In substitution in $\text{Zn}_{13}\text{Sb}_{10}$, the structure also has a larger number of vacancies due to the larger oxidation state of In (3+ for In vs 2+ for Zn). Similarly the thermal conductivity of $\alpha\text{-Zn}_3\text{Sb}_2$, which has many deficient/partially occupied Zn sites in the structure, features point defect as the dominant phonon scattering pathway¹³³. Thus, further studies are needed to fully understand the phonon scattering pathways in the Zn-Sb materials.

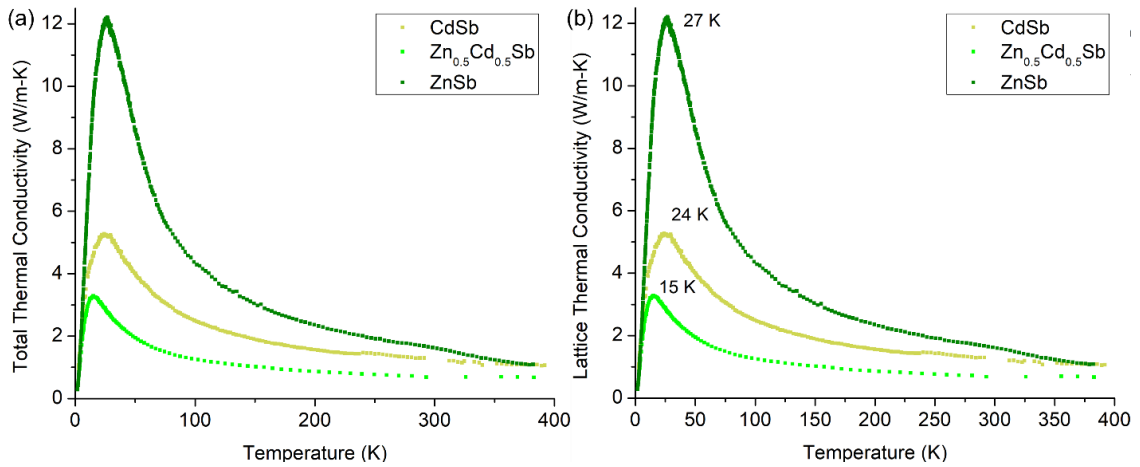


Figure 6.12. Low temperature (a) total and (b) lattice thermal conductivities of $\text{Zn}_{1-x}\text{Cd}_x\text{Sb}$.

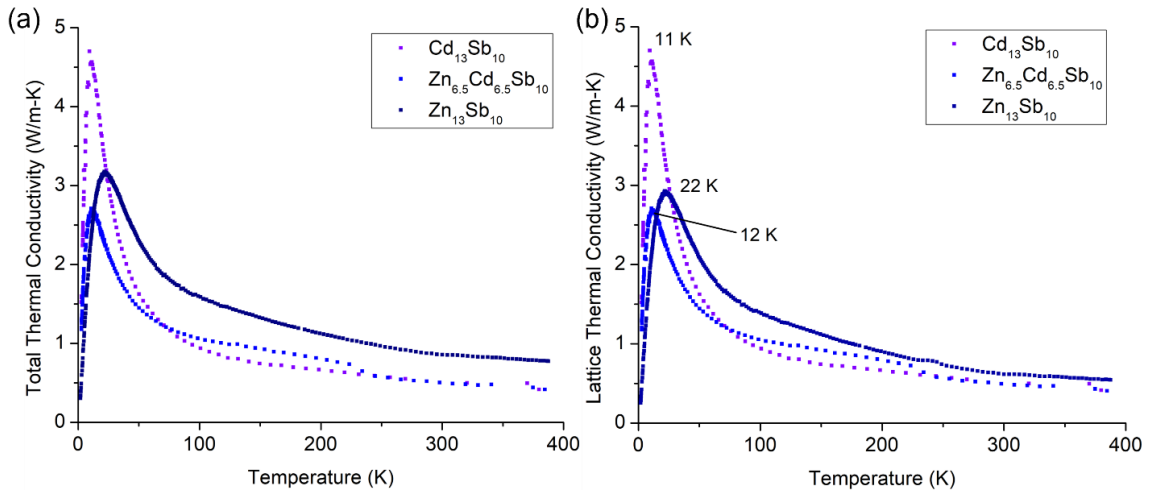


Figure 6.13. Low temperature (a) total and (b) lattice thermal conductivities of $(\text{Zn}_{1-x}\text{Cd}_x)_{13}\text{Sb}_{10}$.

The maxima in the lattice thermal conductivities of the $\text{Zn}_{1-x}\text{Cd}_x\text{Sb}$ samples are observed at 27, 15 and 24 K, for $x = 0, 0.5$ and 1 respectively, and they represent the onset of the Umklapp scattering as the dominant scattering channel. It is worth pointing that thermal conductivity of CdSb is lower than that of ZnSb, which can be attributed to the lower sound velocity in CdSb (2241 m/s in ZnSb to 1590 m/s in CdSb^{175,203}, due to its larger density and potentially lower Young modulus). Thermal conductivity of the $x = 0.5$ sample is even lower, which can be credited to the shorter mean free path due to the additional impurity scattering, i.e. the differences in the mass and size between Zn and Cd as described in the Klemens-Callaway model²⁰⁶.

According to the Matthiessen rule, the phonon relaxation time τ can be written as a combination of relaxation times from different processes:

$$\frac{1}{\tau} = \frac{1}{\tau_B} + \frac{1}{\tau_U} + \frac{1}{\tau_{im}} + \frac{1}{\tau_N} \quad (4)$$

where subscripts B stands for the grain boundary scattering, U for the Umklapp scattering, im for the impurity scattering, and N for the normal scattering. Since the same synthetic method was used, τ_B is assumed to be similar among the $\text{Zn}_{1-x}\text{Cd}_x\text{Sb}$ samples, and is constant with respect to temperature T . The impurity scattering (and the $1/\tau_{im}$ parameter) should be larger in the $\text{Zn}_{0.5}\text{Cd}_{0.5}\text{Sb}$ sample than that in the ZnSb and CdSb ones. Thus, the $\text{Zn}_{0.5}\text{Cd}_{0.5}\text{Sb}$ sample is expected to have the lowest lattice thermal conductivity in the series. While Umklapp scattering and the $1/\tau_U$ parameter may become dominant after a certain

temperature T , the impurity scattering and $1/\tau_{im}$ parameter will still play a significant role in the $\text{Zn}_{0.5}\text{Cd}_{0.5}\text{Sb}$ sample and will contribute to its lower lattice thermal conductivity as seen in **Figure 6.12**.

The maxima in the lattice thermal conductivities of the $(\text{Zn}_{1-z}\text{Cd}_z)_{13}\text{Sb}_{10}$ series are at 22, 12 and 11 K for the $z = 0, 0.5$ and 1, respectively (**Figure 6.13**). Similar to the $\text{Zn}_{1-x}\text{Cd}_x\text{Sb}$ series, the maxima shift to the lower temperatures as the Cd concentration increases. However, there is no clear relationship between the Cd concentration and thermal conductivity in the studied temperature range; and thus the arguments developed for the $\text{Zn}_{1-x}\text{Cd}_x\text{Sb}$ samples are not readily applied to the $(\text{Zn}_{1-z}\text{Cd}_z)_{13}\text{Sb}_{10}$ ones. We therefore suggest that thermal conductivity in the $(\text{Zn}_{1-z}\text{Cd}_z)_{13}\text{Sb}_{10}$ series is dominated by the presence of optical modes with lower frequencies, thus an onset of the Umklapp process occurs at lower temperatures. Optical phonon modes are mostly dispersion-less and can be described by a single frequency using the Einstein model. Therefore, the temperatures of the peaks have a positive correlation with the Einstein temperature θ_E (or the phonon frequency ν_E of the low-frequency optical modes) in the material. The peak shifts to lower temperatures in **Figure 6.14** thus suggest a decreasing ν_E from $\text{Zn}_{13}\text{Sb}_{10}$ to $\text{Cd}_{13}\text{Sb}_{10}$.

Low-frequency optical modes often lead to a low thermal conductivity because the frequency of the acoustic modes is limited by avoiding crossing with the optical modes. While the lattice thermal conductivity should be the highest for $\text{Zn}_{13}\text{Sb}_{10}$, a lower maximum thermal conductivity was measured in the present study. The thermal conductivity at low temperatures is limited by other effects, in particular grain boundary scattering as suggested

by the broad thermal conductivity peak. Increases in the lattice thermal conductivities below the maxima also mirror the changes in the heat capacity (**Figure 6.6**), since the phonon mean free path is not yet dominated by the Umklapp scattering. At higher temperatures, the lattice thermal conductivities of the $(\text{Zn}_{1-z}\text{Cd}_z)_{13}\text{Sb}_{10}$ series become similar, with that of $\text{Zn}_{13}\text{Sb}_{10}$ being slightly larger. It has to be mentioned that while the structures in the $\text{Zn}_{1-x}\text{Cd}_x\text{Sb}$ series remain the same in the studied temperature regions, the structures of $\text{Zn}_{13}\text{Sb}_{10}$ and $\text{Cd}_{13}\text{Sb}_{10}$ in the $(\text{Zn}_{1-z}\text{Cd}_z)_{13}\text{Sb}_{10}$ series are slightly different at lower temperatures.

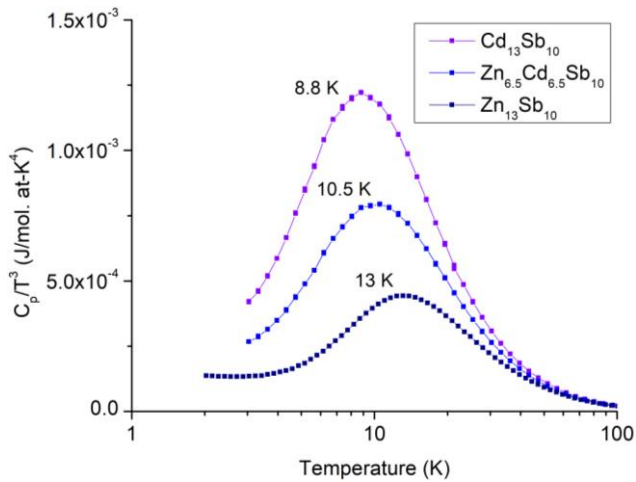


Figure 6.14. C_p/T^3 vs. T curves of the $(\text{Zn}_{1-z}\text{Cd}_z)_{13}\text{Sb}_{10}$ series.

6.4. Conclusions

The thermoelectric properties of the two solid-solution series, $(\text{Zn,Cd})_{13}\text{Sb}_{10}$ and $(\text{Zn,Cd})\text{Sb}$, were studied in this work. The work has revealed non-monotonous changes in the transport properties of the same series upon the Cd substitution, and these changes are dependent on the intrinsic structural and compositional features of the material. It is

surprising that the thermal conductivity of the $(\text{Zn}_{1-z}\text{Cd}_z)_{13}\text{Sb}_{10}$ ($z = 0.5$) sample with the largest atomic disorder does not resemble that of the previously reported In-doped $\text{Zn}_{13}\text{Sb}_{10}$, in which point defect scattering is the dominant mechanism for phonon suppression.

The large monoclinic structure (α polymorph) was confirmed for $\text{Cd}_{13}\text{Sb}_{10}$ at low temperatures, with the high-temperature β polymorph adopting the rhombohedral $R\bar{3}c$ space group, similar to the pristine $\beta\text{-Zn}_{13}\text{Sb}_{10}$ phase. The $\alpha - \beta$ phase transition of $\text{Cd}_{13}\text{Sb}_{10}$ at 368 K is assumed to be 1st order in nature.

The ELF analysis of ZnSb suggests the presence of the covalent Sb – Sb, metallic Zn – Zn and ionic Zn – Sb interactions in the structure. Due to the structural similarities between $\text{Zn}_{13}\text{Sb}_{10}$ and ZnSb, the bonding picture in $\text{Zn}_{13}\text{Sb}_{10}$ phase is assumed to be similar to that in the ZnSb phase.

6.5. Supplementary Materials

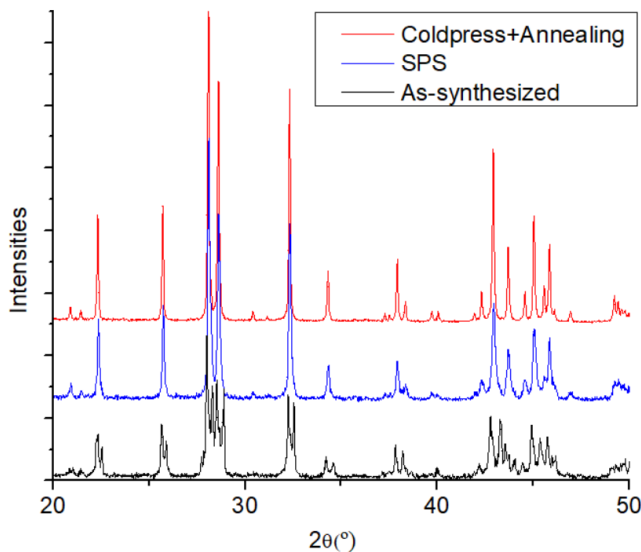


Figure 6.S1. X-ray diffraction pattern of $\text{Zn}_{0.6}\text{Cd}_{0.4}\text{Sb}$ sample: as-synthesized, after SPS, and after reannealing following cold-press.

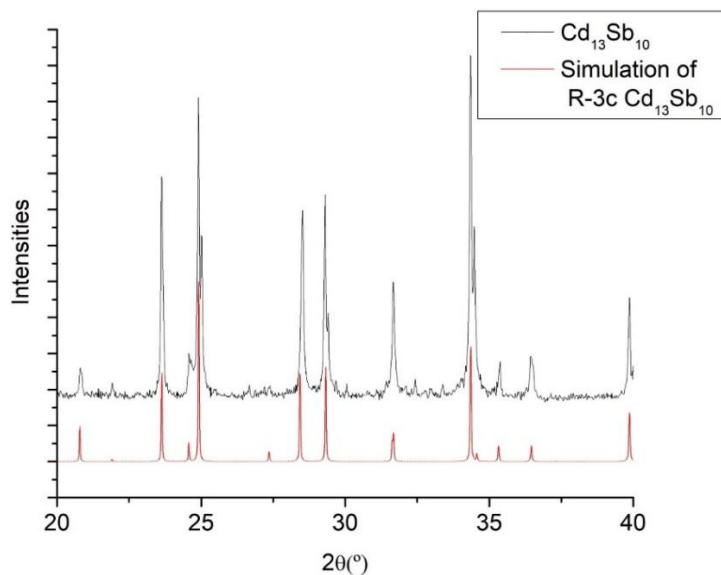
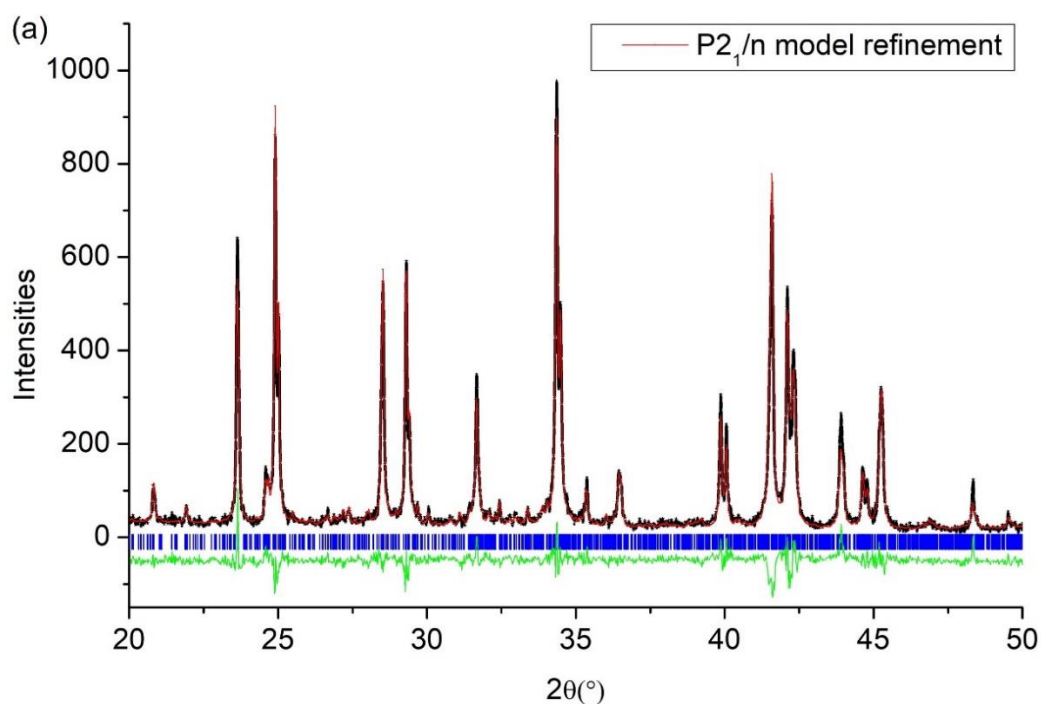


Figure 6.S2. PXRD pattern of $\text{Cd}_{13}\text{Sb}_{10}$, taken experimentally (black) and simulated pattern without symmetry reduction (structure of $\beta\text{-Cd}_{13}\text{Sb}_{10}$, red).



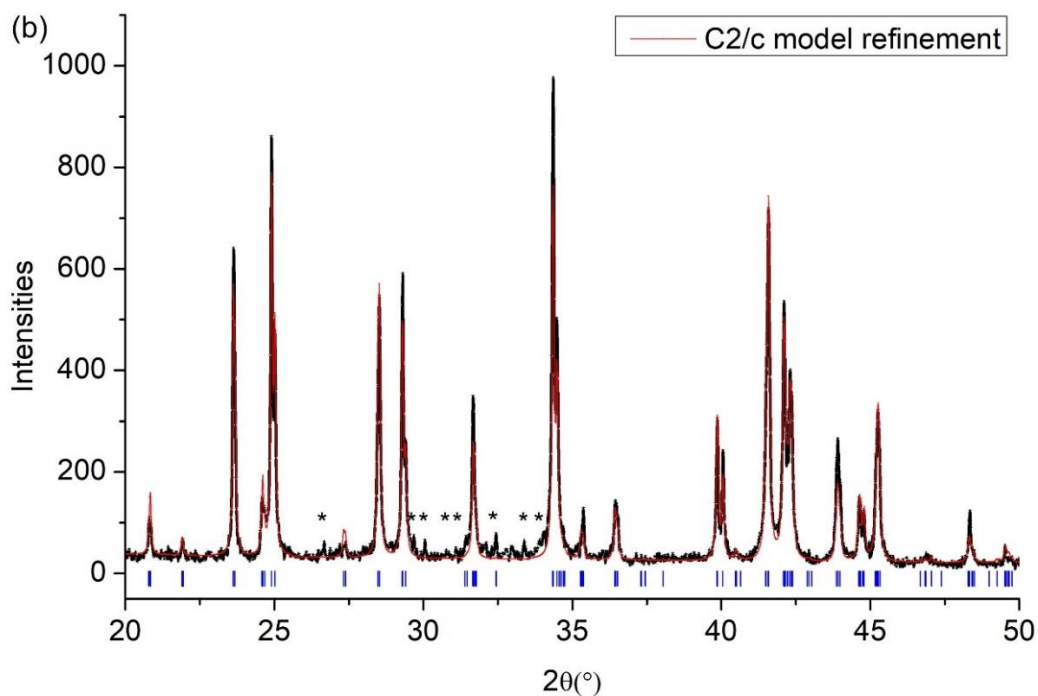


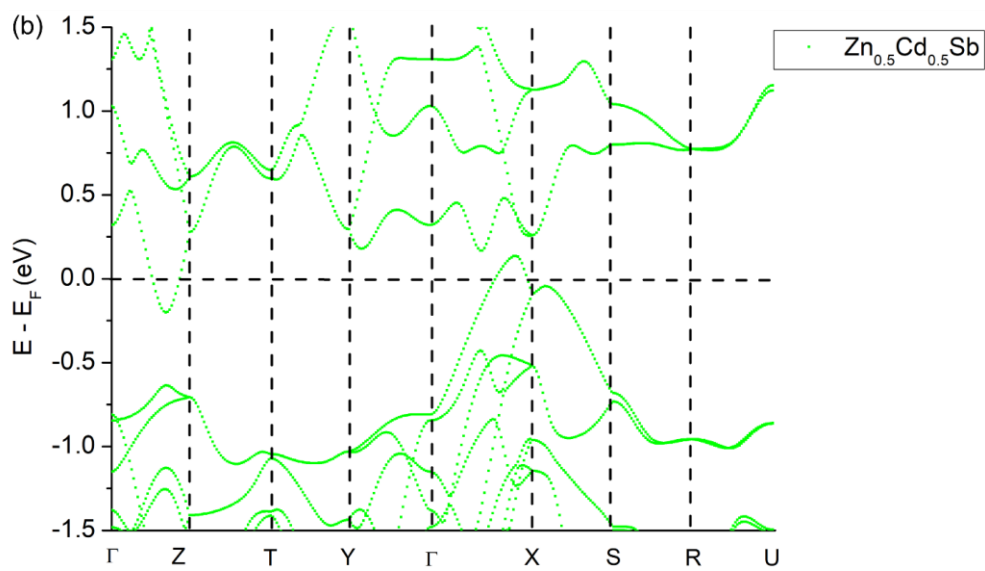
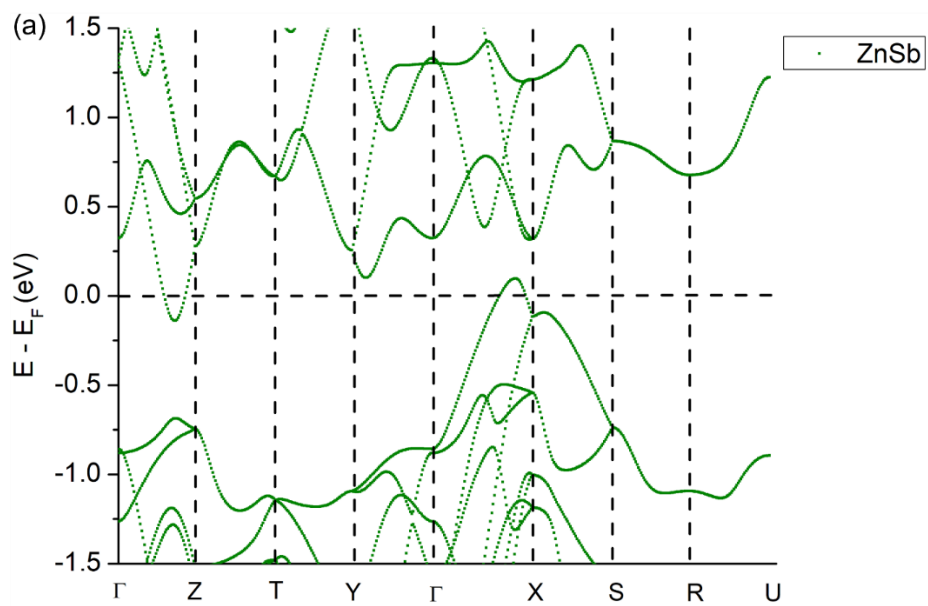
Figure 6.S3. Rietveld refinement of the $\text{Cd}_{13}\text{Sb}_{10}$ sample with (a) the current structural model, and (b) the $C2/c$ cell, derived from the low temperature $\alpha\text{-Zn}_{13}\text{Sb}_{10}$ phase.

Table 6.S1. Atomic and isotropic displacement (U_{eq}) parameters of the grain from the $\text{Cd}_{13}\text{Sb}_{10}$ melt ingot sample.

Atom	Site	Occu- pancy	x/a	y/b	z/c	$U_{\text{eq}}(\text{\AA}^2)$
Sb1	4e	1	0.14381(8)	0.25118(3)	0.04847(3)	0.0152(2)
Sb2	4e	1	0.35960(8)	0.25182(3)	0.12077(3)	0.0152(2)
Sb3	4e	1	0.85872(8)	0.50152(3)	0.11989(3)	0.0151(2)
Sb4	4e	1	0.24800(6)	0.42858(4)	0.08424(3)	0.0156(2)
Sb5	4e	1	0.75085(7)	0.17709(4)	0.75141(3)	0.0170(2)
Sb6	4e	1	0.42073(8)	0.65747(3)	0.95978(3)	0.0172(2)
Sb7	4e	1	0.93283(8)	0.41079(3)	0.96788(3)	0.0156(2)
Sb8	4e	1	0.13997(8)	0.25145(3)	0.71567(3)	0.0160(2)
Sb9	4e	1	0.64201(8)	0.50226(3)	0.04835(3)	0.0153(2)
Sb10	4e	1	0.24957(6)	0.42804(4)	0.41712(3)	0.0161(2)
Sb11	4e	1	0.74976(6)	0.17986(4)	0.08176(3)	0.0163(2)

Sb12	4e	1	0.86128(8)	0.50152(3)	0.45296(3)	0.0159(2)
Sb13	4e	1	0.13940(8)	0.74679(3)	0.04275(3)	0.0157(2)
Sb14	4e	1	0.85866(8)	0.49646(3)	0.78926(3)	0.0157(2)
Sb15	4e	1	0.07179(8)	0.66197(3)	0.86486(3)	0.0159(2)
Sb16	4e	1	1.25091(6)	0.42205(4)	0.74750(3)	0.0156(2)
Sb17	4e	1	0.57217(8)	0.41297(3)	0.53391(3)	0.0159(2)
Sb18	4e	1	0.25109(6)	0.32812(4)	0.91756(3)	0.0162(2)
Sb19	4e	1	0.92326(8)	0.40862(3)	0.62954(3)	0.0167(2)
Sb20	4e	1	0.42896(8)	0.66286(3)	0.29880(3)	0.0164(2)
Sb21	4e	1	0.58020(8)	0.40876(3)	0.87369(3)	0.0174(2)
Sb22	4e	1	0.64058(8)	0.50359(4)	0.38245(4)	0.0185(2)
Sb23	4e	1	0.07299(8)	0.66002(3)	0.20334(3)	0.0165(2)
Sb24	4e	1	0.07379(8)	0.08444(4)	0.69807(4)	0.0208(2)
Sb25	4e	1	0.36145(8)	0.25367(4)	0.78526(4)	0.0197(2)
Sb26	4e	1	0.57399(8)	0.83465(4)	0.03073(4)	0.0206(2)
Sb27	4e	1	0.64233(8)	0.49267(4)	0.71407(4)	0.0192(2)
Sb28	4e	1	0.35548(8)	0.74294(4)	0.11823(4)	0.0195(2)
Sb29	4e	1	0.06054(8)	0.16093(4)	0.87226(3)	0.0214(2)
Sb30	4e	1	0.55980(8)	0.91252(4)	0.20362(3)	0.0205(2)
Cd1	4e	1	0.17358(9)	0.66698(4)	0.97257(4)	0.0232(2)
Cd2	4e	1	0.02336(9)	0.47991(4)	0.05531(4)	0.0225(2)
Cd3	4e	1	0.97645(10)	0.22873(4)	1.11110(4)	0.0233(2)
Cd4	4e	1	0.63334(9)	0.60521(4)	0.34305(4)	0.0250(2)
Cd5	4e	1	0.82855(9)	0.41766(4)	0.86139(4)	0.0239(2)
Cd6	4e	1	0.13727(9)	0.35130(4)	0.01002(4)	0.0235(2)
Cd7	4e	1	0.52950(10)	0.22738(4)	0.72173(4)	0.0243(2)
Cd8	4e	1	0.31893(9)	0.17424(4)	0.18885(4)	0.0249(2)
Cd9	4e	1	0.32219(9)	0.66721(4)	0.19255(4)	0.0253(2)
Cd10	4e	1	0.67488(9)	0.41581(4)	0.64115(4)	0.0244(2)
Cd11	4e	1	0.86842(9)	0.59981(4)	0.16248(4)	0.0236(2)
Cd12	4e	1	0.82546(9)	0.42145(4)	0.18662(4)	0.0245(2)
Cd13	4e	1	0.62411(9)	0.59875(4)	0.00096(4)	0.0246(2)
Cd14	4e	1	0.82222(10)	0.42347(4)	0.52161(4)	0.0259(2)

Cd15	4e	1	0.68635(9)	0.42441(4)	0.98157(4)	0.0251(2)
Cd16	4e	1	0.86398(9)	0.60259(4)	0.49284(4)	0.0264(2)
Cd17	4e	1	0.18011(10)	0.17344(4)	0.64806(4)	0.0258(2)
Cd18	4e	1	0.17550(10)	0.17073(4)	0.98190(4)	0.0248(2)
Cd19	4e	1	0.37462(9)	0.35291(4)	0.82995(4)	0.0256(2)
Cd20	4e	1	0.47184(10)	0.47680(4)	0.44476(4)	0.0257(2)
Cd21	4e	1	0.87304(9)	0.59862(4)	0.83015(4)	0.0257(2)
Cd22	4e	1	0.02855(10)	0.48270(4)	0.38761(4)	0.0249(2)
Cd23	4e	1	0.12806(9)	0.34927(4)	0.66801(4)	0.0254(2)
Cd24	4e	1	0.97210(10)	0.23115(4)	0.78015(4)	0.0265(2)
Cd25	4e	1	0.36303(9)	0.35198(4)	0.15927(4)	0.0262(2)
Cd26	4e	1	0.46826(10)	0.48133(4)	0.10810(4)	0.0267(2)
Cd27	4e	1	0.52968(10)	0.23284(4)	0.05873(4)	0.0263(2)
Cd28	4e	1	0.37472(9)	0.34916(4)	0.49760(4)	0.0256(2)
Cd29	4e	1	0.01215(10)	0.46662(5)	0.72310(4)	0.0333(3)
Cd30	4e	1	0.48844(11)	0.46917(5)	0.78448(4)	0.0351(3)
Cd31	4e	1	0.29626(11)	0.33188(4)	0.36873(4)	0.0356(2)
Cd32	4e	1	0.70257(11)	0.08097(4)	0.79956(4)	0.0347(2)
Cd33	4e	1	0.26844(15)	0.22563(5)	0.87761(7)	0.0603(5)
Cd34	4e	0.558(4)	0.21673(18)	0.59867(7)	0.62279(8)	0.0347(6)
Cd34A	4e	0.442(4)	0.2834(2)	0.65139(9)	0.70879(10)	0.0365(8)
Cd35	4e	0.392(7)	0.0085(4)	0.07564(17)	0.8088(2)	0.044(2)
Cd35A	4e	0.608(7)	0.9677(2)	0.09634(11)	0.78417(11)	0.0344(8)
Cd36	4e	0.503(8)	0.4699(3)	0.84584(14)	0.11716(14)	0.038(1)
Cd36A	4e	0.497(8)	0.5107(3)	0.82552(12)	0.14139(16)	0.040(1)
Cd37	4e	0.49(6)	0.2861(7)	0.5270(2)	0.71665(18)	0.026(1)
Cd37A	4e	0.51(6)	0.259(3)	0.5237(4)	0.7045(13)	0.051(4)
Cd38	4e	0.51(5)	0.9847(7)	0.7110(9)	0.1072(4)	0.046(2)
Cd38A	4e	0.49(5)	0.9887(6)	0.7206(3)	0.1095(3)	0.021(1)
Cd39	4e	0.32(6)	0.500(2)	0.7119(14)	0.0504(6)	0.047(3)
Cd39A	4e	0.68(6)	0.5152(7)	0.7205(2)	0.0484(2)	0.026(1)



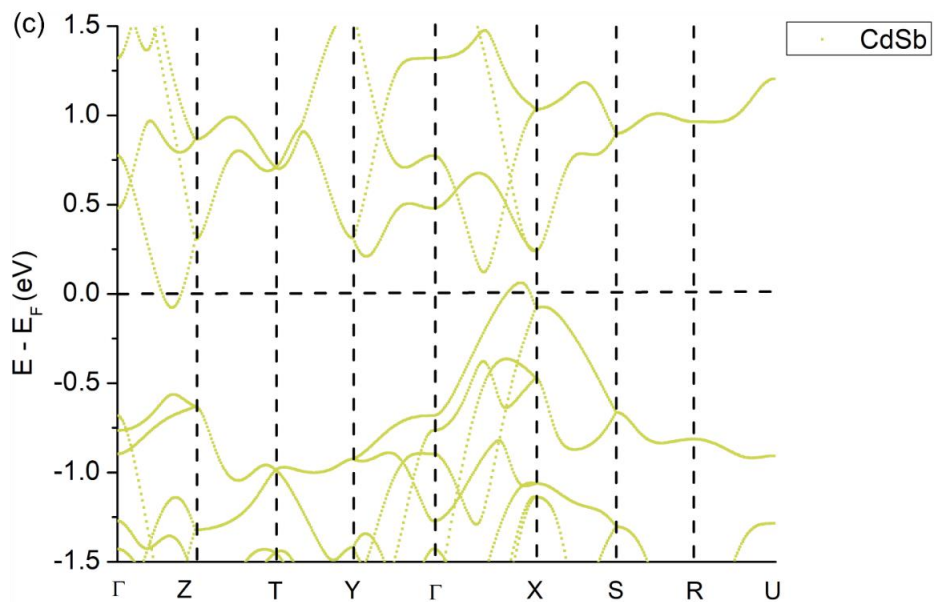
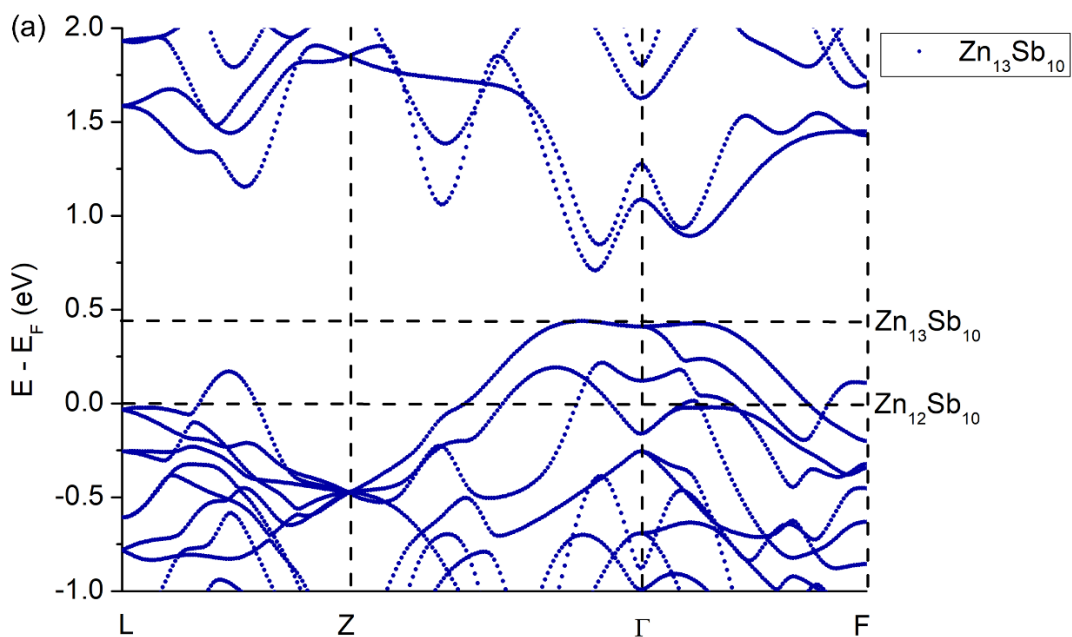


Figure 6.S4. Electronic band structures of $x = (a) 0$, $(b) 0.5$ and $(c) 1$ in the $\text{Zn}_{1-x}\text{Cd}_x\text{Sb}$ series.



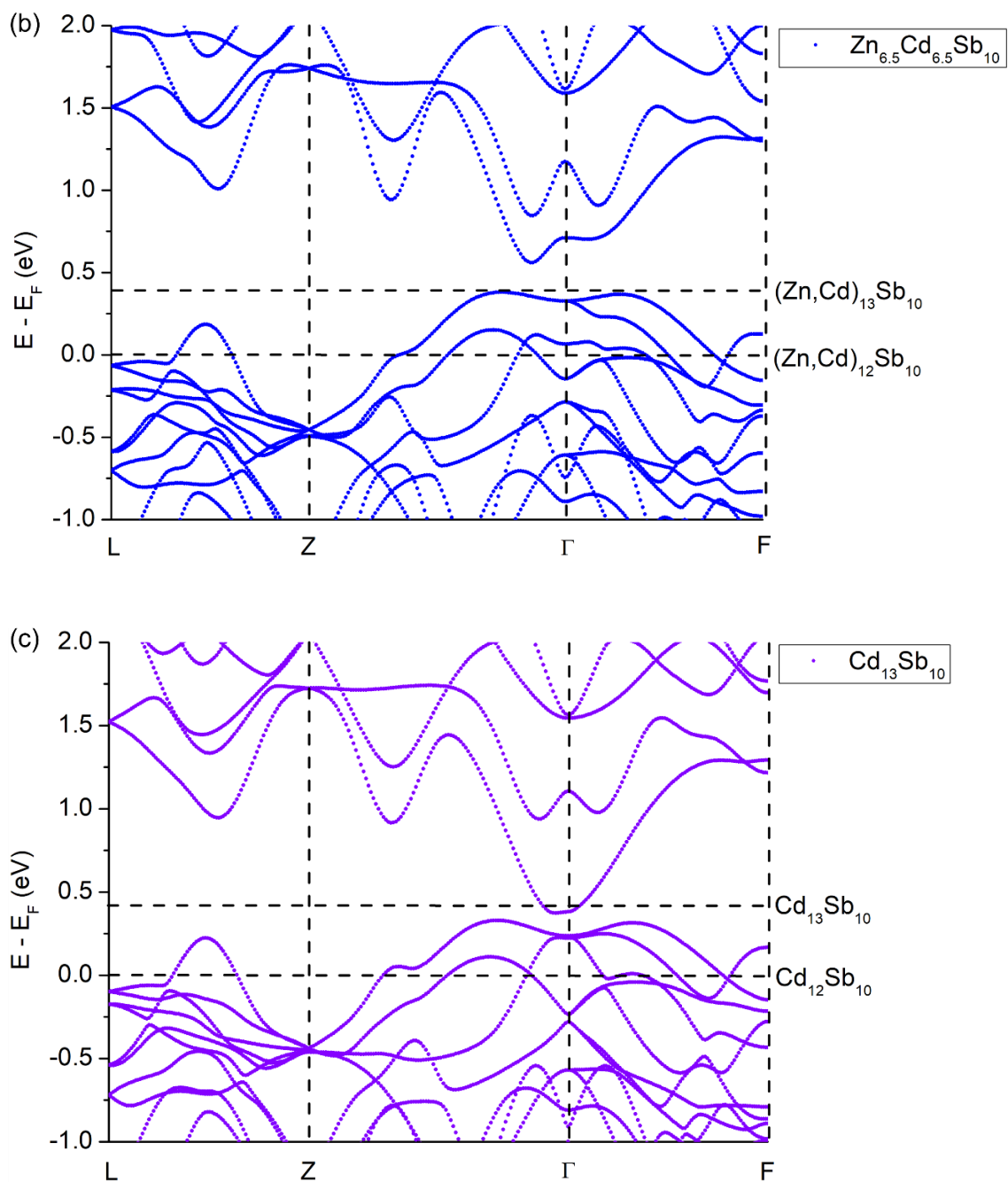
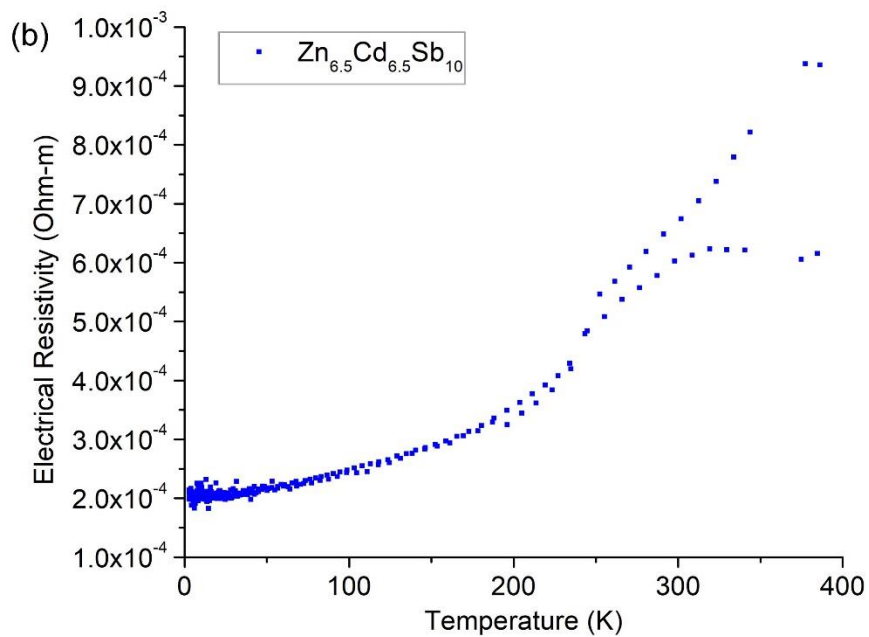
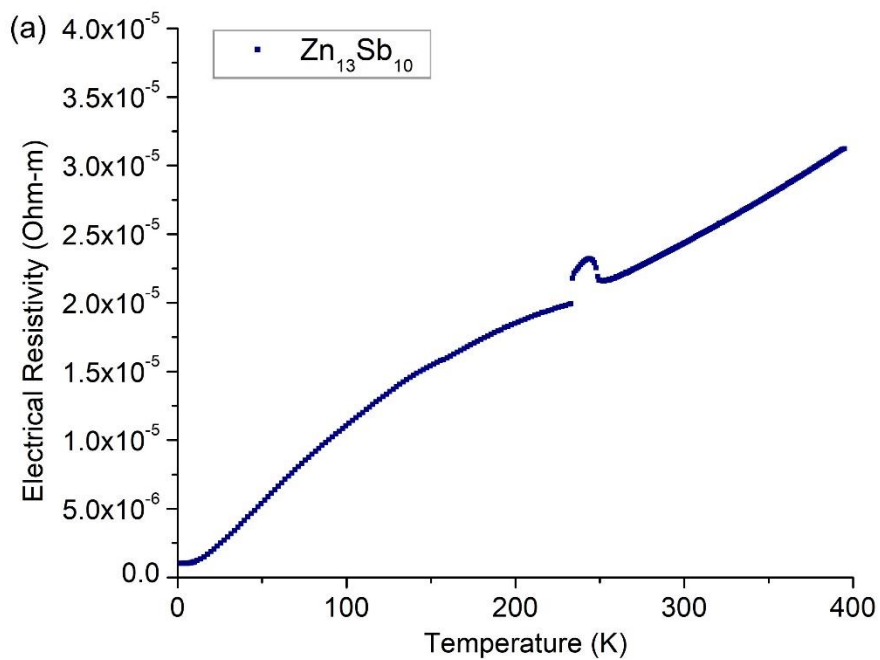


Figure 6.S5. Electronic band structures of $z =$ (a) 0, (b) 0.5 and (c) 1 in the $(\text{Zn}_{1-z}\text{Cd}_z)_{13}\text{Sb}_{10}$ series.



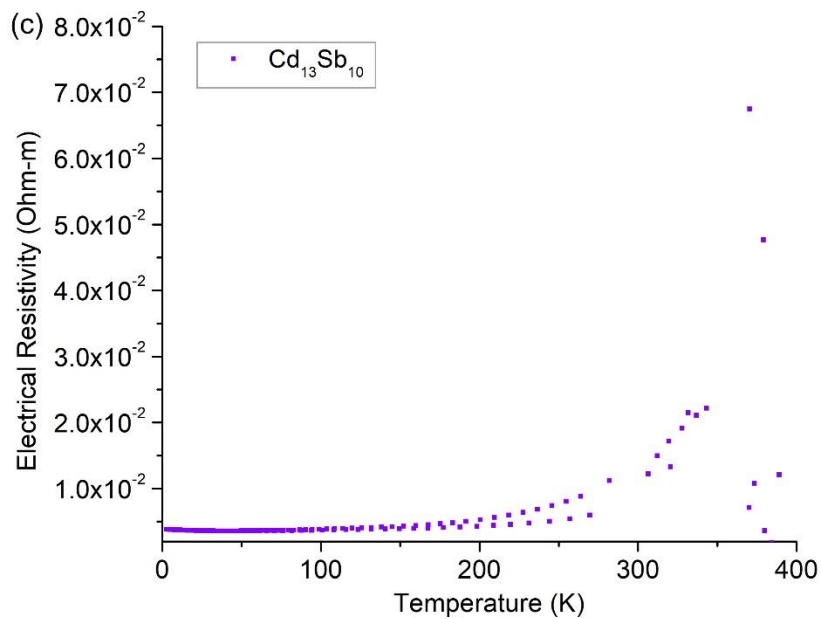


Figure 6.S6. LT electrical resistivities of the $(\text{Zn}_{1-z}\text{Cd}_z)_{13}\text{Sb}_{10}$ series, $z =$ (a) 0, (b) 0.5 and (c) 1.

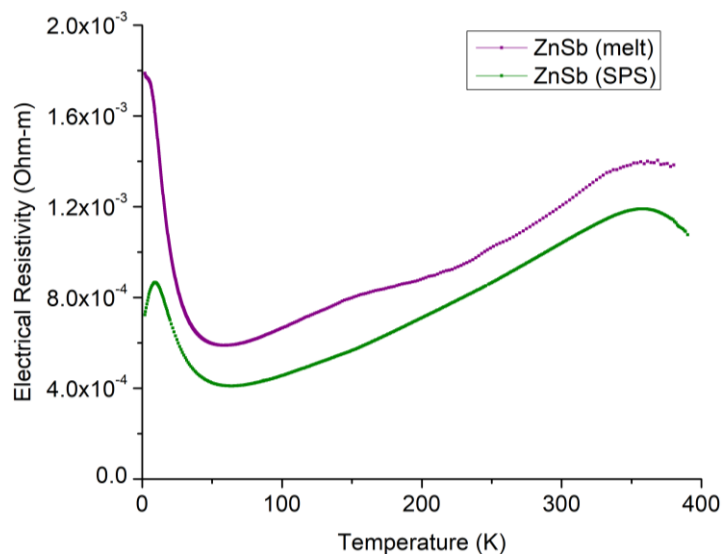


Figure 6.S7. LT Electrical resistivities of melt ZnSb and SPS ZnSb.

Chapter 7. Synthesis, Structure and Thermoelectric Properties of α -Zn₃Sb₂ and Comparison to β -Zn₁₃Sb₁₀

This chapter contains the material covered in the manuscript “Synthesis, Structure and Thermoelectric Properties of α -Zn₃Sb₂ and Comparison to β -Zn₁₃Sb₁₀”, which was published in *Chemistry of Materials* (*Chem. Mater.*, **2017**, 29, 5149 – 5258). The modelling of thermoelectric properties were conducted by Drs. Brenden R. Ortiz and Eric S. Toberer. Dr. Allan He participated in part of sample syntheses. The high-temperature synchrotron data were collected by Drs. Volodymyr Svitlyk and Dmitry Chernyshov at the European Synchrotron Radiation Facility (ESRF), Grenoble, France. The low temperature physical property measurements were collected by Dr. Taras Kolodiazhnyi at the National Institute for Materials Science (NIMS), Tsukuba, Ibaraki, Japan. Dr. Sven Lidin assisted in the structure determination of the α -Zn₃Sb₂ phase. The experimental procedures were completed by the candidate. The candidate assisted in the data interpretation and manuscript preparation, done by my supervisor.

Reproduced with permission from Brenden R. Ortiz, Eric S. Toberer, Allan He, Volodymyr Svitlyk, Dmitry Chernyshov, Taras Kolodiazhnyi, Sven Lidin and Yuriy Mozharivskyj, *Chem. Mater.*, **2017**, 29, 5149 – 5258. Copyright 2017 American Chemical Society.

Zn–Sb Compounds (e.g., ZnSb, β -Zn₁₃Sb₁₀) are known to have intriguing thermoelectric properties, but studies of the Zn₃Sb₂ composition are largely absent. In this work, α -Zn₃Sb₂ was synthesized and studied via temperature-dependent synchrotron powder diffraction. The α -Zn₃Sb₂ phase undergoes a phase transformation to the β form at 425 °C, which is stable until melting at 590 °C. Rapid quenching was successful in stabilizing the α phase at room temperature, although all attempts to quench β -Zn₃Sb₂ were unsuccessful. The structure of α -Zn₃Sb₂ was solved using single crystal diffraction techniques and verified through Rietveld refinement of the powder data. α -Zn₃Sb₂ adopts a large hexagonal cell ($R\bar{3}$ space group, $a = 15.212(2)$, $c = 74.83(2)$ Å) containing a well-defined framework of isolated Sb³⁻ anions but highly disordered Zn²⁺ cations. Dense ingots of both the α -Zn₃Sb₂ and β -Zn₁₃Sb₁₀ phases were formed and used to characterize and compare the low temperature thermoelectric properties. Resistivity and Seebeck coefficient measurements on α -Zn₃Sb₂ are consistent with a small-gap, degenerately doped, p-type semiconductor. The temperature-dependent lattice thermal conductivity of α -Zn₃Sb₂ is unusual, resembling that of an amorphous material. Consistent with the extreme degree of Zn disorder observed in the structural analysis, phonon scattering in α -Zn₃Sb₂ appears to be completely dominated by point-defect scattering over all temperatures below 350 K. This contrasts with the typical balance between point-defect scattering and Umklapp scattering seen in β -Zn₁₃Sb₁₀. Using the Debye–Callaway interpretation of the lattice thermal conductivity, we use the differences between α -Zn₃Sb₂ and β -Zn₁₃Sb₁₀ to illustrate the potential significance of cation/anion disorder in the Zn–Sb system.

7.1. Introduction

Investigating a narrow composition space can reveal how specific differences in crystal structure and disorder influence transport properties, while the chemical bonding remains largely similar. The Zn–Sb binary system is one example in which a structurally complex landscape and diverse properties are found within a relatively small compositional range (**Figure 7.1**)¹²⁵. The system contains two well-known thermoelectric materials, ZnSb^{207,208} and Zn₁₃Sb₁₀ (known as “Zn₄Sb₃”)^{90,94,96}, as well as four other phases, Zn₈Sb₇⁹⁸, Zn_{9-δ}Sb₇⁹⁹, Zn_{17+α}Sb₁₂²⁰⁹, and Zn₃Sb₂, that are only stable at higher temperatures. Additionally, a Zn_{1+δ}Sb phase has been prepared in nanoparticle form²¹⁰.

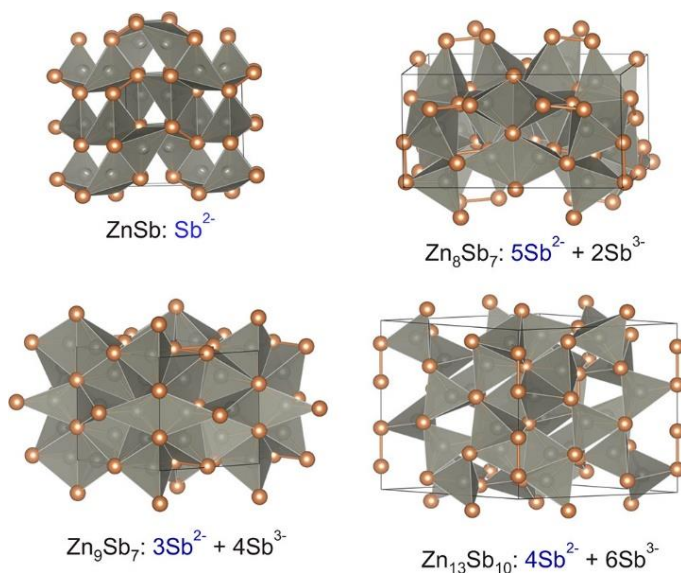


Figure 7.1. Structures of the Zn–Sb phases that were obtained in bulk form. Orange atoms are Sb, gray atoms are Zn. Bonds in orange are Sb–Sb dimers. In each structure, Sb²⁻ anions make the Sb–Sb dimers, Sb³⁻ anions are isolated anions surrounded by only

Zn²⁺ cations. In Zn₈Sb₇, two split Zn sites are not shown; in Zn₁₃Sb₁₀, only the major Zn site is shown.

ZnSb is an ordered phase that follows the Zintl-Klemm formalism via the formation of Sb₂⁴⁻ dimers. For the other Zintl-like Zn–Sb compounds, the ratio between Sb₂⁴⁻ dimers and isolated Sb³⁻ anions is adjusted to meet the charge balance. Zn₃Sb₂ should provide an ionic boundary, with a structure composed strictly of isolated Sb³⁻ anions. When compared to ZnSb, all other Zn–Sb compounds are Zn richer and exhibit substantial Zn disorder. In Zn₈Sb₇, ²/₈ of the Zn sites are split⁹⁸. In Zn_{9-δ}Sb₇ all Zn sites are highly deficient, but since this phase is stable above 514 °C, such Zn disorder cannot be directly compared to those in Zn₁₃Sb₁₀ and Zn₈Sb₇ at room temperature⁹⁹. In incommensurate Zn_{17+α}Sb₁₂, ⁷/₁₁ of the Zn sites are split and one out of six Sb sites (Sb6) tends to make Sb–Sb dimers²⁰⁹. The composition of this phase can be written as (Zn²⁺)_{17+α}(Sb³⁻)_{10+2α}(Sb²⁻)_{2-2α}, with α being a fraction of unpaired Sb6 atoms. Since α < 1, (Zn²⁺)_{17+α}(Sb³⁻)_{10+2α}(Sb²⁻)_{2-2α} is not the Zn₃Sb₂ phase, which contains only Sb³⁻ anions. In Zn₁₃Sb₁₀ the only major Zn site (36f) is ~10% deficient and there are at least three extra Zn sites with occupancies of ~6 % or less^{94,96,113,131,211}. The excellent thermoelectric performance in Zn₁₃Sb₁₀ has been attributed to structural disorder and nonstoichiometry. Furthermore, charge carrier concentration can be tuned via adjustment of Zn vacancy concentration¹¹⁶ and the random distribution of Zn is believed to dictate the extremely low thermal conductivity of Zn₁₃Sb₁₀⁹⁶ (as well as of Zn₈Sb₇⁹⁸).

As point defects are poor scattering centers for acoustic phonons, the extremely low thermal conductivity of $\text{Zn}_{13}\text{Sb}_{10}$ requires further explanation. Inelastic neutron scattering reveals the presence of low-energy optical phonons from the Sb_2 dimers¹⁹⁵. Such modes can increase anharmonicity-driven phonon–phonon scattering rates as well as providing additional scattering channels. The specific source of these low lying optical modes is in question as a subsequent theoretical analysis of the lattice thermal conductivity of $\text{Zn}_{13}\text{Sb}_{10}$ and ZnSb has revealed low-lying optical modes involving both Zn and Sb vibrations, thus questioning the specific role of the Sb_2 dimers²¹². Prior work has also proposed that the anharmonic motion of free Sb^{3-} anions (not the Sb_2 dimers) coordinated only by Zn atoms leads to low lattice thermal conductivity. A further source of low thermal conductivity may simply be intrinsic to the ground state phonon band structure. $\text{Zn}_{13}\text{Sb}_{10}$ has 23 atoms in the hypothetical primitive, ordered cell, leading to extremely low velocity optical modes and acoustic branches that carry little heat. Given this ambiguity, comparing the thermal transport of $\text{Zn}_{13}\text{Sb}_{10}$ to other Zn–Sb binaries with disorder may provide insight into the relative importance of different scattering mechanisms.

In this paper, we investigate the synthesis, structural chemistry, and transport properties of $\alpha\text{-Zn}_3\text{Sb}_2$ and contrast these results to those of $\text{Zn}_{13}\text{Sb}_{10}$. This comparison is intriguing, as $\alpha\text{-Zn}_3\text{Sb}_2$ provides two distinct structural differences from $\text{Zn}_{13}\text{Sb}_{10}$: an incredibly complex primitive unit cell (630/3 atoms in primitive cell) and the absence of Sb_2 dimers. High temperature synchrotron diffraction data revealed the phase evolution of α - and β - Zn_3Sb_2 . Dense, polycrystalline ingots of both $\alpha\text{-Zn}_3\text{Sb}_2$ and $\text{Zn}_{13}\text{Sb}_{10}$ were formed and the electronic and thermal properties were measured at low temperature. The resulting thermal

data were analyzed within a Debye-Callaway model to understand the roles of phonon velocity and scattering rates for α -Zn₃Sb₂ and Zn₁₃Sb₁₀.

7.2. Experimental Section

7.2.1. Synthesis

Preparation of α -Zn₃Sb₂ utilized elemental Zn (99.99 wt %, Alfa Aesar) and Sb (99.999 wt % Alfa Aesar). The elements were loaded into silica tubes, evacuated until 10⁻⁴ Torr, and sealed. The ampules were heated to 750 °C at 100 °C/h and soaked for 4 h at 750 °C. Ampules were shaken twice during the 4 h soak. Samples were subsequently cooled to 500 °C at 50 °C/h, then to 430 °C at 5 °C/h, annealed at 430 °C for 48 h, and finally quenched in an ice water bath. Different annealing temperatures and loading compositions were tested. The annealing temperature of 430 °C yielded the best quality sample. We have empirically determined that the purest samples of α -Zn₃Sb₂ are produced from samples with nominal composition Zn_{3.26}Sb₂. Relative to nominal, Zn-poor compositions yield significant amounts of Zn₁₃Sb₁₀, while Zn-rich compositions yield elemental Zn in addition to the main phase. The extra elemental zinc used in the Zn_{3.26}Sb₂ sample was deposited on the silica walls and also was found as grouped elemental inclusions inside the sample as verified by the EDS analysis.

To compare physical properties, the β -Zn₁₃Sb₁₀ phase was also prepared. The loading composition was stoichiometric Zn₁₃Sb₁₀ and the synthetic procedure was adopted from ref. ⁹⁵. However, we lowered the annealing temperature to 350 °C and extended the

annealing time to 48 h. On the basis of the X-ray powder diffraction, the sample contained phase-pure β -Zn₁₃Sb₁₀.

7.2.2. Structure Analysis

Room-temperature single crystal data for α -Zn₃Sb₂ were collected on a STOE IPDS II diffractometer with Mo K α radiation. Numerical absorption correction was based on the crystal shapes that were originally derived from optical face indexing, but later optimized against equivalent reflections using the STOE *X-Shape* software¹⁰⁴. Structure refinement was performed using the *SHELXL* program¹⁰⁷. The crystallographic parameters and refinement results are summarized in **Table 7.1**. All 18 Sb sites and 8 Zn sites could be well refined with full occupancies; the other 39 Zn sites had occupancies ranging from 89% to 8% (**Table 7.S1** in the Supporting Information). All deficient Zn sites had other deficient Zn sites at distances closer than the Zn diameter of 2.7 Å. The deficient Zn sites were refined with the same isotropic displacement parameter, but their occupancies were unrestrained. The resulting composition was Zn₃₆₇Sb₂₅₂ or Zn_{2.91}Sb₂.

Table 7.1. Crystallographic and Refinement Data for the α -Zn₃Sb₂ Crystal.

Refined composition	Zn _{2.91(2)} Sb ₂
Formula weight	433.90
Temperature	293(2) K
Wavelength	0.71073 Å
Space group	$R\bar{3}$
Unit cell dimensions	$a = 15.212(2)$ Å $c = 74.83(2)$ Å
Volume	14819.(4) Å ³
Z	126
Density(calc'd)	6.126 g/cm ³
Abs. coeff.	25.769 mm ⁻¹

F(000)	23862
2 θ range for data collection	4.14 to 55.96°
Index ranges	-19 $\leq h \leq$ 9, 0 $\leq k \leq$ 19, -89 $\leq l \leq$ 94
Reflns. collected	15103
Indep. reflns.	7759 [$R(\text{int}) = 0.0709$]
Completeness to 2 $\theta = 55.96^\circ$	97.7 %
Data/restraints/parameters	7759/0/308
GOF on F ²	1.136
Final R indices [$I > 2\sigma(I)$]	$R_1 = 0.0891$, $wR_2 = 0.1461$
R indices (all data)	$R_1 = 0.1672$, $wR_2 = 0.1815$
Extinction coeff.	0.0000000(4)
Largest diff. peak and hole	4.761 and -4.111 e/Å ³

Powder data for the Zn₃Sb₂ sample were collected on a PANalytical X'Pert Pro diffractometer with a linear X'Celerator detector, Cu K α_1 radiation, 2 θ range from 20 to 100°, a step size of 0.0042° and the total collection time of 16 h. A full-profile Rietveld refinement (*Rietica* program¹¹¹, **Figure 7.2**) was performed to verify the structural model derived from the single crystal data. Except for the Zn11 and Zn47 sites, all other atomic sites could be well refined (**Table 7.S3** in Supplementary Information). The occupancy of the Zn11 and Zn47 sites became zero and thus these sites were omitted from the powder diffraction results. The Rietveld refinement yielded Zn₃₈₄₍₄₎Sb₂₅₂ (Zn_{3.05(3)}Sb₂), which is slightly more Zn rich than that derived from the single crystal data. The powder refinement results are summarized in **Table 7.2**.

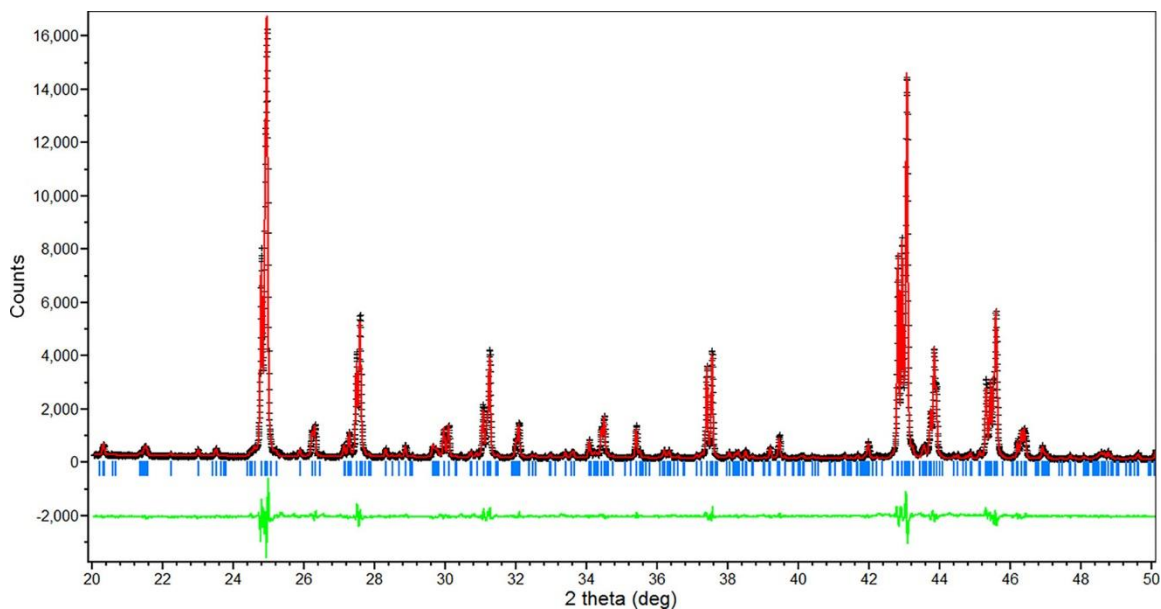


Figure 7.2. Rietveld refinement of the powder diffraction data for Zn_3Sb_2 . Only the $2\theta = 20 - 50^\circ$ range is shown. Black crosses and the red line represent observed and calculated intensities; the green line is the difference between the intensities. The vertical bars show positions of Bragg peaks.

Table 7.2. Powder Refinement Data for the Zn_3Sb_2 Samples at 293 K, $\text{CuK}\alpha_1$ Radiation, $2\theta = 20^\circ - 100^\circ$, Step 0.0042° .

Refined composition	$\text{Zn}_{3.05(3)}\text{Sb}_2$
Space group (Pearson sym.)	$R\bar{3}$
Lattice parameters, \AA	$a = 15.12800(2)$ $c = 74.8269(2)$
Volume, \AA^3	14830.35(5)
Z	126
Reflections	3386
Atomic parameters refined	207
R_I	0.028
R_P	0.070
R_{wP}	0.092
χ^2	2.81

$$R_I = \sum |I_o - I_c| / \sum |I_o|, R_p = \sum |y_{io} - y_{ic}| / \sum |y_{io}|, R_{wp} = (\sum w_i (y_{io} - y_{ic})^2 / \sum w_i (y_{io})^2)^{1/2}, w_i = (y_{io})^{-1/2}.$$

7.2.3. Synchrotron Powder Diffraction Studies

Temperature-dependent powder diffraction data for the Zn_3Sb_2 sample were collected at the Swiss-Norwegian Beamlines, BM01A station at the European Synchrotron Radiation Facility (ESRF, Grenoble, France) with a Dectris Pilatus2M detector in a ramp mode in the 20 – 650 °C temperature range with a typical step width of 1.5 – 1.8 °C. The wavelength was set to 0.968238 Å. The temperature was controlled with an in-house developed heat blower. The heating and cooling were done at a rate of 2 °C/min with a 20 s exposure time per point. The time between the two consecutive diffraction data was close to 1 min. Experimental powder diffraction data were integrated and processed with the FIT2D software²¹³.

7.2.4. Electron Microprobe Analysis (EMPA)

Electron microprobe analysis was performed on the Zn_3Sb_2 sample in order to establish the true composition of the α - Zn_3Sb_2 phase. The sample was mounted in discs of epoxy resin one inch in diameter and approximately 10 mm in thickness. Polishing was accomplished using a Struers Rotopol-31 unit with a Struers RotoForce-4 revolving sample holder. The final step of polishing used a solution of diamond dust of approximately 1 μm in size. Quantitative elemental analysis was performed using wavelength-dispersive (WDS)

X-ray spectroscopy (model JXA-8500F, JEOL). The X-ray lines used for analysis were Zn $K\alpha$ and Sb $L\alpha$; antimony and zinc metals were employed as standards.

7.2.5. Physical Property Measurements

The Zn_3Sb_2 and $Zn_{13}Sb_{10}$ samples were cut into a bar of approximately $8 \times 2 \times 2$ mm in dimensions using a kerosene lubricant to avoid sample oxidation. The surface of the Zn_3Sb_2 sample was checked to ensure that no elemental Zn was present. The density of the two samples was 99 % of the crystallographic densities. Electrical resistivity, Seebeck coefficient, thermal conductivity, and heat capacity were measured on a Quantum Design Physical Property Measurement System (PPMS). Copper leads were attached on the rectangular bars using Epo-Tek H20E silver epoxy. The contacts for all samples were cured under a stream of ultrahigh purity Ar inside a tube furnace. Speed of sound measurements were performed using an Olympus 5072PR Pulser/Receiver system with a gain of 20 dB and a 5 kHz signal. Both longitudinal and shear measurements were made, using Olympus V112 (longitudinal) and Olympus V156 (shear) transducers and an Atten ADS 1102 oscilloscope.

7.3. Results and Discussion

7.3.1. Crystal Structure and Composition

The α - Zn_3Sb_2 phase appears to have the largest and most complex structure in the Zn–Sb system ($V = 14\,819 \text{ \AA}^3$). To understand the origin of such complexity, we will analyze the Sb and Zn frameworks separately (**Figure 7.3**). Both the positional and

displacement parameters of the Sb atoms are well-defined in all directions, indicating high rigidity of the Sb framework. The shortest Sb–Sb distance is 3.806(2) Å (Sb3–Sb12), which excludes any Sb₂ dimer formation in the structure. Absence of the dimers agrees with the (Zn²⁺)₃(Sb³⁻)₂ charge balanced formula. The Sb framework can be divided into four identical slabs with a length of 1/4 of the *c* parameter (18.7 Å). The smaller rhombohedral subcell (*a* = 15.1 Å, *c* = 18.7 Å) is metrically close to the cubic cell with *a* = ~10.7 Å. The formation of the observed, large rhombohedral cell can be treated as the loss of the cubic symmetry concomitant with quadrupling of the resulting *c*_{hex} parameter. The reduction in the rotation symmetry is represented by the splitting of the intense peaks in the powder diffraction pattern (**Figure 7.2**), while the reduction in the translation symmetry is manifested by the appearance of the superstructure peaks of lower intensity.

Ultimately, the symmetry reduction in α-Zn₃Sb₂ is associated with the Zn atoms. In contrast to the Sb framework, the Zn framework displays significant disorder and has the periodicity of the *c* parameter (74.8 Å). While we have no explanation for the reduced symmetry in the Zn framework, it is apparent that Zn distribution is the main driving force for the formation of such a large unit cell. Out of 47 Zn sites, only 8 sites (Zn1–8) are fully occupied, and the Zn–Zn distances for these sites are larger than 2.7 Å. The rest of the Zn sites are partially occupied, and in most cases a partially occupied site has at least another partially occupied Zn site with $d_{\text{Zn-Zn}} < 2.5$ Å (exceptions are Zn9, Zn10, Zn14, Zn16, and Zn38, for which $d_{\text{Zn-Zn}} > 2.5$ Å).

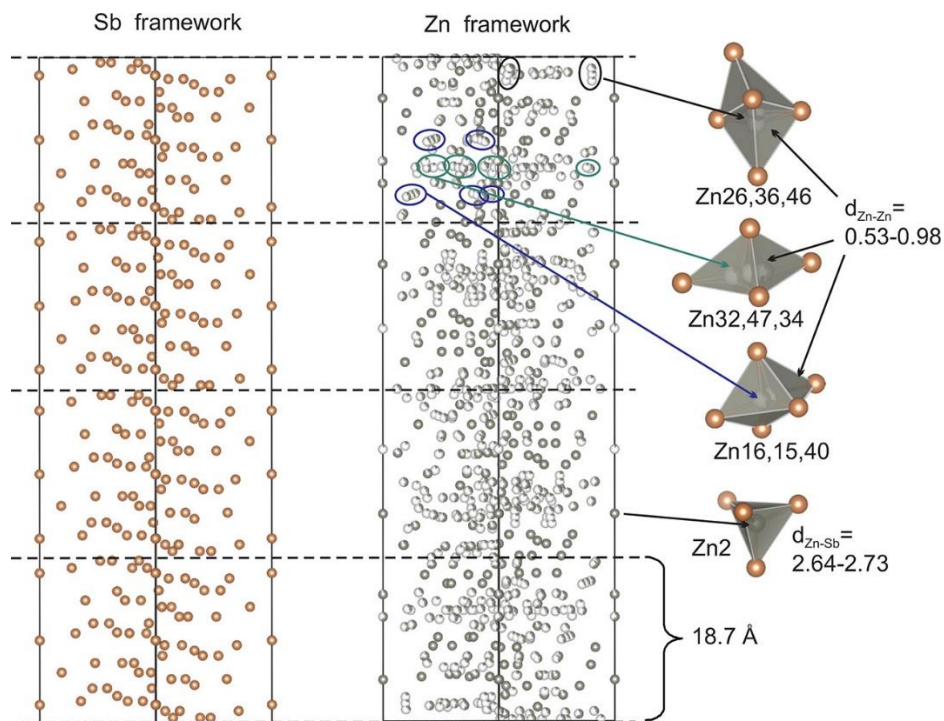


Figure 7.3. Projection of the α - Zn_3Sb_2 unit cell along the [110] direction. Antimony atoms are shown in orange (left) and zinc in gray (center). The fraction of the gray for a given Zn atom represents the occupancy of the corresponding Zn site. The Sb polyhedra (right) show environments for selected deficient Zn atoms that are close to each other.

The fully occupied Zn sites and majority of the deficient Zn sites reside in Sb_4 with $d_{\text{Zn-Sb}} = 2.6\text{--}3 \text{ \AA}$ (e.g., Zn2 environment in **Figure 7.3**). The rest of the deficient Zn sites have only three Sb neighbours. The relative position of the deficient Zn sites is interesting (**Figure 7.3**) and provides insights into the Zn mobility in the α - Zn_3Sb_2 structure. When $d_{\text{Zn-Zn}} < 1 \text{ \AA}$, there are often three Zn sites that reside within a Sb trigonal bipyramid formed by two face-sharing Sb tetrahedra. The two terminal Zn atoms sit almost at the center of the Sb tetrahedra and have four Sb neighbours at $d_{\text{Zn-Sb}} > 2.6 \text{ \AA}$, while the center

Zn site is in the middle of the shared Sb triangular face and has only three Sb neighbours at shorter $d_{\text{Zn-Sb}}$. As an example, in **Figure 7.3** the terminal Zn16 and Zn40 atoms have 4 Sb atoms at $d_{\text{Zn-Sb}} = 2.67\text{--}2.98(1)$ Å, while the center Zn15 atom has 3 Sb atoms at $d_{\text{Zn-Sb}} = 2.58\text{--}2.68(1)$ Å. The established Zn arrangement suggests the following: (i) Zn atoms are highly disordered; (ii) such disorder must stem from Zn mobility, which is significant at high temperatures, but quenched at room temperature; (iii) at high temperatures, Zn atoms migrate between the different Sb₄ tetrahedra via a shared trigonal face. From **Figure 7.3**, it is also apparent that there is a nonuniform distribution of the Zn sites along the *c* direction. Some regions of the unit cell have a larger concentration of the Zn sites (mostly deficient) than the other ones; however, we cannot explain such behaviour.

While the $\alpha\text{-Zn}_3\text{Sb}_2$ is clearly the largest and most structurally complex cell in the Zn–Sb system, $\alpha\text{-Zn}_3\text{Sb}_2$ structure shares many structural similarities with the neighbouring Zn–Sb phases. Namely, Zn atoms occupy the Sb₄ tetrahedra and there is significant Zn disorder, which is observed in all other Zn–Sb phases except for the ZnSb binary. Even the absence of Sb₂ dimers in $\alpha\text{-Zn}_3\text{Sb}_2$ (in contrast to other Zn–Sb phases) is expected on the basis that all Zn–Sb structures are charge balanced. In that respect, the $\alpha\text{-Zn}_3\text{Sb}_2$ structure can be seen as the next, albeit final, member in the Zn–Sb series. However, there are also unique structural properties in $\alpha\text{-Zn}_3\text{Sb}_2$, which could not be extrapolated from the Zn-poor binaries. Specifically, the high degree of Zn disorder and complexity of the unit cell cannot be fully rationalized even based on our knowledge of other Zn–Sb structures.

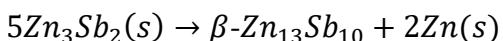
Finally, we would like to address the composition of the $\alpha\text{-Zn}_3\text{Sb}_2$ phase. Compositions obtained from the diffraction experiments are slightly different:

$Zn_{2.91(2)}Sb_2$ and $Zn_{3.05(3)}Sb_2$ from the single crystal and powder data, respectively. Electron microprobe analysis (EMPA) was performed to obtain a more accurate composition. The EMPA yielded $Zn_{2.96(2)}Sb_2$, which suggests that the phase is slightly Zn deficient but very close to the stoichiometric composition. The slight Zn deficiency is further supported by the positive Seebeck coefficient measurement, wherein V_{Zn}^{2-} could represent the primary acceptor defect.

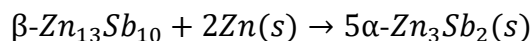
7.3.2. Temperature Stability and Transformations

The α - Zn_3Sb_2 phase can be kinetically stabilized at room temperature by rapid quenching from 430 °C into cold water. On the basis of consecutive powder diffraction results, α - Zn_3Sb_2 showed no detectable decomposition or transformation at ambient conditions for a few months. High temperature synchrotron powder diffraction studies were employed to trace its temperature stability and formation pathway. **Figure 7.4** shows diffraction data in projection during heating from 20 to 650 °C and cooling back to 20 °C at a rate of 2 °C/min. A number of transitions were observed:

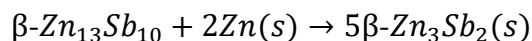
(1): the α - Zn_3Sb_2 phase is stable until 197 °C, at which it decomposes to $Zn_{13}Sb_{10}$ and Zn:



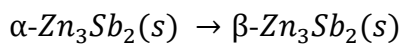
(2) At 410 °C, β - $Zn_{13}Sb_{10}$ and Zn react back to give α - Zn_3Sb_2 :



(3) However, $\beta\text{-Zn}_{13}\text{Sb}_{10}$ and Zn are not fully consumed at 410 °C. They disappear fully only at 425 °C, when the $\beta\text{-Zn}_3\text{Sb}_2$ phase emerges:



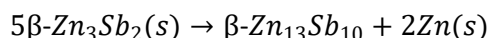
(4) $\alpha\text{-Zn}_3\text{Sb}_2$ and $\beta\text{-Zn}_3\text{Sb}_2$ coexist until 490 °C. Above this temperature only $\beta\text{-Zn}_3\text{Sb}_2$ is stable:



(5) At 590 °C, $\beta\text{-Zn}_3\text{Sb}_2$ melts.

(6) During cooling from the liquid, $\beta\text{-Zn}_3\text{Sb}_2$ forms at 581 °C.

(7) $\beta\text{-Zn}_3\text{Sb}_2$ is stable to 355 °C, below which it abruptly decomposes into $\beta\text{-Zn}_{13}\text{Sb}_{10}$ and Zn.



The stability and decomposition of $\beta\text{-Zn}_3\text{Sb}_2$ is very interesting in several respects. First, $\beta\text{-Zn}_3\text{Sb}_2$ can be supercooled to a much lower temperature when compared to its formation temperature during heating (355 vs. 425 °C). Second, $\beta\text{-Zn}_3\text{Sb}_2$ decomposes very suddenly upon cooling; the diffraction pattern at 355 °C shows only $\beta\text{-Zn}_3\text{Sb}_2$, while the next one at 353.2 °C has strictly $\beta\text{-Zn}_{13}\text{Sb}_{10}$ and Zn. For other transformations, the original phase and products were present at least on two consecutive scans. Third, during cooling, $\beta\text{-Zn}_3\text{Sb}_2$ does not transform into the low-temperature $\alpha\text{-Zn}_3\text{Sb}_2$ polymorph, as expected from the heating data, instead it decomposes into $\beta\text{-Zn}_{13}\text{Sb}_{10}$ and Zn directly. We

emphasize that the cooling rate of 2 °C/min of the diffraction studies is relatively fast and is likely the reason that formation of α -Zn₃Sb₂ is bypassed. Our bulk synthetic procedure, involving the annealing of the Zn₃Sb₂ sample at 430 °C for 48 h, permits full transformation of β -Zn₃Sb₂ into α -Zn₃Sb₂.

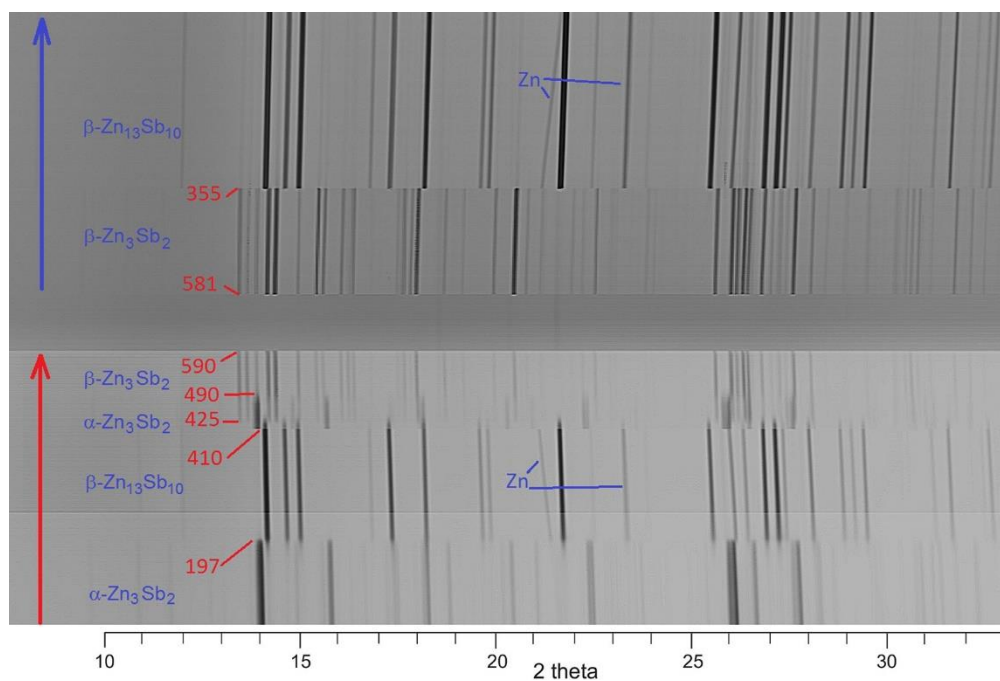


Figure 7.4. High-temperature diffraction patterns in projection during heating and cooling. The phases are in blue and the transformation temperatures (°C) are in red. Red and blue arrows indicate heating and cooling. The region between the lines is a molten liquid.

On the basis of the diffraction results, the compositions of β -Zn₃Sb₂ and α -Zn₃Sb₂ appear to be identical. No detectable impurity formation was observed during transformations between β -Zn₃Sb₂ and α -Zn₃Sb₂. The experimental phase diagram by Izard et al.¹²⁵ indicates that β -Zn₃Sb₂ is Zn-poor compared to α -Zn₃Sb₂. While we cannot verify

this observation, the coexistence of β -Zn₃Sb₂ and α -Zn₃Sb₂ between 425 and 490 °C would be consistent with a small compositional difference. We have attempted to quench β -Zn₃Sb₂ to room temperature from a variety of temperatures; in all cases, the samples contained β -Zn₁₃Sb₁₀ and Zn. We have also tried to derive a unit cell via automatic indexing of the HT data; unfortunately we could not obtain reliable results. The diffraction data of β -Zn₃Sb₂ were also compared to a powder pattern simulated for the incommensurate orthorhombic Zn_{17+ α} Sb₁₂ structure²⁰⁹, but the two patterns were vastly different. This also explains why we were unable to reproduce the results from the previous study, where Zn_{17+ α} Sb₁₂ was produced by quenching. Clearly, Zn_{17+ α} Sb₁₂ is distinct from β -Zn₃Sb₂ both structurally and compositionally. Owing to the Zn-poor composition, Zn_{17+ α} Sb₁₂ must form Sb–Sb dimers to conserve charge balance. Comparison of the diffraction pattern of β -Zn₃Sb₂ to those of α -Zn₃Sb₂ and β -Zn₁₃Sb₁₀ suggests that β -Zn₃Sb₂ has a rather complex structure and likely a large unit cell.

7.3.3. Physical Properties

To examine the effects of the structural differences and phase transitions in α -Zn₃Sb₂ and Zn₁₃Sb₁₀, we measured the heat capacity, electrical resistivity, Seebeck coefficient, and thermal conductivity as a function of temperature from 300 K to 2 K. Because of the metastable nature of α -Zn₃Sb₂, high temperature transport measurements are not feasible. Room temperature transport measurements and some calculated values are summarized in **Table 7.3**.

Table 7.3. Physical Parameters of α -Zn₃Sb₂ and β -Zn₁₃Sb₁₀ at 300 K^a.

property	α -Zn ₃ Sb ₂	β -Zn ₁₃ Sb ₁₀
density, g cm ⁻³	6.13	6.23
atoms in ordered, primitive cell	630/3 = 210	69/3 = 23
heat capacity, J/mol-at K	26.6	26.7
resistivity, mOhm cm	0.67	2.4
Seebeck coefficient, μ V/k	34	97
thermal cond., W/m K	1.87	0.85
Lorentz number, W Ω /K ²	2.25×10^{-8}	1.93×10^{-8}
lattice therm. cond., W/m K	0.86	0.62
longitudinal sound velocity, m/s	3795	3685
shear sound velocity, m/s	1967	2131
mean sound velocity, m/s	2576	2649

^a Values are either experimental or calculated directly from transport measurements.

Both heat capacity and electrical resistivity measurements (**Figure 7.5(a)** and **(b)**) on Zn₁₃Sb₁₀ indicate the presence of two phase transitions at 254 and 235 K during cooling. These transitions have been previously observed in the literature and are associated with the consecutive ordering of the Zn atoms and symmetry reductions: $R\bar{3}c$ (β -Zn₁₃Sb₁₀) \rightarrow $C2/c$ (α' -Zn₁₃Sb₁₀) \rightarrow $P\bar{1}$ (α -Zn₁₃Sb₁₀)^{92-94,114}. We note that Zn₃Sb₂ also undergoes a phase transition at 260 K. However, the nature of the transition in Zn₃Sb₂ is not clear and is the subject of a future investigation. For convenience, we designate the low-temperature phase in Zn₃Sb₂ as ζ -Zn₃Sb₂. None of the phase transitions in Zn₃Sb₂ or Zn₁₃Sb₁₀ appreciably affect the Seebeck coefficient or total thermal conductivity.

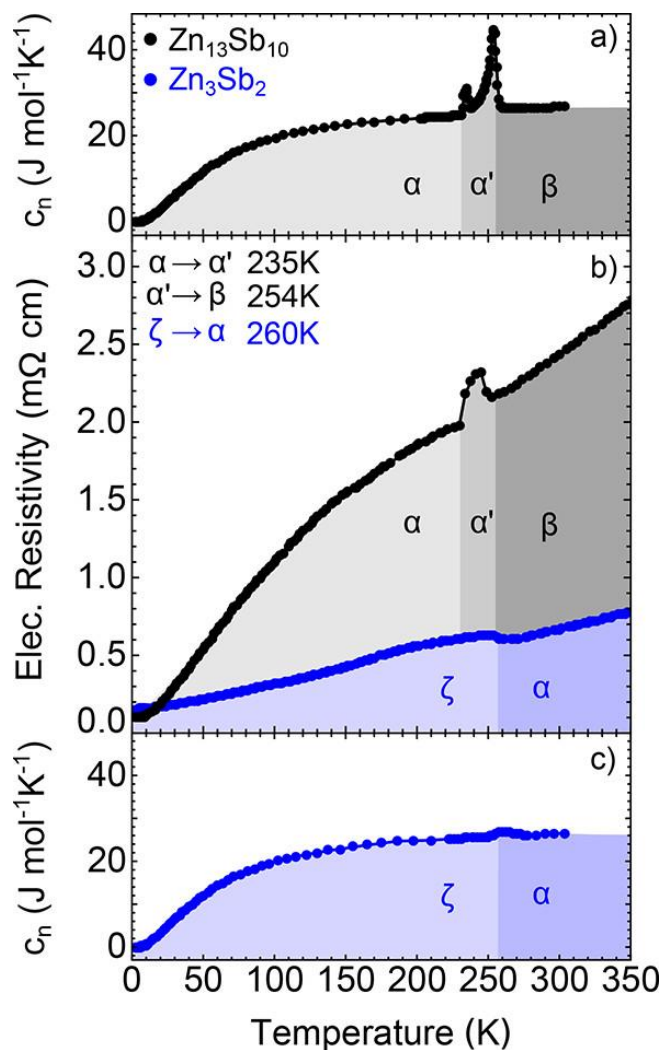


Figure 7.5. Heat capacity (a,c) and electrical resistivity measurements (b) reveal multiple phase transitions in Zn₁₃Sb₁₀ and Zn₃Sb₂. The $\alpha \rightarrow \alpha'$ phase transition in Zn₁₃Sb₁₀ is consistent with a first-order transition, while the $\alpha' \rightarrow \beta$ transition is of a λ -type shape characteristic of a second-order transition. The transition in Zn₃Sb₂ from $\zeta \rightarrow \alpha$ is not well characterized and is the subject of future investigations.

Considering the temperature dependence of the heat capacity (and omitting phase transitions), it appears that Zn₃Sb₂ and Zn₁₃Sb₁₀ are nearly identical. Similar temperature-

dependent behavior is also found with ZnSb^{132} . A direct comparison between the heat capacity curves can be found in Supplementary Information, **Figure 7.S1**. Both compounds exceed the Dulong–Petit limit ($3R \sim 24.9 \text{ J/mol-at K}$, **Figure 7.S1**) for heat capacity by 300 K, indicating a strong contribution to the heat capacity from anharmonic contributions. However, without high-temperature data ($> 300 \text{ K}$), the anharmonic contribution is a strictly qualitative observation. The heat capacity of $\text{Zn}_{13}\text{Sb}_{10}$ reaches 24.8 J/mol-at. K at 232 K , just before the onset of the first phase transition. While the peak is not well-defined, it does not resemble a λ -type shape and is assumed to be first order in nature. The second transition is of a λ -type shape and is presumed to be a second-order transition. Our conclusions agree well with group-theoretical analysis performed in our prior work⁹⁴. After the second transition, the heat capacity of $\text{Zn}_{13}\text{Sb}_{10}$ is 26.6 J/mol-at. K , well above the values recorded before the first transition. It is apparent that extrapolation of low-temperature heat capacity values ($< 235 \text{ K}$) will fall well below the heat capacity after the transition to $\beta\text{-Zn}_{13}\text{Sb}_{10}$ ($> 254 \text{ K}$). Since the transitions in $\text{Zn}_{13}\text{Sb}_{10}$ are known to be associated with Zn-disorder, it follows that the increased heat capacity at higher temperatures reflects the extra internal energy associated with the disordered, mobile Zn atoms (recall that the structure of $\beta\text{-Zn}_{13}\text{Sb}_{10}$ is amenable to Zn migration due to the space afforded by the empty Sb_4 tetrahedra). However, it is interesting to note that above 270 K , the heat capacities of $\beta\text{-Zn}_{13}\text{Sb}_{10}$ and $\alpha\text{-Zn}_3\text{Sb}_2$ are nearly identical. Such behavior is particularly interesting, as our XRD analysis suggests that Zn disorder is quite pronounced in $\alpha\text{-Zn}_3\text{Sb}_2$ when compared to $\beta\text{-Zn}_{13}\text{Sb}_{10}$. While the disorder could be expected to have a significant contribution to the high-temperature heat capacity in Zn_3Sb_2 , the experimental

results indicate that either (i) the disorder plays little role in the overall heat capacity or (ii) there is an additional contribution to the heat capacity in $\text{Zn}_{13}\text{Sb}_{10}$ that produces near identical heat capacities.

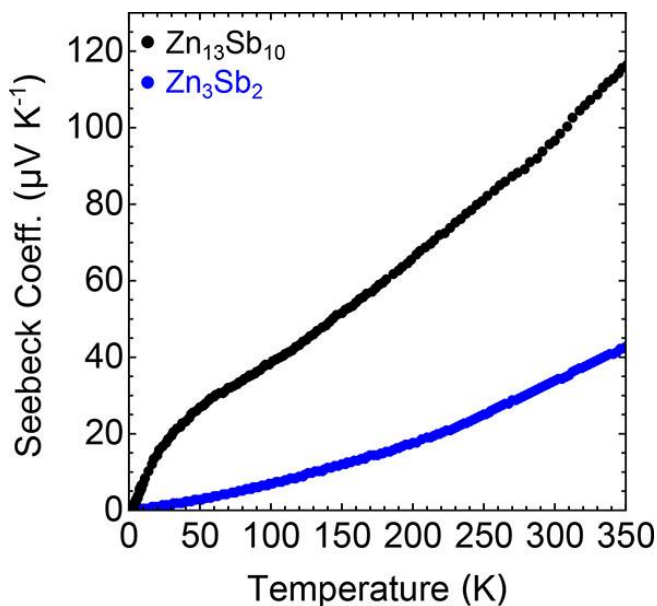


Figure 7.6. Seebeck coefficient measurements on Zn_3Sb_2 and $\text{Zn}_{13}\text{Sb}_{10}$ indicate *p*-type transport and temperature dependence consistent with heavily doped semiconductors. Phase transitions in Zn_3Sb_2 and $\text{Zn}_{13}\text{Sb}_{10}$ appear to have no appreciable effect on the Seebeck coefficient.

The electrical resistivity (**Figure 7.5(b)**) of Zn_3Sb_2 increases nearly linearly with temperature, characteristic of a heavily doped semiconductor. In conjunction with Seebeck coefficient measurements (**Figure 7.6**), we conclude that Zn_3Sb_2 is likely a heavily doped semiconductor. In comparison to $\text{Zn}_{13}\text{Sb}_{10}$, the resistivity of Zn_3Sb_2 is significantly lower except below 18 K. We associate the larger low-temperature resistivity of Zn_3Sb_2 with

either (i) significant remnant Zn disorder and associated ionized impurity scattering or (ii) differences in microstructure leading to increased boundary scattering. The resistivity and Seebeck coefficient measurements on $\text{Zn}_{13}\text{Sb}_{10}$ match existing literature values well²¹⁴. Positive Seebeck coefficient measurements on $\text{Zn}_{13}\text{Sb}_{10}$ and Zn_3Sb_2 indicate *p*-type transport, consistent with possible V_{Zn} or Zn_{Sb} defects. We do not see significant influence of the phase transitions on the Seebeck coefficient in either $\text{Zn}_{13}\text{Sb}_{10}$ or Zn_3Sb_2 , suggesting no strong changes to the valence band edge electronic structure during the transitions.

7.3.4. Thermal Properties and Debye–Callaway Modelling

The excellent thermoelectric properties of $\text{Zn}_{13}\text{Sb}_{10}$ ($zT \sim 1.4$) are largely attributed to its intrinsically low lattice thermal conductivity, stemming from the unit cell complexity and Zn disorder⁹⁶. However, our crystallographic refinement of the α - Zn_3Sb_2 structure demonstrates even further Zn disorder and an even larger unit cell. In this section we examine the thermal transport in both α - Zn_3Sb_2 and $\text{Zn}_{13}\text{Sb}_{10}$ within the framework of the Debye–Callaway model and investigate the various phonon scattering components within each structure.

The total thermal conductivity (**Figure 7.7(a)**) of Zn_3Sb_2 is rather unusual when compared to $\text{Zn}_{13}\text{Sb}_{10}$. We do not observe a low-temperature (~ 25 K) transition from boundary to Umklapp scattering, that is seen in $\text{Zn}_{13}\text{Sb}_{10}$ ²³. Instead, the low-temperature behavior is characteristic of amorphous materials, where the phonon mean free path is intrinsically short. To further investigate phonon transport in Zn_3Sb_2 and $\text{Zn}_{13}\text{Sb}_{10}$, we also

calculated the lattice thermal conductivity κ_l (**Figure 7.7(b)**) via $\kappa_l = \kappa_{total} - \kappa_e$, where κ_{total} is the total thermal conductivity and κ_e is the electronic contribution. The electronic contribution was evaluated using the Wiedemann–Franz law, $\kappa_e = L\sigma T$, where L is the Lorenz number, σ is the electronic conductivity, and T is temperature. The Lorenz number is estimated according to the approximation $L \approx 1.5 + \exp[-|\alpha|/116]$, where L is given in units of $10^{-8} \text{ W}\Omega/\text{K}^2$ and α is in units of $\mu\text{V}/\text{K}^{30}$. It is important to note that the phase transitions observed in both Zn_3Sb_2 and $\text{Zn}_{13}\text{Sb}_{10}$ (**Figure 7.5**) do not affect the total thermal conductivity but are evident in the lattice thermal conductivity due to the electronic contribution's dependence.

To provide insight into underlying thermal transport processes, the temperature-dependent lattice thermal conductivity (**Figure 7.7(b)**) was modeled with the Debye–Callaway model. Both $\text{Zn}_{13}\text{Sb}_{10}$ and Zn_3Sb_2 are exceptionally complex with 23 and 210 atoms in the primitive cells, respectively. The structural complexity can be expected to yield a phonon dispersion that consists of three high-velocity acoustic branches and numerous (66 and 627, respectively) low-velocity optical branches. We model the group velocity and heat capacity of the acoustic branches using the measured speed of sound values and an isotropic Debye approximation. The frequency-dependent scattering rate, $\tau(\omega)$, incorporates grain boundary, Umklapp (phonon–phonon), and point-defect scattering. Combined via Matthiessen's rule, the individual components of $\tau(\omega)$ are modeled using adjustable prefactors determining relative scattering strength with a fixed frequency dependence²¹⁵. The low velocity optical branches are assumed to exhibit glasslike properties, allowing us to apply the Cahill minimum thermal conductivity approximation.

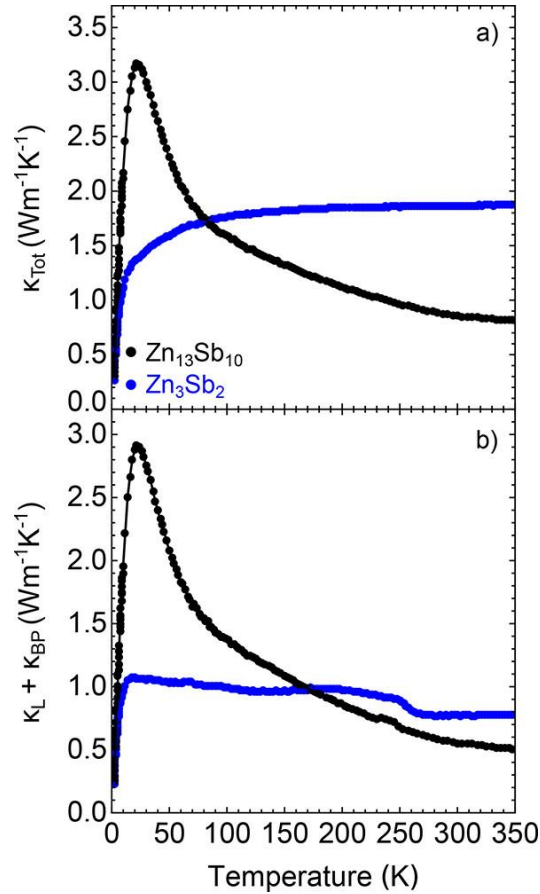


Figure 7.7. Total thermal conductivity (a) and calculated lattice thermal conductivity (b) for Zn_3Sb_2 and $\text{Zn}_{13}\text{Sb}_{10}$ are blue and black, respectively. We note that the thermal conductivity for Zn_3Sb_2 does not display the characteristic transition from boundary scattering to Umklapp scattering at low temperatures (e.g., peak in thermal conductivity for $\text{Zn}_{13}\text{Sb}_{10}$ at ~ 25 K). Instead the low-temperature thermal transport in Zn_3Sb_2 is more similar to that of an amorphous material.

The remaining free parameters for the thermal conductivity model are the point defect scattering strength, the Grüneisen parameter for Umklapp scattering, and the boundary scattering effective length. To determine if the model faced multiple local minima,

an initial brute force search was undertaken across a broad range of parameter values. The temperature-dependent thermal conductivity was calculated at each point in the three-dimensional search space and compared to the experimental values to provide a goodness of fit. The brute force search found only one region for each compound that fit the data well; subsequent refinement was done manually.

At low temperatures, the thermal conductivity of $\text{Zn}_{13}\text{Sb}_{10}$ is well fit simply by a combination of weak boundary scattering ($\sim 10^{-5}$ m) and strong Umklapp scattering. The weak boundary scattering allows the thermal conductivity to spike before rapidly being suppressed. **Figure 7.8** shows the acoustic and optical contributions to the modelled thermal conductivity; the optical contribution only occurs above ~ 20 K, as those modes become increasingly occupied. Recalling that the optical contribution is modelled using a minimum thermal conductivity approximation, the discrepancy at high temperatures must come from an overestimation of the acoustic contribution. As the phase transitions in $\text{Zn}_{13}\text{Sb}_{10}$ are approached, the thermal conductivity drops significantly, which may be related to the increased Zn disorder in $\beta\text{-Zn}_{13}\text{Sb}_{10}$. The discontinuity is modeled explicitly by using a piece-wise valued function at the phase transition and directly increasing the relative weight of point defect scattering. However, the increased slope must be a result of even stronger Umklapp scattering at and above the phase transition. Our current model does not incorporate a temperature-dependent Grüneisen parameter as the functional form is ambiguous and not physically justifiable with current experimental data.

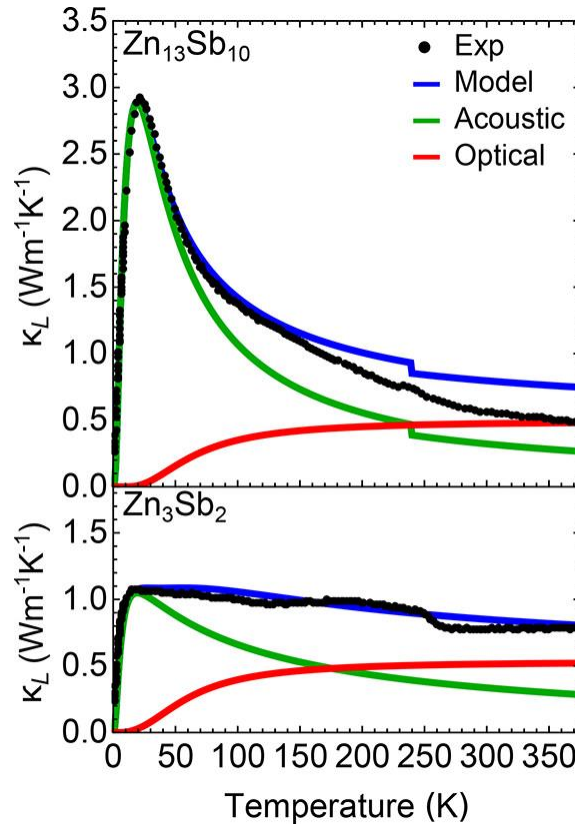


Figure 7.8. Results of Debye–Callaway modeling of lattice thermal conductivity for $\text{Zn}_{13}\text{Sb}_{10}$ and Zn_3Sb_2 . Phase transitions are modeled explicitly using piecewise construction of the acoustic contribution to the model after the phase transitions. The overestimation of thermal conductivity in $\text{Zn}_{13}\text{Sb}_{10}$ for temperatures > 254 K is associated with an overestimation of the acoustic contribution. Considering the complex unit cells and multiple phase transitions, the Debye–Callaway does an adequate job of modeling the lattice thermal conductivity in $\text{Zn}_{13}\text{Sb}_{10}$ and Zn_3Sb_2 .

In the first 20 K, the thermal conductivity values of Zn_3Sb_2 and $\text{Zn}_{13}\text{Sb}_{10}$ are quite similar, indicating similar boundary scattering rates. The large relaxation time for boundary scattering confirms that quenching Zn_3Sb_2 is successful in maintaining homogeneity and

avoiding decomposition. However, above this temperature fitting the thermal transport of the Zn_3Sb_2 phase requires a very different set of parameters than that used in $\text{Zn}_{13}\text{Sb}_{10}$. Specifically, Zn_3Sb_2 exhibits *significantly* stronger point-defect scattering and *significantly* weaker Umklapp scattering when compared to $\text{Zn}_{13}\text{Sb}_{10}$. The increased point-defect scattering appears to persist over all temperatures and is approximately three times stronger than the point-defect scattering in $\text{Zn}_{13}\text{Sb}_{10}$. This is consistent with the disordered Zn sublattice in Zn_3Sb_2 . Conversely, the phonon–phonon scattering rate is approximately three times weaker in Zn_3Sb_2 compared to $\text{Zn}_{13}\text{Sb}_{10}$, which leads to a suppression of thermal conductivity at low temperature from point-defect scattering in Zn_3Sb_2 .

Figure 7.9 explores the individual contributions to the phonon relaxation time in low- and high-temperature regimes (50 and 300 K, respectively) for $\text{Zn}_{13}\text{Sb}_{10}$ and Zn_3Sb_2 . The greater Umklapp scattering in $\text{Zn}_{13}\text{Sb}_{10}$ is particularly visible. At low temperatures in Zn_3Sb_2 , the Umklapp scattering is so weak that point-defect scattering emerges as the dominant scattering source over all frequencies. In all cases, boundary scattering is the dominant scattering source for very low frequency phonons. By multiplying the relaxation time values with the longitudinal and transverse speeds of sound, we estimate an effective mean free path ranging between 10^{-8} and 10^{-6} m for acoustic phonons.

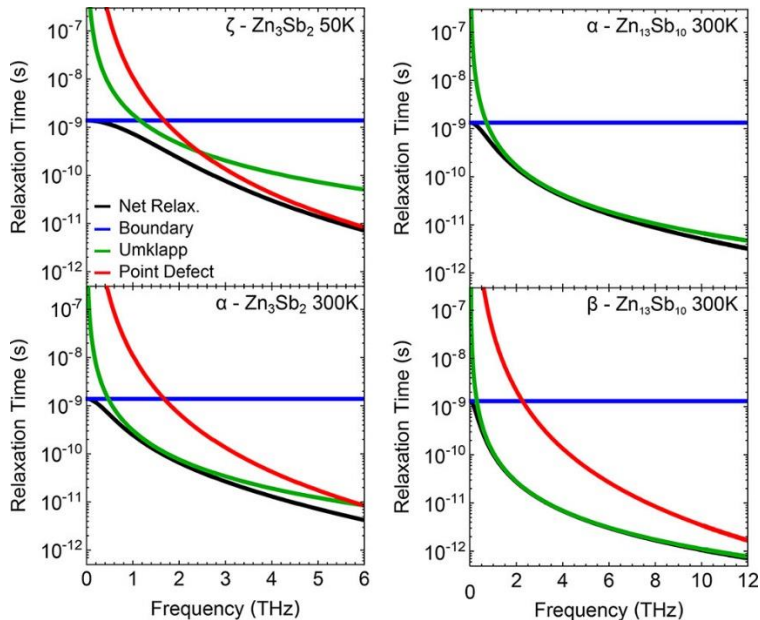


Figure 7.9. Breakdown of net relaxation time into constituent scattering sources as a function of phonon frequency for $\text{Zn}_{13}\text{Sb}_{10}$ and Zn_3Sb_2 at both 50 K and 300 K. As expected, boundary scattering is the primary scattering source of very low frequency phonons. Scattering in Zn_3Sb_2 appears to be dominated by point-defect scattering over all temperatures and most frequencies, whereas $\text{Zn}_{13}\text{Sb}_{10}$ has a much larger contribution from Umklapp scattering.

Our results shed light into the underlying thermal transport phenomenon in $\text{Zn}_{13}\text{Sb}_{10}$, Zn_3Sb_2 , and other systems rich in point defects. Experimental study by Schweika et al. detected a low-energy optical mode originating from the Sb_2 dimer vibrations with an Einstein temperature of 62(1) K in $\text{Zn}_{13}\text{Sb}_{10}$ ¹⁹⁵. A subsequent theoretical analysis by Bjerg et al. questioned the significance of the Sb_2 dimer vibrations, and instead the authors proposed that low-lying optical modes involving both Zn and Sb serve as scattering channels²¹². Further, they showed the isolated Sb1 atom in the $\text{Zn}_{13}\text{Sb}_{10}$ structure has an

unusually high-mode Grüneisen parameter. As these anharmonicity calculations were conducted on defect-free cells, the high-mode Grüneisen is inherent to the parent structure rather than being defect driven. Similar results have been found on ZnSb, with rhomboid Zn_2Sb_2 rings producing low-lying optical phonon modes and unusually high atomic displacement parameters for the Zn site¹³². The results herein confirm that there is significant phonon–phonon scattering within $\text{Zn}_{13}\text{Sb}_{10}$ and initially suggest that Zn_3Sb_2 is a far more harmonic system. Considering the structures of the two compounds, the different Zn and Sb coordination in Zn_3Sb_2 may drive the weaker scattering. Beyond anharmonicity of the local potentials, the observation of low phonon-phonon scattering in Zn_3Sb_2 may also reflect fewer scattering channels for acoustic modes. Considering the strong point defect scattering in Zn_3Sb_2 , we suggest that the high density of disordered Zn atoms, which equals 247 atoms/14 819 Å³ or 1 atom every 60 Å³, strongly influences the lattice thermal conductivity. In contrast, $\beta\text{-Zn}_{13}\text{Sb}_{10}$ has ca. 6 strongly disordered Zn atoms, yielding a density of point scatters of 6 atoms/1606 Å³ or 1 atom every 268 Å³.

7.4. Conclusions

The low-temperature α -modification of Zn_3Sb_2 was successfully prepared by rapid quenching and structurally characterized using single crystal and powder diffraction. The $\alpha\text{-Zn}_3\text{Sb}_2$ phase features the most complex structure observed so far in the Zn–Sb system. Similar to other Zn–Sb phases, the Sb framework is well-defined and creates the tetrahedral voids occupied by highly disordered Zn atoms. As expected from the 3:2 stoichiometry, only isolated Sb^{3-} anions are present in the structure. High-temperature diffraction

measurements reveal two Zn_3Sb_2 polymorphs with stability regions of 410 – 490 (α - Zn_3Sb_2) and 425 – 590 °C (β - Zn_3Sb_2), upon which melting occurs. Only the α -phase was stabilized at room temperature by quenching. Electrical transport measurements are consistent with a heavily doped small gap semiconductor or semimetal, with resistivity one order of magnitude lower than that of $\text{Zn}_{13}\text{Sb}_{10}$. Speed of sound and heat capacity measurements indicated Zn_3Sb_2 and $\text{Zn}_{13}\text{Sb}_{10}$ have similar elastic properties, consistent with their similar stoichiometries. Despite these similarities, the temperature-dependence of the lattice thermal conductivity of these two compounds is quite distinct. Thermal modeling indicates that $\text{Zn}_{13}\text{Sb}_{10}$ has 3-fold stronger phonon–phonon scattering rates than Zn_3Sb_2 , whereas Zn_3Sb_2 has 3-fold stronger point defect scattering. These differences may be attributed to differences in local structure (e.g., Sb dimers and interstitials) and differences in the phonon dispersion (e.g., low-lying optical modes). Together, this work highlights the combined importance of local real space structure and reciprocal space in ultimately determining transport properties.

7.5. Supplementary Materials

Table 7.S1. Atomic coordinates, occupancies and equivalent isotropic displacement parameters from single crystal refinement of α - Zn_3Sb_2 .

Atom	Occup.	x/a	y/b	z/c	$U_{\text{eq}}, \text{\AA}^2$
Sb(1)	1	0	0	0.02689(6)	0.0288(8)
Sb(2)	1	0	0	0.12364(5)	0.0181(6)
Sb(3)	1	0	0	0.22489(4)	0.0136(6)
Sb(4)	1	0	0	0.27683(4)	0.0124(6)
Sb(5)	1	0	0	0.37359(4)	0.0166(6)
Sb(6)	1	0	0	0.46906(4)	0.0168(6)
Sb(7)	1	0.2870(1)	0.0787(1)	0.01757(2)	0.0148(4)
Sb(8)	1	0.2253(1)	0.9172(1)	0.13454(2)	0.0148(4)
Sb(9)	1	0.3798(1)	0.8521(1)	0.99266(2)	0.0167(4)

Sb(10)	1	0.3012(1)	0.2240(1)	0.11644(2)	0.0141(4)
Sb(11)	1	0.1443(1)	0.9554(1)	0.07548(2)	0.0144(4)
Sb(12)	1	0.5943(1)	0.5378(1)	0.10058(2)	0.0119(3)
Sb(13)	1	0.4171(1)	0.9648(1)	0.05169(2)	0.0136(4)
Sb(14)	1	0.3882(1)	0.2537(1)	0.06556(2)	0.0125(4)
Sb(15)	1	0.1869(1)	0.7095(1)	0.08979(2)	0.0149(4)
Sb(16)	1	0.9448(1)	0.8128(1)	0.17401(2)	0.0149(4)
Sb(17)	1	0.0592(1)	0.5965(1)	0.14940(2)	0.0193(4)
Sb(18)	1	0.1115(1)	0.7562(1)	0.03232(3)	0.0157(4)
Zn(1)	1	0	0	0.0621(1)	0.037(2)
Zn(2)	1	0	0	0.31213(8)	0.021(1)
Zn(3)	1	0.1676(3)	0.0107(3)	0.11077(5)	0.0261(8)
Zn(4)	1	0.2056(3)	0.1589(3)	0.08458(5)	0.0212(7)
Zn(5)	1	0.0778(3)	0.7449(3)	0.06661(5)	0.0294(8)
Zn(6)	1	0.3040(3)	0.0596(3)	0.05266(5)	0.0225(7)
Zn(7)	1	0.2190(3)	0.7440(3)	0.12631(5)	0.0284(8)
Zn(8)	1	0.4056(3)	0.4325(3)	0.11318(5)	0.0239(7)
Zn(9)	0.893(1)	0	0	0.1904(1)	0.0249(5)
Zn(10)	0.57(2)	0	0	0.1569(1)	0.0249(5)
Zn(11)	0.08(2)	0	0	0.409(1)	0.0249(5)
Zn(12)	0.87(2)	0.4879(5)	0.8429(4)	0.9313(1)	0.0249(5)
Zn(13)	0.87(1)	0.3908(3)	0.9457(3)	0.9609(1)	0.0249(5)
Zn(14)	0.56(6)	0.487(1)	0.312(1)	0.0973(2)	0.0249(5)
Zn(15)	0.33(2)	0.419(2)	0.148(2)	0.1254(2)	0.0249(5)
Zn(16)	0.40(1)	0.459(1)	0.193(1)	0.1229(1)	0.0249(5)
Zn(17)	0.52(1)	0.3139(5)	0.8179(5)	0.02695(9)	0.0249(5)
Zn(18)	0.50(1)	0.2969(6)	0.8974(6)	0.0231(1)	0.0249(5)
Zn(19)	0.46(1)	0.4599(6)	0.8467(6)	0.0262(1)	0.0249(5)
Zn(20)	0.47(1)	0.0259(6)	0.8368(6)	0.1415(1)	0.0249(5)
Zn(21)	0.47(1)	0.0342(6)	0.7834(6)	0.1448(1)	0.0249(5)
Zn(22)	0.79(1)	0.2052(4)	0.5720(4)	0.0703(1)	0.0249(5)
Zn(23)	0.15(1)	0.141(2)	0.523(2)	0.0808(3)	0.0249(5)
Zn(24)	0.60(1)	0.3111(5)	0.2597(5)	0.01044(8)	0.0249(5)
Zn(25)	0.36(1)	0.1783(8)	0.1755(8)	0.0147(1)	0.0249(5)
Zn(26)	0.27(1)	0.0936(1)	0.1973(1)	0.0172(3)	0.0249(5)
Zn(27)	0.15(1)	0.121(2)	0.108(2)	0.0024(3)	0.0249(5)
Zn(28)	0.48(1)	0.4654(6)	0.1834(6)	0.0028(1)	0.0249(5)
Zn(29)	0.17(1)	0.421(2)	0.048(2)	0.0021(3)	0.0249(5)
Zn(30)	0.68(1)	0.2700(4)	0.9108(4)	0.0973(1)	0.0249(5)
Zn(31)	0.24(1)	0.294(1)	0.915(1)	0.0871(2)	0.0249(5)
Zn(32)	0.46(1)	0.7476(6)	0.7158(7)	0.1661(1)	0.0249(5)
Zn(33)	0.40(1)	0.5984(7)	0.6078(7)	0.1554(1)	0.0249(5)

Zn(34)	0.34(1)	0.7900(8)	0.8440(8)	0.1686(1)	0.0249(5)
Zn(35)	0.29(1)	0.594(1)	0.570(1)	0.1400(2)	0.0249(5)
Zn(36)	0.19(1)	0.081(1)	0.192(1)	0.0265(4)	0.0249(5)
Zn(37)	0.14(1)	0.152(2)	0.692(2)	0.1803(3)	0.0249(5)
Zn(38)	0.41(6)	0.502(1)	0.331(2)	0.0939(3)	0.0249(5)
Zn(39)	0.32(1)	0.4287(9)	0.0243(9)	0.0129(2)	0.0249(5)
Zn(40)	0.31(2)	0.386(2)	0.115(2)	0.1277(2)	0.0249(5)
Zn(41)	0.32(1)	0.2384(9)	0.6957(9)	0.1668(2)	0.0249(5)
Zn(42)	0.082(9)	0.511(3)	0.956(3)	0.0208(6)	0.0249(5)
Zn(43)	0.108(9)	0.391(3)	0.882(3)	0.9560(4)	0.0249(5)
Zn(44)	0.11(1)	0.755(3)	0.701(3)	0.1753(5)	0.0249(5)
Zn(45)	0.15(2)	0.459(3)	0.852(2)	0.9317(4)	0.0249(5)
Zn(46)	0.15(1)	0.068(2)	0.193(2)	0.0359(4)	0.0249(5)
Zn(47)	0.08(1)	0.762(4)	0.771(4)	0.1666(6)	0.0249(5)

Table 7.S2. Anisotropic displacement parameters (\AA^2) from single crystal refinement.

Atom	U^{11}	U^{22}	U^{33}	U^{23}	U^{13}	U^{12}
Sb(1)	0.022(1)	0.022(1)	0.043(2)	0	0	0.011(1)
Sb(2)	0.014(1)	0.014(1)	0.026(2)	0	0	0.007(1)
Sb(5)	0.013(1)	0.013(1)	0.015(2)	0	0	0.006(1)
Sb(6)	0.012(1)	0.012(1)	0.014(2)	0	0	0.006(1)
Sb(3)	0.015(1)	0.015(1)	0.017(2)	0	0	0.007(1)
Sb(4)	0.016(1)	0.016(1)	0.019(2)	0	0	0.008(1)
Sb(7)	0.018(1)	0.015(1)	0.014(1)	0.001(1)	0.000(1)	0.010(1)
Sb(8)	0.014(1)	0.013(1)	0.015(1)	0.01(1)	0.000(1)	0.006(1)
Sb(9)	0.021(1)	0.018(1)	0.016(1)	-0.002(1)	-0.002(1)	0.013(1)
Sb(10)	0.016(1)	0.014(1)	0.012(1)	0.000(1)	0.002(1)	0.007(1)
Sb(11)	0.013(1)	0.013(1)	0.015(1)	-0.001(1)	0.003(1)	0.006(1)
Sb(12)	0.012(1)	0.011(1)	0.012(1)	-0.001(1)	0.000(1)	0.005(1)
Sb(13)	0.014(1)	0.011(1)	0.015(1)	-0.002(1)	0.000(1)	0.006(1)
Sb(14)	0.011(1)	0.014(1)	0.013(1)	0.000(1)	0.001(1)	0.006(1)
Sb(15)	0.016(1)	0.013(1)	0.015(1)	0.000(1)	0.003(1)	0.007(1)
Sb(16)	0.017(1)	0.016(1)	0.014(1)	0.000(1)	0.000(1)	0.010(1)
Sb(17)	0.025(1)	0.017(1)	0.016(1)	0.002(1)	0.007(1)	0.011(1)
Sb(18)	0.012(1)	0.017(1)	0.014(1)	0.001(1)	0.002(1)	0.004(1)

Table 7.S3. Atomic coordinates and occupancies from the Rietveld refinement of the X-ray powder diffraction data. Only the overall displacement parameter, B, for all atoms was refined; B = 0.344(9) Å².

Atom	Occup.	<i>x/a</i>	<i>y/b</i>	<i>z/c</i>
Sb(1)	1	0	0	0.0269(1)
Sb(2)	1	0	0	0.1240(1)
Sb(3)	1	0	0	0.2258(1)
Sb(4)	1	0	0	0.2770(1)
Sb(5)	1	0	0	0.3733(1)
Sb(6)	1	0	0	0.4689(1)
Sb(7)	1	0.2846(4)	0.0767(4)	0.0172(1)
Sb(8)	1	0.2254(4)	0.9180(4)	0.13441(7)
Sb(9)	1	0.3813(4)	0.8543(4)	0.99311(7)
Sb(10)	1	0.3036(4)	0.2232(4)	0.11637(7)
Sb(11)	1	0.1441(4)	0.9561(4)	0.07591(6)
Sb(12)	1	0.5959(4)	0.5400(4)	0.10083(7)
Sb(13)	1	0.4176(4)	0.9644(4)	0.05172(7)
Sb(14)	1	0.3886(4)	0.2516(4)	0.06565(7)
Sb(15)	1	0.1868(4)	0.7099(4)	0.09006(6)
Sb(16)	1	0.9439(4)	0.8137(4)	0.17431(6)
Sb(17)	1	0.0586(4)	0.5958(4)	0.14927(7)
Sb(18)	1	0.1118(4)	0.7545(4)	0.03238(7)
Zn(1)	1	0	0	0.0637(2)
Zn(2)	1	0	0	0.3134(2)
Zn(3)	1	0.1665(8)	0.0101(8)	0.1101(1)
Zn(4)	1	0.1999(8)	0.1565(8)	0.0854(1)
Zn(5)	1	0.0713(7)	0.7370(7)	0.0667(10)
Zn(6)	1	0.3054(8)	0.0546(8)	0.0527(1)
Zn(7)	1	0.2146(8)	0.7437(8)	0.1268(1)
Zn(8)	1	0.4045(8)	0.4327(7)	0.1129(1)
Zn(9)	0.99(2)	0	0	0.1917(2)
Zn(10)	0.76(2)	0	0	0.1567(3)
Zn(12)	0.83(2)	0.490(1)	0.847(1)	0.931(2)
Zn(13)	0.90(1)	0.3930(9)	0.9427(9)	0.9599(1)
Zn(14)	0.61(2)	0.492(2)	0.327(2)	0.0970(4)
Zn(15)	0.30(2)	0.426(2)	0.161(2)	0.1251(4)
Zn(16)	0.33(2)	0.469(2)	0.203(2)	0.1217(4)
Zn(17)	0.49(1)	0.302(2)	0.820(2)	0.0271(2)
Zn(18)	0.51(1)	0.302(2)	0.897(2)	0.0224(3)
Zn(19)	0.55(1)	0.455(1)	0.847(1)	0.0279(2)
Zn(20)	0.53(1)	0.023(2)	0.845(2)	0.1429(2)

Zn(21)	0.53(1)	0.039(2)	0.783(2)	0.1454(3)
Zn(22)	0.78(1)	0.2107(8)	0.5813(8)	0.0702(1)
Zn(23)	0.18(1)	0.131(6)	0.508(6)	0.0835(9)
Zn(24)	0.67(1_	0.309(1)	0.260(1)	0.0099(2)
Zn(25)	0.38(1)	0.183(2)	0.180(2)	0.0163(4)
Zn(26)	0.29(1)	0.097(3)	0.188(3)	0.0157(5)
Zn(27)	0.24(1)	0.128(5)	0.124(4)	0.0010(9)
Zn(28)	0.47(1)	0.464(2)	0.177(2)	0.0027(3)
Zn(29)	0.30(1)	0.414(5)	0.051(5)	0.9964(8)
Zn(30)	0.67(1)	0.268(1)	0.907(1)	0.0988(2)
Zn(31)	0.23(1)	0.299(3)	0.938(3)	0.0852(5)
Zn(32)	0.43(2)	0.747(4)	0.710(4)	0.1675(5)
Zn(33)	0.45(2)	0.588(2)	0.601(2)	0.1557(3)
Zn(34)	0.38(1)	0.792(2)	0.843(2)	0.1694(3)
Zn(35)	0.33(1)	0.593(3)	0.550(2)	0.1380(4)
Zn(36)	0.25(1)	0.097(3)	0.221(4)	0.0283(7)
Zn(37)	0.17(1)	0.154(5)	0.687(5)	0.1815(9)
Zn(38)	0.38(2)	0.499(3)	0.315(3)	0.0942(5)
Zn(39)	0.39(1)	0.424(2)	0.029(2)	0.0145(3)
Zn(40)	0.26(2)	0.387(3)	0.116(3)	0.1294(5)
Zn(41)	0.36(1)	0.238(2)	0.688(2)	0.1651(4)
Zn(42)	0.20(1)	0.512(8)	0.966(8)	0.017(1)
Zn(43)	0.16(1)	0.443(7)	0.896(7)	0.961(1)
Zn(44)	0.16(2)	0.74(1)	0.70(1)	0.173(1)
Zn(45)	0.18(2)	0.463(6)	0.859(6)	0.933(1)
Zn(46)	0.18(1)	0.071(6)	0.192(6)	0.0391(9)

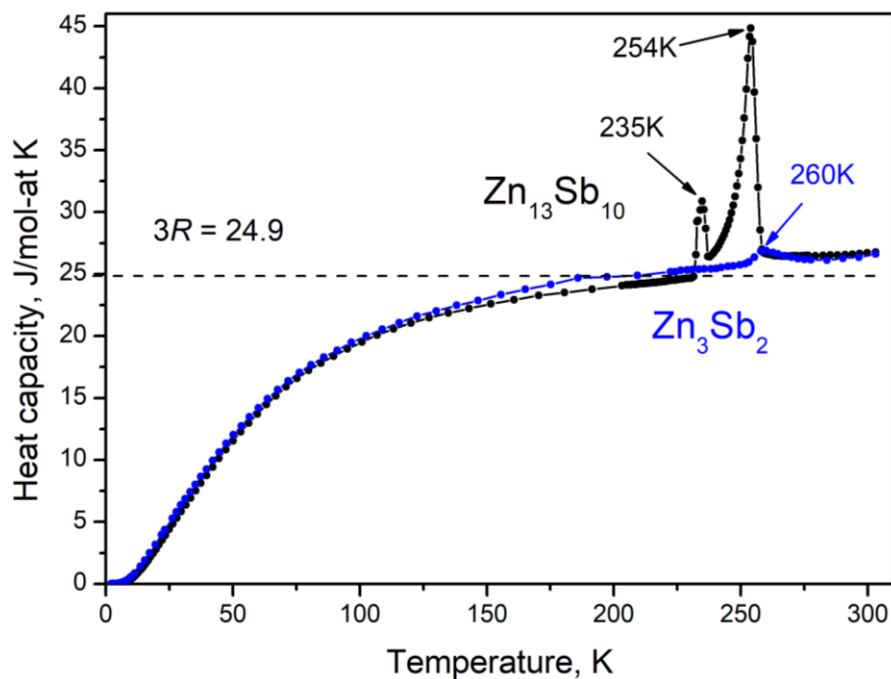


Figure 7.S1. Temperature dependent heat capacities for both $\text{Zn}_{13}\text{Sb}_{10}$ and Zn_3Sb_2 exhibit near identical temperature dependence. Phase transitions for $\text{Zn}_{13}\text{Sb}_{10}$ are well documented in the literature and agree well with our experimental data. The phase transition observed in Zn_3Sb_2 has not been previously observed; its nature is subject of a future investigation.

Chapter 8. Conclusions and Future Work.

In this dissertation, the structures and physical properties of several Zn-Sb phases have been explored and studied, with a primary focus on the thermoelectric $\text{Zn}_{13}\text{Sb}_{10}$ phase. In comparison to some current benchmark thermoelectric materials, the $\text{Zn}_{13}\text{Sb}_{10}$ -based materials have fallen off from the top of the list due to the discovery of materials with higher thermoelectric figure-of-merits. Nonetheless, the transport properties are still of great scientific interest, especially its extraordinarily low thermal conductivity and its electrical properties that are similar to those of a heavily-doped semiconductor. Also, studying these chemically similar Zn-Sb phases enables us to rationalize their structures and properties, and ultimately allows us to improve the thermoelectric performance of other materials.

The Zn-Sb phases in the middle part of the Zn-Sb binary phase diagram were synthesized and studied, including $\text{Zn}_{13}\text{Sb}_{10}$ (the primary focus of this dissertation, Chapter 3, 4, 5, 6 and 7), followed by $\alpha\text{-Zn}_3\text{Sb}_2$ (Chapter 3 and 7), ZnSb (Chapter 3 and 6), and $\beta\text{-Zn}_3\text{Sb}_2$ (Appendix 1). It was found beneficial to study these materials together to gain insights into their structure-property relationship (Chapter 3, 6 and 7), and this was also one of the main goals of this work. Establishing optimal synthetic procedures and temperature-dependent phase analyses (Chapter 3) laid foundation for the synthesis of pure phases and robust characterization of the Zn – Sb phases.

8.1. α -Zn₃Sb₂

α -Zn₃Sb₂ crystallizes with the largest unit cell among the Zn-Sb phases. In general, a material with a larger unit cell is favoured for a lower lattice thermal conductivity. However, α -Zn₃Sb₂ with its large unit cell has a higher lattice thermal conductivity than the pristine Zn₁₃Sb₁₀, which is likely due to a dominant phonon scattering by point defects, as opposed to the phonon-phonon Umklapp scattering in Zn₁₃Sb₁₀. The point defects in α -Zn₃Sb₂ stem from the vast Zn disorder in the crystal structure; only 8 of the 47 Zn sites are fully occupied and the rest are partially occupied. We have suggested that such Zn disorder stems from the Zn mobility, as also seen in the Zn₁₃Sb₁₀ phase.

It is also intriguing that the α -Zn₃Sb₂ phase is more electrically conductive than Zn₁₃Sb₁₀. Currently, such behaviour cannot be rationalized via electronic structure calculations due to the structural complexity of α -Zn₃Sb₂. Possibly, such electrical transport properties stem from the relative position of the Fermi level with respect to the electronic bands, and/or Zn deficiencies as indicated by X-ray diffraction experiments and elemental analyses.

8.2. Zn₁₃Sb₁₀-based Materials

8.2.1. Synthesis, Structure and Properties

A new synthesis procedure was developed for Zn₁₃Sb₁₀ in this work, which allowed a systematic study of the synthesis-composition-property relationship of the Zn₁₃Sb₁₀-based materials.

The heat capacity measurements on the doped $\text{Zn}_{13}\text{Sb}_{10}$ samples (Chapter 5) suggested a suppressed Zn mobility in the $\text{Zn}_{13}\text{Sb}_{10}$ phase through the incorporation of foreign atoms, evident from the suppressed $\alpha' - \alpha$ and $\alpha - \beta$ phase transitions at low temperatures. Single crystal X-ray diffraction analysis of the In-doped sample at 100 K indicated a phase transition similar to that of the α - $\text{Zn}_{13}\text{Sb}_{10}$ polymorph, into the $C2/c$ space group. On the other hand, the Cd-doped $\text{Zn}_{13}\text{Sb}_{10}$ (the $\text{Zn}_{6.5}\text{Cd}_{6.5}\text{Sb}_{10}$ sample, Chapter 6) has shown a 1st order phase transition at 247 K, with its low temperature polymorph also resembling the α - $\text{Zn}_{13}\text{Sb}_{10}$ polymorph.

The experimental survey of dopants in $\text{Zn}_{13}\text{Sb}_{10}$ (Chapter 5) has shown the limited ability to substitute Zn with foreign elements in the structure, largely due to Zn tetrahedral coordination in the Sb sublattice. Successful dopants have d^5 (Mn^{2+}) and d^{10} (Ga^{3+} , Cd^{2+} , In^{3+}) electron configurations, and they tend to adopt tetrahedral environments.

The charge transport properties of the Mn-, Cd-, Ga-, and In-doped $\text{Zn}_{13}\text{Sb}_{10}$ materials were investigated in Chapter 4, 5 and 6. The $\text{Zn}_{12.75}\text{Mn}_{0.25}\text{Sb}_{10}$, $\text{Zn}_{12.55}\text{Ga}_{0.3}\text{Sb}_{10}$, $\text{Zn}_{11.96}\text{Cd}_{1.04}\text{Sb}_{10}$ and $\text{Zn}_{10.4}\text{Cd}_{2.6}\text{Sb}_{10}$ samples have higher hole concentrations than that in the pristine $\text{Zn}_{13}\text{Sb}_{10}$ sample, while the $\text{Zn}_{11.5}\text{In}_1\text{Sb}_{10}$ sample has a similar hole concentration to the pristine $\text{Zn}_{13}\text{Sb}_{10}$ sample. The origin of such changes in carrier concentrations in the Mn-, Ga- and In-doped $\text{Zn}_{13}\text{Sb}_{10}$ remains unclear. The Cd substitution in the $\text{Zn}_{13}\text{Sb}_{10}$ structure was explored in Chapter 6, along with the $\text{Zn}_{1-x}\text{Cd}_x\text{Sb}$ solid solution. The study presented in Chapter 6 revealed a non-monotonous change of hole concentrations in both the $(\text{Zn}_{1-z}\text{Cd}_z)_{13}\text{Sb}_{10}$ and the $\text{Zn}_{1-x}\text{Cd}_x\text{Sb}$ series.

Studies on the thermal properties of the $\text{Zn}_{13}\text{Sb}_{10}$ materials have shown the ability to alter the dominant phonon scattering pathway of the $\text{Zn}_{13}\text{Sb}_{10}$ -based material, by substituting different elements into the material. For example, a point-defect scattering becomes dominant in the In- and Ga-doped $\text{Zn}_{13}\text{Sb}_{10}$, while the Mn- and Cd-doped $\text{Zn}_{13}\text{Sb}_{10}$ retain the Umklapp scattering. On the other hand, the thermal conductivity of a Cd-doped $\text{Zn}_{13}\text{Sb}_{10}$ sample with the Zn:Cd ratio close to 1:1 (Chapter 6) suggests Umklapp scattering to be the dominant phonon scattering pathway. It was surprising to find that the Zn/Cd disorder in this $(\text{Zn}_{0.5}\text{Cd}_{0.5})_{13}\text{Sb}_{10}$ sample was not enough to alter the dominant phonon scattering mechanism to the point defect scattering, as seen in the In-/Ga-doped $\text{Zn}_{13}\text{Sb}_{10}$ samples (Chapter 4 and 5). Also, the $\text{Cd}_{13}\text{Sb}_{10}$ sample was found to have the lowest thermal conductivity at room temperatures in the $(\text{Zn}_{1-z}\text{Cd}_z)_{13}\text{Sb}_{10}$ series, due to lower-lying optical phonon modes and an onset of Umklapp scattering at lower temperatures than in the other two samples in the series.

8.2.2. Thermoelectric Performance

Results presented in Chapter 5 show that although the In-doped $\text{Zn}_{13}\text{Sb}_{10}$ sample has an improved power factor, the thermoelectric figure-of-merit zT is lower than that of the pristine $\text{Zn}_{13}\text{Sb}_{10}$ sample due to the significantly increased thermal conductivity. On the other hand, the Mn-doped $\text{Zn}_{13}\text{Sb}_{10}$ sample has a higher zT than that of the pristine sample mainly due to the increased power factor, while maintaining a similar thermal conductivity at ~ 400 K.

8.2.3. Stability Under Different Conditions

The stability of $\text{Zn}_{13}\text{Sb}_{10}$ -based materials under elevated pressure appeared to be a major issue during the synthesis. $\text{Zn}_{13}\text{Sb}_{10}$ -based materials densified via spark plasma sintering (Appendix 2) showed significant decomposition. Such findings echo the results obtained by pressing the samples in bakelite at 175 °C and ~30 MPa (Chapter 5), by hot pressing, or by hot extrusion as described in Appendix 2 (along with the hot extrusion of ZnSb-based materials). Due to this issue, the traditional melt-and-solidification approach remains the most feasible way to prepare $\text{Zn}_{13}\text{Sb}_{10}$ -based materials.

8.3. ZnSb-based Materials

Since ZnSb was extensively studied in the past, it was mainly used by us as a model to facilitate the investigation of the $\text{Zn}_{13}\text{Sb}_{10}$ materials (Chapter 6). ZnSb-based materials studied in this dissertation were synthesized by melting, followed by spark plasma sintering.

The bonding picture of the ZnSb phase was examined using the ELF method. Results from the ELF method suggested the Zintl-Klemm formalism to be an accurate description of the ZnSb phase, involving covalent Sb – Sb, ionic Zn – Sb and metallic Zn – Zn interactions. Due to the similar local environments of Zn and Sb in ZnSb and $\text{Zn}_{13}\text{Sb}_{10}$, the Zintl-Klemm formalism should also be an accurate description of the $\text{Zn}_{13}\text{Sb}_{10}$ structure.

Study of the charge transport properties of the $\text{Zn}_{1-x}\text{Cd}_x\text{Sb}$ series (Chapter 6) revealed non-monotonous changes upon Cd substitution similar to the $(\text{Zn}_{1-z}\text{Cd}_z)_{13}\text{Sb}_{10}$ series. The hole concentrations of samples initially increase due to a bond softening effect when Cd content is low, and then dropped due to an increase in the Zn/Cd content, resulting in a

smaller (Zn,Cd) deficiency, when the Cd content is high. Additionally, we suggest that the sample-dependent local maximum in electrical resistivity of ZnSb stems from a Zn deficiency in the ZnSb sample.

The thermal conductivity of the $\text{Zn}_{1-x}\text{Cd}_x\text{Sb}$ series (Chapter 6) satisfies the Klemens-Callaway model: the ZnSb and CdSb sample have higher thermal conductivities than the $x = 0.5$ sample. On the other hand, CdSb has a lower thermal conductivity than that of ZnSb, stemming from a lower sound velocity in CdSb.

8.4. Future Work in the Zn–Sb Phases

Considering the non-monotonous change in the charge transport properties upon Cd substitution, the effects of dopants on the charge transport properties in $\text{Zn}_{13}\text{Sb}_{10}$ should be revisited. This observation is further collaborated by the outcomes from the Ga and In substitution. Ga and In are isoelectronic, so similar effects on the transport properties of $\text{Zn}_{13}\text{Sb}_{10}$ were expected. However, the effects of the In- and Ga-doping on $\text{Zn}_{13}\text{Sb}_{10}$ reported in Chapter 5 are different, most likely due to the difference in doping levels of In (8 at.%) and Ga (2 at.%). The ρ and α of the $\text{Zn}_{12.55}\text{In}_{0.3}\text{Sb}_{10}$, $\text{Zn}_{12.55}\text{Ga}_{0.3}\text{Sb}_{10}$ and pristine $\text{Zn}_{13}\text{Sb}_{10}$ samples indicate that Ga/In incorporation at the same dopant level leads to a similar change in ρ and α , suggesting an increase in the hole concentration (**Figure 8.1**).

Combining the results of the $\text{Zn}_{11.5}\text{In}_1\text{Sb}_{10}$ sample, there is a non-monotonous change of charge transport properties in the $(\text{Zn}_{1-1.5x}\text{In}_x)_{13}\text{Sb}_{10}$ system, with a peak carrier

concentration between ~2 – 8 at. % of In. This non-monotonous change in the In-doped $Zn_{13}Sb_{10}$ samples should be confirmed by further charge transport property measurements.

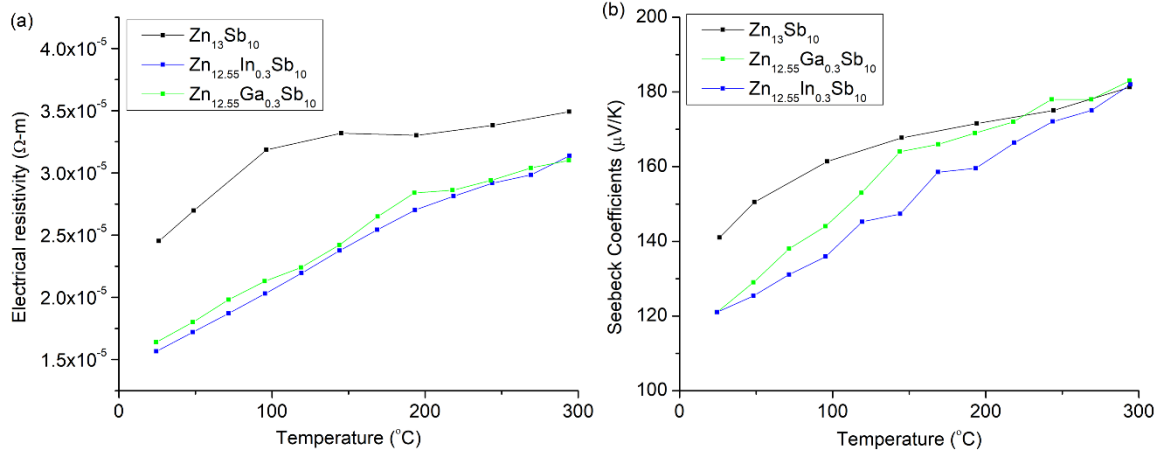


Figure 8.1. (a) Electrical resistivity and (b) Seebeck coefficients of the $Zn_{13}Sb_{10}$, $Zn_{12.55}Ga_{0.3}Sb_{10}$ and $Zn_{12.55}In_{0.3}Sb_{10}$ samples above room temperatures.

The effect of additional vacancies introduced by the In/Ga doping on thermal conductivities should also be revisited. Both the In-/Ga-doped $Zn_{13}Sb_{10}$ samples have shown to possess larger thermal conductivities above room temperatures due to a significant point defect scattering and a weakened Umklapp scattering of phonons (**Figure 5.S2**). The thermal conductivity of the Ga-doped $Zn_{13}Sb_{10}$ sample should be collected at low temperatures to confirm this effect. Furthermore, if the point defect scattering dominates the phonon scattering pathway, then together with the α - Zn_3Sb_2 and the $(Zn_{1-x}Cd_x)_{13}Sb_{10}$ material, the phonon scattering power of atomic disorder and atomic vacancies will be of fundamental interest. The Klemens model serves as a suitable choice to describe the effects of vacancies and interstitial defects on the thermal conductivities in materials³¹.

The fact that both Umklapp- and point defect-dominant scattering occurring in the same base material ($\text{Zn}_{13}\text{Sb}_{10}$) is likely beneficial for modelling and comparison.

The anisotropic transport properties of the $\text{Zn}_{13}\text{Sb}_{10}$ material may be also of interest due to its structure. A considerable amount of work has been done throughout this dissertation to grow $\text{Zn}_{13}\text{Sb}_{10}$ crystals using Sn or Bi flux. The flux-grown $\text{Zn}_{13}\text{Sb}_{10}$ crystals, however, were seldom large enough for property measurements. We suspected that the inability for us to grow large $\text{Zn}_{13}\text{Sb}_{10}$ crystals is due to our apparatus set up, as larger $\text{Zn}_{13}\text{Sb}_{10}$ single crystals have been synthesized and reported in the literature^{128,129,216,217}.

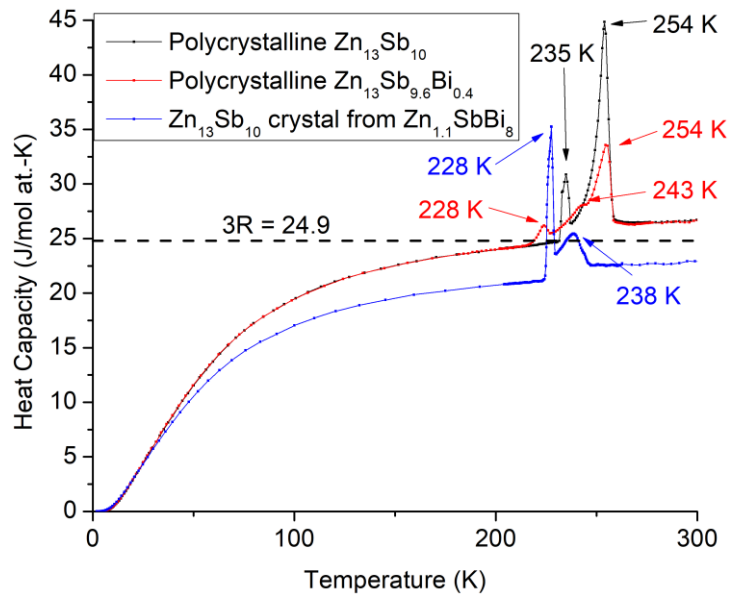


Figure 8.2. Heat capacities of a polycrystalline, pristine $\text{Zn}_{13}\text{Sb}_{10}$ sample (black), a polycrystalline $\text{Zn}_{13}\text{Sb}_{9.6}\text{Bi}_{0.4}$ sample, and a single-crystalline $\text{Zn}_{13}\text{Sb}_{10}$ from the $\text{Zn}_{1.1}\text{SbBi}_8$ flux.

On the other hand, heat capacity measurements on these $\text{Zn}_{13}\text{Sb}_{10}$ materials have shown signs of Sn/Bi incorporations into the $\text{Zn}_{13}\text{Sb}_{10}$ structure (see **Figure 8.2** for Bi and **Figure 5.3** for Sn), and such incorporations alter the properties of the pristine $\text{Zn}_{13}\text{Sb}_{10}$ material. In comparison to the polycrystalline $\text{Zn}_{13}\text{Sb}_{10}$, the Bi-flux grown $\text{Zn}_{13}\text{Sb}_{10}$ crystal has phase transitions at different temperatures, which is likely an indication of Bi incorporation into the structure. Also, the grown crystal has a lower heat capacity than the pristine, polycrystalline $\text{Zn}_{13}\text{Sb}_{10}$ sample. On the other hand, the polycrystalline $\text{Zn}_{13}\text{Sb}_{9.6}\text{Bi}_{0.4}$ sample shows 3 peaks in its heat capacity, which suggests a mixture of pristine and Bi-doped $\text{Zn}_{13}\text{Sb}_{10}$ phases. A dopant-free, single-crystalline $\text{Zn}_{13}\text{Sb}_{10}$ sample may shed some light on this issue.

As stated in the Appendix 2, future studies on the $\text{Zn}_{13}\text{Sb}_{10}$ -based materials should consider optimization of the synthetic procedures, especially the cooling step, in order to minimize the time and cost needed to prepare the $\text{Zn}_{13}\text{Sb}_{10}$ -based materials suitable for property measurements.

Appendix 1. Syntheses and Characterizations of the Metastable, High-Temperature β -Zn₃Sb₂ phase

This chapter contains the material covered in the manuscript “Syntheses and Characterizations of the Metastable, High-Temperature β -Zn₃Sb₂ phase”, which is unpublished. The structure determination was done with the assistance of Dr. James Britten in the McMaster Analytical X-Ray Diffraction Facility (MAX), Hamilton, Ontario, Canada. The experimental procedures, data interpretation and manuscript preparation were completed by the candidate.

Our investigations have shown the possibility to obtain the bulk $\text{Zn}_{17+\alpha}\text{Sb}_{12}$ ($\beta\text{-Zn}_3\text{Sb}_2$) phase, at room temperatures. This conclusion is achieved by comparing powder and single-crystal X-ray diffraction data of the bulk samples to the high-temperature powder X-ray diffraction and single-crystal data in the literature. Thermoelectric properties of polycrystalline $\beta\text{-Zn}_3\text{Sb}_2$ materials were not collected, since a high purity $\beta\text{-Zn}_3\text{Sb}_2$ sample could not be prepared.

A1.1. Introduction

At the end of the 20th century, the $\beta\text{-Zn}_{13}\text{Sb}_{10}$ phase (“ Zn_4Sb_3 ”) was identified as one of the promising p-type thermoelectric materials⁹⁰. There is also the ZnSb phase in the Zn – Sb phase diagram, which was previously investigated as a potential thermoelectric material^{161,207,208,218}. These two well-known materials, with close compositions and some structural similarities, display rather different thermoelectric properties.

The Zn – Sb system also features some other phases with slightly different compositions, as shown in our previous work¹⁴³. These phases are located in the central part of the Zn – Sb phase diagram: Zn_8Sb_7 ⁹⁸, $\text{Zn}_{9-\delta}\text{Sb}_7$ ⁹⁹, $\text{Zn}_{1+\delta}\text{Sb}$ ²¹⁰, $\alpha\text{-Zn}_3\text{Sb}_2$ ¹³³ and $\text{Zn}_{17+\alpha}\text{Sb}_{12}$ ²⁰⁹. The $\text{Zn}_{1+\delta}\text{Sb}$ nanophase was observed by HRTEM and crystallizes with a hexagonal pseudosymmetry in the $P\bar{1}$ space group; the $\text{Zn}_{9-\delta}\text{Sb}_7$ phase on the other hand is

stable only at high-temperatures^{99,143}. The thermoelectric properties of both $Zn_{1+\delta}Sb$ and $Zn_{9-\delta}Sb_7$ phases were not studied. On the other hand, the Zn_8Sb_7 and the α - Zn_3Sb_2 phases could be stabilized at room temperatures and they again show distinct thermoelectric properties in comparison to the other Zn-Sb phases. The last phase yet to be investigated in terms of thermoelectric properties is the $Zn_{17+\alpha}Sb_{12}$, which was reported to have an incommensurably modulated (3+1) structure²⁰⁹.

It is possible to obtain the $Zn_{17+\alpha}Sb_{12}$ phase at room temperatures; single crystals of the $Zn_{17+\alpha}Sb_{12}$ phase were synthesized using a self-flux method, and subsequently its crystal structure was established²⁰⁹. This study attempted to synthesize the bulk $Zn_{17+\alpha}Sb_{12}$ phase and characterize its thermoelectric properties to complete the thermoelectric analysis of the Zn – Sb phases.

A1.2. Experimental

A1.2.1. Synthesis

Pieces of pure elements Zn (99.99 wt. % CERAC) and Sb (99.999 wt. % 5N. Plus), were used as starting materials. The first unintentional synthesis of the β - Zn_3Sb_2 phase (which was later found to be the $Zn_{17+\alpha}Sb_{12}$ phase, in contrary to the findings in Chapter 7¹³³), was achieved when the sample with the loading composition of Zn_3Sb_2 was quenched from 450 °C in cold water after annealing for 2 days (**Figure A1.1**). The sample contained $Zn_{13}Sb_{10}$ as the main phase, and (an) impurity phase(s). Based on the high-temperature X-ray diffraction data obtained previously in our group¹⁴³ (**Figure A1.2**), the impurity was identified as the β - Zn_3Sb_2 phase.

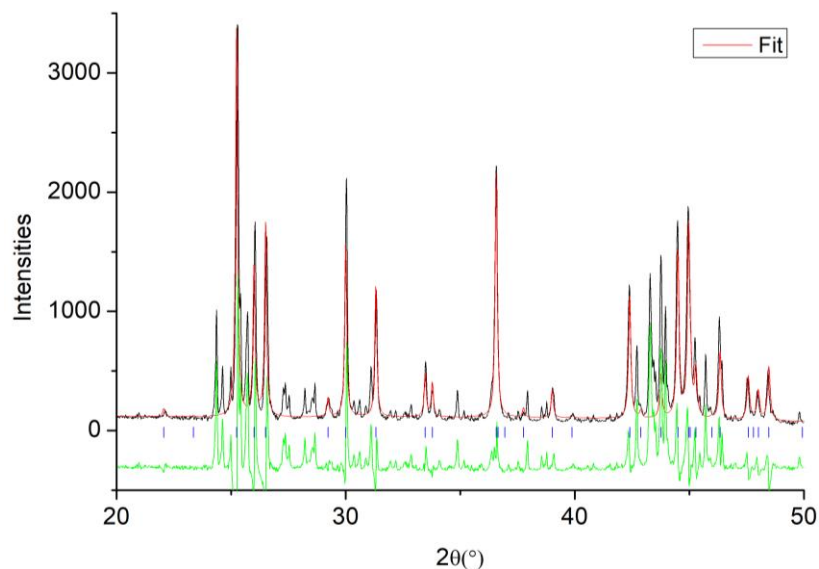


Figure A1.1. Rietveld refinement of the Zn_3Sb_2 sample which contained the $\text{Zn}_{13}\text{Sb}_{10}$ phase as the main phase and $\beta\text{-Zn}_3\text{Sb}_2$ as a minority phase, described above, and its peaks are not described by refinement.

Experiments were attempted to synthesize a pure sample and potentially obtain a crystal for single-crystal X-ray diffraction. According to the high-temperature diffraction data, the sample is pure at temperatures above 490 °C. Samples with loading compositions Zn_3Sb_2 and $\text{Zn}_{62}\text{Sb}_{38}$ were made and quenched at 450 °C and 500 °C. The zinc-richer $\text{Zn}_{62}\text{Sb}_{38}$ samples yielded significantly less $\beta\text{-Zn}_3\text{Sb}_2$, although this Zn-richer composition was used to synthesize pure $\alpha\text{-Zn}_3\text{Sb}_2$ ¹³³. (Extra zinc was employed to compensate for Zn loss due to its high vapour pressure.)

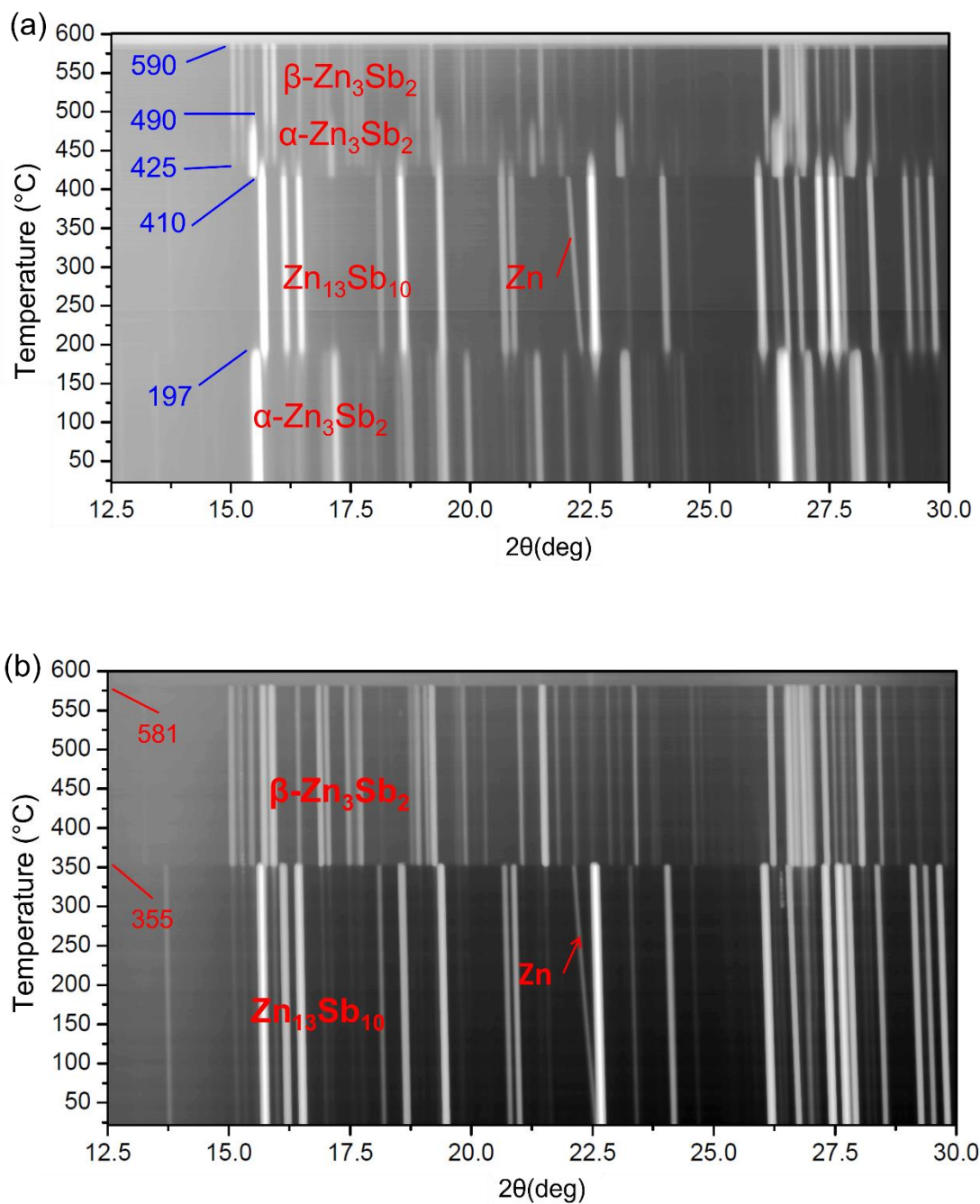


Figure A1.2. Synchrotron powder X-ray diffraction data for the $\alpha\text{-Zn}_3\text{Sb}_2$ sample (a) during heating from room temperature up to 600 °C, and (b) during cooling from 600 °C to room temperature.

Table A1.1. Samples loading compositions, annealing temperatures, and annealing times to synthesize bulk β -Zn₃Sb₂.

Sample loading compositions	Heat treatment	Annealing time before quenching (h)
Zn _{2.9-3.2} Sb ₂ ($\delta = 0.05$)	750 °C → (100 °C/h) 500 °C	12
Zn ₃ Sb ₂ , Zn _{3.2} Sb ₂	750 °C → (100 °C/h) 520 °C	0
	750 °C → (100 °C/h) 520 °C	48
	750 °C → (100 °C/h) 520 °C → (100 °C/h) 420 °C	0, 96
	750 °C → (100 °C/h) 600 °C	0

Samples of 2 g with different loading compositions were weighed and sealed in the evacuated silica tubes and placed in the same box furnace to eliminate temperature variances. The samples were heated to 750 °C at 150 °C/h and annealed for 14 h, while being shaken in between to ensure mixing of the molten elements. The samples were then cooled at different rates, annealed at different temperatures and for different times before quenching. Attempts to obtain the bulk β -Zn₃Sb₂ are summarized in **Table A1.1**. All products in **Table A1.1** have detectable amounts of the β -Zn₃Sb₂ phase as a minor phase, with β -Zn₁₃Sb₁₀ as the major phase, except for the Zn_{3.2}Sb₂ sample that was quenched from 600 °C, which had only β -Zn₁₃Sb₁₀ and elemental Zn.

A1.2.2. Powder and Single Crystal X-ray Diffractions

Polycrystalline samples were analyzed on a PANalytical X'Pert Cu K α ₁ powder X-ray diffractometer (PXRD) at room temperature. The samples were ground and deposited on a silicon zero background holder. The data were collected with the 2θ range of 20 – 80

degrees and the total collection time of 1 hour. Rietveld refinement¹¹¹ was performed to evaluate samples' purity and to derive lattice parameters.

Room-temperature single-crystal data in the full reciprocal sphere were collected on a Bruker SMART APEX II diffractometer with a 3 kW sealed-tube Mo generator and APEX II CCD detector at the McMaster Analytical X-Ray (MAX) Diffraction Facility. A semi-empirical absorption correction was applied using redundant and symmetry related reflections. Structural determinations and refinements were performed using the OLEX2 program¹⁶⁰ and the JANA2006 program package²¹⁹.

A1.3. Results and Discussion

A1.3.1. Structure Solution

An automatic indexing of the reflections yielded a large orthorhombic cell with $a = 15.3567 \text{ \AA}$, $b = 25.0173 \text{ \AA}$ and $c = 7.2564 \text{ \AA}$ and incommensurate superstructural peaks (**Figure A1.3**). An incommensurably modulated structure with similar cell parameters was reported earlier by M. Boström et al., that it crystallizes in a $Pnna(\alpha 00)0s0$, $\alpha = 0.383$ super space group ($a = 7.283 \text{ \AA}$, $b = 15.398 \text{ \AA}$, $c = 25.06 \text{ \AA}$). Using the JANA2006 program package²¹⁹, the collected data were indexed with the super space group $Pccn(00\gamma)s00$, $\gamma = 0.383$ (the alternate setting is $Pnaa(\alpha 00)0s0$, $\alpha = 0.383$, to match the cell parameters reported by M. Boström et al., but in a different super space group.). The current data set cannot be solved using the super space group $Pnna(\alpha 00)0s0$ reported by M. Boström et al. due to the significant violation of the symmetry conditions. Note that the data collected from the Bruker SMART APEX II diffractometer was used in attempt to solve the

incommensurably modulated structure. A $R_1 = 0.0529$ value was obtained for the refinement using the main reflections only in the Olex2 program. The structural model from this refinement was imported into the JANA2006 program. The refinement results, however, were poor due to the satellite reflections, yielding the total R factor of 0.2585 and the R factor of 0.1134 for the main reflections.

A more detailed examination of the report of M. Boström et al. and its subsequent reported structure, however, has revealed a mistake in the reported structure. The crystallographic information file provided in the Inorganic Crystal Structure Database (ICSD) did not result in the structure described in the literature. The provided data however resulted in the described structure after the space group was changed to $Pnaa$, while using the same atomic parameters. The described structure also resembles our refined structure, which suggests that our obtained structural solution is correct.

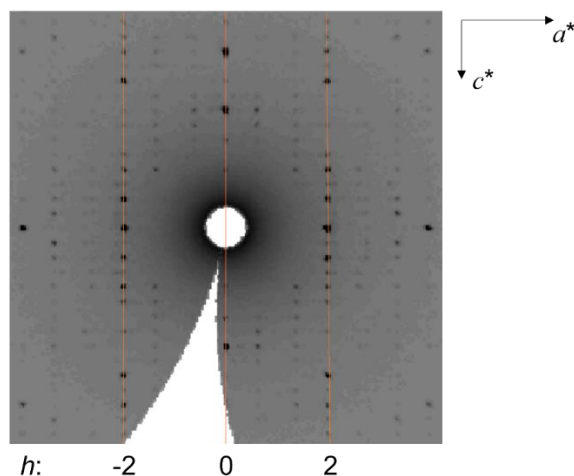


Figure A1.3. Cross section of the reciprocal space, the $h0l$ layer for the β - Zn_3Sb_2 grain, generated from STOE IPDS II diffractometer and the X-area software¹⁰³.

The collected data was also imported to the JANA2006 program directly to obtain a structural solution using the Superflip, and a better refinement was obtained. Unfortunately, this model still suffers from high R factors from the satellite peaks, although the R-factor for the main reflections remains relatively low. The resulting R factors are higher than those reported by M. Boström et al.²⁰⁹. The main issue lies in the occupancy modulation parameters of Zn, and they were not optimized. The refinement results in **Table A1.2** and **A1.3** largely follows the recommended refinement conditions from the literature²⁰⁹.

Table A1.2. Comparison of R-factors of those obtained in this work and by Boström et al..

	This work	Boström et al.
R(F), wR(F) all reflections	15.43, 16.05	11.7, 10.4
R(F), wR(F) main reflections	9.61, 11.96	6.9, 7.2
R(F), wR(F) 1 st order satellite reflections	16.84, 17.12	15.2, 14.7
R(F), wR(F) 2 nd order satellite reflections	31.85, 36.16	28.2, 29.6

Table A1.3. Details of refinement of the β -Zn₃Sb₂ crystal using the JANA2006 program.

Chemical formula	Zn _{2.324} Sb ₂
Chemical formula weight	395.53
Super space group	<i>Pnaa</i> (<i>a</i> 00) <i>s</i> 00
Unit cell parameters	$a = 7.2564 \text{ \AA}$, $V = 2787.8 \text{ \AA}^3$ $b = 15.3567 \text{ \AA}$, $c = 25.0173 \text{ \AA}$,
Modulation wave vector	-0.383, 0, 0

Z	24
Density (calculated), g/cm ³	5.65
No. of measured reflection	21024
No. of indices observed main reflection	3114
No. of indices observed 1 st first satellite reflection	3952
No. of indices observed 2 nd first satellite reflection	2124
Observation criterium	$F^2 > 3\sigma(F^2)$
Ranges of h, k, l and m	0 – 11, 0 – 21, 0 – 35, -2 – 2
$R_{\text{int(obs)}}$, $R_{\text{int(all)}}$	8.44, 13.36
GOF	4.02
No. of used reflections	9158
No. of parameters	583
Min/Max theta	1.56, 30.54

A1.3.2. Synthetical Attempts of the β -Zn₃Sb₂ phase

According to **Figure A1.2**, the β -Zn₃Sb₂ phase is stable from 425 – 590 °C, and can co-exist with the α -Zn₃Sb₂ phase at 425 – 490 °C. To obtain a pure bulk β -Zn₃Sb₂, the samples were generally quenched at temperatures higher than 500 °C, as shown in **Table A1.1**. Also, the loading amount of Zn was explored, since the amount of Zn in the structure of β -Zn₃Sb₂ could not be reliably established, and to also compensate for the Zn losses due to its high vapour pressure. All attempts shown in **Table A1.1** failed to yield β -Zn₃Sb₂ as the main phase, but rather as a minor phase to the dominant β -Zn₁₃Sb₁₀.

Considering the reported crystal structure, the loading composition should have the Zn:Sb ratio of more than 17:12 \approx 2.83:2, to account for the “+ α ” in the crystallographic composition and compensate for the Zn losses at high temperatures. As the quenching temperature increases, more Zn is needed to compensate for the increased Zn vapour pressure in the evacuated silica ampoules.

The synthesis of α - Zn_3Sb_2 phase has a crystallographic composition of $\text{Zn}_{2.91}\text{Sb}_2$ and its bulk sample was synthesized using a $\text{Zn}_{3.26}\text{Sb}_2$ ($\text{Zn}_{62}\text{Sb}_{38}$) composition, quenched from 430 °C. In retrospect, more Zn amount than in the $\text{Zn}_{3.2}\text{Sb}_2$ samples may be needed to compensate for the Zn losses to synthesize a pure bulk β - Zn_3Sb_2 bulk sample, quenched from higher temperatures. However, a synthetic attempt with Zn-rich loading compositions $\text{Zn}_{3.5}\text{Sb}_2$ and $\text{Zn}_{3.8}\text{Sb}_2$ quenched from 550 °C after 12 hours of annealing, yielded only β - $\text{Zn}_{13}\text{Sb}_{10}$ and Zn.

Phase analyses of the quenched samples resembled the results obtained shown in **Figure A1.2(b)**, i.e., a mixture of β - $\text{Zn}_{13}\text{Sb}_{10}$, Zn and β - Zn_3Sb_2 was obtained at room temperatures. Furthermore, there appears to be a sudden phase change at 355 °C, in contrary to a more continuous change in the heating process (**Figure A1.2(a)**) at 425 – 490 °C. A more rigorous method may be needed to kinetically stabilize the β - Zn_3Sb_2 phase at room temperatures, if possible.

A1.4. Conclusions

Although the synthesis of bulk β - Zn_3Sb_2 phase was unsuccessful, this work suggests the possibility to obtain the polycrystalline β - Zn_3Sb_2 phase in bulk. Next steps would be to establish the composition of the β - Zn_3Sb_2 phase through wavelength dispersive spectroscopy on the single crystalline samples, and then to synthesize the β - Zn_3Sb_2 phase in bulk.

Appendix 2. Compaction Methods of the Thermoelectric Zn₁₃Sb₁₀-based materials.

This chapter contains the material covered in the manuscript “Compaction Methods of the Thermoelectric Zn₁₃Sb₁₀-based materials”, which is unpublished. The experimental procedures, data interpretation and manuscript preparation were completed by the candidate.

Zn₁₃Sb₁₀-based materials made from melt and solidification method contains visible cracks, which are undesirable for industrial application. Neither spark plasma sintering (SPS), hot press (HP) nor hot extrusion (HE) can be used to efficiently make Zn₁₃Sb₁₀-based materials due to the poor stability of the Zn₁₃Sb₁₀ phase under high pressure and elevated temperatures. The melt-and-solidification method should be improved to further reduce cracks in the sample for industrialization.

A2.1. Introduction

Stability and suitable compaction methods of thermoelectric materials are crucial factors for their commercialization. For the last two decades, the Zn₁₃Sb₁₀ phase has been extensively investigated as a potential candidate for thermoelectric applications, however, it has not moved downstream because of the stability issues.

In this work we aim to investigate the stability of the Zn₁₃Sb₁₀ materials densified by some compaction methods. Zn₁₃Sb₁₀ materials made by the melt and solidification method in this dissertation often contained cracks inside the ingots, most likely due to the built-up tension from the solid-solid phase transition at high temperatures¹⁴³. Efforts have been done to reduce cracks in ingots by modifying the heat treatment and cooling. Altering the cooling process helped reduce cracks in Zn₁₃Sb₁₀-based ingots such that materials can be cut for physical property measurements, still some observable cracks remained in the ingots, which is undesirable during the industrial production of Zn₁₃Sb₁₀. Furthermore,

remelting and solidifying the $Zn_{13}Sb_{10}$ -based samples leads to Zn losses due to Zn high vapour pressure, which in turn affects the purity of the material. High vapour pressure of Zn and decomposition of undoped β - $Zn_{13}Sb_{10}$ is associated with Zn migration inside the β - $Zn_{13}Sb_{10}$ materials²²⁰. Decomposition of $Zn_{13}Sb_{10}$ was also observed during densification, for example the spark plasma sintering (SPS) of Zn_4Sb_3 .¹²⁷ At the same time SPS direct synthesis of Zn_4Sb_3 materials from elemental powders with additional Zn foil was reported²²¹. This work explores SPS sintering of the $Zn_{13}Sb_{10}$ -based materials and the effect of foreign elements on phase stability. The composition and density of the densified pellets were the primary factors used to determine the feasibility of the SPS methods.

A2.2. Experimental

A2.2.1. Synthesis

Pieces of pure elements Zn (99.99 wt. % CERAC), Sb (99.999 wt. % 5N. Plus), Mn (99.9 wt. % Alfa Aesar) and In (99.99 wt. % Alfa Aesar) were used as starting materials. Incorporation of Mn and In followed the $Zn_{13-x}M_xSb_{10}$ loading formula. Note that the loading composition of the In-doped samples is not charge balanced. The weighted elements were sealed in the evacuated silica tubes and placed in the same box furnace to eliminate temperature variances. The samples were heated to 750°C at 150°C/h and annealed for 16 h, while being shaken in between to ensure mixing of the molten elements. The samples were cooled from 750 °C to 350 °C at a rate of 50°C/h and annealed at 350 °C for 2 days to achieve phase homogeneity. The samples were finally cooled down to room temperature at a rate of 50 °C/h. Ingots were hand-ground into powders and taken for

powder X-ray diffraction before pressing. Phase-pure powders were either pressed spark plasma sintering (SPS), hot pressing (HP) or hot extrusion (HE) method, the pressed samples were analyzed again through X-ray diffraction to examine their composition and purity.

A2.2.2. Powder X-ray Diffractions

Polycrystalline samples were analyzed on a PANalytical X'Pert Cu $K\alpha_1$ powder X-ray diffractometer (PXRD) at room temperature. The samples were ground and deposited on a silicon zero background holder. The data were collected with the 2θ range of $20 - 70^\circ$ and a scanning speed of 1 degree/min. Rietveld refinement¹¹¹ was performed to evaluate samples' purity.

A2.2.3. Spark Plasma Sintering

Ground powders were loaded into a graphite die of 10 mm in diameter, and sintered in a Dr. Sinter instrument. To avoid direct contact between the powdered samples and the die plungers, a layer of graphite sheet was placed in between. The samples were heated to 250, 300 and 350 °C at 50 °C/min under 45 MPa pressure and kept at the temperature for 5 min. The output power of the instrument was then turned off, and the samples were allowed to cool to room temperature.

A2.2.4. Hot Pressing

Ground powders were loaded into a graphite-hardened die of 12.7 mm in diameter, and hot-pressed in an Oxy-Gon FR-210-30T-ASA-160-EVC hot press furnace system. The

samples were heated to 200, 250 and 300 °C at 50 °C/min under 70 MPa pressure for 30 min.

A2.3. Results and Discussion

A2.3.1. Composition and Purity of the Pressed Pellets

Table A2.1. SPS conditions and results of the pressed samples.

Powdered sample	Sintering temperature (°C)	Zn ₁₃ Sb ₁₀ unit cell volume (Å ³)	Composition (wt. %)
Zn ₁₃ Sb ₁₀	350	1610.95(5)	Zn ₁₃ Sb ₁₀ (59.3(6) %) ZnSb (40.3(3) %) Zn (0.43(3) %)
	300	1611.75(4)	Zn ₁₃ Sb ₁₀ (67.8(4) %) ZnSb (31.7(2) %) Zn (0.49(3) %)
	300 (*)	1611.35(5)	Zn ₁₃ Sb ₁₀ (75.5(5) %) ZnSb (24.1(3) %) Zn (0.34(2) %)
	250 (^)	1610.74(5)	Zn ₁₃ Sb ₁₀ (91.6(9) %) ZnSb (8.1(3) %) Zn (0.34(3) %)
Zn _{12.5} In _{0.5} Sb ₁₀	250	1616.84(4)	Zn ₁₃ Sb ₁₀ (90.9(7) %) ZnSb (8.6(3) %) Zn (0.44(2) %)
Zn _{12.75} Mn _{0.25} Sb ₁₀	250 (^)	1610.71(4)	Zn ₁₃ Sb ₁₀ (88.9(8) %) ZnSb (10.8(3) %) Zn (0.27(2) %)

The standard deviations reported in brackets are derived from the Rietveld refinements.
*: Mica film was used to replace graphite paper in this sample to prevent electrical current going through the sample.

The composition and purity of the pressed samples from X-ray diffractions are summarized in **Table A2.1**. All pre-pressed powders were phase-pure according to powder X-ray diffraction, except for the non-charge-balanced Zn_{12.5}In_{0.5}Sb₁₀ sample, which has

elemental Zn as an impurity. Powders from the pressed pellets can be scraped off easily using a scalpel, which shows a poor compaction and the relatively low density of the pellets.

Note that the Zn content in the pressed pellets was generally underestimated by powder X-ray diffraction; some elemental Zn fell from the sample holder during sample preparation for X-ray diffractions. From **Table A2.1**, all pressed $\text{Zn}_{13}\text{Sb}_{10}$ samples contained ZnSb, which suggests the decomposition of $\text{Zn}_{13}\text{Sb}_{10}$: $\text{Zn}_{13}\text{Sb}_{10} \rightarrow 10 \text{ZnSb} + 3 \text{Zn}$. The extent of decomposition appeared to decrease with decreasing sintering temperatures. The introduction of electrically insulating mica film slows down decomposition, although not completely.

Earlier works in this dissertation (Chapter 5) have suggested suppression of Zn mobility due to the incorporation of foreign elements¹⁸⁸. Incorporation of In and Mn was expected to slow down the decomposition. However, the pressed In- and Mn-doped $\text{Zn}_{13}\text{Sb}_{10}$ samples did not show improvement in stability; the ratio of $\text{Zn}_{13}\text{Sb}_{10}$:ZnSb in the doped samples remained the same as in the undoped sample sintered at the same temperature.

The unit cell volume of the $\text{Zn}_{13}\text{Sb}_{10}$ phase was used as an indicator of dopant incorporation. As shown in **Table A2.1**, the refined unit cell volume of the SPS $\text{Zn}_{12.75}\text{Mn}_{0.25}\text{Sb}_{10}$ sample ($1610.71(4) \text{ \AA}^3$) was similar to that of the pristine sample ($1610.74(5) \text{ \AA}^3$), which suggests Mn was no longer present in the $\text{Zn}_{13}\text{Sb}_{10}$ sample. Before SPS, the $\text{Zn}_{12.75}\text{Mn}_{0.25}\text{Sb}_{10}$ phase had a refined unit cell volume of $1609.32(4) \text{ \AA}^3$.

Table A2.2. X-ray diffraction analyses of SPS-ed pellets after reannealing.

Pressed samples	Zn ₁₃ Sb ₁₀ unit cell volume (Å ³)	Composition (wt. %)
Zn ₁₃ Sb ₁₀	1611.05(3)	Only Zn ₁₃ Sb ₁₀
Zn _{12.75} Mn _{0.25} Sb ₁₀	1611.00(3)	Zn ₁₃ Sb ₁₀ (88.9(8) %) ZnSb (11.1(3) %)

The SPS samples marked with (^) were sealed in evacuated silica tubes and reannealed at 350 °C for 16 h in a box furnace, and their composition and lattice parameters are given in **Table A2.2**. Interestingly, the purity of the SPS Zn₁₃b₁₀ sample was recovered after annealing, but not of the Mn-doped sample. It is not clear about the inability of the Mn-doped sample to regain its phase purity after the reannealing. The ability to regain the phase purity likely depends on the loss of Zn (and Mn) in the sample during SPS and heat treatments.

A2.3.2. Hot Pressing of Zn₁₃Sb₁₀

Hot pressing (HP) was employed to densify the pristine Zn₁₃Sb₁₀ material. Zn₁₃Sb₁₀ powder was pressed under 70 MPa and at 200, 250 and 300 °C for ~30 min. The pressed pellets again show the presence of ZnSb, which indicates the decomposition of the Zn₁₃Sb₁₀ powders. Additionally, the pellets did not stay intact, which suggests that hot pressing at such pressure is not feasible to densify the Zn₁₃Sb₁₀ material.

A2.3.3. Hot Extrusion of Zn₁₃Sb₁₀

This section covers some work of Mohsen K. Keshavarz et al.¹⁶¹. Hot extrusion (HE) was employed to densify the Zn₁₃Sb₁₀ sample at 590 K (317 °C) and under ~500 MPa.

The extruded $\text{Zn}_{13}\text{Sb}_{10}$ sample showed significant decomposition, having 58.53(3), 40.33(3) and 1.21(3) wt. % of $\text{Zn}_{13}\text{Sb}_{10}$, ZnSb and Zn , respectively. This echoes the findings in this work, where $\text{Zn}_{13}\text{Sb}_{10}$ is not stable at high pressures in elevated temperatures. The melt-and-solidification remains to be the most feasible way to make dense $\text{Zn}_{13}\text{Sb}_{10}$ -based materials. Generally, the geometric density of crack-free $\text{Zn}_{13}\text{Sb}_{10}$ -based materials in this dissertation has 99 % of the crystallographic density.

A2.4. Conclusion

The SPS, HP and HE method are not feasible ways to densify $\text{Zn}_{13}\text{Sb}_{10}$ -based materials since the $\text{Zn}_{13}\text{Sb}_{10}$ phase is not stable under pressure at elevated temperatures. Although the purity of the $\text{Zn}_{13}\text{Sb}_{10}$ sample was recovered through reannealing, the melt-and-solidification method remains to be the more feasible way to make dense $\text{Zn}_{13}\text{Sb}_{10}$ -based materials. The melt-and-solidification parameters should be improved to further reduce cracks in samples and to optimize synthesis of the crack-free $\text{Zn}_{13}\text{Sb}_{10}$ -based materials.

Bibliography

- (1) Rowe, David. M. Introduction. In *CRC Handbook of Thermoelectrics*, edited by D. M. Rowe; CRC Press: Florida, USA, 1995; pp 1–6.
- (2) Beretta, D.; Neophytou, N.; Hodges, J. M.; Kanatzidis, M. G.; Narducci, D.; Martin-Gonzalez, M.; Beekman, M.; Balke, B.; Cerretti, G.; Tremel, W.; Zevalkink, A.; Hofmann, A. I.; Müller, C.; Döring, B.; Campoy-Quiles, M.; Caironi, M. Thermoelectrics: From History, a Window to the Future. *Mater. Sci. Eng. R Rep.* **2019**, *138*, 100501. <https://doi.org/10.1016/j.mser.2018.09.001>.
- (3) Seebeck, T. J. Über Die Magnetische Polarisation Der Metalle Und Erze Durch Temperaturdifferenz. *Ann. Phys.* **1826**, *82* (3), 253–286. <https://doi.org/10.1002/andp.18260820302>.
- (4) Thermodynamics and Thermoelectricity. In *Continuum Theory and Modeling of Thermoelectric Elements*, Edited by Christophe Goupil; Wiley-PCH: Weinheim, Germany, 2016; pp 1–73.
- (5) Oersted. Notiz von Neuen Electricch - Magnetischen Versuchen Des Herrn Seebeck in Berlin. *Ann. Phys.* **1823**, *73* (4), 430–432. <https://doi.org/10.1002/andp.18230730410>.
- (6) Goldsmid, H. J. The Seebeck and Peltier Effects. In *The physics of Thermoelectric Energy Conversion*; Morgan & Claypool, IOP concise Physics: California, USA, 2017; pp 1-1-1–3.
- (7) Thomson, W. 4. On a Mechanical Theory of Thermo-Electric Currents. *Proc. R. Soc. Edinb.* **1857**, *3*, 91–98. <https://doi.org/10.1017/S0370164600027310>.
- (8) Thomson, W. Account of Researches in Thermo-Electricity. *Proc. R. Soc. Lond.* **1854**, *7*, 49–58.
- (9) Lee, H. The Thomson Effect and the Ideal Equation on Thermoelectric Coolers. *Energy* **2013**, *56*, 61–69. <https://doi.org/10.1016/j.energy.2013.04.049>.
- (10) Landau, L. D.; Lifshitz, E. M. Chapter III - Steady Current. In *Electrodynamics of Continuous Media*; Course of Theoretical Physics; Pergamon Press Ltd.: Moscow, USSR, 1984; Vol. 8, pp 86–104.
- (11) mars.nasa.gov. *Mars 2020's MMRTG*. NASA's Mars Exploration Program. <https://mars.nasa.gov/resources/24773/mars-2020s-mmrtg> (accessed 2021-01-22).

- (12) mars.nasa.gov. *Fueling of NASA's Mars 2020 Rover Power System Begins*. NASA's Mars Exploration Program. <https://mars.nasa.gov/news/8495/fueling-of-nasas-mars-2020-rover-power-system-begins> (accessed 2021-01-22).
- (13) Tsynaeva, A. A. Cathode Protection Systems of Cross-Country Pipelines. *Procedia Eng.* **2015**, *111*, 777–782. <https://doi.org/10.1016/j.proeng.2015.07.145>.
- (14) Andrei, V.; Bethke, K.; Rademann, K. Thermoelectricity in the Context of Renewable Energy Sources: Joining Forces Instead of Competing. *Energy Environ. Sci.* **2016**, *9* (5), 1528–1532. <https://doi.org/10.1039/C6EE00247A>.
- (15) Liu, L. Feasibility of Large-Scale Power Plants Based on Thermoelectric Effects. *New J. Phys.* **2014**, *16* (12), 123019. <https://doi.org/10.1088/1367-2630/16/12/123019>.
- (16) Huen, P.; Daoud, W. A. Advances in Hybrid Solar Photovoltaic and Thermoelectric Generators. *Renew. Sustain. Energy Rev.* **2017**, *72*, 1295–1302. <https://doi.org/10.1016/j.rser.2016.10.042>.
- (17) Zhu, X.; Yu, Y.; Li, F. A Review on Thermoelectric Energy Harvesting from Asphalt Pavement: Configuration, Performance and Future. *Constr. Build. Mater.* **2019**, *228*, 116818. <https://doi.org/10.1016/j.conbuildmat.2019.116818>.
- (18) Ding, L. C.; Akbarzadeh, A.; Tan, L. A Review of Power Generation with Thermoelectric System and Its Alternative with Solar Ponds. *Renew. Sustain. Energy Rev.* **2018**, *81*, 799–812. <https://doi.org/10.1016/j.rser.2017.08.010>.
- (19) Aghaali, H.; Ångström, H.-E. A Review of Turbocompounding as a Waste Heat Recovery System for Internal Combustion Engines. *Renew. Sustain. Energy Rev.* **2015**, *49*, 813–824. <https://doi.org/10.1016/j.rser.2015.04.144>.
- (20) Taylor, A. M. K. P. Science Review of Internal Combustion Engines. *Energy Policy* **2008**, *36* (12), 4657–4667. <https://doi.org/10.1016/j.enpol.2008.09.001>.
- (21) Polozine, A.; Sirovinskaya, S.; Schaeffer, L. History of Development of Thermoelectric Materials for Electric Power Generation and Criteria of Their Quality. *Mater. Res.* **2014**, *17* (5), 1260–1267. <https://doi.org/10.1590/1516-1439.272214>.
- (22) Ioffe, A. F. Thermoelectric Generators. In *Semiconductor Thermoelements and Thermoelectric Cooling*; Infosearch Limited: London, Great Britain, 1957; pp 36–73.
- (23) Kittel, C. *Introduction to Solid State Physics*, 8th ed.; John Wiley and Sons, Inc.: United States of America, 2005.
- (24) Omar, M. A. *Elementary Solid State Physics: Principles and Applications*; Addison-Wesley Publishing Company, Inc., 1993.

- (25) Hoffman, R. *Solids and Surfaces: A Chemist's View of Bonding in Extended Structures*; VCH Publishers, Inc.: New York, United States of America, 1988.
- (26) Cutler, M.; Leavy, J. F.; Fitzpatrick, R. L. Electronic Transport in Semimetallic Cerium Sulfide. *Phys. Rev.* **1964**, *133* (4A), A1143–A1152. <https://doi.org/10.1103/PhysRev.133.A1143>.
- (27) Snyder, G. J.; Toberer, E. S. Complex Thermoelectric Materials. *Nat. Mater.* **2008**, *7* (2), 105–114. <https://doi.org/10.1038/nmat2090>.
- (28) Goldsmid, H. J.; Sharp, J. W. Estimation of the Thermal Band Gap of a Semiconductor from Seebeck Measurements. *J. Electron. Mater.* **1999**, *28* (7), 869–872. <https://doi.org/10.1007/s11664-999-0211-y>.
- (29) Gibbs, Z. M.; Kim, H.-S.; Wang, H.; Snyder, G. J. Band Gap Estimation from Temperature Dependent Seebeck Measurement—Deviations from the $2e|S|_{\max}T_{\max}$ Relation. *Appl. Phys. Lett.* **2015**, *106* (2), 022112. <https://doi.org/10.1063/1.4905922>.
- (30) Kim, H.-S.; Gibbs, Z. M.; Tang, Y.; Wang, H.; Snyder, G. J. Characterization of Lorenz Number with Seebeck Coefficient Measurement. *APL Mater.* **2015**, *3* (4), 041506. <https://doi.org/10.1063/1.4908244>.
- (31) Gurunathan, R.; Hanus, R.; Dylla, M.; Katre, A.; Snyder, G. J. Analytical Models of Phonon--Point-Defect Scattering. *Phys. Rev. Appl.* **2020**, *13* (3), 034011. <https://doi.org/10.1103/PhysRevApplied.13.034011>.
- (32) Jeong, C.; Kim, R.; Lundstrom, M. S. On the Best Bandstructure for Thermoelectric Performance: A Landauer Perspective. *J. Appl. Phys.* **2012**, *111* (11), 113707. <https://doi.org/10.1063/1.4727855>.
- (33) Jeong, C.; Kim, R.; Luisier, M.; Datta, S.; Lundstrom, M. On Landauer versus Boltzmann and Full Band versus Effective Mass Evaluation of Thermoelectric Transport Coefficients. *J. Appl. Phys.* **2010**, *107* (2), 023707. <https://doi.org/10.1063/1.3291120>.
- (34) Mahan, G. D.; Sofo, J. O. The Best Thermoelectric. *Proc. Natl. Acad. Sci.* **1996**, *93* (15), 7436–7439. <https://doi.org/10.1073/pnas.93.15.7436>.
- (35) Jonson, M.; Mahan, G. D. Mott's Formula for the Thermopower and the Wiedemann-Franz Law. *Phys. Rev. B* **1980**, *21* (10), 4223–4229. <https://doi.org/10.1103/PhysRevB.21.4223>.
- (36) Cutler, M.; Mott, N. F. Observation of Anderson Localization in an Electron Gas. *Phys. Rev.* **1969**, *181* (3), 1336–1340. <https://doi.org/10.1103/PhysRev.181.1336>.

- (37) Chen, Z.; Guo, X.; Zhang, F.; Shi, Q.; Tang, M.; Ang, R. Routes for Advancing SnTe Thermoelectrics. *J. Mater. Chem. A* **2020**, *8* (33), 16790–16813. <https://doi.org/10.1039/D0TA05458E>.
- (38) Cantarero, A.; Álvarez, F. X. Thermoelectric Effects: Semiclassical and Quantum Approaches from the Boltzmann Transport Equation. In *Nanoscale Thermoelectrics*; Wang, X., Wang, Z. M., Eds.; Springer International Publishing: Cham, 2014; pp 1–39. https://doi.org/10.1007/978-3-319-02012-9_1.
- (39) Ziman, J. M. Chapter 2 - Lattice Waves. In *Principles of the Theory of Solids*; Cambridge University Press: New York, United States of America, 1972; pp 27–76.
- (40) Vočadlo, N. L.; Price, G. D. The Grüneisen Parameter — Computer Calculations via Lattice Dynamics. *Phys. Earth Planet. Inter.* **1994**, *82* (3), 261–270. [https://doi.org/10.1016/0031-9201\(94\)90076-0](https://doi.org/10.1016/0031-9201(94)90076-0).
- (41) Ziman, J. M. Chapter 7 - Transport Properties. In *Principles of the Theory of Solids*; Cambridge University Press: New York, United States of America, 1972; pp 27–76.
- (42) Slack, G. A. New Materials and Performance Limits for Thermoelectric Cooling. In *CRC Handbook of Thermoelectrics (edited by D.M. Rowe)*; CRC Press: Boca Raton, 1995; pp 407–440.
- (43) Datta, A.; Popescu, A.; Woods, L.; Nolas, G., S. The Bottom-up Approach to Bulk Thermoelectric Materials with Nanoscale Domains. In *Materials, Preparation, and Characterization in Thermoelectrics (Edited by D. M. Rowe)*; CRC Press: Boca Raton, FL, 2012.
- (44) Hicks, L. D.; Dresselhaus, M. S. Effect of Quantum-Well Structures on the Thermoelectric Figure of Merit. *Phys. Rev. B* **1993**, *47* (19), 12727–12731. <https://doi.org/10.1103/PhysRevB.47.12727>.
- (45) Ma, Y.; Heijl, R.; Palmqvist, A. E. C. Composite Thermoelectric Materials with Embedded Nanoparticles. *J. Mater. Sci.* **2013**, *48* (7), 2767–2778. <https://doi.org/10.1007/s10853-012-6976-z>.
- (46) Chattopadhyay, T.; Boucherle, J. X.; vonSchnering, H. G. Neutron Diffraction Study on the Structural Phase Transition in GeTe. *J. Phys. C Solid State Phys.* **1987**, *20* (10), 1431–1440. <https://doi.org/10.1088/0022-3719/20/10/012>.
- (47) Liu, Z.; Sun, J.; Mao, J.; Zhu, H.; Ren, W.; Zhou, J.; Wang, Z.; Singh, D. J.; Sui, J.; Chu, C.-W.; Ren, Z. Phase-Transition Temperature Suppression to Achieve Cubic GeTe and High Thermoelectric Performance by Bi and Mn Codoping. *Proc. Natl. Acad. Sci.* **2018**, *115* (21), 5332–5337. <https://doi.org/10.1073/pnas.1802020115>.

- (48) Shportko, K.; Kremers, S.; Woda, M.; Lencer, D.; Robertson, J.; Wuttig, M. Resonant Bonding in Crystalline Phase-Change Materials. *Nat. Mater.* **2008**, *7* (8), 653–658. <https://doi.org/10.1038/nmat2226>.
- (49) Akhmedova, G. A.; Abdinov, D. Sh. Effect of Thallium Doping on the Thermal Conductivity of PbTe Single Crystals. *Inorg. Mater.* **2009**, *45* (8), 854–858. <https://doi.org/10.1134/S0020168509080056>.
- (50) Zhong, Y.; Tang, J.; Liu, H.; Chen, Z.; Lin, L.; Ren, D.; Liu, B.; Ang, R. Optimized Strategies for Advancing N-Type PbTe Thermoelectrics: A Review. *ACS Appl. Mater. Interfaces* **2020**, *12* (44), 49323–49334. <https://doi.org/10.1021/acsami.0c15730>.
- (51) Delaire, O.; Ma, J.; Marty, K.; May, A. F.; McGuire, M. A.; Du, M.-H.; Singh, D. J.; Podlesnyak, A.; Ehlers, G.; Lumsden, M. D.; Sales, B. C. Giant Anharmonic Phonon Scattering in PbTe. *Nat. Mater.* **2011**, *10* (8), 614–619. <https://doi.org/10.1038/nmat3035>.
- (52) Tan, G.; Shi, F.; Hao, S.; Zhao, L.-D.; Chi, H.; Zhang, X.; Uher, C.; Wolverton, C.; Dravid, V. P.; Kanatzidis, M. G. Non-Equilibrium Processing Leads to Record High Thermoelectric Figure of Merit in PbTe–SrTe. *Nat. Commun.* **2016**, *7* (1), 12167. <https://doi.org/10.1038/ncomms12167>.
- (53) Lee, M. H.; Yun, J. H.; Kim, G.; Lee, J. E.; Park, S.-D.; Reith, H.; Schierning, G.; Nielsch, K.; Ko, W.; Li, A.-P.; Rhyee, J.-S. Synergetic Enhancement of Thermoelectric Performance by Selective Charge Anderson Localization–Delocalization Transition in n-Type Bi-Doped PbTe/Ag₂Te Nanocomposite. *ACS Nano* **2019**, *13* (4), 3806–3815. <https://doi.org/10.1021/acsnano.8b08579>.
- (54) Pandit, A.; Haleoot, R.; Hamad, B. Thermal Conductivity and Enhanced Thermoelectric Performance of SnTe Bilayer. *J. Mater. Sci.* **2021**, *56* (17), 10424–10437. <https://doi.org/10.1007/s10853-021-05926-x>.
- (55) Hwang, J.; Kim, H.; Han, M.-K.; Hong, J.; Shim, J.-H.; Tak, J.-Y.; Lim, Y. S.; Jin, Y.; Kim, J.; Park, H.; Lee, D.-K.; Bahk, J.-H.; Kim, S.-J.; Kim, W. Gigantic Phonon-Scattering Cross Section To Enhance Thermoelectric Performance in Bulk Crystals. *ACS Nano* **2019**, *13* (7), 8347–8355. <https://doi.org/10.1021/acsnano.9b03805>.
- (56) Boschker, J. E.; Wang, R.; Calarco, R. GeTe: A Simple Compound Blessed with a Plethora of Properties. *CrystEngComm* **2017**, *19* (36), 5324–5335. <https://doi.org/10.1039/C7CE01040K>.
- (57) Liu, W.-D.; Wang, D.-Z.; Liu, Q.; Zhou, W.; Shao, Z.; Chen, Z.-G. High-Performance GeTe-Based Thermoelectrics: From Materials to Devices. *Adv. Energy Mater.* **2020**, *10* (19), 2000367. <https://doi.org/10.1002/aenm.202000367>.

- (58) Hong, M.; Wang, Y.; Liu, W.; Matsumura, S.; Wang, H.; Zou, J.; Chen, Z.-G. Arrays of Planar Vacancies in Superior Thermoelectric $\text{Ge}_{1-x-y}\text{Cd}_x\text{Bi}_y\text{Te}$ with Band Convergence. *Adv. Energy Mater.* **2018**, *8* (30), 1801837. <https://doi.org/10.1002/aenm.201801837>.
- (59) Samanta, M.; Ghosh, T.; Arora, R.; Waghmare, U. V.; Biswas, K. Realization of Both N- and p-Type GeTe Thermoelectrics: Electronic Structure Modulation by AgBiSe_2 Alloying. *J. Am. Chem. Soc.* **2019**, *141* (49), 19505–19512. <https://doi.org/10.1021/jacs.9b11405>.
- (60) Witting, I. T.; Chasapis, T. C.; Ricci, F.; Peters, M.; Heinz, N. A.; Hautier, G.; Snyder, G. J. The Thermoelectric Properties of Bismuth Telluride. *Adv. Electron. Mater.* **2019**, *5* (6), 1800904. <https://doi.org/10.1002/aelm.201800904>.
- (61) Kim, S. I.; Lee, K. H.; Mun, H. A.; Kim, H. S.; Hwang, S. W.; Roh, J. W.; Yang, D. J.; Shin, W. H.; Li, X. S.; Lee, Y. H.; Snyder, G. J.; Kim, S. W. Dense Dislocation Arrays Embedded in Grain Boundaries for High-Performance Bulk Thermoelectrics. *Science* **2015**, *348* (6230), 109–114. <https://doi.org/10.1126/science.aaa4166>.
- (62) Shin, W. H.; Roh, J. W.; Ryu, B.; Chang, H. J.; Kim, H. S.; Lee, S.; Seo, W. S.; Ahn, K. Enhancing Thermoelectric Performances of Bismuth Antimony Telluride via Synergistic Combination of Multiscale Structuring and Band Alignment by FeTe_2 Incorporation. *ACS Appl. Mater. Interfaces* **2018**, *10* (4), 3689–3698. <https://doi.org/10.1021/acsami.7b18451>.
- (63) Deng, R.; Su, X.; Zheng, Z.; Liu, W.; Yan, Y.; Zhang, Q.; Dravid, V. P.; Uher, C.; Kanatzidis, M. G.; Tang, X. Thermal Conductivity in $\text{Bi}_{0.5}\text{Sb}_{1.5}\text{Te}_{3+x}$ and the Role of Dense Dislocation Arrays at Grain Boundaries. *Sci. Adv.* **2018**, *4* (6), eaar5606. <https://doi.org/10.1126/sciadv.aar5606>.
- (64) Zhao, L.-D.; Chang, C.; Tan, G.; Kanatzidis, M. G. SnSe: A Remarkable New Thermoelectric Material. *Energy Environ. Sci.* **2016**, *9* (10), 3044–3060. <https://doi.org/10.1039/C6EE01755J>.
- (65) Zhao, L.-D.; Tan, G.; Hao, S.; He, J.; Pei, Y.; Chi, H.; Wang, H.; Gong, S.; Xu, H.; Dravid, V. P.; Uher, C.; Snyder, G. J.; Wolverton, C.; Kanatzidis, M. G. Ultrahigh Power Factor and Thermoelectric Performance in Hole-Doped Single-Crystal SnSe. *Science* **2016**, *351* (6269), 141–144. <https://doi.org/10.1126/science.aad3749>.
- (66) Zhao, L.-D.; Lo, S.-H.; Zhang, Y.; Sun, H.; Tan, G.; Uher, C.; Wolverton, C.; Dravid, V. P.; Kanatzidis, M. G. Ultralow Thermal Conductivity and High Thermoelectric Figure of Merit in SnSe Crystals. *Nature* **2014**, *508* (7496), 373–377. <https://doi.org/10.1038/nature13184>.

- (67) Eikeland, E.; Blichfeld, A. B.; Borup, K. A.; Zhao, K.; Overgaard, J.; Shi, X.; Chen, L.; Iversen, B. B. Crystal Structure across the β to α Phase Transition in Thermoelectric Cu_{2-x}Se . *IUCrJ* **2017**, *4* (4), 476–485. <https://doi.org/10.1107/S2052252517005553>.
- (68) Gulay, L.; Daszkiewicz, M.; Strok, O.; Pietraszko, A. Crystal Structure of Cu_2Se . *Chem. Met. Alloys* **2011**, *4* (3/4), 200–205. <https://doi.org/10.30970/cma4.0184>.
- (69) Danilkin, S. A.; Avdeev, M.; Sale, M.; Sakuma, T. Neutron Scattering Study of Ionic Diffusion in Cu–Se Superionic Compounds. *Solid State Ion.* **2012**, *225*, 190–193. <https://doi.org/10.1016/j.ssi.2012.02.046>.
- (70) Olvera, A. A.; Moroz, N. A.; Sahoo, P.; Ren, P.; Bailey, T. P.; Page, A. A.; Uher, C.; Poudeu, P. F. P. Partial Indium Solubility Induces Chemical Stability and Colossal Thermoelectric Figure of Merit in Cu_2Se . *Energy Environ. Sci.* **2017**, *10* (7), 1668–1676. <https://doi.org/10.1039/C7EE01193H>.
- (71) Caillat, T.; Borshchevsky, A.; Fleurial, J. Preparation and Thermoelectric Properties of P- and N-type CoSb_3 . *AIP Conf. Proc.* **1994**, *316* (1), 58–61. <https://doi.org/10.1063/1.46835>.
- (72) Luo, H.; Krizan, J. W.; Muechler, L.; Haldolaarachchige, N.; Klimczuk, T.; Xie, W.; Fucillo, M. K.; Felser, C.; Cava, R. J. A Large Family of Filled Skutterudites Stabilized by Electron Count. *Nat. Commun.* **2015**, *6* (1), 6489. <https://doi.org/10.1038/ncomms7489>.
- (73) Rull-Bravo, M.; Moure, A.; Fernández, J. F.; Martín-González, M. Skutterudites as Thermoelectric Materials: Revisited. *RSC Adv.* **2015**, *5* (52), 41653–41667. <https://doi.org/10.1039/C5RA03942H>.
- (74) He, Z.; Stiewe, C.; Platzek, D.; Karpinski, G.; Müller, E.; Li, S.; Toprak, M.; Muhammed, M. Thermoelectric Properties of Hot-Pressed Skutterudite CoSb_3 . *J. Appl. Phys.* **2007**, *101* (5), 053713. <https://doi.org/10.1063/1.2538036>.
- (75) Toprak, M. S.; Stiewe, C.; Platzek, D.; Williams, S.; Bertini, L.; Müller, E.; Gatti, C.; Zhang, Y.; Rowe, M.; Muhammed, M. The Impact of Nanostructuring on the Thermal Conductivity of Thermoelectric CoSb_3 . *Adv. Funct. Mater.* **2004**, *14* (12), 1189–1196. <https://doi.org/10.1002/adfm.200400109>.
- (76) Su, X.; Li, H.; Wang, G.; Chi, H.; Zhou, X.; Tang, X.; Zhang, Q.; Uher, C. Structure and Transport Properties of Double-Doped $\text{CoSb}_{2.75}\text{Ge}_{0.25-x}\text{Te}_x$ ($x = 0.125\text{--}0.20$) with in Situ Nanostructure. *Chem. Mater.* **2011**, *23* (11), 2948–2955. <https://doi.org/10.1021/cm200560s>.

- (77) Slack, G. A.; Tsoukala, V. G. Some Properties of Semiconducting IrSb₃. *J. Appl. Phys.* **1994**, *76* (3), 1665–1671. <https://doi.org/10.1063/1.357750>.
- (78) Shi, X.; Yang, J.; Salvador, J. R.; Chi, M.; Cho, J. Y.; Wang, H.; Bai, S.; Yang, J.; Zhang, W.; Chen, L. Multiple-Filled Skutterudites: High Thermoelectric Figure of Merit through Separately Optimizing Electrical and Thermal Transports. *J. Am. Chem. Soc.* **2011**, *133* (20), 7837–7846. <https://doi.org/10.1021/ja111199y>.
- (79) Shevelkov, A. V. Thermoelectric Power Generation by Clathrates. *Thermoelectr. Power Gener. - Look Trends Technol.* **2016**. <https://doi.org/10.5772/65600>.
- (80) Christensen, M.; Johnsen, S.; Iversen, B. B. Thermoelectric Clathrates of Type I. *Dalton Trans.* **2010**, *39* (4), 978–992. <https://doi.org/10.1039/B916400F>.
- (81) Kishimoto, K.; Koda, S.; Akai, K.; Koyanagi, T. Thermoelectric Properties of Sintered Type-II Clathrates (K, Ba)₂₄(Ga, Sn)₁₃₆ with Various Carrier Concentrations. *J. Appl. Phys.* **2015**, *118* (12), 125103. <https://doi.org/10.1063/1.4931433>.
- (82) Saramat, A.; Svensson, G.; Palmqvist, A. E. C.; Stiewe, C.; Mueller, E.; Platzek, D.; Williams, S. G. K.; Rowe, D. M.; Bryan, J. D.; Stucky, G. D. Large Thermoelectric Figure of Merit at High Temperature in Czochralski-Grown Clathrate Ba₈Ga₁₆Ge₃₀. *J. Appl. Phys.* **2006**, *99* (2), 023708. <https://doi.org/10.1063/1.2163979>.
- (83) Wang, L.-H.; Chang, L.-S. Thermoelectric Properties of P-Type Ba₈Ga₁₆Ge₃₀ Type-I Clathrate Compounds Prepared by the Vertical Bridgman Method. *J. Alloys Compd.* **2017**, *722*, 644–650. <https://doi.org/10.1016/j.jallcom.2017.06.110>.
- (84) Dolyniuk, J.-A.; Owens-Baird, B.; Wang, J.; Zaikina, J. V.; Kovnir, K. Clathrate Thermoelectrics. *Mater. Sci. Eng. R Rep.* **2016**, *108*, 1–46. <https://doi.org/10.1016/j.mser.2016.08.001>.
- (85) Ramachandran, G. K.; Dong, J.; Diefenbacher, J.; Gryko, J.; Marzke, R. F.; Sankey, O. F.; McMillan, P. F. Synthesis and X-Ray Characterization of Silicon Clathrates. *J. Solid State Chem.* **1999**, *145* (2), 716–730. <https://doi.org/10.1006/jssc.1999.8295>.
- (86) Kauzlarich, S. M.; Brown, S. R.; Snyder, G. J. Zintl Phases for Thermoelectric Devices. *Dalton Trans.* **2007**, No. 21, 2099–2107. <https://doi.org/10.1039/B702266B>.
- (87) He, A.; Wille, E. L. K.; Moreau, L. M.; Thomas, S. M.; Lawrence, J. M.; Bauer, E. D.; Booth, C. H.; Kauzlarich, S. M. Intermediate Yb Valence in the Zintl Phases Yb₁₄MSb₁₁(M=Zn, Mn, Mg): XANES, Magnetism, and Heat Capacity. *Phys. Rev. Mater.* **2020**, *4* (11), 114407. <https://doi.org/10.1103/PhysRevMaterials.4.114407>.

- (88) Brown, S. R.; Kauzlarich, S. M.; Gascoin, F.; Snyder, G. J. Yb₁₄MnSb₁₁: New High Efficiency Thermoelectric Material for Power Generation. *Chem. Mater.* **2006**, *18* (7), 1873–1877. <https://doi.org/10.1021/cm060261t>.
- (89) Toberer, E. S.; Cox, C. A.; Brown, S. R.; Ikeda, T.; May, A. F.; Kauzlarich, S. M.; Snyder, G. J. Traversing the Metal-Insulator Transition in a Zintl Phase: Rational Enhancement of Thermoelectric Efficiency in Yb₁₄Mn_{1-x}Al_xSb₁₁. *Adv. Funct. Mater.* **2008**, *18* (18), 2795–2800. <https://doi.org/10.1002/adfm.200800298>.
- (90) Caillat, T.; Fleurial, J.-P.; Borshchevsky, A. Preparation and Thermoelectric Properties of Semiconducting Zn₄Sb₃. *J. Phys. Chem. Solids* **1997**, *58* (7), 1119–1125. [https://doi.org/10.1016/S0022-3697\(96\)00228-4](https://doi.org/10.1016/S0022-3697(96)00228-4).
- (91) Mayer, H. W.; Mikhail, I.; Schubert, K. Über Einige Phasen Der Mischungen ZnSb_N Und CdSb_N. *J. Common Met.* **1978**, *59* (1), 43–52. [https://doi.org/10.1016/0022-5088\(78\)90109-1](https://doi.org/10.1016/0022-5088(78)90109-1).
- (92) Nylén, J.; Andersson, M.; Lidin, S.; Häussermann, U. The Structure of α -Zn₄Sb₃: Ordering of the Phonon-Glass Thermoelectric Material β -Zn₄Sb₃. *J. Am. Chem. Soc.* **2004**, *126* (50), 16306–16307. <https://doi.org/10.1021/ja044980p>.
- (93) Nylén, J.; Lidin, S.; Andersson, M.; Iversen, B. B.; Newman, N.; Häussermann, U. Low-Temperature Structural Transitions in the Phonon-Glass Thermoelectric Material β -Zn₄Sb₃: Ordering of Zn Interstitials and Defects. *Chem. Mater.* **2007**, *19* (4), 834–838. <https://doi.org/10.1021/cm062384j>.
- (94) Mozharivskyj, Y.; Janssen, Y.; Haringa, J. L.; Kracher, A.; Tsokol, A. O.; Miller, G. J. Zn₁₃Sb₁₀: A Structural and Landau Theoretical Analysis of Its Phase Transitions. *Chem. Mater.* **2006**, *18* (3), 822–831. <https://doi.org/10.1021/cm0515505>.
- (95) Mozharivskyj, Y.; Pecharsky, A. O.; Bud'ko, S.; Miller, G. J. A Promising Thermoelectric Material: Zn₄Sb₃ or Zn_{6- δ} Sb₅. Its Composition, Structure, Stability, and Polymorphs. Structure and Stability of Zn_{1- δ} Sb. *Chem. Mater.* **2004**, *16* (8), 1580–1589. <https://doi.org/10.1021/cm035274a>.
- (96) Snyder, G. J.; Christensen, M.; Nishibori, E.; Caillat, T.; Iversen, B. B. Disordered Zinc in Zn₄Sb₃ with Phonon-Glass and Electron-Crystal Thermoelectric Properties. *Nat. Mater.* **2004**, *3* (7), 458–463. <https://doi.org/10.1038/nmat1154>.
- (97) Yoshioka, S.; Hayashi, K.; Yokoyama, A.; Saito, W.; Li, H.; Takamatsu, T.; Miyazaki, Y. Crystal Structure, Electronic Structure and Thermoelectric Properties of β - and γ -Zn₄Sb₃ Thermoelectrics: A (3 + 1)-Dimensional Superspace Group Approach. *J. Mater. Chem. C* **2020**, *8* (27), 9205–9212. <https://doi.org/10.1039/D0TC01497D>.

- (98) Wang, J.; Kovnir, K. Elusive β -Zn₈Sb₇: A New Zinc Antimonide Thermoelectric. *J. Am. Chem. Soc.* **2015**, *137* (39), 12474–12477. <https://doi.org/10.1021/jacs.5b08214>.
- (99) He, A.; Svitlyk, V.; Chernyshov, D.; Mozharivskyj, Y. Identification, Structural Characterization and Transformations of the High-Temperature Zn₉₋₈Sb₇ Phase in the Zn–Sb System. *Dalton Trans.* **2015**, *44* (48), 20983–20990. <https://doi.org/10.1039/C5DT03509K>.
- (100) Pecharsky, V. K.; Zavalij, P. Y. Fundamentals of Diffraction. In *Fundamentals of powder diffraction and structural characterization of materials*; Springer Science+Business Media, Inc.: United States of America, 2005; pp 99–260.
- (101) Fathi, M. B. History of the Reciprocal Lattice. *Powder Diffr.* **2019**, *34* (3), 260–266. <https://doi.org/10.1017/S0885715619000496>.
- (102) Bennett, D. W. Crystal Diffraction: Data. In *Understanding Single-Crystal X-Ray Crystallography*; Wiley-PCH Verlag GmbH & Co.: Weinheim, Germany, 2010; pp 339–496.
- (103) Darmstadt: Germany. X-Area, STOE & Cie GmbH, 2004.
- (104) Darmstadt: Germany. X-SHAPE, STOE & Cie GmbH, 2004.
- (105) Madison, WI 53711, USA. XPREP, Bruker AXS, 2008.
- (106) Sheldrick, G. M. A Short History of SHELX. *Acta Crystallogr. A* **2008**, *64* (1), 112–122. <https://doi.org/10.1107/S0108767307043930>.
- (107) Sheldrick, G. M. SHELXS-97 and SHELXL-97, 1997.
- (108) Sheldrick, G. M. SHELXT – Integrated Space-Group and Crystal-Structure Determination. *Acta Crystallogr. Sect. Found. Adv.* **2015**, *71* (1), 3–8. <https://doi.org/10.1107/S2053273314026370>.
- (109) Dolomanov, O. V.; Bourhis, L. J.; Gildea, R. J.; Howard, J. a. K.; Puschmann, H. OLEX2: A Complete Structure Solution, Refinement and Analysis Program. *J. Appl. Crystallogr.* **2009**, *42* (2), 339–341. <https://doi.org/10.1107/S0021889808042726>.
- (110) Prescher, C.; Prakapenka, V. B. DIOPTAS: A Program for Reduction of Two-Dimensional X-Ray Diffraction Data and Data Exploration. *High Press. Res.* **2015**, *35*, 223–230.
- (111) Hunter, B. Rietica - A Visual Rietveld Program, 1998.
- (112) ZEM-3 series / Seebeck Coefficient / Electric Resistance Measurement System / Thermoelectric Evaluation System / Heat Treatment And Thermal Properties /

Products / *ULVAC SHOWCASE*. *ULVAC SHOWCASE*.
<https://showcase.ulvac.co.jp/en/products/heat-treatment-and-thermal-properties/thermoelectric-evaluation-device/thermoelectric-properties/zem-3series.html> (accessed 2021-06-16).

- (113) Cargnoni, F.; Nishibori, E.; Rabiller, P.; Bertini, L.; Snyder, G. J.; Christensen, M.; Gatti, C.; Iversen, B. B. Interstitial Zn Atoms Do the Trick in Thermoelectric Zinc Antimonide, Zn_4Sb_3 : A Combined Maximum Entropy Method X-Ray Electron Density and Ab Initio Electronic Structure Study. *Chem. – Eur. J.* **2004**, *10* (16), 3861–3870. <https://doi.org/10.1002/chem.200400327>.
- (114) Nylén, J.; Lidin, S.; Andersson, M.; Liu, H.; Newman, N.; Häussermann, U. Effect of Metal Doping on the Low-Temperature Structural Behavior of Thermoelectric β - Zn_4Sb_3 . *J. Solid State Chem.* **2007**, *180* (9), 2603–2615. <https://doi.org/10.1016/j.jssc.2007.07.013>.
- (115) Nakamoto, G.; Akai, N.; Kurisu, M.; Kim, I.-H.; Ur, S.-C.; Kuznetsov, V. L. Homogeneity Range of ϵ -Phase Zn_4Sb_3 . *J. Alloys Compd.* **2007**, *432* (1), 116–121. <https://doi.org/10.1016/j.jallcom.2006.05.118>.
- (116) Toberer, E. S.; Rauwel, P.; Gariel, S.; Taftø, J.; Snyder, G. J. Composition and the Thermoelectric Performance of β - Zn_4Sb_3 . *J. Mater. Chem.* **2010**, *20* (44), 9877–9885. <https://doi.org/10.1039/C0JM02011G>.
- (117) Prytz, Ø.; Gunnæs, A. E.; Karlsen, O. B.; Breivik, T. H.; Toberer, E. S.; Snyder, G. J.; Taftø, J. Nanoscale Inclusions in the Phonon Glass Thermoelectric Material Zn_4Sb_3 . *Philos. Mag. Lett.* **2009**, *89* (6), 362–369. <https://doi.org/10.1080/09500830902950464>.
- (118) Castellero, A.; Fanciulli, C.; Carlini, R.; Fiore, G.; Mele, P.; Passaretti, F.; Baricco, M. Effect of Processing Routes on the Synthesis and Properties of Zn_4Sb_3 Thermoelectric Alloy. *J. Alloys Compd.* **2015**, *653*, 54–60. <https://doi.org/10.1016/j.jallcom.2015.08.251>.
- (119) Pan, L.; Qin, X. Y.; Xin, H. X.; Li, D.; Sun, J. H.; Zhang, J.; Song, C. J.; Sun, R. R. Enhanced Thermoelectric Properties of Iron Doped Compound $(Zn_{1-x}Fe_x)_4Sb_3$. *Intermetallics* **2010**, *18* (5), 1106–1110. <https://doi.org/10.1016/j.intermet.2010.01.008>.
- (120) Carlini, R.; Marré, D.; Pallecchi, I.; Ricciardi, R.; Zanicchi, G. Thermoelectric Properties of Zn_4Sb_3 Intermetallic Compound Doped with Aluminum and Silver. *Intermetallics* **2014**, *45*, 60–64. <https://doi.org/10.1016/j.intermet.2013.10.002>.

- (121) Li, D.; Qin, X. Y. Effects of Te Doping on the Transport and Thermoelectric Properties of Zn_4Sb_3 . *Intermetallics* **2011**, *19* (11), 1651–1655. <https://doi.org/10.1016/j.intermet.2011.07.002>.
- (122) Ren, B.; Liu, M.; Li, X.; Qin, X.; Li, D.; Zou, T.; Sun, G.; Li, Y.; Xin, H.; Zhang, J. Enhancement of Thermoelectric Performance of $\beta\text{-Zn}_4\text{Sb}_3$ through Resonant Distortion of Electronic Density of States Doped with Gd. *J. Mater. Chem. A* **2015**, *3* (22), 11768–11772. <https://doi.org/10.1039/C5TA01778E>.
- (123) Souma, T.; Nakamoto, G.; Kurisu, M. Low-Temperature Thermoelectric Properties of α - and $\beta\text{-Zn}_4\text{Sb}_3$ Bulk Crystals Prepared by a Gradient Freeze Method and a Spark Plasma Sintering Method. *J. Alloys Compd.* **2002**, *340* (1), 275–280. [https://doi.org/10.1016/S0925-8388\(02\)00113-5](https://doi.org/10.1016/S0925-8388(02)00113-5).
- (124) Souma, T.; Nakamoto, G.; Kurisu, M. Hall Effect of α - and $\beta\text{-Zn}_4\text{Sb}_3$ Compounds Prepared by the Gradient Freeze and Spark-Plasma Sintering Methods. In *Proceedings ICT'03. 22nd International Conference on Thermoelectrics (IEEE Cat. No.03TH8726)*; 2003; pp 279–281. <https://doi.org/10.1109/ICT.2003.1287503>.
- (125) Izard, V.; Record, M. C.; Tedenac, J. C.; Fries, S. G. Discussion on the Stability of the Antimony-Zinc Binary Phases. *Calphad* **2001**, *25* (4), 567–581. [https://doi.org/10.1016/S0364-5916\(02\)00008-1](https://doi.org/10.1016/S0364-5916(02)00008-1).
- (126) Zhang, T.; Zhou, K.; Li, X. F.; Chen, Z. Q.; Su, X. L.; Tang, X. F. Reversible Structural Transition in Spark Plasma-Sintered Thermoelectric Zn_4Sb_3 . *J. Mater. Sci.* **2016**, *51* (4), 2041–2048. <https://doi.org/10.1007/s10853-015-9514-y>.
- (127) Yin, H. (殷浩); Christensen, M.; Lock, N.; Iversen, B. B. Zn Migration during Spark Plasma Sintering of Thermoelectric Zn_4Sb_3 . *Appl. Phys. Lett.* **2012**, *101* (4), 043901. <https://doi.org/10.1063/1.4731764>.
- (128) Shai, X.; Deng, S.; Shen, L.; Meng, D.; Li, D.; Zhang, Y.; Jiang, X. Preparation, Thermal Stability, and Electrical Transport Properties of In/Sn Codoped $\beta\text{-Zn}_4\text{Sb}_3$ Single Crystal. *Phys. Status Solidi B* **2015**, *252* (4), 795–799. <https://doi.org/10.1002/pssb.201451366>.
- (129) Liu, H.; Deng, S.; Li, D.; Shen, L.; Cheng, F.; Wang, J.; Deng, S. Preparation and Oxidation Resistance of Single Crystalline $\beta\text{-Zn}_4\text{Sb}_3$. *Phys. B Condens. Matter* **2016**, *500*, 9–13. <https://doi.org/10.1016/j.physb.2016.07.028>.
- (130) Lin, J.; Li, X.; Qiao, G.; Wang, Z.; Carrete, J.; Ren, Y.; Ma, L.; Fei, Y.; Yang, B.; Lei, L.; Li, J. Unexpected High-Temperature Stability of $\beta\text{-Zn}_4\text{Sb}_3$ Opens the Door to Enhanced Thermoelectric Performance. *J. Am. Chem. Soc.* **2014**, *136* (4), 1497–1504. <https://doi.org/10.1021/ja410605f>.

- (131) Pomrehn, G. S. Entropic Stabilization and Retrograde Solubility in Zn_4Sb_3 . *Phys. Rev. B* **2011**, *83* (9). <https://doi.org/10.1103/PhysRevB.83.094106>.
- (132) Fischer, A.; Scheidt, E.-W.; Scherer, W.; Benson, D.; Wu, Y.; Eklöf, D.; Häussermann, U. Thermal and Vibrational Properties of Thermoelectric $ZnSb$ - Exploring the Origin of Low Thermal Conductivity. *ArXiv150205901 Cond-Mat* **2015**.
- (133) Lo, C.-W. T.; Ortiz, B. R.; Toberer, E. S.; He, A.; Svitlyk, V.; Chernyshov, D.; Kolodiazny, T.; Lidin, S.; Mozharivskiy, Y. Synthesis, Structure, and Thermoelectric Properties of α - Zn_3Sb_2 and Comparison to β - $Zn_{13}Sb_{10}$. *Chem. Mater.* **2017**, *29* (12), 5249–5258. <https://doi.org/10.1021/acs.chemmater.7b01214>.
- (134) Yin, H.; Blichfeld, A. B.; Christensen, M.; Iversen, B. B. Fast Direct Synthesis and Compaction of Homogenous Phase-Pure Thermoelectric Zn_4Sb_3 . *ACS Appl. Mater. Interfaces* **2014**, *6* (13), 10542–10548. <https://doi.org/10.1021/am502089a>.
- (135) Yin, H.; Christensen, M.; Pedersen, B. L.; Nishibori, E.; Aoyagi, S.; Iversen, B. B. Thermal Stability of Thermoelectric Zn_4Sb_3 . *J. Electron. Mater.* **2010**, *39* (9), 1957–1959. <https://doi.org/10.1007/s11664-009-1053-3>.
- (136) Caillat, T.; Borshchevsky, A.; Fleurial, J.-P. Thermal Conductivity of $Zn_{4-x}Cd_xSb_3$ Solid Solutions. *MRS Online Proc. Libr. Arch.* **1997**, *478*. <https://doi.org/10.1557/PROC-478-103>.
- (137) Wang, S.; Fu, F.; She, X.; Zheng, G.; Li, H.; Tang, X. Optimizing Thermoelectric Performance of Cd-Doped β - Zn_4Sb_3 through Self-Adjusting Carrier Concentration. *Intermetallics* **2011**, *19* (12), 1823–1830. <https://doi.org/10.1016/j.intermet.2011.07.020>.
- (138) Nakamoto, G.; Tajima, Y.; Kurisu, M. Preparation of the Crack-Free Single Phase $(Zn_{1-x}Cd_x)_{13}Sb_{10}$ by a Gradient Freeze Method and Their Structural and Thermoelectric Properties. *Intermetallics* **2012**, *23*, 163–168. <https://doi.org/10.1016/j.intermet.2011.11.021>.
- (139) Qin, X. Y.; Liu, M.; Pan, L.; Xin, H. X.; Sun, J. H.; Wang, Q. Q. Effects of Bi Doping on the Thermoelectric Properties of β - Zn_4Sb_3 . *J. Appl. Phys.* **2011**, *109* (3), 033714. <https://doi.org/10.1063/1.3544479>.
- (140) Tang, D.; Zhao, W.; Cheng, S.; Wei, P.; Yu, J.; Zhang, Q. Crystal Structure and Bonding Characteristics of In-Doped β - Zn_4Sb_3 . *J. Solid State Chem.* **2012**, *193*, 89–93. <https://doi.org/10.1016/j.jssc.2012.03.059>.
- (141) Wei, P.-C.; Yang, C.-C.; Chen, J.-L.; Sankar, R.; Chen, C.-L.; Hsu, C.-H.; Chang, C.-C.; Chen, C.-L.; Dong, C.-L.; Chou, F.-C.; Chen, K.-H.; Wu, M.-K.; Chen, Y.-Y.

- Enhancement of Thermoelectric Figure of Merit in β -Zn₄Sb₃ by Indium Doping Control. *Appl. Phys. Lett.* **2015**, *107* (12), 123902. <https://doi.org/10.1063/1.4931361>.
- (142) Liu, F.; Qin, X. Y.; Xin, H. X. Thermoelectric Properties of (Zn_{0.98}M_{0.02})₄Sb₃ (M = Al, Ga and In) at Low Temperatures. *J. Phys. Appl. Phys.* **2007**, *40* (24), 7811. <https://doi.org/10.1088/0022-3727/40/24/033>.
- (143) Lo, C.-W. T.; Svitlyk, V.; Chernyshov, D.; Mozharivskyj, Y. The Updated Zn–Sb Phase Diagram. How to Make Pure Zn₁₃Sb₁₀ (“ β -Zn₄Sb₃”). *Dalton Trans.* **2018**, *47* (33), 11512–11520. <https://doi.org/10.1039/C8DT02521E>.
- (144) Zobač, O.; Sopoušek, J.; Kroupa, A. Calphad-Type Assessment of the Sb–Sn–Zn Ternary System. *Calphad* **2015**, *51*, 51–56. <https://doi.org/10.1016/j.calphad.2015.08.002>.
- (145) Liu, H.; Deng, S.; Li, D.; Shen, L.; Cheng, F.; Wang, J.; Deng, S. Preparation and Oxidation Resistance of Single Crystalline β -Zn₄Sb₃. *Phys. B Condens. Matter* **2016**, *500*, 9–13. <https://doi.org/10.1016/j.physb.2016.07.028>.
- (146) Darmstadt: Germany. *X-SHAPE, STOE & Cie GmbH*; 2004.
- (147) Sheldrick, G. M. *SHELXL-97*; Program for crystal-structure refinement. University of Gottingen, Germany., 1997.
- (148) Wu, Y.; Lidin, S.; Groy, T. L.; Newman, N.; Häussermann, U. Zn₅Sb₄In_{2- δ} — a Ternary Derivative of Thermoelectric Zinc Antimonides. *Inorg. Chem.* **2009**, *48* (13), 5996–6003. <https://doi.org/10.1021/ic900302a>.
- (149) Pauling, L. Atomic Radii and Interatomic Distances in Metals. *J. Am. Chem. Soc.* **1947**, *69* (3), 542–553. <https://doi.org/10.1021/ja01195a024>.
- (150) Omar, M. A. *Elementary Solid State Physics: Principles and Applications*; Addison-Wesley Publishing Company, Inc., 1993.
- (151) Bhattacharya, S.; Hermann, R. P.; Keppens, V.; Tritt, T. M.; Snyder, G. J. Effect of Disorder on the Thermal Transport and Elastic Properties in Thermoelectric Zn₄Sb₃. *Phys. Rev. B* **2006**, *74* (13), 134108. <https://doi.org/10.1103/PhysRevB.74.134108>.
- (152) Snyder, G. J.; Toberer, E. S. Complex Thermoelectric Materials. *Nat. Mater.* **2008**, *7* (2), 105–114. <https://doi.org/10.1038/nmat2090>.
- (153) Kim, H.-S.; Gibbs, Z. M.; Tang, Y.; Wang, H.; Snyder, G. J. Characterization of Lorenz Number with Seebeck Coefficient Measurement. *APL Mater.* **2015**, *3* (4), 041506. <https://doi.org/10.1063/1.4908244>.

- (154) Pomrehn, G. S. Entropic Stabilization and Retrograde Solubility in Zn_4Sb_3 . *Phys. Rev. B* **2011**, 83 (9). <https://doi.org/10.1103/PhysRevB.83.094106>.
- (155) Zhou, L.; Li, W.; Jiang, J.; Zhang, T.; Li, Y.; Xu, G.; Cui, P. Effect of Bi Doping on the Thermoelectric Properties of Zn_4Sb_3 . *J. Alloys Compd.* **2010**, 503 (2), 464–467. <https://doi.org/10.1016/j.jallcom.2010.05.034>.
- (156) Shai, X.; Deng, S.; Shen, L.; Meng, D.; Li, D.; Zhang, Y.; Jiang, X. Preparation, Thermal Stability, and Electrical Transport Properties of In/Sn Codoped $\beta\text{-Zn}_4\text{Sb}_3$ Single Crystal. *Phys. Status Solidi B* **2015**, 252 (4), 795–799. <https://doi.org/10.1002/pssb.201451366>.
- (157) Deng, S.; Tang, Y.; Li, D.; Liu, H.; Chen, Z.; Shen, L.; Deng, S. Thermal Stability and Electrical Transport Properties of Single-Crystalline $\beta\text{-Zn}_4\text{Sb}_3$ Co-Doped by Ga/Sn. *J. Electron. Mater.* **2017**, 46 (12), 6804–6810. <https://doi.org/10.1007/s11664-017-5747-7>.
- (158) Deng, S.; Li, D.; Zheng, L.; Tang, Y.; Chen, Z.; Sun, L.; Liu, W.; Shen, L.; Deng, S. Crystal Growth, Thermal Stability and Electrical Transport Property of Double-Doping (Sn/Cd) System in Single-Crystal $\beta\text{-Zn}_4\text{Sb}_3$. *Phys. Status Solidi A* **2018**, 215 (11), 1700905. <https://doi.org/10.1002/pssa.201700905>.
- (159) Lo, C.-W. T.; Kolodiaznyy, T.; Mozharivskyj, Y. Incorporation of Indium into the $\text{Zn}_{13}\text{Sb}_{10}$ Thermoelectric Material. *J. Alloys Compd.* **2019**, 780, 334–340. <https://doi.org/10.1016/j.jallcom.2018.11.339>.
- (160) Dolomanov, O. V.; Bourhis, L. J.; Gildea, R. J.; Howard, J. a. K.; Puschmann, H. OLEX2: A Complete Structure Solution, Refinement and Analysis Program. *J. Appl. Crystallogr.* **2009**, 42 (2), 339–341. <https://doi.org/10.1107/S0021889808042726>.
- (161) Keshavarz, M. K.; Lo, C.-W. T.; Turenne, S.; Mozharivskyj, Y.; Quitarano, N. J. Hot Extrusion of ZnSb-Based Thermoelectric Materials; A Novel Approach for Scale-Up Production. *J. Manuf. Mater. Process.* **2019**, 3 (3), 58. <https://doi.org/10.3390/jmmp3030058>.
- (162) Andersen, O. K.; Pawlowska, Z.; Jepsen, O. Illustration of the Linear-Muffin-Tin-Orbital Tight-Binding Representation: Compact Orbitals and Charge Density in Si. *Phys. Rev. B* **1986**, 34 (8), 5253–5269. <https://doi.org/10.1103/PhysRevB.34.5253>.
- (163) Pauling, L.; Kamb, B. A Revised Set of Values of Single-Bond Radii Derived from the Observed Interatomic Distances in Metals by Correction for Bond Number and Resonance Energy. *Proc. Natl. Acad. Sci.* **1986**, 83 (11), 3569–3571. <https://doi.org/10.1073/pnas.83.11.3569>.

- (164) Zelinska, O. Ya.; Bie, H.; Mar, A. Structure of $\text{Cd}_{12.7(1)}\text{Sb}_{10}$. *Chem. Mater.* **2007**, *19* (6), 1518–1522. <https://doi.org/10.1021/cm0629659>.
- (165) Shriver, D.; Weller, M.; Overton, T.; Rourke, J.; Armstrong, F. D-Metal Complexes: Electronic Structure and Properties. In *Inorganic Chemistry*; Oxford University Press, 2014; pp 515–549.
- (166) Qiu, A. N.; Zhang, L. T.; Wu, J. S. Crystal Structure, Electronic Structure, and Thermoelectric Properties of $\beta\text{-Zn}_4\text{Sb}_3$. *Phys. Rev. B* **2010**, *81* (3), 035203. <https://doi.org/10.1103/PhysRevB.81.035203>.
- (167) Tapiero, M.; Tarabichi, S.; Gies, J. G.; Noguet, C.; Zielinger, J. P.; Joucla, M.; Loison, J. L.; Robino, M.; Herion, J. Preparation and Characterization of Zn_4Sb_3 . *Sol. Energy Mater.* **1985**, *12* (4), 257–274. [https://doi.org/10.1016/0165-1633\(85\)90051-6](https://doi.org/10.1016/0165-1633(85)90051-6).
- (168) Goldsmid, H. J.; Sharp, J. W. Estimation of the Thermal Band Gap of a Semiconductor from Seebeck Measurements. *J. Electron. Mater.* **1999**, *28* (7), 869–872. <https://doi.org/10.1007/s11664-999-0211-y>.
- (169) Wang, S. Y.; She, X. Y.; Zheng, G.; Fu, F.; Li, H.; Tang, X. F. Enhanced Thermoelectric Performance and Thermal Stability in $\beta\text{-Zn}_4\text{Sb}_3$ by Slight Pb-Doping. *J. Electron. Mater.* **2012**, *41* (6), 1091–1099. <https://doi.org/10.1007/s11664-012-1927-7>.
- (170) Zou, T. H.; Qin, X. Y.; Li, D.; Li, L. L.; Sun, G. L.; Wang, Q. Q.; Zhang, J.; Xin, H. X.; Liu, Y. F.; Song, C. J. Enhanced Thermoelectric Performance of $\beta\text{-Zn}_4\text{Sb}_3$ Based Composites Incorporated with Large Proportion of Nanophase Cu_3SbSe_4 . *J. Alloys Compd.* **2014**, *588*, 568–572. <https://doi.org/10.1016/j.jallcom.2013.11.049>.
- (171) Ueno, K.; Yamamoto, A.; Noguchi, T.; Li, C. H.; Inoue, T.; Sodeoka, S.; Obara, H. Effect of Impurity Oxygen Concentration on the Thermoelectric Properties of Hot-Pressed Zn_4Sb_3 . *J. Alloys Compd.* **2006**, *417* (1), 259–263. <https://doi.org/10.1016/j.jallcom.2005.09.014>.
- (172) Zhang, L. T.; Tsutsui, M.; Ito, K.; Yamaguchi, M. Effects of ZnSb and Zn Inclusions on the Thermoelectric Properties of $\beta\text{-Zn}_4\text{Sb}_3$. *J. Alloys Compd.* **2003**, *358* (1), 252–256. [https://doi.org/10.1016/S0925-8388\(03\)00074-4](https://doi.org/10.1016/S0925-8388(03)00074-4).
- (173) May, A. F.; Snyder, G. J. Introduction to Modeling Thermoelectric Transport at High Temperatures. In *Materials, Preparation, and Characterization in Thermoelectrics* (Edited by D. M. Rowe); CRC Press: Boca Raton, FL, 2012.
- (174) Johnson, V.; Jeitschko, W. Ferromagnetic Anti-PbFCI-Type ZnMnSb . *J. Solid State Chem.* **1977**, *22* (1), 71–75. [https://doi.org/10.1016/0022-4596\(77\)90190-6](https://doi.org/10.1016/0022-4596(77)90190-6).

- (175) Bjerg, L.; Iversen, B. B.; Madsen, G. K. H. Modeling the Thermal Conductivities of the Zinc Antimonides ZnSb and Zn₄Sb₃. *Phys. Rev. B* **2014**, *89* (2), 024304. <https://doi.org/10.1103/PhysRevB.89.024304>.
- (176) Song, X.; Finstad, T. G. Review of Research on the Thermoelectric Material ZnSb. *Thermoelectr. Power Gener. - Look Trends Technol.* **2016**. <https://doi.org/10.5772/65661>.
- (177) Blichfeld, A. B.; Iversen, B. B. Fast Direct Synthesis and Compaction of Phase Pure Thermoelectric ZnSb. *J. Mater. Chem. C* **2015**, *3* (40), 10543–10553. <https://doi.org/10.1039/C5TC01611H>.
- (178) Shaver, P. J.; Blair, J. Thermal and Electronic Transport Properties of P-Type ZnSb. *Phys. Rev.* **1966**, *141* (2), 649–663. <https://doi.org/10.1103/PhysRev.141.649>.
- (179) Heikes, R. R.; Miller, R. C.; Ure, R. W. Jr. Survey of Known Thermoelectric Materials. In *Thermoelectricity: Science and engineering*; Interscience Publishers: New York, 1961; p 405.
- (180) Bjerg, L.; Madsen, G. K. H.; Iversen, B. B. Enhanced Thermoelectric Properties in Zinc Antimonides. *Chem. Mater.* **2011**, *23* (17), 3907–3914. <https://doi.org/10.1021/cm201271d>.
- (181) Häussermann, U.; Mikhaylushkin, A. S. Electron-Poor Antimonides: Complex Framework Structures with Narrow Band Gaps and Low Thermal Conductivity. *Dalton Trans.* **2010**, *39* (4), 1036–1045. <https://doi.org/10.1039/B915724G>.
- (182) Tengå, A.; Lidin, S.; Belieres, J.-P.; Newman, N.; Wu, Y.; Häussermann, U. Metastable Cd₄Sb₃: A Complex Structured Intermetallic Compound with Semiconductor Properties. *J. Am. Chem. Soc.* **2008**, *130* (46), 15564–15572. <https://doi.org/10.1021/ja805454p>.
- (183) Štourač, L. The Thermoelectric Efficiency of CdSb and Solid Solutions of Zn_xCd_{1-x}Sb with Hole Conductivity. *Czechoslov. J. Phys. B* **1967**, *17* (6), 543–551. <https://doi.org/10.1007/BF01695177>.
- (184) Zhou, J.; Huang, L.; Wang, Z.; Liu, Z.; Cai, W.; Sui, J. Effect of Cd Isoelectronic Substitution on Thermoelectric Properties of Zn_{0.995}Na_{0.005}Sb. *J. Materiomics* **2016**, *2* (4), 324–330. <https://doi.org/10.1016/j.jmat.2016.08.003>.
- (185) Wang, S.; Li, H.; Qi, D.; Xie, W.; Tang, X. Enhancement of the Thermoelectric Performance of β-Zn₄Sb₃ by in Situ Nanostructures and Minute Cd-Doping. *Acta Mater.* **2011**, *59* (12), 4805–4817. <https://doi.org/10.1016/j.actamat.2011.04.023>.

- (186) Wang, S.; Yang, J.; Wu, L.; Wei, P.; Yang, J.; Zhang, W.; Grin, Y. Anisotropic Multicenter Bonding and High Thermoelectric Performance in Electron-Poor CdSb. *Chem. Mater.* **2015**, *27* (3), 1071–1081. <https://doi.org/10.1021/cm504398d>.
- (187) Zhou, B.; Sun, C.; Wang, X.; Bu, Z.; Li, W.; Ang, R.; Pei, Y. Transport Properties of CdSb Alloys with a Promising Thermoelectric Performance. *ACS Appl. Mater. Interfaces* **2019**, *11* (30), 27098–27103. <https://doi.org/10.1021/acsami.9b10042>.
- (188) Lo, C.-W. T.; Kolodiazny, T.; Song, S.; Tseng, Y.-C.; Mozharivskyj, Y. Experimental Survey of Dopants in Zn₁₃Sb₁₀ Thermoelectric Material. *Intermetallics* **2020**, *123*, 106831. <https://doi.org/10.1016/j.intermet.2020.106831>.
- (189) Giannozzi, P.; Baroni, S.; Bonini, N.; Calandra, M.; Car, R.; Cavazzoni, C.; Ceresoli, D.; Chiarotti, G. L.; Cococcioni, M.; Dabo, I.; Corso, A. D.; Gironcoli, S. de; Fabris, S.; Fratesi, G.; Gebauer, R.; Gerstmann, U.; Gougoussis, C.; Kokalj, A.; Lazzeri, M.; Martin-Samos, L.; Marzari, N.; Mauri, F.; Mazzarello, R.; Paolini, S.; Pasquarello, A.; Paulatto, L.; Sbraccia, C.; Scandolo, S.; Sclauzero, G.; Seitsonen, A. P.; Smogunov, A.; Umari, P.; Wentzcovitch, R. M. QUANTUM ESPRESSO: A Modular and Open-Source Software Project for Quantum Simulations of Materials. *J. Phys. Condens. Matter* **2009**, *21* (39), 395502. <https://doi.org/10.1088/0953-8984/21/39/395502>.
- (190) Perdew, J. P.; Burke, K.; Ernzerhof, M. Generalized Gradient Approximation Made Simple. *Phys. Rev. Lett.* **1996**, *77* (18), 3865–3868. <https://doi.org/10.1103/PhysRevLett.77.3865>.
- (191) Ponou, S.; Lidin, S. α -Cd_{13-x}Sb₁₀ – The Devil Is in the Details. *Z. Für Anorg. Allg. Chem.* **2009**, *635* (12), 1747–1752. <https://doi.org/10.1002/zaac.200900205>.
- (192) Eklöf, D.; Fischer, A.; Wu, Y.; Scheidt, E.-W.; Scherer, W.; Häussermann, U. Transport Properties of the II–V Semiconductor ZnSb. *J. Mater. Chem. A* **2012**, *1* (4), 1407–1414. <https://doi.org/10.1039/C2TA00509C>.
- (193) Benson, D.; Sankey, O. F.; Häussermann, U. Electronic Structure and Chemical Bonding of the Electron-Poor II-V Semiconductors ZnSb and ZnAs. *Phys. Rev. B* **2011**, *84* (12), 125211. <https://doi.org/10.1103/PhysRevB.84.125211>.
- (194) Koumpouras, K.; Larsson, J. A. Distinguishing between Chemical Bonding and Physical Binding Using Electron Localization Function (ELF). *J. Phys. Condens. Matter* **2020**, *32* (31), 315502. <https://doi.org/10.1088/1361-648X/ab7fd8>.
- (195) Schweika, W.; Hermann, R. P.; Prager, M.; Perßon, J.; Keppens, V. Dumbbell Rattling in Thermoelectric Zinc Antimony. *Phys. Rev. Lett.* **2007**, *99* (12), 125501. <https://doi.org/10.1103/PhysRevLett.99.125501>.

- (196) Faghaninia, A.; Lo, C. S. Electronic Transport Calculations for Lightly-Doped Thermoelectrics Using Density Functional Theory: Application to High-Performing Cu-Doped Zinc Antimonides. *arXiv* January 10, 2014. <https://doi.org/10.48550/arXiv.1401.2494>.
- (197) Turner, W. J.; Fischler, A. S.; Reese, W. E. Physical Properties of Several II-V Semiconductors. *Phys. Rev.* **1961**, *121* (3), 759–767. <https://doi.org/10.1103/PhysRev.121.759>.
- (198) Bercha, D. M.; Slipukhina, I. V.; Sznajder, M.; Rushchanskii, K. Z. Elementary Energy Bands in the Band Structure of the Narrow-Band-Gap Semiconductor CdSb. *Phys. Rev. B* **2004**, *70* (23), 235206. <https://doi.org/10.1103/PhysRevB.70.235206>.
- (199) Komiya, H.; Masumoto, K.; Fan, H. Y. Optical and Electrical Properties and Energy Band Structure of ZnSb. *Phys. Rev.* **1964**, *133* (6A), A1679–A1684. <https://doi.org/10.1103/PhysRev.133.A1679>.
- (200) Závětová, M. Absorption Edge of CdSb. *Czechoslov- Fiz. Zurnal B* **1964**, *14* (8), 615–621. <https://doi.org/10.1007/BF01688606>.
- (201) Qiu, A. N.; Zhang, L. T.; Wu, J. S. Crystal Structure, Electronic Structure, and Thermoelectric Properties of β -Zn₄Sb₃. *Phys. Rev. B* **2010**, *81* (3), 035203. <https://doi.org/10.1103/PhysRevB.81.035203>.
- (202) Song, X.; Böttger, P. H. M.; Karlsen, O. B.; Finstad, T. G.; Taftø, J. Impurity Band Conduction in the Thermoelectric Material ZnSb. *Phys. Scr.* **2012**, *T148*, 014001. <https://doi.org/10.1088/0031-8949/2012/T148/014001>.
- (203) Wang, S.; Yang, J.; Wu, L.; Wei, P.; Yang, J.; Zhang, W.; Grin, Y. Anisotropic Multicenter Bonding and High Thermoelectric Performance in Electron-Poor CdSb. *Chem. Mater.* **2015**, *27* (3), 1071–1081. <https://doi.org/10.1021/cm504398d>.
- (204) Gainza, J.; Serrano-Sánchez, F.; Nemes, N. M.; Dura, O. J.; Martínez, J. L.; Alonso, J. A. Lower Temperature of the Structural Transition, and Thermoelectric Properties in Sn-Substituted GeTe. *Mater. Today Proc.* **2021**, *44*, 3450–3457. <https://doi.org/10.1016/j.matpr.2020.03.044>.
- (205) Liu, W.; Shi, X.; Hong, M.; Yang, L.; Moshwan, R.; Chen, Z.-G.; Zou, J. Ag Doping Induced Abnormal Lattice Thermal Conductivity in Cu₂Se. *J. Mater. Chem. C* **2018**, *6* (48), 13225–13231. <https://doi.org/10.1039/C8TC04129F>.
- (206) Klemens, P. G. The Scattering of Low-Frequency Lattice Waves by Static Imperfections. *Proc. Phys. Soc. Sect. A* **1955**, *68* (12), 1113–1128. <https://doi.org/10.1088/0370-1298/68/12/303>.

- (207) Shaver, P. J.; Blair, J. Thermal and Electronic Transport Properties of P-Type ZnSb. *Phys. Rev.* **1966**, *141* (2), 649–663. <https://doi.org/10.1103/PhysRev.141.649>.
- (208) Okamura, C.; Ueda, T.; Hasezaki, K. Preparation of Single-Phase ZnSb Thermoelectric Materials Using a Mechanical Grinding Process. *Mater. Trans.* **2010**, *51* (5), 860–862. <https://doi.org/10.2320/matertrans.MH200902>.
- (209) Boström, M.; Lidin, S. The Incommensurably Modulated Structure of ζ -Zn_{3-x}Sb₂. *J. Alloys Compd.* **2004**, *376* (1), 49–57. <https://doi.org/10.1016/j.jallcom.2003.12.017>.
- (210) Birkel, C. S.; Mugnaioli, E.; Gorelik, T.; Kolb, U.; Panthöfer, M.; Tremel, W. Solution Synthesis of a New Thermoelectric Zn_{1+x}Sb Nanophase and Its Structure Determination Using Automated Electron Diffraction Tomography. *J. Am. Chem. Soc.* **2010**, *132* (28), 9881–9889. <https://doi.org/10.1021/ja1035122>.
- (211) Toberer, E. S.; Sasaki, K. A.; Chisholm, C. R. I.; Haile, S. M.; Goddard III, W. A.; Snyder, G. J. Local Structure of Interstitial Zn in β -Zn₄Sb₃. *Phys. Status Solidi RRL – Rapid Res. Lett.* **2007**, *1* (6), 253–255. <https://doi.org/10.1002/pssr.200701168>.
- (212) Bjerg, L.; Iversen, B. B.; Madsen, G. K. H. Modeling the Thermal Conductivities of the Zinc Antimonides ZnSb and Zn₄Sb₃. *Phys. Rev. B* **2014**, *89* (2), 024304. <https://doi.org/10.1103/PhysRevB.89.024304>.
- (213) Hammersley, A. P.; Svensson, S. O.; Hanfland, M.; Fitch, A. N.; Hausermann, D. Two-Dimensional Detector Software: From Real Detector to Idealised Image or Two-Theta Scan. *High Press. Res.* **1996**, *14* (4–6), 235–248. <https://doi.org/10.1080/08957959608201408>.
- (214) Wu, Y.; Nylén, J.; Naseyowma, C.; Newman, N.; Garcia-Garcia, F. J.; Häussermann, U. Comparative Study of the Thermoelectric Properties of Amorphous Zn₄₁Sb₅₉ and Crystalline Zn₄Sb₃. *Chem. Mater.* **2009**, *21* (1), 151–155. <https://doi.org/10.1021/cm802893v>.
- (215) Toberer, E. S.; Zevalkink, A.; Snyder, G. J. Phonon Engineering through Crystal Chemistry. *J. Mater. Chem.* **2011**, *21* (40), 15843–15852. <https://doi.org/10.1039/C1JM11754H>.
- (216) Deng, S.; Li, D.; Zheng, L.; Tang, Y.; Chen, Z.; Sun, L.; Liu, W.; Shen, L.; Deng, S. Crystal Growth, Thermal Stability and Electrical Transport Property of Double-Doping (Sn/Cd) System in Single-Crystal β -Zn₄Sb₃. *Phys. Status Solidi A* **2018**, *215* (11), 1700905. <https://doi.org/10.1002/pssa.201700905>.
- (217) Deng, S.; Tang, Y.; Li, D.; Liu, H.; Chen, Z.; Shen, L.; Deng, S. Thermal Stability and Electrical Transport Properties of Single-Crystalline β -Zn₄Sb₃ Co-Doped by

Ga/Sn. *J. Electron. Mater.* **2017**, *46* (12), 6804–6810.
<https://doi.org/10.1007/s11664-017-5747-7>.

- (218) Pothin, R.; Ayrat, R. M.; Berche, A.; Granier, D.; Rouessac, F.; Jund, P. Preparation and Properties of ZnSb Thermoelectric Material through Mechanical-Alloying and Spark Plasma Sintering. *Chem. Eng. J.* **2016**, *299*, 126–134.
<https://doi.org/10.1016/j.cej.2016.04.063>.
- (219) Petříček, V.; Dušek, M.; Palatinus, L. Crystallographic Computing System JANA2006: General features. *Z. Kristallogr. - Cryst. Mater.* **2014**, *229* (5), 345–352.
<https://doi.org/10.1515/zkri-2014-1737>.
- (220) Jakob, M.; Grauer, M.; Ziolkowski, P.; Oeckler, O. Decomposition Phenomena of $\text{Zn}_{13-\delta}\text{Sb}_{10}$ under Working Conditions of Thermoelectric Generators and Minimum Current Densities for Electromigration. *ACS Appl. Energy Mater.* **2020**, *3* (3), 2103–2109. <https://doi.org/10.1021/acsaem.9b02138>.
- (221) Yin, H.; Blichfeld, A. B.; Christensen, M.; Iversen, B. B. Fast Direct Synthesis and Compaction of Homogenous Phase-Pure Thermoelectric Zn_4Sb_3 . *ACS Appl. Mater. Interfaces* **2014**, *6* (13), 10542–10548. <https://doi.org/10.1021/am502089a>.